INVESTIGATING THE SELF-MONITORING POTENTIALS OF AN ENGINEERED CEMENTITIOUS COMPOSITE

By

Danah Saraireh

Submitted for the degree of Doctor of Philosophy

Heriot-Watt University

School of Energy, Geoscience, Infrastructure and Society

May 2022

1

ABSTRACT

Cement-based materials are an important group of structural materials, and the ability of such materials to respond to internal and external changes could provide an added feature which could further enhance their range of application. One area of development that has received increasing attention within the research community is making use of the self-monitoring features of concrete with respect to deformation and damage. Ordinary concrete is, however, a poor conductor of electricity, particularly after cracking and under dry conditions, and attention is therefore directed towards a highly damage-tolerant family of concrete types with superior tensile strain capacities and controllable crack widths, generally known as the Engineered Cementitious Composite (ECC).

This thesis explores the self-monitoring capabilities of the ECC under mechanical and non-mechanical loading and presents the a.c. electrical properties of ECC over the frequency range 1 Hz–10 MHz. The project was developed on three general fronts, focusing on key factors affecting the electrical properties of ECC:

(i)   investigation of the influence of cement hydration and temperature;

(ii)   evaluation of the influence of tensile straining and cracking; and

(iii)   investigation of the influence of wetting and drying.

Laboratory samples of different geometries were fabricated and tested under various curing regimes and test conditions. Results are presented from each of the sub-themes listed above, with measured data presented in a range of formats to provide insights into features that could potentially be exploited for self-monitoring. This includes the Nyquist format, which has been generally used in a.c. electrical property measurements, and the permittivity and conductivity, which were de-embedded from the measured impedance and presented in the frequency domain to elucidate the nature of the conduction and polarization processes. Equivalent circuit models were also developed to simulate the measured response and offer a phenomenological interpretation of the origin of some of the features observed in the electrical response.

It was found that, over a curing period of 180 days, the ECC displayed a classic impedance response comprising an electrode spur, a weak intermediate "plateau" region and a single bulk arc. Both conductivity and relative permittivity were found to be

frequency dependent due to bulk relaxation processes operating within the composite. It was found that cement hydration has a negligible effect on the relative permittivity at high frequencies (i.e., > 1 MHz), as evidenced by the merging of the relative permittivity at different curing ages when presented in a logarithmic format. Moreover, the knowledge regarding the temperature effects on the electrical properties (through the activation energy approach) will have direct practical significance for removing the effect of natural temperature fluctuations.

Tensile straining was shown to result in a detectable change in the impedance response but retained a similar overall profile. When presented in the frequency domain, a downward displacement in relative permittivity at high frequency (i.e., 1 MHz) was evident with increasing tensile strain for ECC with average crack widths in the range 50 μm–65 μm. In the ECC with larger average crack widths (i.e., >100 μm), a downward displacement in relative permittivity profiles together with an enhancement of the relative permittivity within the frequency range (> 10 kHz to ~low MHz) was observed. Overall, it is shown that the relative permittivity at the high-frequency end could be exploited as a potentially useful indicator for strain/damage detection.

The electrical properties of ECC display significant increases in the impedance response when the material is subjected to drying. When presented in the frequency domain, an enhancement of the relative permittivity within the frequency range > 1 kHz to ~low MHz was observed. Within the low-frequencies range of ~1Hz to < 1 kHz, the relative permittivity of the un-cracked ECC curves showed a slight decrease, while the cracked-ECC was sensitive to drying. When subjected to wetting, a reduction of the impedance response was observed, and the enhancement of the relative permittivity at high frequencies disappeared, due to the presence of water in the micro-cracks.

This thesis demonstrates the use of multi-frequency measurements to characterise the electrical properties of ECC under mechanical and non-mechanical loading.

DEDICATION

To my dad, Mohammad Saraireh for his great support

ACKNOWLEDGMENTS

I would like to express my sincere gratitude to Dr. Benny Suryanto for his unconditional assistance, invaluable advice, and patience during my PhD journey. His vast knowledge and abundant experience have enhanced me personally and professionally. My special thanks go to my external examiner, Dr. Richard Ball, and my internal examiner, Dr. Demitrios Cotsovos, for their kindness and patience in going through my manuscript. I would also like to thank Prof. W. John McCarter, Prof. Dimitry Val, and Dr. Gerry Starrs for their support. I am also grateful to the technical staff, who participated in this great experience and gave me the support I needed when needed. I would also like to acknowledge the financial support of the Engineering and Physical Sciences Research Council, U.K. (Grant EP/N028597/1).

Then, I would like to express all my love and kindness to my parents (Mohammad Saraireh and Iman Muwafi) for their endless support and love. I would not have made it here without you both. I'm deeply grateful to my husband (Hussein Hasan) for his continuous love, help, and support, as well as to my son (Kinan Hasan), who has illuminated my days and nights for two years. Also, without forgetting, my sister (Linah Saraireh), and my brothers (Hamzeh, Zaid, and Omar Saraireh) for always being there for me as friends and support.

Last but not least, a special thanks to my friends, Dr. Asdam Tambusay, Dr. Michael Gerges, Mohamed Suliman, Mohammed Bolbol, Aseel Nawaiseh, and Nada Al Ali for all the support they gave me.

RESEARCH THESIS SUBMISSION

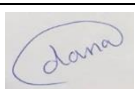| Name:	Danah Saraireh		
School:	EGIS		
Version: (i.e. First, Resubmission, Final)	Final	Degree Sought:	PhD

Declaration

In accordance with the appropriate regulations I hereby submit my thesis and I declare that:

1. The thesis embodies the results of my own work and has been composed by myself
2. Where appropriate, I have made acknowledgement of the work of others
3. The thesis is the correct version for submission and is the same version as any electronic versions submitted*.
4. My thesis for the award referred to, deposited in the Heriot-Watt University Library, should be made available for loan or photocopying and be available via the Institutional Repository, subject to such conditions as the Librarian may require
5. I understand that as a student of the University I am required to abide by the Regulations of the University and to conform to its discipline.
6. I confirm that the thesis has been verified against plagiarism via an approved plagiarism detection application e.g. Turnitin.
7. Where the thesis contains published outputs under Regulation 6 (9.1.2) or Regulation 43 (9) these are accompanied by a critical review which accurately describes my contribution to the research and, for multi-author outputs, a signed declaration indicating the contribution of each author (complete)
8. Inclusion of published outputs under Regulation 6 (9.1.2) or Regulation 43 (9) shall not constitute plagiarism.

* *Please note that it is the responsibility of the candidate to ensure that the correct version of the thesis is submitted.*

Signature of Candidate:	*dana*	Date:	04-05-2022

Submission

Submitted By (name in capitals):	DANAH SARAIREH
Signature of Individual Submitting:	*dana*
Date Submitted:	04-05-2022
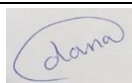
For Completion in the Student Service Centre (SSC)
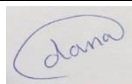
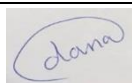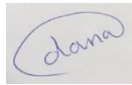| Limited Access	Requested	Yes		No		Approved	Yes		No	
E-thesis Submitted (mandatory for final theses)										
Received in the SSC by (name in capitals):						Date:				

INCLUSION OF PUBLISHED WORKS

Declaration

This thesis contains one or more multi-author published works. In accordance with Regulation 6 (9.1.2) I hereby declare that the contributions of each author to these publications is as follows:

Citation details	**Saraireh, D.**, Suryanto, B., McCarter, W. J. and Walls, S. (2021) 'The electro-mechanical tensile properties of an engineered cementitious composite', Advances in Cement Research, pp.1-18. https://doi.org/10.1680/jadcr.19.00119
Author 1	Performing experiment, data curation, writing draft, data visualisation
Author 2	Supervision, reviewing/revising draft, funding acquisition.
Signature:	
Date:	04-05-2022

Citation details	**Saraireh, D.**, Walls, S., Suryanto, B., Starrs, G. and McCarter, W. J. (2017) 'The influence of multiple micro-cracking on the electrical impedance of an engineered cementitious composite', *In International Conference on Strain-Hardening Cement-Based Composites*, pp.292-299. https://doi.org/10.1007/978-94-024-1194-2_34
Author 1	Performing experiment, data curation, writing draft, data visualization.
Author 2	Supervision, reviewing/revising draft, funding acquisition.
Signature:	
Date:	04-05-2022

Citation details	**Saraireh, D.**, Suryanto, B. and Tambusay, A. (2020) 'Effect of micro-cracking on the electrical and self-sensing properties of an engineered cementitious composite under tensile straining', *In IOP Conference Series: Materials Science and Engineering*, 930(1), pp. 012054. https://doi.org/10.1088/1757-899X/930/1/012054
Author 1	Supervision, reviewing/revising draft, funding acquisition.
Author 2	Funding acquisition, supervision, reviewing draft.
Signature:	
Date:	04-05-2022

Citation details	Suryanto, B., **Saraireh, D.** and Tambusay, A. (2020) 'Temperature dependence and activation energy of electrical conduction in an engineered cementitious composite', In *IOP Conference Series: Materials Science and Engineering*, 930(1), pp. 012053. https://doi.org/10.1088/1757-899X/930/1/012053
Author 1	Supervision, reviewing/revising draft, funding acquisition.
Author 2	Performing experiment, data curation, writing draft, data visualization.
Signature:	*dana*
Date:	04-05-2022

TABLE OF CONTENTS

TABLE OF FIGURES

TABLE OF TABLES

LIST OF ANOTIATIONS

A	cross-sectional area
T_k	temperature (Kelvin)
f_t	tensile stresses
p	an exponent (it has a value between 0 to 1)
t_{28}	time at 28-day of curing
C_o	a coefficient
ΔL	length change
P	load recorded from the load cell mounted in the Instron (in N)
a	correction factor (within the range of 0.4 to 2.5)
$\kappa_{r,t}$	bulk relative permittivity of the composite at strain ε_t after the start of the test
g_p	geometrical constant for the prism specimen (=88.48/m)
κ_o	permittivity of free space (8.854×10^{-12} Farads/m)
$\sigma(\omega)$	bulk conductivity (S/m)
$Z(\omega)$	electrical impedance (Ω)
$Z''(\omega)$	reactive (imaginary) component of impedance (Ω)
$\kappa_r'(\omega)$	relative permittivity
$Z'(\omega)$	resistive (real) component of impedance (Ω)
ρ_{28}	28 d electrical resistivity (Ωm)
$\rho(\omega)$	bulk resistivity (Ωm)
ρ_i	initial bulk resistivity (at time = 0) (Ωm)
ε_t	tensile strain at time t after the start of the test
$R_{db,28}$	28 d electrical resistance for the dog-bone specimen (Ω)
$R_{p,28}$	28 d electrical resistance for the prism specimen (Ω)
κ_{cr}	average relative permittivity of the micro-cracks
g_{db}	geometrical constant for the dog-bone specimen (=245.28/m)
$\kappa_{r,i}$	initial bulk relative permittivity of the composite (at time = 0)
$\phi_{r,i}$	initial volume at the start of the test
$\phi_{r,t}$	total volume at strain ε_t after the start of the test
ϕ_{cr}	volume fraction of the micro-cracks at strain ε_t
ρ_t	bulk resistivity at strain ε_t after the start of the test (Ωm)
σ_{28}	conductivity at a 28-day of curing

B	binder
C	cement
C_i	constant coefficient
CoV	coefficient of variation
CPE_c	capacitive effect results from the physical separation of the matrix due to cracks
CPE_{c-cp}	capacitive component of the matrix between the carbon fibres
CPE_{ci}	capacitive component represents the carbon-fibre/matrix interface
CPE_{el}	capacitive component of the matrix between the electrode/matrix interface
CPE_{fi}	capacitive component represents the fibre/matrix interface
CPE_{f-sm}	capacitive component of the matrix between the fibres
CPE_{sm}	constant phase element represents the solid matrix
CWD	crack width distribution
DB	Dog-bone
E_a	activation energy (J mol^{-1})
ECC	engineered cementitious composite
ECM	equivalent circuit modelling
E-ECC-NC	non pre-cracked samples
E-ECC-P	ECC mix without PVA fibres
f	the applied-field frequency (hertz)
F	formation factor
F_{180}	180 d compressive strength (50 mm cube)
F_{28}	28 d compressive strength (50 mm cube)
F_{90}	90 d compressive strength (50 mm cube)
FA	fly-ash
f_c	cusp-point frequency (Hz)
FCR	fractional change in resistivity
f_p	peak frequency (Hz)
f_{tcr}	first crack tensile stress (MPa)
f_{tu}	tensile strength (MPa)
GF	gauge factor
GF_e	elastic gauge factor
HFA	high-volume fly-ash ECC mix

HRWR	high-range water-reducing
K_i	constant coefficient
L	gauge length
ln (ρ)	natural logarithm of bulk resistivity
LVDTs	linear variable differential transducers
m	mean
M	cementation exponent (within the range of 1.2 to 2.5)
M(ω)	electric-modulus
M45	moderate-volume fly-ash ECC mix
MB	base ECC mix
MF0	mortar
MF15	ECC with 15% fly-ash replacement
MF30	ECC with 30% fly-ash replacement
MF64	ECC with 64% fly-ash replacement
n	numbers of cracks
N	aging (or hydration) exponent
N_c	change in conductivity in relation to its initial value
NDE	non-destructive evaluation
O	arc centre
OPC	ordinary Portland cement
PC	mortar
PDF	probability density function
PVA	polyvinyl Alcohol
PZT	lead zirocondate titanate
R	bulk resistance
R(ε)	changes in resistance at strain ε_t (Ω)
R_0	initial resistance (at t = 0) (Ω)
R_c	resistor represents the conduction through the micro-cracks
R_{c-cp}	resistor represents the conduction through the matrix between the carbon fibres
R_{c-f}	resistor represents the conduction through the carbon fibres
R_{ci}	resistor represents the conduction through the carbon fibre/matrix interface
R_{cp}	resistor represents the ionic conduction

R_{el}	resistor represents the conduction through the electrode/matrix interface
R_f	resistor represents the conduction through the fibre-fibre contact
R_{f-cp}	resistor represents the conduction through the matrix between the fibres
R_{fi}	resistor represents the conduction through the fibre/matrix interface
R_g	universal gas constant ($8.3141\ J\ mol^{-1}K^{-1}$)
R_s	resistor represents the projected intercept
R_t	measured resistance at any time
R_x	the bulk resistance at reference temperatures
R_y	the bulk resistance at measured temperatures
S	sand
SA or s	standard deviation
SHM	structural health monitoring
SMAs	shape memory alloys
S_r	degree of saturation of the pore network
t	time
T-ECC-L	second series of ECC mix with larger crack width
T-ECC-PC	pre-cracked samples
T-ECC-S	first series of ECC mix with smaller crack width
T-ECC-TF	ECC samples tested till failure
$T_{k,x}$	reference temperature (Kelvin)
$T_{k,y}$	measured temperature (Kelvin)
VBDD	vibration-based damage detection
VCCTL	virtual cement and concrete testing laboratory
W	water
WP	work plan
$Y(\omega)$	admittance
α	arc depression angle
δ	crack width
ΔR	changes in resistance (Ω)
ΔR_c	change of resistance due to strain caused by cracking
ΔR_e	change of resistance due to elastic strain
ε	tensile strain
ε_c	strain caused by cracking
ε_e	elastic strain

ε_{tu}	tensile strain capacity
θ	phase angle
ρ_f	resistivity of the water saturating the pores (i.e., pore solution) (Ωm)
ρ_r	resistivity of a fully water-saturated rock-sample (Ωm)
ρ_w	resistivity of pore water
σ_o	initial conductivity (at time = 0)
σ_{ref}	reference conductivity at a reference time
σ_t	conductivity at a time (t)
ϕ	rock porosity
ω	angular frequency
ε_{tu}	tensile strain capacity
$\sigma_d(\omega)$	conductivity resulting from dissipative polarization processes
$\sigma(0)$	ionic conduction process via the percolated capillary pore network

1 Introduction

1.1 Background

Concrete is the most widely used construction material, with a large proportion of infrastructure worldwide built using concrete in one form or another. While most key infrastructure is designed for an intended working life of at least 100 years, premature deterioration remains commonplace (Li et al., 2009). Although some deterioration may not have a direct impact on structural integrity, immediate repair may be required so as not to impair in-service performance (Frangopol et al., 2017; Highways England, 2017). The earlier any deterioration is detected, the earlier appropriate remedial measures can be taken, thereby avoiding the need for costly repairs at a later stage (Kharroub et al., 2015; McCarter et al., 2017). With the ever-increasing amount of infrastructure around the world and the continual deterioration of existing infrastructure caused by aging of materials, severe weather events, overloading, prolonged usage, and/or poor maintenance (Rana et al., 2016), it is expected that structural inspection and maintenance will have an increasing role to play for the foreseeable future.

The common practice for structural performance evaluation is performed through visual inspections (Chang et al., 2003). This requires direct site visits by qualified engineers at predetermined times during the life of a structure. For instance, the Highways Agency, which is an executive agency of the UK government in charge of operating and maintaining the UK's strategic highway network, requires the bridge to be visually inspected (general inspections) every two years, with principal inspections must take place every six years (Highways Agency, 2007) to allow for early detection of structural damage (Rana et al., 2016; Riches et al., 2019). While visual inspection is relatively straightforward to undertake and allows evidence to be gathered directly on-site, it only provides a snapshot of information in time; it is the change in condition with time which needs to be assessed so as to provide a reliable assessment of structural health (Choi et al., 2004; Hedegaard, 2017). A further limitation of visual inspection is that some damage may not be readily visible, thereby remaining undetected until advanced stages, which are costly to repair. There is a need for advanced monitoring systems to be developed not only for structural integrity monitoring (Sasmal et al., 2017), but also for condition monitoring under day-to-day service conditions. Implementing such a Structural Health Monitoring (SHM) system has the potential to mitigate the shortcomings of traditional on-site inspection (i.e., reliability, variability, and

subjectivity) (Brownjohn et al., 2001). Automating such a monitoring system also has the potential not only to reduce man-hours but also to provide continuous feedback in real-time on the current condition of a structure (Chowdhury et al., 2015; Brownjohn, 2007), which can be used to provide an early warning of incipient problems (Wu, 2003) and assess the future performance of the structure (Culshaw, 1998). The availability of monitoring data can also assist in the scheduling of repair and maintenance (McCarter et al., 2010).

There are a number of SHM systems already implemented in real structures and bridges. Consider, for example, the Queensferry Crossing in Scotland, the UK, which was opened in 2017. The bridge is located in the Forth estuary, meaning that it has been, and will be, constantly exposed to a harsh environment, thereby increasing the likelihood of premature deterioration. A SHM system was therefore installed, involving approximately 2000 sensors (see Table 1.1) for monitoring the bridge and exposure data (Riches et al., 2019). Another example is the Jiangyin Bridge in China, which was completed in 1999. A large number of sensors were installed after the bridge's completion, comprising displacement transducers, anemometers, temperature sensors, and GPS antennae (Sun and Sun, 2018), the schematic of which is presented in Figure 1.1.

Table 1.1: Sensors at Queensferry Crossing (Riches et al., 2019).

	Sensor	Number
Environmental actions	Anemometers	11
	Rainfall gauges	2
	Barometers	2
	Asphalt temperature sensors	40
	Concrete deck temperature sensors	70
	Concrete tower temperature sensors	46
	Stay-cable temperature sensors	56
	Steel surface temperature sensors	158
	Air temperature sensors	13
	Relative humidity sensors	12
	Corrosion sensors	360
Bridge actions	Dynamic weigh-in-motion sensors	96
Bridge response	Accelerometers	102
	Bearing gauges	16
	Displacement transducers	32
	Tilt meters	48
	GPS sensors	21
	Static strain gauges and thermistors	284
	Dynamic strain gauges and thermistors	603
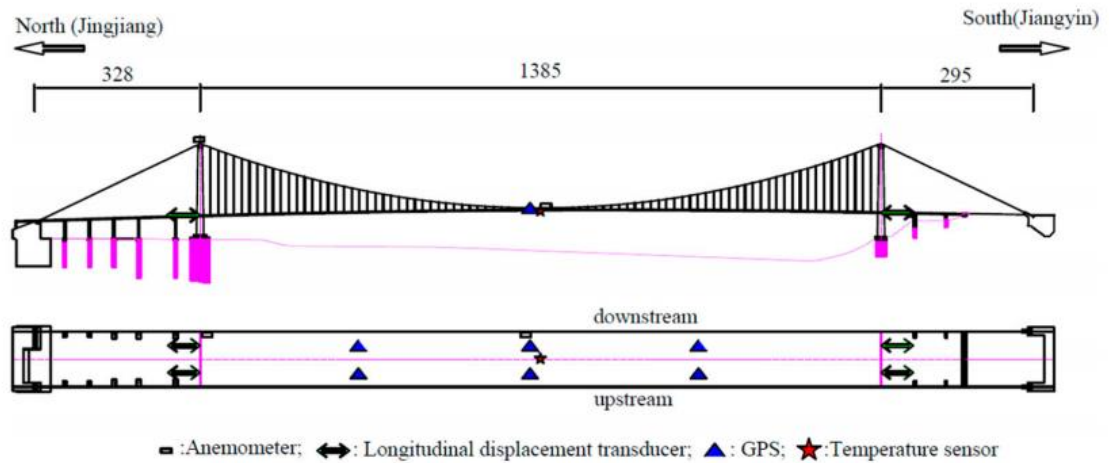
Figure 1.1: Schematic diagram of the Jiangyin Bridge's SHM system (Sun and Sun, 2018).

Implementation of such a SHM system in a large-scale real-world infrastructure poses considerable technical challenges and costs (García-Macías et al., 2017), mainly due to the requirement for the installation of an extensive number of sensors (Chintalapudi et al., 2006; Jayawardhana et al., 2017). Sensor maintenance and replacement with time should also be mentioned. Given that, with more demands being made on resilient reinforced concrete structures, a 100-year life becomes a necessity, which would clearly pose a significant challenge to the life of sensors that are currently available on the market.

A significant body of research has therefore been conducted over the years to explore the use of concrete itself as a sensor, making it literally a self-monitoring material. Due to the omnipresence of concrete (Ranade et al., 2014), this added function of concrete, if successfully developed, could offer a more cost-effective solution. Recent developments in the field include moisture sensors (McCarter et al., 2001; McCarter et al., 2012), weight in-motion and traffic sensors (Shi and Chung, 1999; Han et al., 2013) and strain/damage sensors (Chung, 2000; Azhari and Banthia, 2012). While the sensing capabilities of cement-based strain/damage sensors have been well documented (Chen and Chung, 1993; Wen and Chung, 2000; Wen and Chung; 2001; Wen and Chung, 2005; Wen and Chung, 2006; Wen and Chung, 2007a; Wen and Chung, 2007b; Chen and Wu, 2005; Han and Ou, 2007; Vilaplana et al., 2013; Reza et al., 2003), this type of cement-based sensors may only be able to be employed under limited damage levels as the relationship between damage and strain increases nonlinearly after cracking. This intrinsic limitation of concrete has directed this research

towards the use of a damage-tolerant cement-based material known as the Engineered Cementitious Composite (ECC).

An ECC is a highly ductile group of fiber-reinforced cementitious composites with a superior tensile strain capacity (typically greater than 1%, or two orders of magnitude greater than traditional concrete) and damage tolerance due to its inherent crack control ability (typical crack width is less than 0.1 mm) (Li, 2003; Li, 2008; Ranade et al., 2014). An ECC shares similar constituents with other types of fibre reinforced concrete (FRC), with the exception of the absence of coarse aggregates in the ECC, thereby making it technically regarded as mortar rather than concrete. However, unlike ordinary concrete and FRC in general, an ECC behaves differently when subjected to tension, exhibiting a strain-hardening behaviour with a high tensile ductility, typically well in excess of 1% (see Figure 1.2). This is achieved through the development of multiple micro-cracks, which are the source of the high tensile ductility (Li, 2012). The width of these micro-cracks is typically less than 100 μm (Li, 2008; Suryanto et al., 2015; Lee et al., 2018; Chen et al., 2018; Frank et al., 2018; Ma et al., 2019) and, as such, they are barely visible to the naked eye, making it essentially a damage-tolerant material.
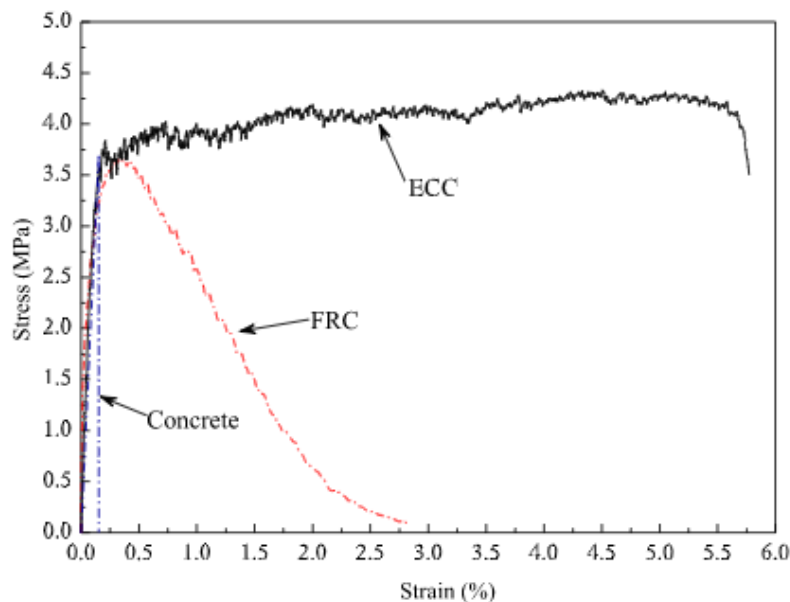
Figure 1.2: Tensile stress-strain diagram illustrating the tensile strain-hardening behaviour of ECC, tension-softening fibre reinforced concrete (FRC) and the quasi-brittle nature of ordinary concrete (Li et al., 2015).

Apart from possessing a damage-tolerant property, recent studies have shown that ECCs have distinctive piezo-resistive properties and hence have been identified as potential damage sensors (Hou and Lynch, 2005a; Hou, 2008; Lin et al., 2011; Ranade et al., 2014; Suryanto et al., 2015; Liu et al., 2016; Huang et al., 2018; Deng and Li, 2018; Yıldırım et al., 2020). Hou and Lynch (2005a) demonstrated, for example, that ECC behaves as a piezo-resistive material with bulk resistivity comparable to that of a semi-conductor, which typically lies in the range of 1×10^1 to 1×10^5 Ω-cm (Chung, 2002; Hou and Lynch, 2005a; Ranade et al., 2014). In this work, the term piezo resistivity was used to represent the change in resistivity due to mechanical strain, a feature that has been investigated in a number of studies to explore the potential of ECC as a self-sensing material (Hou and Lynch, 2005a; Hou, 2008; Lin et al., 2011; Ranade et al., 2014; Suryanto et al., 2015; Liu et al., 2016; Huang et al., 2018; Deng and Li, 2018; Yıldırım et al., 2020). However, it is worth noting that, given that ECC is a cement-based material by its nature, its electrical properties (including the resistivity) will also be affected by a number of other factors such as hydration (Suryanto et al., 2016), moisture change (Suryanto et al., 2017a), and temperature (Suryanto et al., 2020a). It is, therefore, necessary to have a fuller understanding of the effect of these factors on the electrical properties of ECC when exploring the self-sensing abilities of ECC. Accordingly, there is a need to develop a systematic approach that can be used to address the influence of each contributing factor, such as hydration, moisture, cracking, and temperature in isolation. This thesis provides a better understanding of these factors through three series of experiments focusing on the electrical properties of ECC in the un-cracked and cracked conditions when subjected to mechanical and non-mechanical loading.

As a way of illustration, Figure 1.3 displays the potential application of self-monitoring ECC in reinforced concrete structures. Two areas of application are noteworthy:

(i)   the use of ECC in moisture and/or temperature sensors; and

(ii)   condition and/or damage monitoring.

Regarding the former (i), a thin ECC layer could possibly be applied to the surface region of reinforced concrete structures (as a surface coating material) and be used to monitor moisture (and possibly ionic) movement within the surface zone, thereby providing an added monitoring function. It is noteworthy that in this situation, the presence of ECC in the surface region could also provide additional protection to the

base concrete due to its superior damage tolerant property. Regarding the thin ECC layer, this could be applied through spraying the ECC material directly onto the surface. According to Kojima et al. (2014), the 60-plus-year-old Mitaka Dam in Hiroshima Prefecture, Japan was repaired from cracks, water leakage, and spalling by spraying a 20 mm ECC layer on about 600 m^2 of the upper dam surface. For moisture sensors, stainless steel electrode pins can be embedded within the thin ECC layer during the casting time. An alternating electrical field can be used to measure the impedance. Although the concept is simple, the electrode size and geometry are very important. According to McCarter et al. (2005), the electrical field between the electrode pins should be limited to a small volume of material, as the sensitivity will be decreased if the electrical field propagates to occupy a large volume. Based on experimental programs conducted by McCarter et al. (2005) and Suryanto et al. (2017), the horizontal centre-to-centre spacing between the electrode pairs was 5 mm. Furthermore, the electrode pairs will be placed at different depths and arranged in a staggered position, while the maximum depth should not exceed 20 mm. This is because at a depth higher than 20 mm, the ECC is more affected by the microstructural changes (on-going hydration and pozzolanic reactions) not the drying action (Suryanto et al., 2017a). In addition, thermistors will also be mounted on the thin ECC layer, enabling temperature to be monitored.

With regard to the potential of ECC as a condition/damage monitoring system, such features could be incorporated within concrete structures by embedding an insulated ECC block into structural components such as beams, columns, and walls during construction (It could be installed in critical areas of structural components). Although this potential of ECC would be ideally suited for new-built construction, the same concept could possibly be applied to existing structures, with concrete at different locations being cored, the ECC 'sensor' being inserted, and the remaining gaps then grouted to ensure continuity with the surrounding concrete. With regard to the filler, it must have the same mechanical properties as the existing concrete in order to accurately monitor the condition of the structure. Since the damage detection in new-and existing-buildings was demonstrated by Downey et al. (2017) and Meoni et al. (2018) using smart bricks, the same concept can be followed using ECC-blocks. Therefore, based on Downey et al. (2017) and Meoni et al. (2018) visions, the ECC blocks will be placed at critical locations within the structure.

For monitoring purposes, simple electrical devices could be connected to these sensors and be used to stream data for remote monitoring, as demonstrated in the trial remote interrogation system installed at a marine site on the Dornoch Firth in North East Scotland (McCarter et al., 2012; Kim et al., 2018), and data will be uploaded by a dial-up modem and then recorded in a CSV file using software installed on the office-based computer. Regarding the electrical measurements, multi-frequency measurements must be performed covering at least 13 spot frequencies (i.e., 100 Hz, 200 Hz, 500 Hz, 1 kHz, 2 kHz, 5 kHz, 10 kHz, 20 kHz, 50 kHz, 100 kHz, 200 kHz, 500 kHz, and 1 MHz).
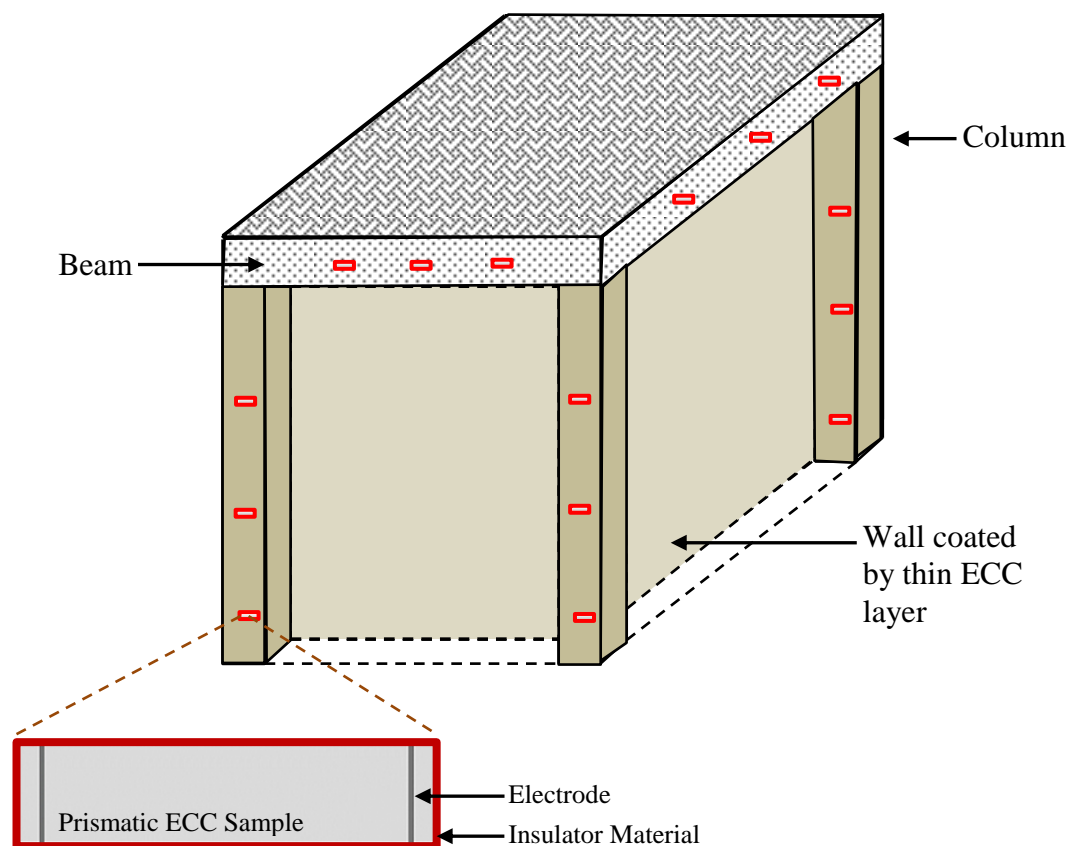
Figure 1.3: Potential applications of self-monitoring ECC in existing or new-built reinforced concrete structures.

1.2   Aims and Objectives

The primary aim of this PhD is to explore the self-monitoring potential of Engineered Cementitious Composites (ECC) through exploiting its electrical properties under both mechanical and non-mechanical loading. The primary motivation of this work is to

distinguish features in the electrical properties of ECC arising from mechanically induced phenomena and those arising from non-mechanical loading such as cement hydration and related phenomena; changing levels of pore saturation due to the ingress and egress of moisture in the surface region of concrete structures; and fluctuations in temperature, as would be expected in general structures. Other than this, the aim of the work presented in this thesis is to demonstrate the sensitivity of the electrical properties of an ECC mix developed at Heriot-Watt University, with an outlook for exploiting its self-monitoring feature in the future. More specifically, the objectives of this research are:

1) To investigate the fundamental electrical properties of ECC while in the un-cracked state, covering three main strands of themes:
   a) To examine the influence of cement hydration in ECC on the electrical properties of the cement composite over the frequency range 1 Hz–10 MHz. This wide frequency range was particularly considered to provide detailed information on the fundamental electrical properties of ECC;
   b) To assess the nature of conduction and polarization processes within the composite, with the main emphasis on exploring features of response which could potentially be exploited for monitoring purposes;
   c) To investigate the effect of temperature on the electrical properties of ECC over the frequency range 20 Hz–1 MHz;

2) To investigate the electrical properties of ECC in the cracked state. More specifically,
   a) To explore the relationship between mechanical and electrical properties over the frequency range 100 Hz–1 MHz;
   b) To relate the electrical properties with the occurring crack patterns under loading. Both direct (visual) observations and an automated technique (digital image correlation) will be undertaken to provide supporting evidence on the electrical response measured at the composite level;
   c) To examine the influence of micro-cracking and tensile straining on the composite electrical behavior and investigate features for self-monitoring;
   d) To explain the changes in electrical properties at the composite level based on the response of individual micro-crack;

3) To investigate the electrical properties of ECC in the un-cracked and cracked states. Within this objective,

   a) To investigate the effect of moisture gain/loss on the electrical behaviour of ECC with and without the presence of cracking over the frequency range 1 Hz–10 MHz;

   b) To relate the electrical properties of ECC with the fundamental properties (i.e. porosity and degree of saturation).

In each objective strand above, the Equivalent Circuit Modelling (ECM) was undertaken to assist data interpretation and provide explanations of the underlying phenomena affecting the observed changes in electrical properties at the macro (composite) level.

1.3 Originality and Significance

To date, only limited work has been done to study the electrical properties of ECC (Hou and lynch, 2005; Hou, 2008; Lin et al., 2011; Ranade et al., 2014; Suryanto et al., 2015; Huang et al., 2018; Deng and Li, 2018; Yıldırım et al., 2020). In the majority of existing experimental studies, the electrical properties of this composite have been investigated using d.c. and fixed-frequency a.c. resistivity measurements, and little attention has been directed towards investigating the electrical properties of ECC over a wide frequency range. When subjected to an alternating current, porous materials such as the ECC can be expected to display both conductive and capacitive behaviour: the former due primarily to ionic conduction processes and the latter due to polarization processes operative within the material (Suryanto et al., 2016; Suryanto et al., 2018). Measurement of both quantities could provide more detailed information with regard to the self-monitoring capabilities of ECCs.

Impedance spectroscopy was therefore utilised in this research and results are presented in a number of formats of data presentation, including the general Nyquist format (McCarter et al., 1999; Suryanto et al., 2016), frequency domain (McCarter et al., 1999; Suryanto et al., 2016), and the Arrhenius format (McCarter et al., 2012), in order to provide detailed information about the nature of conduction and polarization processes within the composite (Starrs and McCarter, 1998; McCarter et al., 1999). Furthermore, from an electrical point of view, apart from investigating the influence of micro-cracks,

which is an inherent property of an ECC, there is also a need to be able to distinguish the influence of cement hydration, temperature, and moisture ingress; all of these aspects have been overlooked in prior studies. These aspects are addressed in this work and form the novelty of the work presented.

1.4   Organization of the thesis

Chapter 1 introduces a brief background on the importance of developing intelligent infrastructure and how to apply the ECC as a sensor in a real structure, followed by the aim and objectives of this study.

Chapter 2 presents a review of literature focusing on the structural health monitoring system and advancements in various smart sensors and sensing materials, including non-intrinsic self-sensing concrete and intrinsic self-sensing concrete, and explains why they are not a sustainable method for monitoring structural damage. Furthermore, the development of Engineered Cementitious Composite (ECC) and the factors that affect its ability to self-sensing comprising hydration studies, temperature, piezo-resistivity, and wetting-drying impacts, together with the ability to model the obtained results. This section of the thesis is used to derive the knowledge gaps that are based on the premise of this research.

Chapter 3 provides a description of three experimental work plans, including hydration, piezo-impedance, and wetting-drying studies. These work plans cover the materials and mixture properties, fabrication and curing, and test equipment and procedures.

Chapters 4, 5, and 6 present and discuss the results obtained from the hydration and temperature studies, piezo-impedance response, and wetting-drying cycle studies, respectively. These chapters display the variation needed to differentiate between the mechanical and non-mechanical loading based on the electrical properties of the ECC mix.

Chapter 7 summarizes the findings obtained from Chapters 4, 5, and 6. This chapter also provides the limitations of this research and recommendations for future investigations.
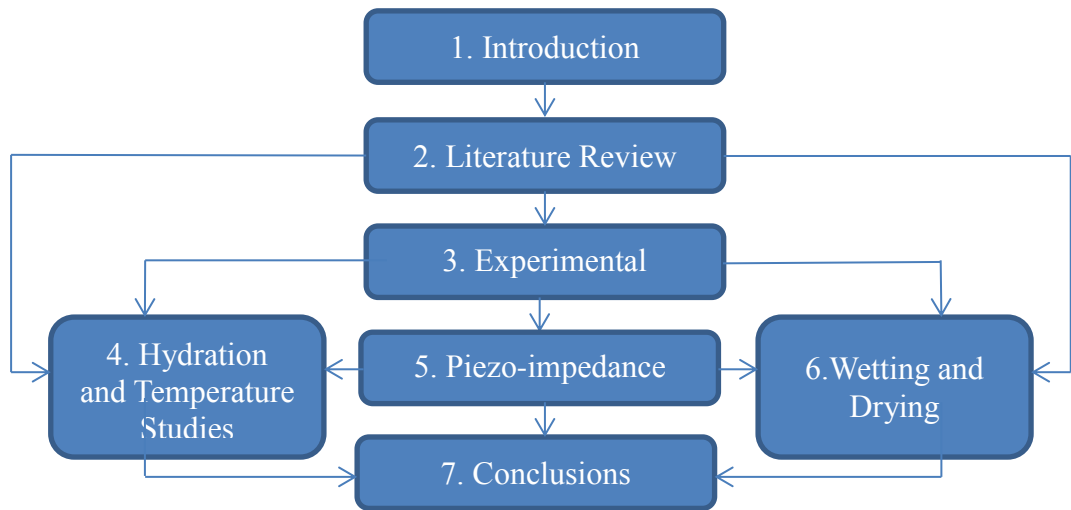
Figure 1.4: Diagram **provides an organization structure for the thesis.**

2 Literature Review

2.1 Structural Health Monitoring (SHM)

Concrete infrastructure is vulnerable to different degradations due to mechanical loading and/or environmental events (corrosion, cracking, and freeze-thaw). In the vast majority of developed countries, the investment required for periodic inspection and maintenance of infrastructure is enormous. In the United Kingdom alone, for example, around half of the £110 billion construction output in 2010 was spent on refurbishment and maintenance for three prime sub-sectors: commercial and social (£49 billion), infrastructure (£18 billion), and residential (£42 billion) (Cabinet Office, 2011). This figure has increased eightfold in less than 35 years (Suryanto et al., 2015). Furthermore, the national infrastructure plan forecasted that by 2020 the UK would need around £383 billion to develop its infrastructure to an acceptable standard (UK HM Treasury, 2014). This issue is not limited to the UK and is of concern to various developed countries, such as Japan and the USA (ASCE, 2013).

In recent years, there has been a marked increase in research on the development of strategies to identify damage and defects in infrastructure before a failure, which may result in costly repairs or even a loss of life. This has led to an increase in demand for systems that can evaluate the structural integrity to ensure reliability and safety. Initial damage detection and interpretation refers to a system known as Structural Health Monitoring (SHM). SHM is regarded as a non-destructive method of structural assessment to achieve crack detection and characterization strategy that aims to establish a continuous monitoring system. SHM arises from the idea of making the manufactured structures like human bodies and creating a sensing skin for those structures, which could be achieved through attaching a network of sensors to the monitored structures in order to provide significant economic benefits and longevity potential (Elwalwal et al., 2017).

In an ideal situation, the concept of health monitoring of infrastructure in civil engineering includes determining the location and severity of damage in the structure when it occurs through some parameters that are measured. However, the state-of-the-art methods of health monitoring do not provide accurate and sufficient information on the extent of damage. These methods have only the ability to determine whether there is damage in the structure. This kind of method is called "global health monitoring". In

order to identify the damage in the structure on a local scale, several Non-Destructive Evaluation (NDE) methods were used, such as eddy current techniques and ultrasonic guided waves. Eddy current can be used to find the location and extent of cracking, whilst ultrasonic can measure the structure's stress state. This kind of method is called "local health monitoring". However, the NDE methods are often costly, time-consuming, and hard to access. Thus, it is required to have both local and global health monitoring (Chang et al., 2003).

One of the most popular non-destructive testing methods that have been used on a large scale is a set of techniques that rely on measurements of vibrations. The common Vibration-Based Damage Detection (VBDD) NDT methods utilise modal parameters (e.g. structural mode shape and natural frequencies) and monitor changes in the vibration characteristics of a structure (Cowled, 2017; Hu et al., 2018). However, this approach faces challenges, such as damage that occurs locally that may not impact the dynamic properties of the structure (Cowled, 2017). It also faces the difficulty of obtaining a record of accumulated changes over a long period in large civil structures (Farrar and Worden, 2007; Deraemaeker and Worden, 2010; Song, 2017); data reliability (Farhey, 2005); data storage (Kim et al., 2019); and damage prognosis (Farrar and Lieven, 2007).

Environmental and operational impacts have been considered one of the biggest challenges that affect the accuracy of VBDD. According to Peeters et al. (2001), in which the impact of temperature on the Z24 concrete bridge was examined, it was found that temperature has a high impact on the dynamic response of the bridge and that environmental and operational variation changes can remove the defect impacts on the vibration properties (Sohn, 2006). Sohn (2006) stated a number of factors that affect the dynamic response of the structure more than defects, such as wind, temperature impacts, mass loading from traffic, boundary conditions, and secondary impacts originating from moving vehicles/bridge interaction, thereby making it difficult to implement in practice.

These methods are incapable of detecting local damages such as cracks in concrete, although this type of damage can lead to more serious damage (i.e., exposing reinforcement bars to the natural environment). As a result, early detection of damage in composite structures could prevent unexpected failure.

2.2 Self-sensing concrete

2.2.1 Overview

Self-sensing concrete is the ability of the concrete to sense its own condition and environmental factors that comprise cracks, temperature, damage, humidity, stress, and strain (Han et al., 2015). Concrete makes up a large part of civil infrastructure and is prone to degradation due to exposure to complex environments (Ou et al., 2005). Therefore, it is desirable to observe the condition and performance of concrete during its service life. This has been done since the 1930s through the use of electrical strain gauges to create self-sensing concrete for strain measurement (Park et al., 2006; Han et al., 2015). Since then, there has been an evolution of the self-sensing concrete for SHM through the use of smart sensors and sensing materials such as piezoelectric materials, optic fibres, Shape Memory Alloys (SMAs) and self-diagnosing polymer structural composites due to their ability to sense several chemical and physical factors (Park et al., 2006; Han et al., 2015). These smart sensors and sensing materials are classified as non-intrinsic self-sensing concrete. In 1992, a new concept called intrinsic self-sensing concrete emerged (Chen and Chung, 1993). This concept uses conductive fillers (e.g. steel fibres, carbon fibres) as part of the concrete mix. Since this concrete can implement self-sensing, there is no need for sensing materials or external sensors. Furthermore, adding these conductive fillers to the mix will improve its mechanical properties and durability compared with conventional concrete (Chen and Chung, 1993).

2.2.2 Non-intrinsic self-sensing concrete

There are several types of sensors and smart materials under the non-intrinsic self-sensing concrete classifications that were used previously by researchers. Table 2.1 shows a summary of the advantages and disadvantages of using these sensors and smart materials, together with the testing parameters.

Table 2.1: Summary of the advantages and disadvantages of non-intrinsic self-sensing concrete.

Name of the sensor	Testing Parameters	Advantages	Disadvantages
Strain Gauges Sensor	Strain.	Low cost, easy to install, excellent reproducibility of sensing property and good reliability (good match between the measured and predicted strain readings) (Vishay Micro-Measurements, 2007; Ackermann, 2018).	Unsuitable for long-term monitoring purposes, low sensitivity (range between 2 to 5), prone to drift, highly influenced by humidity and moisture, and easily influenced by electromagnetic interference (Vishay Micro-Measurements, 2007; Ackermann, 2018).
Optical Fibre and Fibre Bragg Grating Sensor	Displacement, strain, corrosion, moisture, temperature, crack, and Concrete hydration process.	Optical Fibre: Light weight, embedding ability, small size, immunity to corrosion and electromagnetic interference (Pang et al., 2013). Fibre Bragg Grating Sensor (a type of fibre optic sensor): High sensitivity to multi-band environmental parameters (Jacobs et al., 2007; Capoluongo et al., 2007), low maintenance cost, non-corrosive, and remote sensing (Chan et al., 2006).	High cost (Campanella et al., 2018), perceived complexity and novelty, the difficulty of dealing with fragile optical fibres (Doyle et al., 2006), challenges related to the long timespan requirement and guaranteeing operational reliability (Chen et al., 2017). In addition, severe environments could lead to strength degradation and mechanical damage (Risch et al., 2010), resulting in the sensors' stopping functioning, which could lead to many failures and expensive repairs for some inaccessible (Chen et al., 2017).
Piezoelectric Sensor	Stress, damage, crack, detect and localize disbond, temperature, impact detection, concrete strength monitoring, and structural health monitoring.	Piezoelectric ceramics (Lead Zirocondate Titanate, symbolized as PZT): Strong electro-mechanical coupling, good reliability, high dielectric constants, low cost, and a simple structure to fabricate (Duan et al., 2010; Li et al., 2014). PZT patches: The PZT patch can be used for two purposes (sensing and actuation), which may reduce the number of needed sensors and actuators and electrical wiring and related hardware (Presas et al., 2018). In addition, it has a negligible weight and size in comparison with the host structures, thus its association with the structure does not have any effect on the dynamic properties of the structure (Park et al., 2003). Furthermore, PZT patch can come in different sizes, shapes, and thicknesses (ranging from finite rectangular patches to complicated forms) (Bhalla, 2004).	High stiffness and fragility, and when it comes to design flexibility, it is considered very limited due to the complexity of using it on curved surfaces and is unable to withstand bending. It's also very sensitive to temperature, as PZT materials exhibit electrical property fluctuations with temperature changes (Bhalla, 2004; Annamdas and Soh, 2010).

Table 2.1: Summary of the advantages and disadvantages of non-intrinsic self-sensing concrete (Continued).			
Shape Memory Alloys (SMAs)	Strain, crack, and displacement.	Excellent fatigue resistance, very good deformation behaviour (Janke et al., 2005), resistance to corrosion and excellent durability.	The SMAs sensitivity (i.e., gauge factor) is very low (in a range from 3.8 to 6.2); it is also very expensive (Liu, 2006). The cooling and heating inertance can restrain SMAs' usage in concrete structures (Janke et al., 2005).
Self-monitoring polymer composites	Strain, crack, displacement, and damage.	The self-monitoring polymer materials have a clear advantage as they act as structural materials and sensors (Wang et al., 2007).	Aging of the polymer materials has a significant influence on the sensing stability and repeatability. Moreover, these polymer materials have a comparatively low sensitivity, which ranges between 30 and 40 (Wang et al., 2007).

2.2.3 Intrinsic self-monitoring concrete

Intrinsic self-monitoring concrete can be produced by introducing some filler to the conventional concrete matrix, such as steel fibre, carbon fibre, nickel powder, and carbon nanotube. These fillers will grant the concrete the capability to sense crack, stress, strain, temperature or damage in itself while preserving or even enhancing the mechanical characteristics of the matrix (Han et al., 2015).

These fillers create a conductive network inside the matrix. Any changes in the composite (e.g., strain or stress) or the environment around the composite will change the conductive network by influencing the electrical characteristics of the composite. For further clarification (Han et al., 2008), see Figure 2.1 which shows the tension and compression typical sensing behaviour of self-monitoring concrete. Therefore, cracks, temperature, damage, stress, and strain can be detected under both static and dynamic states by measuring the electrical characteristics (Han et al., 2015).
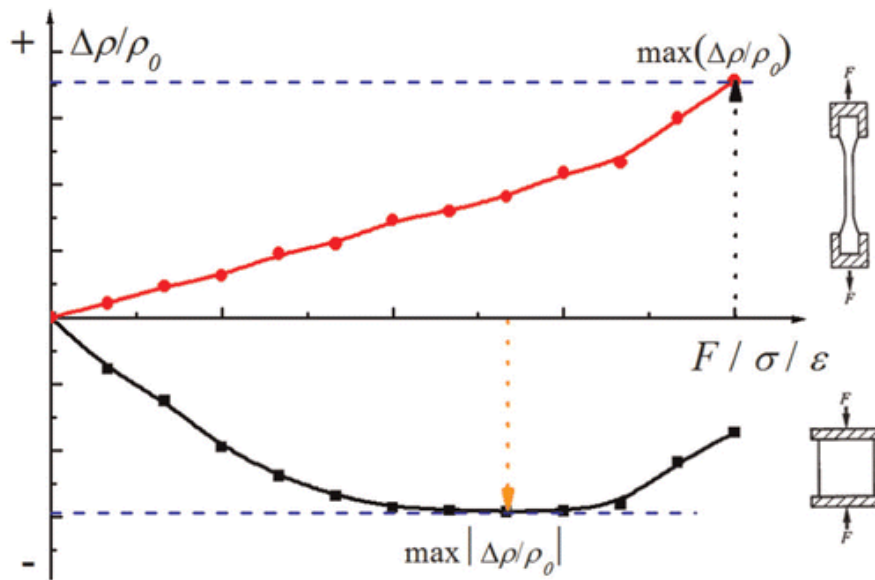
Figure 2.1: Typical sensing behaviour of self-monitoring concrete under tension and compression (Han et al., 2015).

Since the early 1990s, researchers have aimed to produce intrinsic self-monitoring concrete with the results of strain sensing characteristics of concrete with the use of short-carbon fibres. Ever since, researchers on the mechanisms and behaviours of self-monitoring concrete with various fillers have carried out tests under different environments, structures, and loadings. For example, Teomete and Kocyigit (2013) produced a self-sensing concrete with steel fibre inclusions, which was tested under a split tensile test in order to identify the relationship between the electrical resistance variation and tensile strain. They found that gauge factors of the composite reached 5195, which is considered high enough to sense its damage and strain.

Reza et al. (2004) examined the behaviour of carbon fibre-reinforced mortar under compact-tension. They found that there was a good correlation between the mechanical behaviour and the electrical resistance behaviour, which can be utilized to give insight on the fracture process evolution and mechanisms, and also predict the propagating crack length. Wang et al. (2006) examined a four-point bending reinforced concrete beam which was fabricated with carbon fibres and assessed the correlation between the fatigue life and electrical characteristics under cyclic flexural loading. It was found that the carbon-fibres reinforced concrete can be utilized to estimate the fatigue life through measuring residual resistance.

Baeza et al. (2013) attached multiple sensors relying on cement composites consisting of carbon fibre and carbon nanofiber to different positions (top, bottom, and side) of a conventional reinforced concrete beam. They found that the self-monitoring concrete was able to strain sense even for highly damaged structures close to their collapse.

The intrinsic self-monitoring concrete has several advantages, such as high stress/strain sensitivity, which goes up to 0.16 MPa−1/1500 (Han et al., 2008); being easy to install and maintain; long-service time and good mechanical characteristics. However, the intrinsic brittleness of conventional concrete directed the research towards the Engineered Cementitious Composite (ECC), and since the self-sensing ECC serves under different environments, the factors affecting the ECC need to be studied.

2.3   Immittance Spectroscopy

The fundamental electrical properties of any material can be determined using frequency-dependent parameters (conductivity ($\sigma(\omega)$) and dielectric constant ($\kappa r'(\omega)$)) specified by the movement of free and bound charges and the polarization process within the composite. While in the case of heterogeneous materials (such as concrete, cement-paste, or mortar), the conductivity and dielectric constant will be associated with the characteristics of each component separately and the way in which they are merged (McCarter et al., 1999).

Often, such an association appears in the frequency band as a relaxation dispersion response. As shown in Figure 2.2, the rises in conductivity and the drops in dielectric constant refer to the appearance of a relaxation region (Starrs and McCarter, 1998; McCarter et al., 1999; McCarter et al., 2001). Therefore, it can be hypothesized that it is possible to detect different features of heterogeneous materials through electrical characteristics while taking into account conducting electrical measurements over a wide frequency range (McCarter et al., 1999).
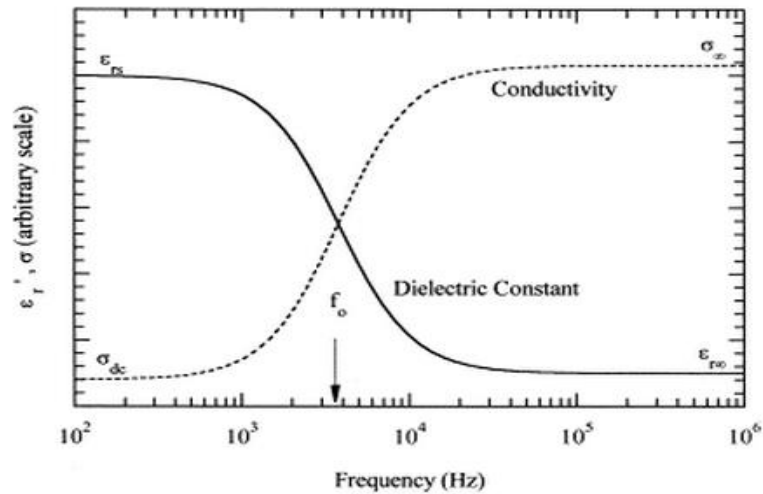
Figure 2.2: Classic Approach of Debye Relaxation Dispersion Response (Starrs and McCarter, 1998; McCarter et al., 1999). *Note: the symbol ε_r' presents the relative permittivity. However, in this thesis, the relative permittivity symbol is $\kappa r'$.

The term "immittance" consists of four main levels of response that can be resulted by the a.c electrical measurements: impedance $Z(\omega)$ and its reciprocal (the admittance $Y(\omega)$); relative-permittivity $\kappa r'(\omega)$ and its reciprocal (electric-modulus $M(\omega)$) (Macdonald, 1996; McCarter et al., 2015; Suryanto et al., 2016). This PhD study emphasises the impedance and permittivity levels.

2.3.1 Impedance Response of General Cementitious Systems

Significant research has been focused on the application of a.c. impedance spectroscopy in the study of cement-based systems with regards to the microstructural evolution and characterization and pore structure development (Starrs and McCarter, 1998; McCarter et al., 1999). In addition, the electrical impedance response of concrete, mortars, and pastes in the liquid and hardened states is now extensively documented (McCarter et al., 2004).

The typical complex impedance response of Ordinary Portland Cement (OPC) displays two distinct regions, as shown in Figure 2.3(a): the 'V'-shaped plot on the right-hand side of the spectrum formed by electrode polarization, and the bulk-arc response on the left-hand side of the plot (Starrs and McCarter, 1998; McCarter et al., 2004). In addition, the complex impedance response is displayed graphically in the Nyquist plot (Z'_{real} versus $Z''_{imaginary}$) with frequency increasing from right to left across the

spectrum, and the bulk resistance (R) is located at the minimum spot within the valley zone (Suryanto et al., 2016). The presence of fly-ash influences the shape of the complex response by forming an intermediate region, or "plateau" between the two arcs, as shown in Figure 2.3(b) (Starrs and McCarter, 1998; McCarter et al., 2004).
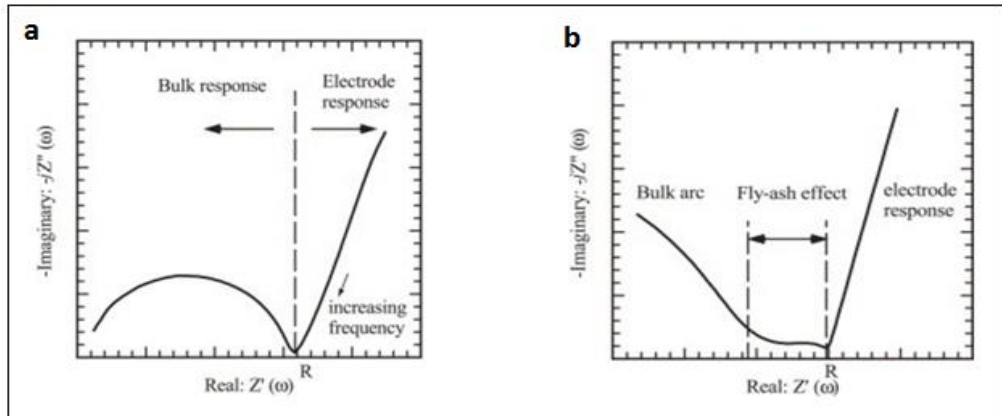
Figure 2.3: Schematic drawing of (a) the complex impedance response of an ordinary Portland cement (OPC) system and (b) the response of a fly ash binder (McCarter et al., 2004).

Therefore, according to Suryanto et al. (2016), the impedance response can be characterised by three prominent regions consisting,

a) A low-frequency "*Spur*" (<1 kHz) on the right-hand side of the curve.

b) An intermediate region "*Plateau*" (1-150 kHz) due to the addition of fly-ash, appears as a 'U'-shaped valley zone, and

c) A high-frequency semi-circular "*arc*" (>150 kHz) on the left-hand-side of the curve.

The low-frequency spur is a result of the polarization phenomena that occur at the electrode/sample interface (McCarter et al., 1988; McCarter and Brousseau, 1990; Suryanto et al., 2016), and it constitutes a part of a larger arc that appears only at a frequency <1 Hz (Suryanto et al., 2016). The intermediate region "Plateau" is a distinctive character of cementitious systems that contain fly-ash (McCarter et al., 2004; Suryanto et al., 2016). As shown in Figure 2.4, introducing the fly-ash as a cementitious component resulted in significant changes in the electrical response of the system, most notably, a displacement of the spectrum to the right, which implies that the system becomes more resistive (Starrs and McCarter, 1998) and an enhancement in the dielectric constant (emergence of a "bump" in the dielectric response) over a certain frequency band, indicating that there is an additional polarization mechanism within the

system (McCarter et al., 2004). While the direct influence on the prominence of the "Plateau" region was initially hypothesized by McCarter et al. (1999), that it was a result of the natural spherical shape of the fly-ash particles (double-layer polarization process). However, later on, McCarter et al. (2004) discovered that the presence of unburnt carbon in the fly-ash (loss on ignition (LOI) during production) was responsible for this feature. Moreover, a double-layer polarization mechanism on the unburned-carbon surface that is contained within the fly-ash was postulated to interpret that (McCarter et al. (2004). The high frequency semi-circular arc describes the bulk response that occurs as a result of the polarization process within the cementitious system, and it evolves to become more noticeable with increasing the hydration/curing time (Suryanto et al., 2016).
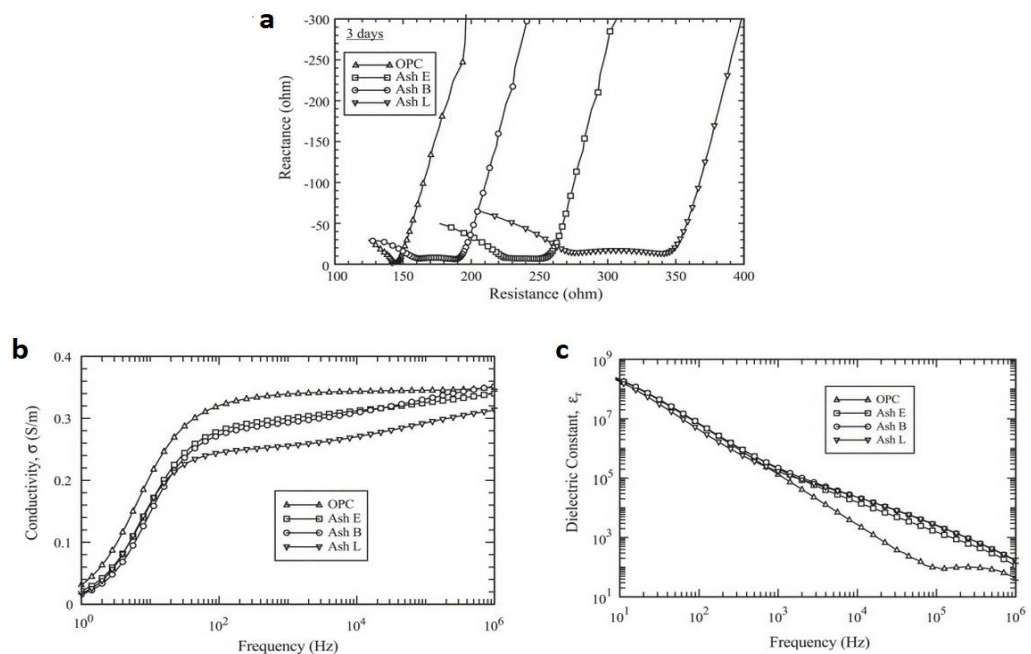
Figure 2.4: Plots of (a) complex impedance, (b) conductivity, and (c) dielectric constant for ordinary Portland Cement (OPC) mortars and mortars with three levels of fly-ash replacement after three days of hydration (McCarter et al., 2004). *Note: the symbol ε_r represents the relative permittivity, which is labelled as κ_r' in this thesis.

2.3.2 Impedance Response of Conductive Cementitious Systems

The addition of conductive materials (e.g., steel fibres) below the percolation threshold to the cementitious system results in a noticeable transformation of the electrical impedance spectrum from the typical single-arc response into two-arc response as shown in Figure 2.5(a) (Torrents et al., 2001; Mason et al., 2002). To explain this phenomenon, Torrents et al. (2000; 2001) proposed the 'frequency-switchable fibre

coating' model (see Figure 2.5(b)) in which 'polarization layers' (coatings) (resulting from charge transfer resistance/double layer) are sought to form on the interface between the conductive inclusions and the surrounding medium. These layers are expected to insulate the conductive fibres, thereby making their presence non-existent. In the proposed equivalent circuit, this is represented by an open switch in the lower path. With increasing frequency, the impedance of the coating layer is expected to decrease rendering the fibres to serve as short-circuits in the matrices. In this situation, the 'switch' on the bottom-path of the equivalent circuit is open.
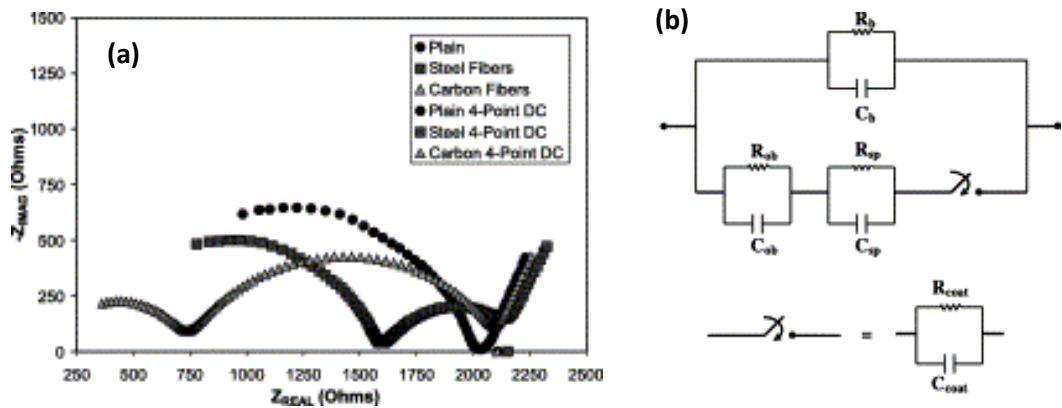
Figure 2.5: (a) Complex impedance response for OPC composites without and with fibres (1 wt% of either carbon or steel fibres) at 3 days of hydration; (b) Equivalent circuit that represents the "frequency-switchable fibre coating" model (Mason et al., 2002).

2.4 Engineered Cementitious Composites (ECC)

2.4.1 Overview of ECC

A damage-tolerant cement-based material known as the Engineered Cementitious Composite (ECC) has been identified as a potential damage sensor (Hou, 2008; Hou and Lynch, 2005a; Lin et al., 2011; Ranade et al., 2014). The damage-tolerant property of ECC originates primarily from its ability to exhibit multiple-fine cracking when subjected to tensile stresses beyond the elastic range, generally displaying tensile strain hardening behaviour with a strain capacity in excess of 1% and an average crack width less than100 μm at maximum strain (Li, 2008; Suryanto et al., 2015; Lee et al., 2018; Chen et al., 2018; Frank et al., 2018; Ma et al., 2019). This is different from ordinary concrete and fiber-reinforced concrete, which generally fail locally by a single crack.

As previously introduced in Section 1.1, ECC owns a distinctive piezo-resistive property, with bulk resistivity comparable to that of a semi-conductor (10^1–10^5 Ω-cm) (Chung, 2002; Hou and Lynch, 2005a; Ranade et al., 2014). This led the researchers to identify the ECC as a potential damage sensor. However, the piezo-resistive response is very sensitive to non-mechanical loading (i.e. hydration, moisture change, and temperature) as well as mechanical loading (i.e. cracking and strain). Therefore, this drew attention to the factors that affect the electrical properties of the ECC.

2.4.2   Factors affecting the electrical properties of ECC

2.4.2.1   Cement hydration within the ECC matrix

Hou (2008) monitored the resistivity of the M-45 ECC mix using DC measurements with 2-point probe and 4-point probe methods. It was found that the polarization effects (which result from the separation of ion concentrations when an electrical field is applied) are more prominent with the 2-point probe method. Therefore, the 4-point probe method was adopted to study the hydration effects at different curing ages (i.e., 1, 7, 14, 21, 28, and 35 days). Figure 2.6 displays the first 600 seconds of resistivity measurements of 10 M-45 ECC samples under conditions of 100% relative humidity (RH) curing environments. It was observed that at 1 day of curing, the initial resistivity (at t = 0) is 158 kOhm-cm and increases to 200 kOhm-cm (both the resistivity and the material polarization) after 600 seconds of polarization; at 14 days of curing, the initial resistivity grows from 524 kOhm-cm to 720 kOhm-cm; and at 35 days of curing, the initial resistivity increases from 652 kOhm-cm to 880 kOhm-cm. This increase in the initial and polarized resistivity values with increasing curing age is attributed to the higher concentration of trapped ions by the hardening hydration products, which make ion mobilization more difficult, thus higher resistivity. Figure 2.6 also displays that at an early age of curing (i.e., 1 day), the electrical properties of the M-45 ECC can be described by their initial resistivity. However, as hydration increases, the polarization properties become more apparent.
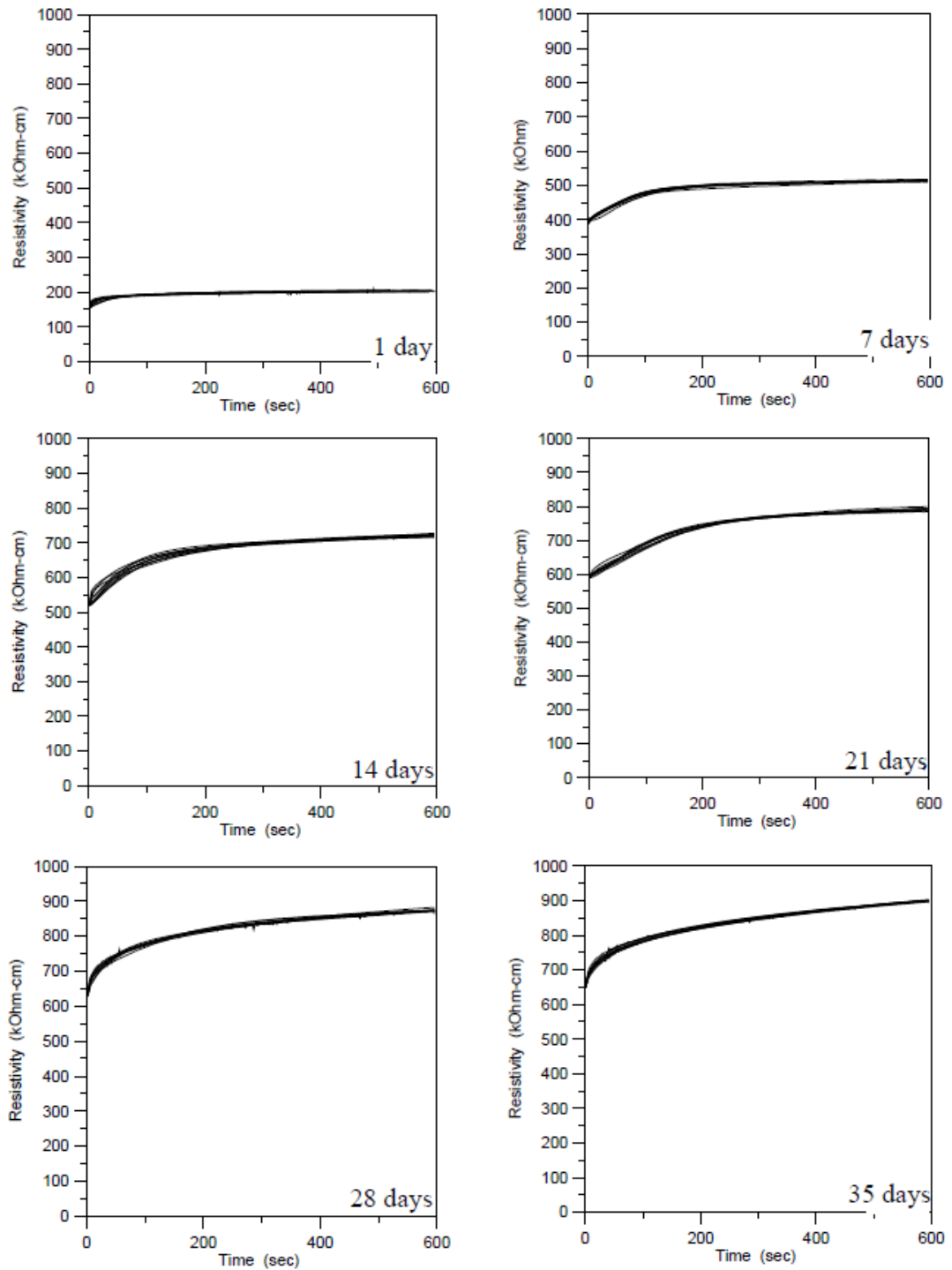
Figure 2.6: Resistivity measurement of M-45 ECC (10 samples) using the 4-point probe method over the initial 35 days after casting (Hou, 2008).

Li et al. (2012; 2013) investigated the bulk resistivity of ECC specimens with different carbon black nano-particles (CB) dosages (0, 0.25, 0.5, and 1.0 wt%) over a 140-day period. The 152.4 mm × 76.2 mm × 12.7 mm rectangular tensile specimens were cast and then covered with plastic sheets. After 1 day, the specimens were demolded and

cured in plastic bags for 6 days at $95 \pm 5\%$ relative humidity (RH) and $20 \pm 3°C$. After 6 days, the specimens were taken out of the plastic bags and kept in ordinary laboratory air to cure (at $20 \pm 5\%$ RH and 20 ± 3 °C (63 - 73 °F)) for a period of at least 28 days prior to testing.

The electrical response was measured using an impedance analyser operated at a fixed frequency (100 Hz). Figure 2.7 presents the results of such measurements, which reveal a rapid increase in resistivity during the early age of curing (up to approximately 28 days). The response thereafter appears to level off, particularly from about 90 days of curing. The increase in bulk resistivity over time was attributed to cement hydration and pozzolanic reaction (see Table 2.2), which involved the reactions of tricalcium-silicate (C_3S), dicalcium-silicate (C_2S), tricalcium-aluminate (C_3A), and tetracalcium-alumina-ferrite (C_4AF) in the cement, producing calcium-silicate-hydrate (C-S-H) and calcium-hydroxid. This process results in a refinement of the pore structure that causes isolation of pore-water, causing ions in the remaining pore water to move through a tortuous path around the cement gels. In terms of the pozzolanic reaction, high levels of fly-ash in the CB-ECC specimens were thought to produce more C-S-H gels as a result of the reaction between the silica material and calcium hydroxide ($Ca(OH)_2$) in the presence of water (Li et al., 2013).

Table 2.2: Cement hydration and pozzolanic reactions (Li et al., 2013).

Cement hydration:
$2C_3S + 11H \rightarrow C_3S_3H_8 + 3CH$
$2C_2S + 9H \rightarrow C_3S_3H_8 + CH$
$C_3A + 3C\bar{s}H_2 + 6H \rightarrow C_6A\bar{s}_3H_{32}$
$2C_3A + C_6A\bar{s}_3H_{32} + 4H \rightarrow 3C_4A\bar{s}H_{12}$
$C_4AF + 3C\bar{s}H_2 + 21H \rightarrow C_6(A,F)\bar{s}_3H_{32} + (F,A)H_3$
$C_4AF + C_6(A,F)\bar{s}_3H_{32} + 7H \rightarrow 3C_4(A,F)\bar{s}H_{12} + (F,A)H_3$
Pozzolanic reaction:
$CH + SH \rightarrow CSH$
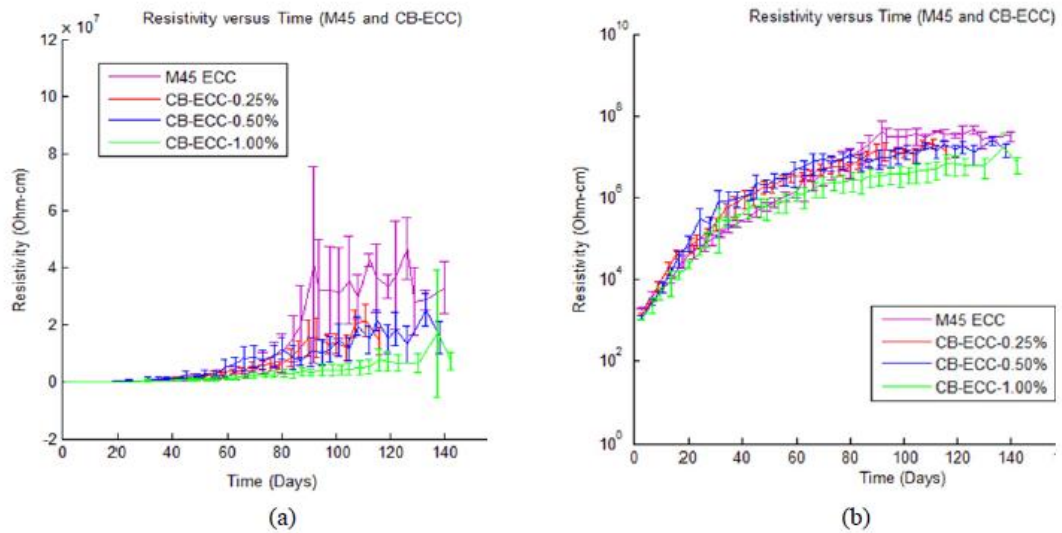
Figure 2.7: Resistivity of ECC specimens with different CB dosages is presented on (a) a linear scale and (b) a logarithmic scale (Li et al., 2013).

2.4.2.2 Temperature effects

McCarter et al. (2012) developed a remote monitoring system that can be used for intelligent monitoring of concrete structures from an office setting. This was implemented through the use of an electrode array embedded within the cover-zone concrete to obtain the electrical resistivity and temperature measurements. Electrical measurements were taken through an auto-ranging logger using an AC voltage (1.0V) at a 1KHz fixed frequency.

Figure 2.8 presents the changes in cover-zone resistivity for three different types of concrete called CEM I concrete mix, CEM III/A concrete mix (concrete with GGBS), and CEM II/B-V (concrete with fly-ash) in the submerged zone environment during the first 150 days after installing the monitoring system (November–March). It is evident that the resistivity of plain Portland cement binder displayed in Figure 2.8(a) is significantly lower than the resistivity of samples with replacement materials (GGBS and fly-ash) shown in Figures 2.8(b) and (c). Additionally, the resistivity of the samples exhibits significant fluctuations during the 150-day period, which happen at specific times in the three mixes. Since the electrical conduction across concrete will be dominated by the ionic conduction that occurs through the capillary pore network; as a result, it will be temperature dependent (Whittington et al., 1981; Castellote et al., 2002; McCarter et al., 2012). Although it's possible to control the laboratory ambient temperature, this is not the case in the field as the temperature can vary significantly.

Therefore, it's necessary to standardize the resistivity measurements obtained in the field to a reference temperature.

The Arrhenius approach can be used to model the impact of temperature on resistivity. It can be clearly seen from Figure 2.9 that the plot of the natural logarithm of bulk resistivity ($\ln(\rho)$) versus $1000/T_k$ (Time in Kelvin) will be a straight line of slope E_a/R_g (Where: E_a is the activation energy (J mol^{-1}) and R_g is the universal gas constant (8.3141 J mol^{-1}K^{-1})), which then can be used to standardize the resistivity values to 25°C. Table 2.3 presents the E_a/R_g Ratio and the activation energy E_a of the three different mixes.
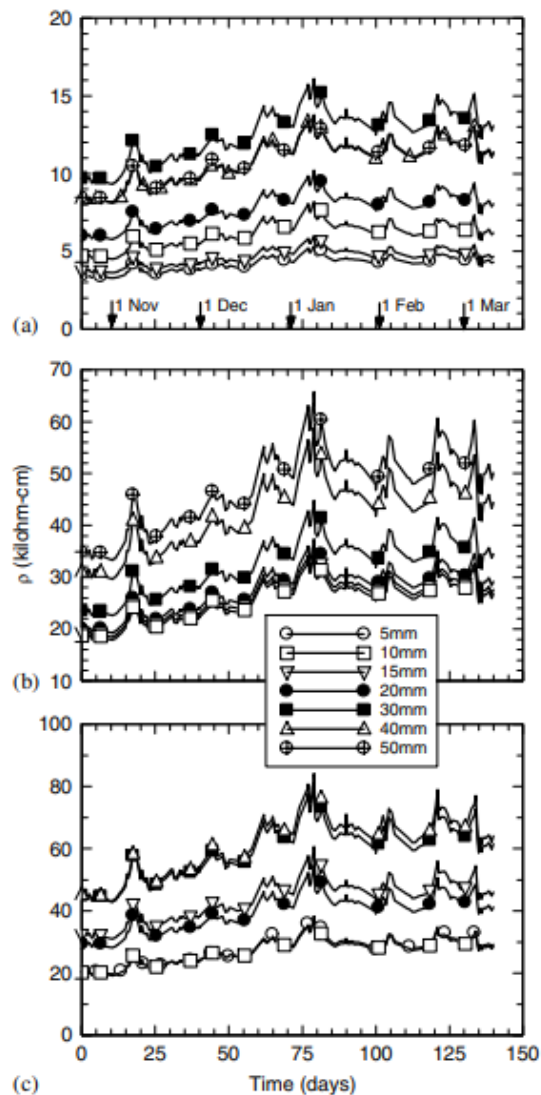
Figure 2.8: Temporal and spatial variations in cover-zone resistivity (in kΩ-cm) for a) CEM I concrete mix; (b) CEM III/A concrete mix and (c) CEM II/B-V. Note: the data for 5-mm depth in (b) was lost, and the response at 50-mm depth in (c) has been omitted for clarity reasons as the values are higher than 100 kΩ-cm (McCarter et al., 2012).
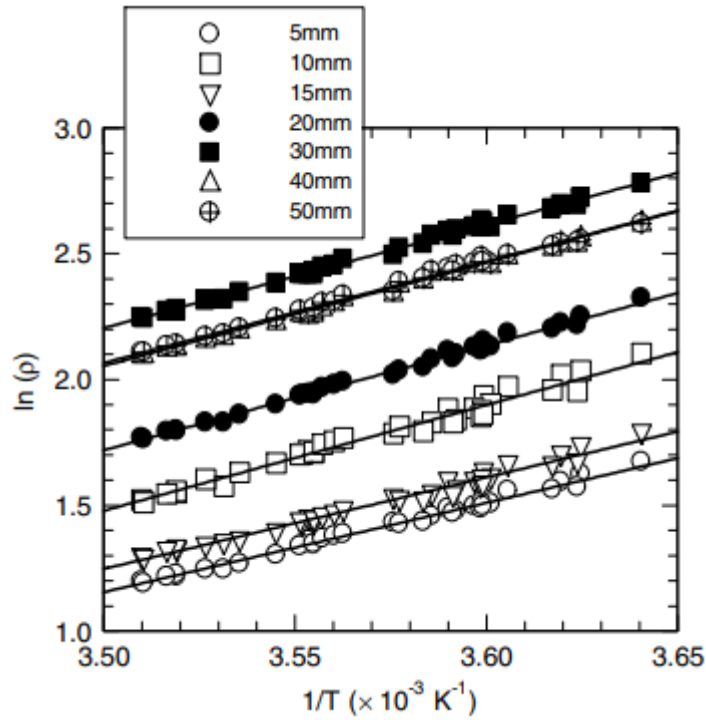
Figure 2.9: Data in Figure 2.8(a) plotted in Arrhenius format (McCarter et al., 2012).

Table 2.3: The E_a/R_g Ratio and the activation energy E_a for the three concrete mixes (McCarter et al., 2012).

Depth (mm)	CEM I 42.5N		CEM III/A		CEM II/B-V	
	E_a/R_g (K)	E_a (kJ/M)	E_a/R_g (K)	E_a (kJ/M)	E_a/R_g (K)	E_a (kJ/M)
5	3,554	29.55	+	+	3,753	31.20
10	4,027	33.48	4,134	34.37	3,651	30.35
15	3,644	30.30	4,040	33.59	3,790	31.51
20	4,167	34.64	4,053	33.70	3,725	30.97
30	4,113	34.20	4,012	33.36	3,551	29.52
40	4,160	34.59	3,915	32.55	3,817	31.73
50	4,106	34.14	3,920	32.59	3,011	25.03

Note: + = data lost for 5-mm depth.

Figure 2.10 displays the electrical measurements after being standardized to the reference temperature (in this case, 25°C) for the three mixes. It can be clearly seen that the resistivity becomes almost constant over the 150-day period, indicating that the fluctuations in resistivity shown in Figures 2.8(a)-(c) were caused by temperature. This concludes that the Arrhenius approach can be used to explain the impact of temperature on resistivity, and can be used to standardize the field date to a reference temperature.
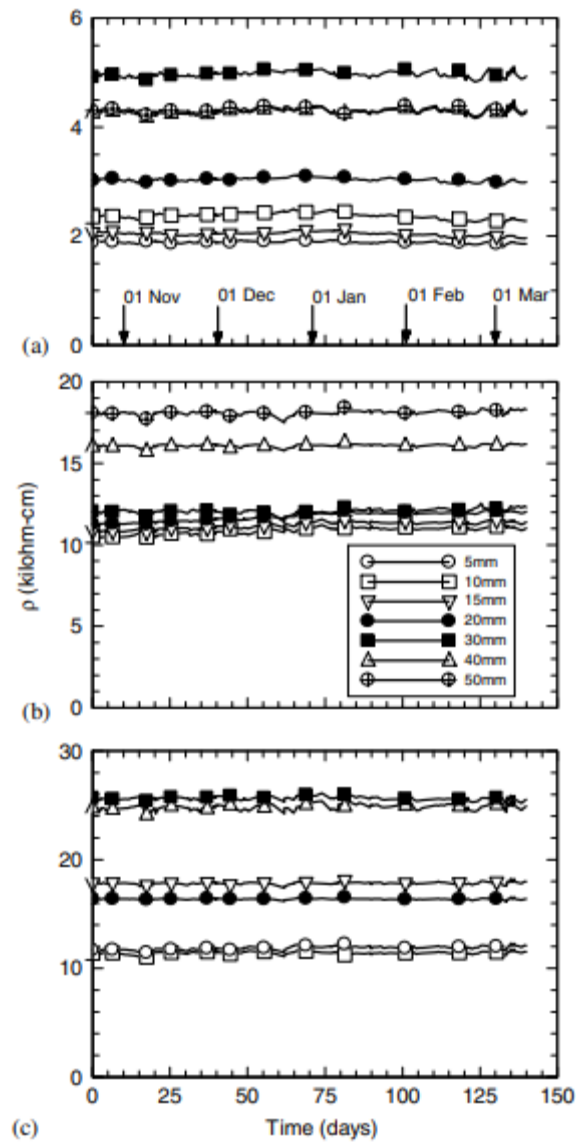
Figure 2.10: The resistivity measurements displayed in Figure 2.8 are standardized to the reference temperature of 25°C for a) the CEM I concrete mix; b) the CEM III/A concrete mix; and c) the CEM II/B-V. *Note: in (c), the curve for 50-mm depth is omitted for clarity reasons as the values are higher than 30 kΩ-cm.

2.4.2.3 *Moisture loss/gain due to wetting and drying cycles*

Cementitious materials can be utilized in novel applications, like using cement-based materials as humidity or moisture sensors. These sensors can be integrated into concrete structures to observe the online condition or moisture movement (McCartert and Garvin, 1989). Suryanto et al. (2017) evaluated the permeation properties of ECC by performing electrical measurements at a frequency of 1 kHz during the wetting and drying cycles at regular intervals. This was carried out with stainless steel electrode pins (two-point sensor) embedded within the surface region of

the ECC specimen, which allowed the movement of moisture within the surface region to be observed. Figure 2.11 displays the cover-zone response to the wetting and drying cycles, with the response measured from the electrodes arranged in a staggered position at different depths. From this figure, the normalized conductivity N_c is symbolized as the change in conductivity in relation to its initial value before the cyclic exposure, which can be expressed as the ratio σ_t/σ_o where σ_t presents the conductivity obtained across a pair of electrodes at a time (t), after starting the wetting and drying cycles (in this case, it was the 21st day after casting), and σ_o presents the conductivity measured across the relevant electrode pair before starting the wetting and drying cycles.
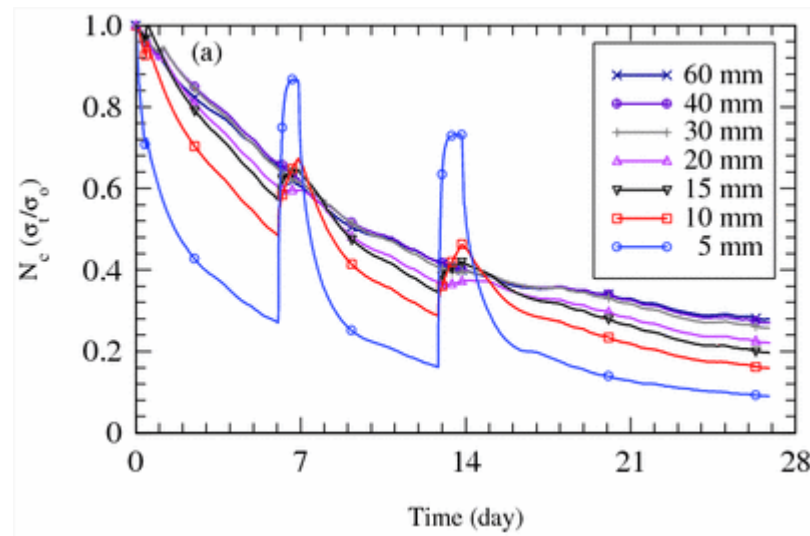
Figure 2.11: The temporal and spatial change in N_c (σ_t/σ_o) for ECC subjected to wetting/drying cycles (Suryanto et al., 2017a).

It can be clearly seen in Figure 2.11 that during the wetting and drying cycles, the normalized conductivity (N_c) of each electrode pair placed at different depths exhibits a marked change in value. It was found that the N_c value increases during the wetting and decreases during the drying, indicating a direct impact of the surface wetting/drying effects. In addition to this feature, there is a general decrease in N_c value with time caused by the on-going hydration and pozzolanic reaction as the capillary pores are progressively refined. The gradual decrease in the N_c value during the drying indicates the reducing degree of pore saturation due to the surface drying. It was also found that the extent of this feature becomes less obvious as the depth increases, especially for the electrodes placed > 20 mm away from the exposed surface. Suryanto et al. (2016) suggest that the ECC at depths > 20 mm is affected mainly by the microstructural

changes (hydration and pozzolanic reactions) and not the drying process. Moreover, it is obvious from Figure 2.11 that the N_c value increases dramatically after absorption.

Sahmaran and Li (2009) examined the water absorption and sorptivity properties of cracked ECC samples (with or without water repellent admixture). The sorptivity tests were performed to identify the influence of micro-cracks on the capillary suction (absorption) of concrete. Figure 2.12 presents the typical cumulative volumetric gain per unit area (mm^3/mm^2) against the square root of time. It is obvious that there is an increase in the cumulative volume of water absorbed per unit surface area with the increase of the square root of time. It can be clearly seen that the cracked ECC samples without water repellent admixture highly change the measured transport properties based on the micro-crack number, which means the water absorption becomes faster with the increase in the crack number, as the cracks and capillary pores reach the saturation state in a shorter time.

A non-linear relationship was found between the cumulative water absorption and the square root of time for the cracked ECC sample without water repellent admixture (crack number = 14). This nonlinearity could be related to i) the poor capillary absorption into the crack system, which attains capillary rise equilibrium against gravity in the middle of the sorptivity test by Hall and Hoff (2002); and/or ii) the incorrect cross-sectional area of the sample used to measure the water front (Sahmaran and Li, 2009). Sahmaran and Li (2009) found that the non-use of water repellent admixture makes the water ingress into the cracked ECC easier, while using water repellent admixture makes the cracked ECC more resistant to water absorption.
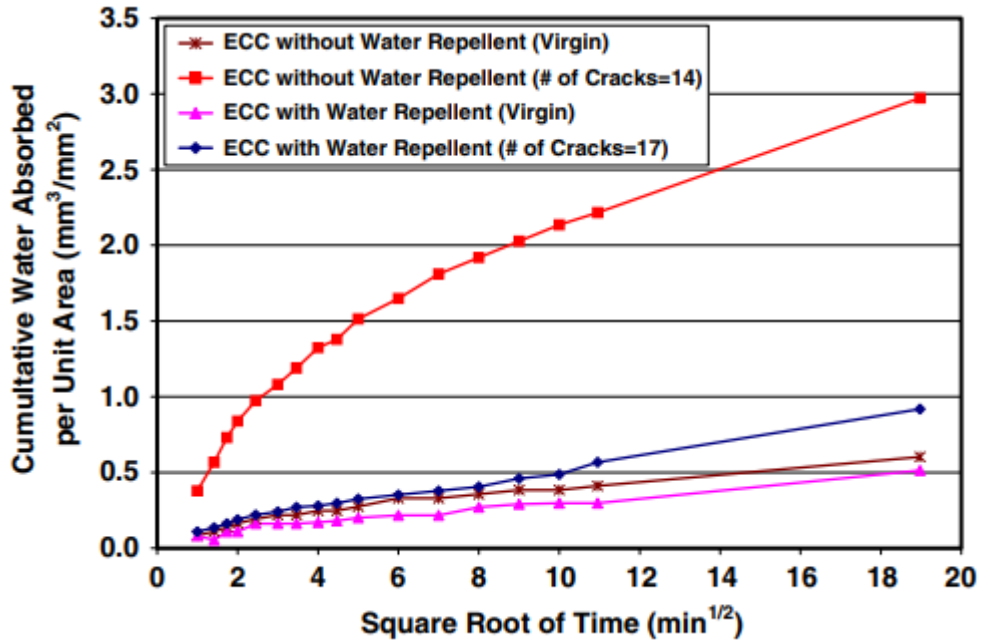
Figure 2.12: Cumulative water absorbed per unit area against the square root of time (Sahmaran and Li, 2009).

McCarter and Garvin (1989) investigated the electrical properties and sensitivity of mortar to moisture conditions. Figure 2.13 displays the impedance plots for mortar after drying and then submersion in water. Curve A in Figure 2.13 shows the mortar specimen after drying at 70 °C for 24 h and then cooling in the laboratory environment. It was found that the resistance and the reactance values were increased significantly after the evaporation of high a proportion of the free capillary water from the matrix. It was also found that the impedance plot showed another small arc at the high frequencies that separate between two potential relaxation processes, which are in the kilohertz and megahertz regions. Free capillary water can be removed at 70 °C, whilst the adsorbed water needs a greater energy input to be removed from the gel surface.

Curve B in Figure 2.13 illustrates the impedance plot for mortar after 10 minutes of submersion in water. The specimen absorbed the water through capillary suction forces. It was observed that the shape of the impedance plot has changed and become flatter, and the resistance and reactance values have decreased. After a 1-day (24-hour) submersion in water (see Curve C in Figure 2.13), the resistance and reactance values had decreased even further, and the impedance plot of the mortar specimen was nearly the same as the impedance when the specimen was fully saturated.
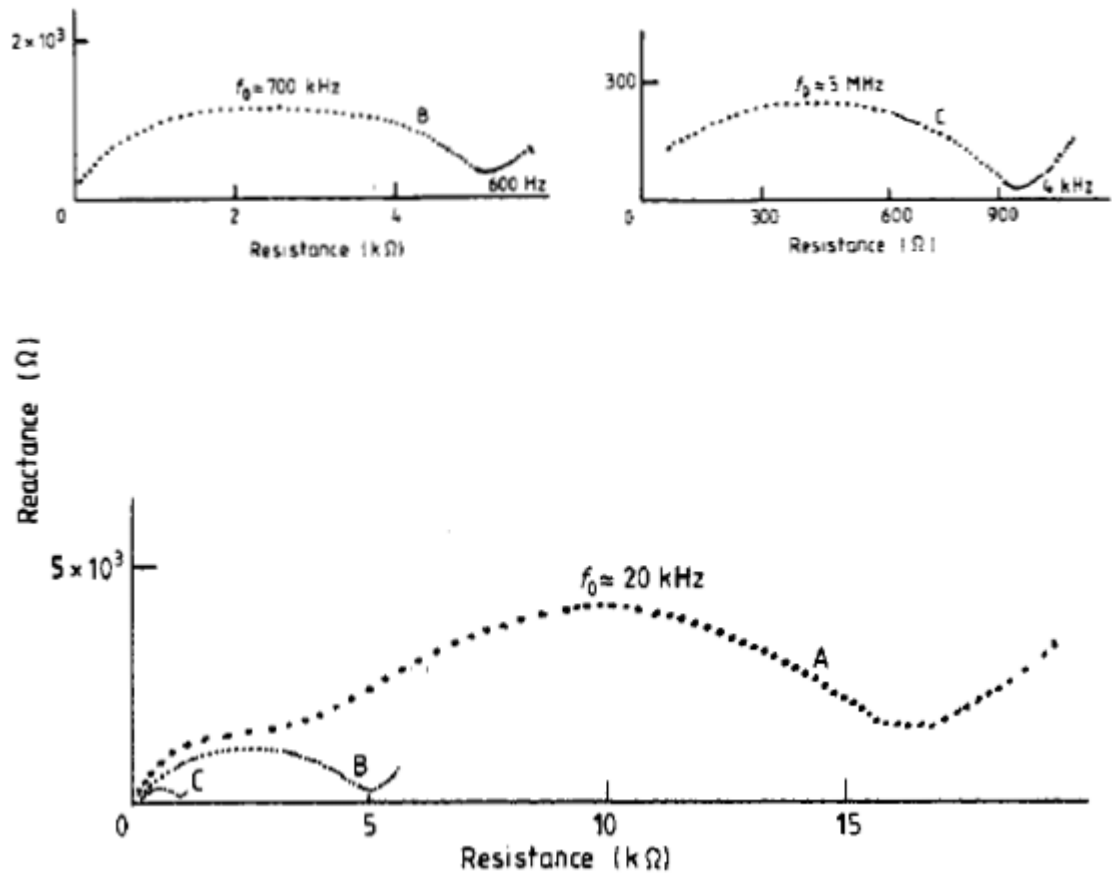
Figure 2.13: Impedance plots for mortar after drying (Curve A) and then submersion in water (Curve B, 10 min submersion in water; Curve C, 24 hr submersion in water) (McCarter and Garvin, 1989).

2.4.2.4 Micro-cracking in the ECC matrix

Investigation of the influence of matrix cracking within the ECC matrix on composite resistivity goes back to the middle of 2000 (Hou and Lynch, 2005a; Hou and Lynch, 2005b), with the aim of exploring the potential of ECC for damage detection in concrete structures. Work has mostly focused on the piezo-resistive properties (i.e., the resistivity change induced by mechanical strain) of ECC under tensile loading. To date, most of the work has studied these properties primarily through d.c. or fixed-frequency a.c. resistivity measurements.

Figures 2.14(a)-(f) and 2.15(a)-(e) summarize the piezo-resistive properties of various versions of ECCs reported in the literature. (Hou and lynch, 2005a; Hou, 2008; Lin et al., 2011; Ranade et al., 2014; Suryanto et al., 2015; Huang et al., 2018; Deng and Li, 2018; Yıldırım et al., 2020). In this Figures, all data are presented following the original format of data presentation, including electrical resistivity,

resistivity changed, relative change in resistivity, fractional change in resistivity, and gauge factors. The main findings from each work are summarized below.

Hou (2008) employed the four-point measurement technique to study the piezo-resistivity of the standard ECC mix under both d.c. and a.c. currents, with the latter applied at 5 kHz. As illustrated in Figure 2.14(a), they demonstrated that the composite displays a quasi linear piezo-resistive response during strain-hardening, with resistivity during strain-hardening found to increase from 350 kΩ-cm at 0.2% of strain to 760 kΩ-cm at 2.3% of strain. The formation of multiple micro-cracks was found to be responsible for the increase. The gauge factor was found to range from 10 to 20 in the elastic region and from 30 to 80 in the strain-hardening region. Hou and Lynch (2005) also studied the piezo-resistive response of ECC mixes containing steel and carbon fibre using the four-point d.c. measurement (see Figure 2.14(b)). They demonstrated that the ECCs display a linear relationship between the change in resistivity and tensile strain, with resistivity found to increase from approximately 2.5 MΩ-cm at zero strain to around 10 MΩ-cm at 3% strain. It was found that the ECCs with conductive fibres were less sensitive to mechanical strain due to the presence of crack-bridging conductive fibres. The gauge factor during the strain hardening was found to be ~100 for the standard ECC mix and ~20 for the other mixes containing steel and carbon fibres. This finding suggests that conductive fibres are not preferred to be used in ECCs due to their knock-on effects on sensitivity.

Since the steel and carbon fibres decrease the material sensitivity to cracking, Lin et al. (2011) added carbon black to the standard ECC mix to increase the contrast of the composite resistivity before and after cracking, thereby increasing its sensitivity for damage detection. The four-point a.c. measurement technique was employed, with measurements undertaken at 100 Hz. As shown in Figure 2.14(c), the resistivity of M45-ECC increases to 60 MΩ-cm as the material is loaded in tension to 1% strain, while the carbon black ECC increases from 4 to 40 MΩ-cm at the same strain level. The gauge factors of the M45-ECC during strain-hardening were found to be generally larger than those of the standard ECC, which was around 283, (considerably higher than those reported earlier), possibly due to the macro-crack formation between the current and the sensing electrodes. Suryanto et al. (2015) added recycled milled carbon fibres to the ECC mix. The average length of the fibres was ~100µm (the same order to the micro-crack width of ECC), in an attempt to maintain the material sensitivity to crack formation. The a.c. electrical measurements at a fixed frequency of 100 kHz were

employed. It was found that the gauge factors of the ECC were in the range of 200 to 340 (see, for example, Figure 2.14(d). However, the addition of milled carbon fibres at 0.75% by volume was found to reduce the gauge factors to the range of 80–130, possibly due to the presence of crack-bridging conductive fibres at micro-cracks with a crack width of less than ~100 μm.

Employing the two-point method and a constant a.c. current of 1 kHz, Ranade et al. (2014) tested moderate- and high-volume fly-ash ECC mixes with different micro-crack characteristics. The moderate fly-ash ECC mix contained fly-ash to cement at a ratio of 1.2, whereas the corresponding ratio in the high-volume fly-ash ECC was 2.8. It was found that, although the moderate-volume fly-ash mix exhibits less micro-cracking, due to its greater micro-crack widths, this mix was more sensitive to mechanical loading, as demonstrated by the greater relative change in resistivity which was found to increase to approximately 5 as the composite was loaded to around 2% in tension (see Figure 2.14(e)). Higher gauge factors were obtained, in the range from 24 to 232. They also found that the high-volume fly-ash ECC mix exhibited less increase in relative change in resistivity, to a value of approximately 3 at 4% of tensile strain (see Figure 2.14(f)). Accordingly, the gauge factors of this high-volume fly-ash ECC mix were found to be smaller, in the range of 13 to 78, indicating that this mix exhibits less sensitivity to cracking than the moderate-volume fly-ash ECC mix due to its smaller micro-crack widths.

Huang et al. (2018) investigated the piezo-resistive properties of moderate- and high-volume fly-ash ECC mixes with fly-ash to cement (FA/C) ratios of 1.2 and 3, respectively. The modified two-probe method under direct current was employed, and it was found that the gauge factors were in the range around of 75–235 for the moderate-volume fly-ash ECC mix (see Figure 2.15(a)), and around 17–50 for the high-volume fly-ash ECC mix (see Figure 2.15(b)). Deng and Li (2018) employed the four-point probe-method with high frequency a.c. supply (1 KHz frequency). It was found that the moderate fly-ash ECC (with fly-ash to cement ratio of 1.5) produced gauge factors in the range 130–257 (see Figure 2.15(c)), while the high-volume fly-ash ECC mix (fly-ash to cement ratio of 3) produced values in the range 50–94 (see Figure 2.15(d)). These values are comparable to the results found by Ranade et al. (2014), and the findings highlighted in the articles also confirm that the crack pattern of ECC (i.e., crack width and number) has a significant influence on its electrical response.

Yıldırım et al. (2020) utilised the 2-probe a.c. concrete resistivity meter at 1 kHz frequency to investigate the self-sensing capability of the ECC at different curing ages (i.e., at 7, 28, 90, and 180 days of curing). It was observed that the ECC specimens at different ages were able to sense the damage in the ECC matrix due to multiple crack formation. However, it was reported that due to the limitations of the 2-probe a.c. concrete resistivity meter, no results were able to be obtained for the specimens cured for 180 days. As illustrated in Figure 2.15(e), the gauge factors of the ECC mix at 28 days of curing ranged from approximately 60 to 150.

In order to allow direct comparison of the piezo-resistive data from the previous researchers, the data displayed in Figures 2.14(a)-(f) and 2.15(a)-(e) were digitized in the OriginLab Software and now presented as the Fractional Change in Resistivity (FCR) against tensile strain in Figure 2.16. It is apparent that there is clearly a wide scatter in published FCR values due to the different ECC mixes used in each experiment and the different test procedures employed in each dataset. With regard to the apparent value of the FCR at 1% tensile strain, this varies from approximately 8 in Deng and Li (2018) and 15 in Huang et al. (2018) to as high as approximately 170 in Ranade et al. (2014), 200 in Suryanto et al. (2015) and 260 in Lin et al. (2011). It is worth noting that a higher value of FCR would produce a higher slope between FCR and tensile strain and would indicate higher sensitivity to tensile straining. It is interesting to note that in cases where the FCR values are relatively low, the mix contains a high volume of fly-ash, and such a mix would exhibit smaller crack widths, as reported in Ranade et al. (2014), Huang et al. (2018), and Deng and Li (2018). The large scatter in data could therefore be partly attributed to difference in crack width between the moderate- and high-volume fly-ash mixes. In addition, it is worth nothing there has been a few data published at strains levels of greater than approximately 4% as this would largely depend on the available tensile strain capacity of the ECC under study.
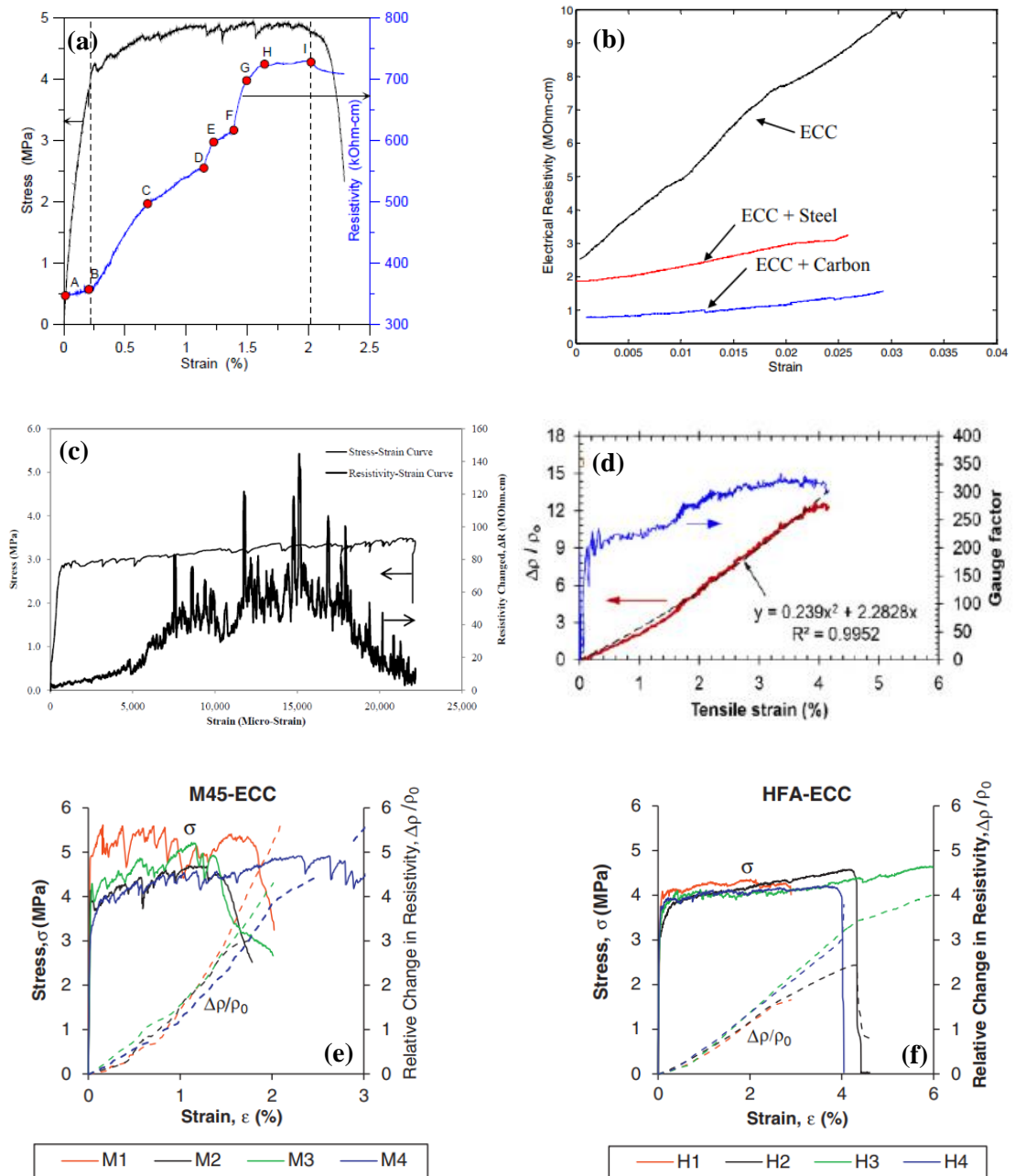
Figure 2.14: Piezo-resistive data available in the literature (Part 1): (a) M45 ECC mix (Hou, 2008); (b) ECC with different conductive materials (Hou and Lynch, 2005); (c) M45 ECC mix (Lin et al., 2011); (d) Control ECC mix (Suryanto et al., 2015); (e) M45 mix incorporating moderate volume of fly-ash (Ranade et al., 2014); and (f) ECC mix incorporating high volume of fly-ash (Ranade et al., 2014).
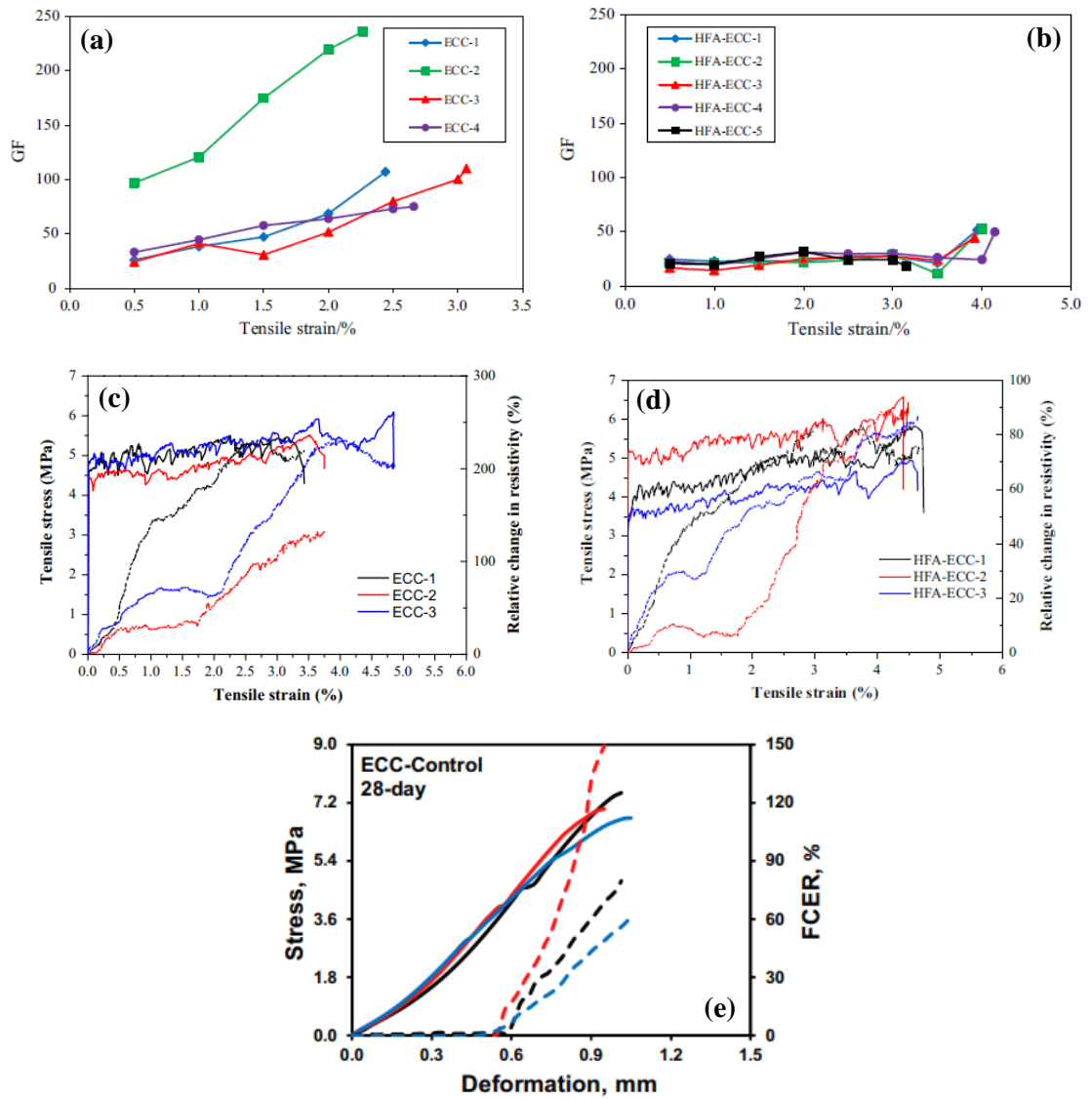
Figure 2.15: Piezo-resistive data available in the literature (Part 2): (a) Control ECC mix (Huang et al., 2018); (b) ECC mix incorporating high volume of fly-ash (Huang et al., 2018); (c) Control ECC mix (Deng and Li, 2018); (d) ECC mix incorporating high volume of fly-ash (Deng and Li, 2018); and (e) ECC-Control mixtures (Yıldırım et al., 2020).
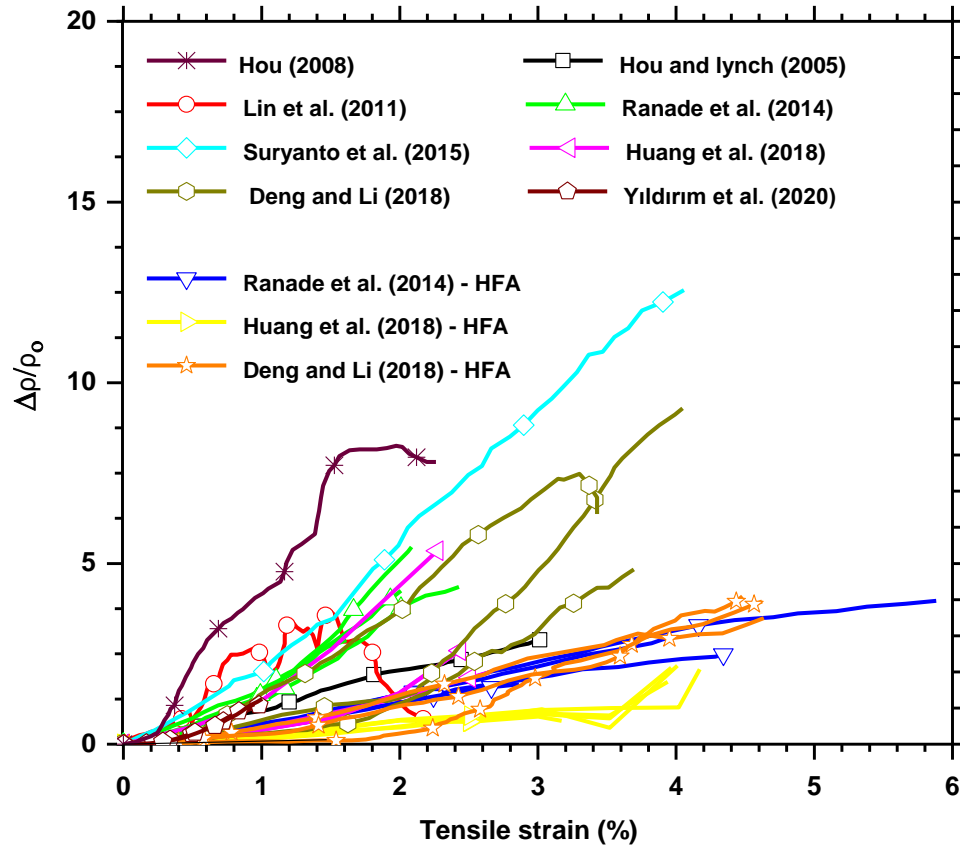
Figure 2.16: A summary of the piezo-resistivity response figures from previous researchers is presented in Figures 2.14 and 2.15. In this figure, the original data were converted to the relative change in resistivity and plotted against tensile strain.

To better understand the influence of the width and number of micro-cracks in the ECC matrix, a review on the distribution of cracking reported in the articles where the electrical properties were reported is made in Figures 2.17(a)-(g). To allow direct comparisons of all the data available in the literature, the best-fitting lognormal distribution curves of crack width for different versions of ECCs at failure are presented in Figure 2.18.

In Ranade et al. (2014), photographs of coupon specimens were taken at regular intervals during tensile loading, with the aim of documenting the crack patterns during testing. It was found that the crack patterns in moderate- and high-volume fly-ash ECC mixes (M45 and HFA ECC mixes, respectively) were very different. The average crack width in the M45 mix was almost double that observed in the HFA mix.

Ranade et al. (2014) stated that the mean crack width at 1% strain of HFA-ECC was 40 μm, while the M45-ECC is approximately 66 μm. Ranade and co-workers argued that this was the reason for the apparent higher values of gauge factors of the M45-ECC than those of the HFA-ECC (see Figure 2.14(d) and 2.14(e)).

Liu et al. (2016) used a portable microscope with a resolution of 10 μm to determine the crack patterns of the ECC specimens they tested at different tensile strain levels. It was found that crack width and crack number increased significantly up to 1% strain (average crack width = 48 μm and crack number = 13). Subsequently, a slight increase in the crack width was found, and it was noted that the increase in tensile strain was attributed mainly to the increase in crack number. At 2% tensile strain, there were 24 cracks in total, and the average crack width was 55 μm. It was noted that the accuracy of the crack detection was limited as very fine cracks with widths of less than 10 μm were not able to be detected using the portable microscope.

Huang et al. (2018) measured the crack widths in the ECC specimens they tested using an optical microscope with a magnification of 30 times. It was found that the mean crack number in their ECC specimens was 19, which is about one-fifth of the crack number in the high-volume fly-ash (HFA) ECC mix, where 100 cracks were found. The crack widths in the control ECC mix were found to be in a wide range of 10–120 μm, while those in the HFA-ECC were within a narrow range of 7–15 μm. They suggested that both the crack number and crack width had an impact on the trend of the gauge factors observed, with larger crack widths producing a more upward trend. For the control ECC mix they tested, it was suggested that the relationship between tensile strain and resistivity is non-linear and that the increase in crack width with increasing tensile strain contributed to the increase in gauge factor. For the HFA ECC mix, a constant gauge factor was evident, and it was suggested that this was due to the small crack widths experienced by this series of specimens. While the number of cracks increased the apparent tensile strain, the widths remained small enough to allow electrical current to flow across the cracks. As such, the formation of further cracks was not seen electrically, and the gauge factor was therefore constant.

Deng and Li (2018) investigated the relationship between gauge factor and crack width in the ECC matrix. Two mixes were produced, with a moderate-volume of fly-ash (FA/C = 1.5) and an HFA-ECC mix (FA/C = 3.0). They found that at 3.84 ± 0.34 mean

tensile strain, the average crack width of their standard ECC mix was within the range of 10–100 μm, with a mean crack width of 44 μm and a crack number of 14. On the other hand, at 4.51 ± 0.10 tensile strain, the average crack width of the HFA mix was within the range of 5–50 μm, with a mean crack width of 14 μm and an average crack number of 38. They also found that regardless of the tensile strain level applied, the gauge factor was affected more significantly by the crack width than the crack number.
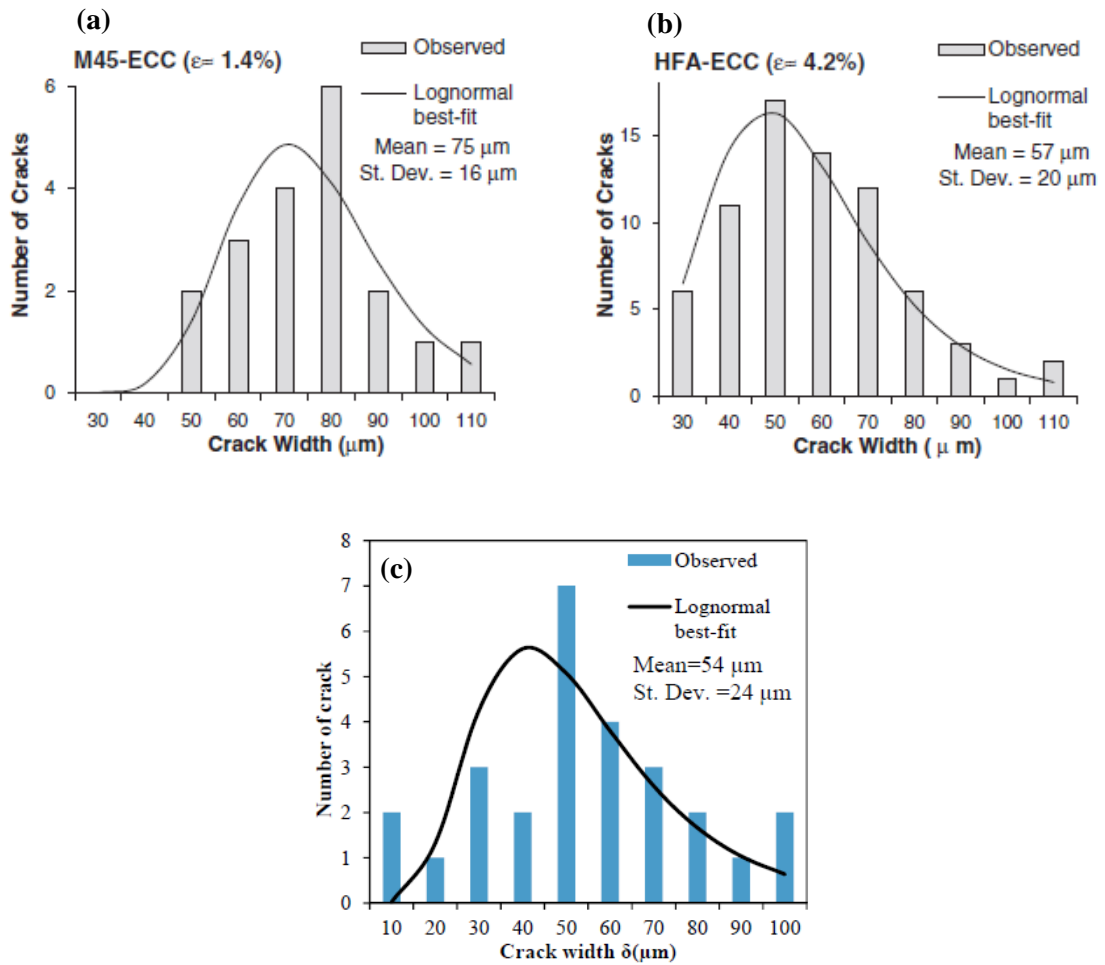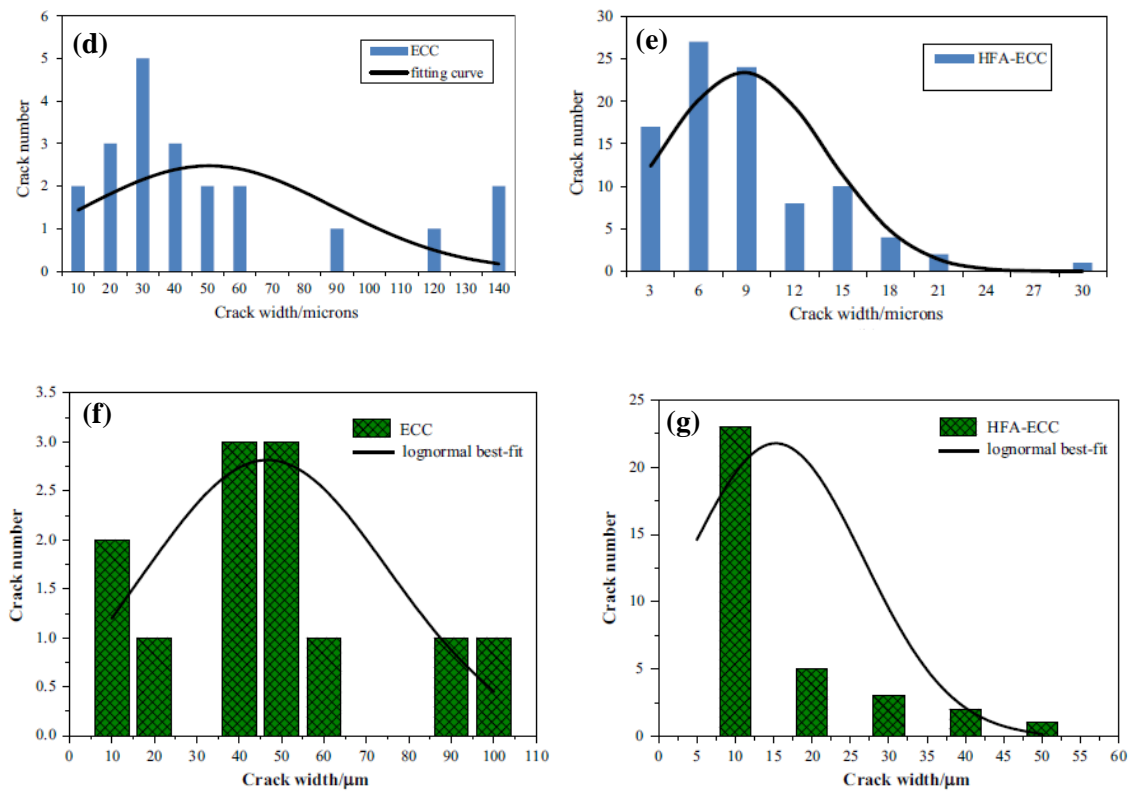
Figure 2.17: A summary of lognormal best-fit curves figures from previous researchers of (a) M45 mix incorporating moderate volume of fly-ash (Ranade et al., 2014); (b) ECC mix incorporating high volume of fly-ash (Ranade et al., 2014); (c) ECC mix (Liu et al., 2016); (d) control ECC mix (Huang et al., 2018); (e) ECC mix incorporating high volume of fly-ash (Huang et al., 2018); (f) control ECC mix (Deng and Li, 2018); (g) ECC mix incorporating high volume of fly-ash (Deng and Li, 2018).
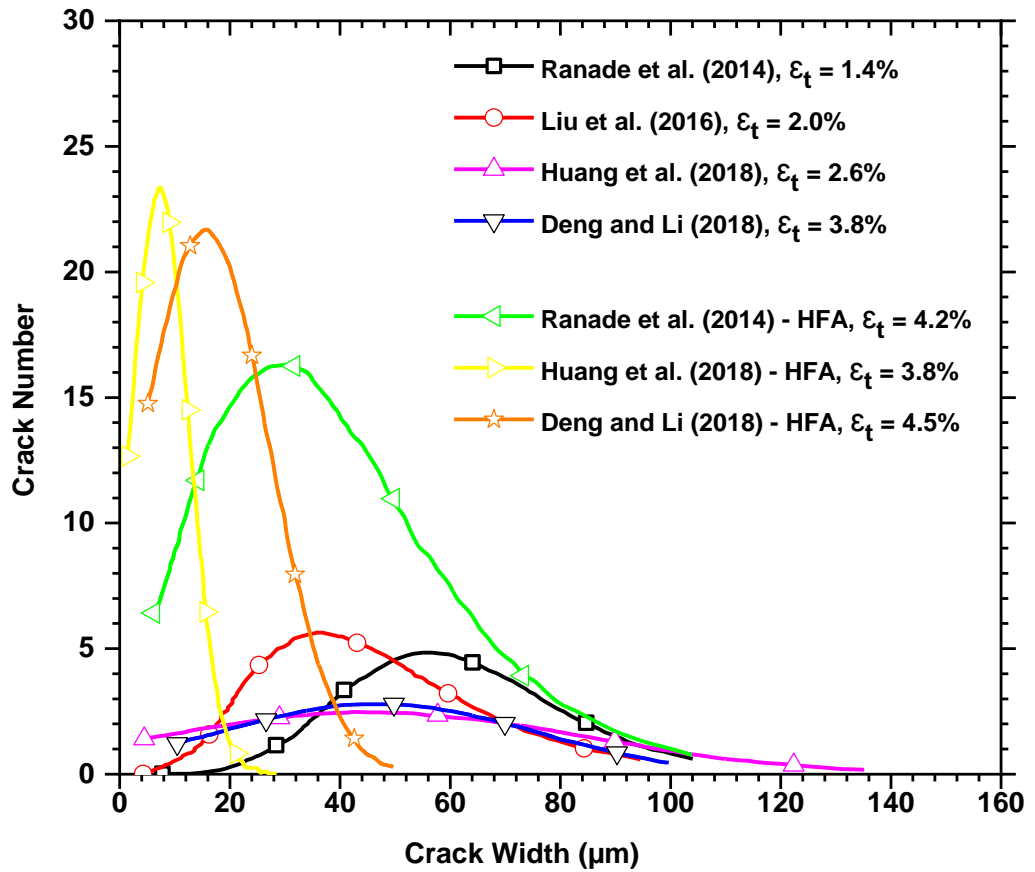
Figure 2.18: A summary of the lognormal best-fit curves figures from previous researchers presented in Figure 2.17.

2.5 Analytical and Equivalent Circuit Models

2.5.1 Modelling of the Piezo-resistive Response

Ranade et al. (2014) proposed an analytical model in order to predict the piezo-resistive response of ECC. The schematic representation of the model is illustrated in Figure 2.19. This model was derived based on the electrical behaviour of a single-crack A.ΔR(δ) specimen and crack-width distribution p(δ,ε) obtained from a coupon specimen experiencing multiple cracking.

With reference to Figure 2.19, a coupon specimen with a gauge length (L) exposed to tensile strain (ε) causing the formation of multiple micro-cracks, is taken into account for the derivation below. According to the series resistor theory (Kirchhoff's voltage law), the resistance (R(ε)) appears in Equation 2.1, across L is equal to the sum of the resistances, including the initial resistance (at strain = 0) (R_0) and the changes in

resistance (ΔR) caused by the small elastic strain (ε_e) and strain as a result of cracking (ε_c).

$$R(\varepsilon) = R_0 + \Delta R_e \, (\varepsilon_e) + \Delta R_c \, (\varepsilon_c) \qquad (2.1)$$

The changes in resistance (ΔR) resulting from the εe are calculated through the elastic Gauge Factor (GF_e), while the change in resistance resulted from the ε_c is calculated through the sum of increases in resistance resulting from the individual cracks. It is presumed that n_i numbers of cracks formed during tensile loading with crack width (δ_i), and total crack number n ($n_1 + n_2 + \ldots$) (See Figure 2.19).

$$R(\varepsilon) = R_0 + \frac{\Delta \rho \, (\varepsilon_e)}{\rho_0} \, R_0 \; + \; \sum_i n_i(\varepsilon) \, \Delta R_i \, (\delta)_i \qquad (2.2)$$

With reference to Figure 2.17(a)-(b) which displays the observed crack width distributions (CWDs) and the lognormal distributions best-fitting. It should be noted that the best-fit curves can be plotted through scaling up the probability density function (PDF) through the total crack number at a specific strain-level and histogram class interval. In mathematical terms, the lognormal PDF ($p(\delta,\varepsilon)$) (See Equation 2.3), for crack width distribution (CWD) in a coupon specimen under tensile strain can be expressed by the crack width (δ), mean (μ) and standard deviation (σ). Equations 2.4 and 2.5 show how to further express the μ and σ in terms of mean (m) and standard deviation (s) of the lognormal distribution as a function of strain (ε). The constant coefficients C_i and K_i (i = 0,1,2,3) can be measured through the regression analysis. *Note: Generally in this thesis, the symbol μ represents the micro and σ represents the conductivity.

Therefore, It can postulate that the crack width (δ_i) has a real number between 0 to ∞, ruled by PDF ($p(\delta,\varepsilon)$), which can be determined through Equations 2.3, 2.4 and 2.5 mentioned below. Therefore, it can express the total crack number at a specific strain (ε) with crack width (δ_i) as shown in Equation 2.6, where $d\delta \rightarrow 0$ is a small neighborhood around δ.

$$p(\delta,\varepsilon) = \frac{1}{\delta \sigma \sqrt{2\pi}} \, e^{\frac{-(\ln \delta - \mu)^2}{2\sigma^2}} \qquad (2.3)$$

$$\text{Where, } \mu = \ln \frac{m^2}{\sqrt{s^2 + m^2}} \, \& \, \sigma = \sqrt{\ln(\frac{s^2}{m^2} + 1)} \qquad (2.4)$$

$$m = C_3\,\varepsilon^3 + C_2\,\varepsilon^2 + C_1\,\varepsilon + C_0 \ \& \ s = K_3\,\varepsilon^3 + K_2\,\varepsilon^2 + K_1\,\varepsilon + K_0 \tag{2.5}$$

$$n_i(\varepsilon) = n.p(\delta,\varepsilon)d\delta \tag{2.6}$$

Thus, it can express the total resistance $R(\varepsilon)$ of the coupon specimen as displayed in Equation 2.7.

$$R(\varepsilon) = R_0 + \varepsilon_e\,GF_e\,R_0 + n \int_0^\infty p(\delta,\varepsilon)\,\Delta R(\delta)d\delta \tag{2.7}$$

The total crack number (n) equals the total tensile displacement caused by the cracks ($\varepsilon_c L \approx \varepsilon L$) divided by the presumed crack width value (integral expression in the denominator of Equation 2.8. After rearranging and substituting values in Equation 2.7, Equation 2.8 can be obtained.

$$\frac{R(\varepsilon)\,R_0}{R_0} = \varepsilon_e\,GF_{e\,+}\,\frac{1}{R_0}\left(\frac{\varepsilon L}{\int_0^\infty p(\delta,\varepsilon)\delta d\delta}\right)\int_0^\infty p(\delta,\varepsilon)\,\Delta R(\delta)d\delta \tag{2.8}$$

Equation 2.9 indicates that the R_0 can be expressed in terms of ρ_0, L, and A. Therefore, obtaining Equation 2.10 which has been simplified more to create the most recent expression for the model shown in Equation 2.11.

$$\rho = \frac{R\,A}{L} \tag{2.9}$$

$$\frac{\Delta R(\varepsilon)}{R_0} = \varepsilon_e\,GF_{e\,+}\,\frac{\varepsilon L}{\rho_0\,L/A}\,\frac{\int_0^\infty p(\delta,\varepsilon)\Delta R(\delta)d\delta}{\int_0^\infty p(\delta,\varepsilon)\delta d\delta} \tag{2.10}$$

$$\frac{\Delta \rho(\varepsilon)}{\rho_0} = \varepsilon_e\,GF_{e\,+}\,\frac{\varepsilon}{\rho_0}\,\frac{\int_0^\infty p(\delta,\varepsilon)\{A.\Delta R(\delta)\}d\delta}{\int_0^\infty p(\delta,\varepsilon)\delta d\delta} \tag{2.11}$$

Since the change of ε_e is quite slight after the first crack, it is presumed that the ε_e is a constant equal to the strain when the first crack occurs (It can be calculated from the average first crack strength) and elastic modulus. The justification for assuming ε_e as a constant is due to the negligible resistance value caused by the elastic stretching compared to the resistance caused by cracking.
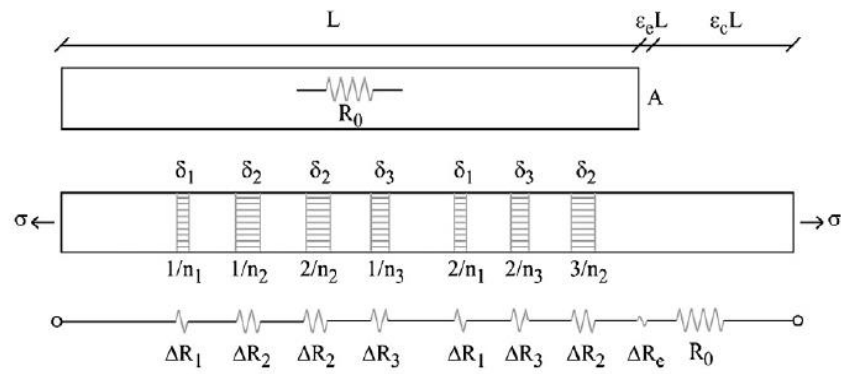
Figure 2.19: Analytical model represents series resistance introduced by the formation of micro-cracks (Ranade et al., 2014).

A comparison between the experimental and analytical results is presented in Figure 2.20, with solid lines showing the predicted values and dotted lines showing the experimental results. Note that in this figure, the M45 mix displays a lower tensile strain capacity than the HFA mix due to the inherent differences in the mechanical properties of the two mixes. A good agreement was observed, although the predicted values slightly overestimated the observed response. It was suggested that this overestimation of resistivity is attributed to the limitations of the analytical model, which does not take into consideration the variable crack-width that may occur in a single crack.
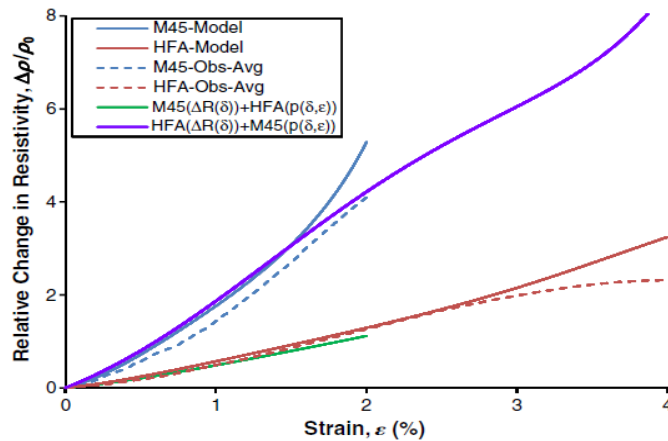
Figure 2.20: Comparison between the modelled and observed average behaviours of M45-ECC and HFA-ECC specimens (Ranade et al., 2014).

2.5.2 Equivalent circuit modelling

The impedance response of a material can be represented as an electrical circuit by using a combination of parallel and/or series circuit elements (McCarter et al., 2015). With regard to the impedance response of a cement-based system, this can be

represented by a resistor (R) and a capacitor (C) connected in parallel (McCarter et al., 2001). Figure 2.21 shows the ideal response of a parallel combination of a 1.0 kΩ resistor and a 10^{-10} F capacitor. It is evident that the response takes the form of a semi-circular arc whose centre is located on the real (Z'(ω)) axis. However, this is in contradiction with the electrical response of general cementitious materials, which, although showing the same semi-circular arc, the centre of the impedance spectrum is depressed below the real axis. It was suggested that this phenomenon is attributed to the relaxation of polarization processes inside the material, which causes dielectric dispersion (i.e., a reduction in capacitance with an increase in frequency) (McCarter et al., 2015). In order to consider this dispersive behaviour in modelling, it has been proposed to replace the capacitor with a constant-phase-element (CPE) (see Figure 2.21(a)). The CPE can be defined through the relationship,

$$Z''_{CPE}(\omega) = \frac{1}{C_o \, (i\omega)^p}$$

(2.12)

where C_o represents a coefficient; $i = \sqrt{-1}$; ω is the angular frequency (= 2πf where f is the applied-field frequency in units of hertz); and the exponent, p, has a value between 0 and 1. If p =1, then the equation is similar to the reactive component of a pure capacitor, (C_o having unit in Farad (F)). A CPE with a value of p < 1 set in parallel with the resistor produces a circular arc whose centre is depressed under the Z_{real} axis (C_o having unit in Farad $(F \, (s)^{p-1})$).

The arc depression angle (α) which is shown in Figure 2.21, is associated with the exponent (p) through the relationship,

$$\alpha = \frac{\pi}{2} \, (1 - p \,) \, radians$$

(2.13)
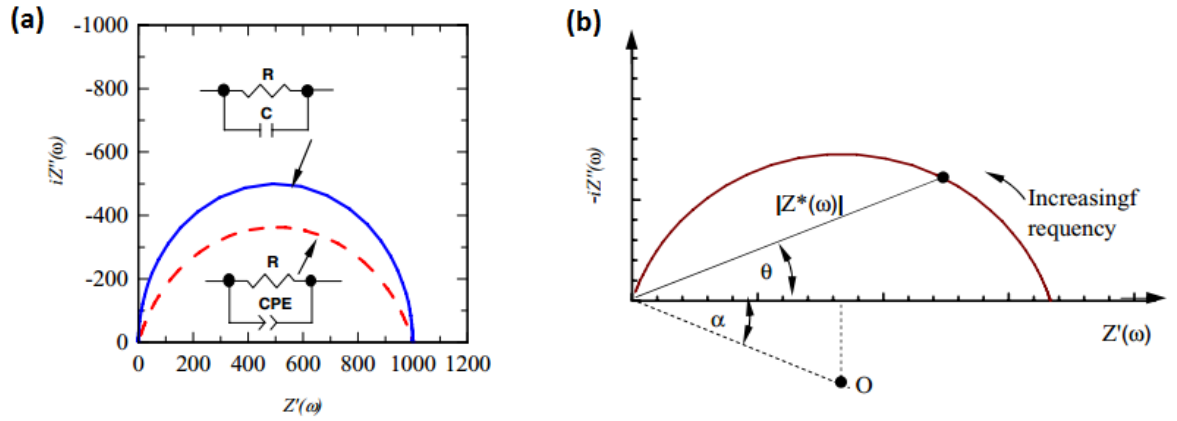
Figure 2.21: (a) Effect of CPE on the Nyquist plot (the solid semicircle is the Nyquist plot for a pure capacitor connected in parallel with a resistor [C = 10^{-10} F and R = 1.0 kΩ], while the dashed semicircle is a CPE [$C_o = 10^{-10}$ Fs$^{-0.2}$, $p = 0.8$] connected in parallel with a resistor [R = 1.0 kΩ]); (b) a schematic of a Nyquist plot for a saturated cement-based material, illustrating arc depression angle (α), impedance (Z*(**ω**)), phase angle (θ) and arc centre (O) (McCarter et al., 2015).

Suryanto et al. (2016) proposed a schematic diagram representing three electrical pathways of an ECC containing conductive fibres well below the percolation threshold (see Figure 2.22(a)). In this model, the upper-path represents continuous capillary pores (conductive ions); the middle-path represents the solid-matrix consisting of hydration products, sand particles, isolated pore-water, un-hydrated cement and 'dead-end' pores; and the bottom path represents the combination of continuous capillary pores, fibre/fibre matrix and interface/solid matrix. These paths are represented by the circuit shown in Figure 2.22(b), which includes:

- A resistor, R_s, which was used to describe the projected intercept of the high-frequency arc with the real-axis at the high-frequency end;

- A parallel combination of a resistor, R_{cp}, and a constant phase element, CPE_{sm}, to describe the ionic conduction through the capillary pore network and the response from the solid matrix, respectively; and

- A complex path comprising a resistor, R_f, which was used to describe the electronic conduction through fibre-fibre contact; and two parallel components: R_{fi}/CPE_{fi}, which was used to represent the interface between the conductive fibre and the cement matrix; and R_{f-cp}/CPE_{f-sm}, which was used to describe the matrix between the conductive fibres.
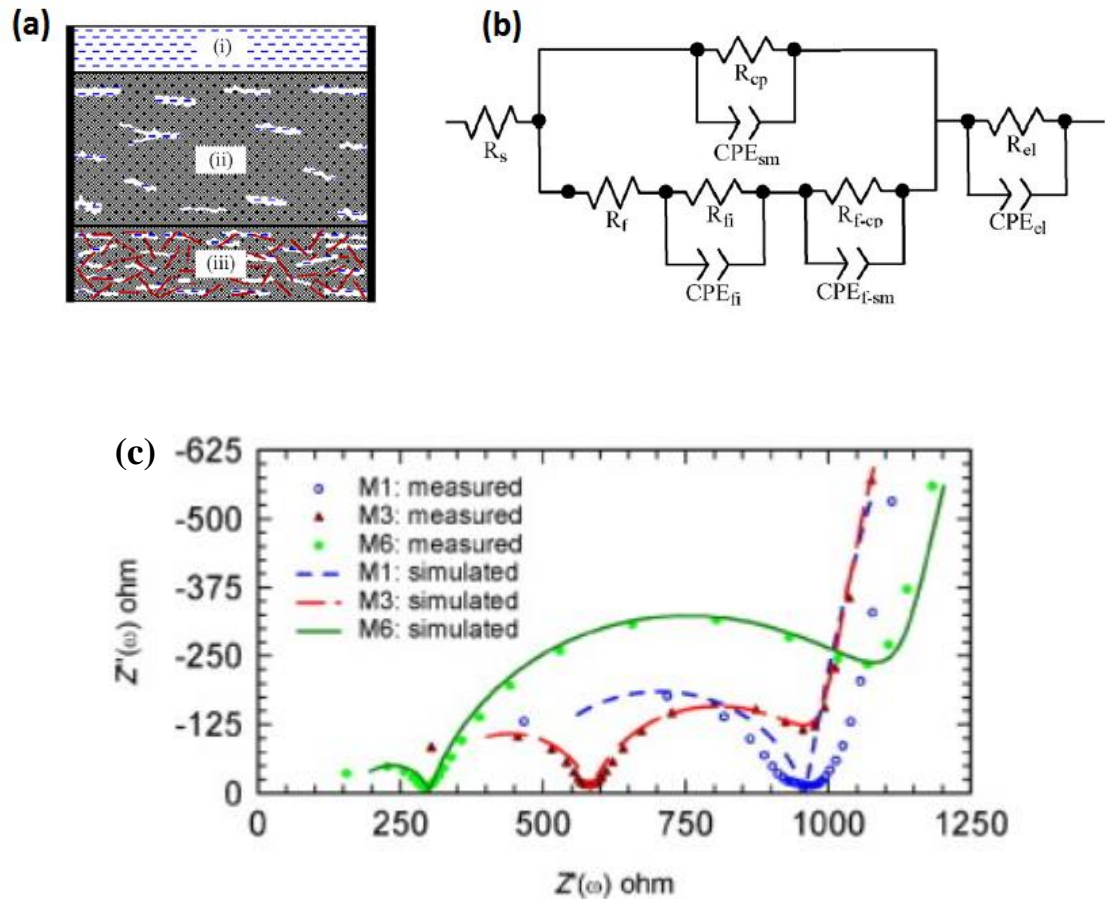
Figure 2.22: (a) Schematic diagram represents the potential electrical pathways in cement-based composite placed between two parallel electrodes; (b) electrical model for the cement-based composite mentioned in (a); and (c) measured and simulated impedance response for Mix 1 (ECC), Mix 3 (ECC with 0.15% steel fibres), Mix 6 (ECC with 1.0% steel fibres) at the 7th day of curing (Suryanto et al., 2016).

Figure 2.22(c) presents an example of the application of the circuit model. It was found that the measured and simulated responses illustrate good compatibility with the slight degradation present at the high frequency end of the impedance response. In addition, Suryanto et al. (2016) suggested the need to define the contribution of the un-burnt carbon in the fly-ash that causes the U-shaped valley development in the impedance response.

2.6   Summary of Knowledge Gaps

From the extensive literature review presented in this chapter, the following knowledge gaps were identified in the literature and were then used as the basis for this PhD:

(1) There have been limited investigations into the electrical properties of ECCs over a wide frequency band, with only one article published by Suryanto et al. (2016), but quite restrictive in terms of the duration of investigation (i.e., 28 days of curing).

(2) Only a few studies (Hou, 2008; Li et al., 2012; Li et al., 2013; Suryanto et al., 2016) have been undertaken to investigate the influence of cement hydration under different curing conditions. Given that cement hydration is one of the key characteristics of cement-based materials, it is surprising that this aspect of investigation has been overlooked in prior studies. A better understanding of ongoing hydration effects is imperative if the material would be used on-site for monitoring purposes.

(3) No systematic study was undertaken on the influence of temperature, despite the fact that ambient temperature in real-world situations always fluctuates. In many countries around the world, in particular those with different seasons, seasonal changes in temperature are present and can have a significant influence on measured electrical response. Given that electrical conduction in cement-based materials is primarily through mobile ions in the aqueous phase inside the matrix, its electrical response will display temperature dependence.

(4) With regard to damage sensing, the current approach has focused primarily on the piezo-resistive properties of ECC, with no consideration of other electrical properties of ECC. In particular, no study was undertaken on the piezo-impedance response of ECCs, or their electrical properties over a wide frequency range under loading.

(5) Only a limited study was conducted to investigate the effect of moisture ingress into the surface region of ECC on the electrical properties of ECC (Suryanto et al., 2017a). Measurements were only taken at a fixed a.c. frequency, and no study was done involving the use of impedance spectroscopy.

(6) There has been a limited study on the use of electrical circuit modelling in ECCs, with the investigation limited to ECCs under no loading. Given that high tensile ductility is the main feature of ECC, this means the conduction through the micro-cracks should be given more attention.

A research programme was therefore setup to address these gaps and is presented in the next chapter.

3 Experimental Programme

3.1 Introduction

This chapter describes an experimental programme that was undertaken for this PhD. Various laboratory test campaigns were undertaken to investigate the influence of mechanical loading and other non-mechanical aspects on the self-monitoring capabilities of ECC. The experimental programme comprises three main work packages, and in each of these work packages, a description of the materials used in this research, mix compositions, details of the fabrication and curing procedures, test equipment, and detailed test procedures are provided.

3.2 Summary of the specimens in this research

Table 3.1 provides a summary of the specimens that were fabricated and tested in this research. A total of 12 prismatic samples and 27 cubes were produced for the first work plan (hydration and temperature studies); a total of 8 dog-bone samples, 5 prismatic samples, and 18 cubes were produced for the second work plan (piezo-impedance study); and a total of 7 dog-bone samples, 2 prismatic samples, and 3 cubes were produced for the third work plan (wetting and drying studies). In addition, a total of 2 prismatic samples and 3 cubes were produced to conduct a small-scale test which was used in the second work plan.

Table 3.1: Summary of test specimens.

Work Plan (WP)	Mixture Name	Number of Specimens
WP1: Hydration and temperature studies	ECC (MB) mix, MF0 (PC), MF15, MF30, and MF64 ECC mix (P1 and P2)	Hydration: 3 cubes and 2 prismatic samples for each mix (10 prismatic samples and 15 cubes in total) + Temperature: 2 prismatic samples and 12 cubes
WP2: Piezo-impedance study and a small-scale test	First series of ECC mix (T-ECC-S) Second series of ECC mix (T-ECC-L) ECC mix without PVA fibres (E-ECC-(P1-P2))	First series: 9 cubes, 4 dog-bone and 3 prismatic samples + Second series: 9 cubes, 4 dog-bone and 2 prismatic samples + 2 prismatic samples and 3 cubes
WP3: Wetting and drying and a small scale test	ECC mix (T-ECC-TF, T-ECC-PC, E-ECC-NC)	3 cubes, 7 dog-bone and 2 prismatic samples

3.3 WP1: Hydration and Temperature Studies

This work package involved the testing of 10 prisms to study the influence of on-going cement hydration over a period of 180 days; 2 other prisms to study the influence of temperature; and 27 cubes to determine the compressive strength of both studies. Table 3.2 provides details of the specimens in this work package, including the number of specimens, test age, and purpose.

Table 3.2: Summary of test specimens in WP1.

Test	Name and number of test specimens	Test age	Purpose
Hydration study	Prisms: -2 ECC mix (MB) and 2 OPC mortar (MF0).	Prisms: 7, 14, 21, 28, 42, 63, 90 and 180 days	Prisms: -To study the influence of on-going hydration on the electrical properties
	-ECC mixes MF15, MF30, and MF64 with fly ash replacements of 15%, 30% and 64% respectively. 2 prisms for each mix	7, 14, 21, 28, 42, 63, 90, 180 and 360 days	-To investigate the effect fly-ash within the ECC mix on the electrical properties.
	Cubes: 3 cubes for each mix	Cubes: 28 days	Cubes: To measure the compressive strength
Temperature study	Prisms: ECC P1 and P2	Prisms: 360 days	Prisms: To study the influence of temperature on the electrical properties.
	Cubes: 12 cubes	Cubes: 28, 90, and 180 days	Cubes: To measure the compressive strength

3.3.1 Materials and Sample preparation

The mix proportions for the ECC used in this experimental programme are presented in Table 3.3. The binder comprised a blend of CEM I 52.5N Portland cement to BS EN197-1 (British Standards Institution, 2000) and fine fly-ash (Superpozz SV80, supplied by ScotAsh Ltd) at a cement/fly-ash ratio of 1:1.8. To improve the dimensional stability of the mix, fine silica sand (RH110, supplied by Minerals Marketing) with a mean particle size of 120 µm was added at a sand/cement (S/C) ratio of 0.6:1 by mass. A typical oxide analysis of these materials is presented in Table 3.4. The water/binder (W/B) ratio was set at a relatively low value (= 0.28) to produce a mix

with adequate viscosity, necessitating breaking up fibre bundles. The only fibres incorporated into the mix were Kuralon K-II REC15 Polyvinyl Alcohol (PVA) fibres, which have been specifically developed for use in ECC by Kuraray Japan. The fibres had an average length of 12 mm and a diameter of 39 μm, and were supplied with a proprietary oil-based coating agent (1.2% by mass) to reduce the fibre/matrix interfacial bonding (Li, 2008). To aid fibre dispersion and improve the workability of the mix, a high-range water-reducing (HRWR) admixture (MasterGlenium ACE499) was added at a dosage of 1% by cement weight.

In order to gain an understanding of the influence of the fly-ash within the ECC on the bulk impedance; a modification was introduced to the base ECC mix (which was presented above). Four mixes were prepared based on the fly-ash replacement with 0%, 15%, 30%, and 64% for MF0, MF15, MF30, and MF64, respectively. For these mixes, the W/B and S/B ratios were kept the same as in the original mix.

Table 3.3: Details of different ECC mix compositions (in kg/m^3).

Mixture Name	Water (kg/m^3)	CEM I 52.5N (kg/m^3)	Fly-ash (kg/m^3)	Silica sand (kg/m^3)	HRWR (kg/m^3)	PVA fibre (kg/m^3)	F$_{28}$ (MPa)
ECC	356	454	818	273	4.54	26 (2%)	33.1
MF0	409	1460	0	313	7.30	0	106.6
MF15	397	1207	212	304	6.04	0	90.9
MF30	386	965	413	295	7.24	0	64.5
MF64	363	464	834	278	4.64	0	31.4

Notes: HRWR: High-range water reducer; F$_{28}$ is compressive strength determined on 50mm cubes at 28 days.

Table 3.4: Oxide analysis of materials (+ = not determined).

	PC	Fly-ash	Silica sand
Chemical analysis			
SiO_2	19.9	52.7	98.8
Al_2O_3	4.8	26.6	0.21
Fe_2O_3	3.1	5.6	0.09
K_2O	0.54	1.0	0.03
Na_2O	0.08	0.2	+
CaO	62.4	2.4	+
MgO	2.2	1.2	+
SO_3	3.0	0.3	+
Free CaO	+	0.03	+
Total phosphate	+	0.5	+
Loss on Ignition (LOI)	+	<2.0	0.14
Physical properties			
Specific gravity	3.15	2.20	2.65
Surface area (m^2/kg)	375	1300	+
Fineness (% retained on 25µm)	+	<25	+
Size distribution (µm) and cumulative retained (%)			
500	+	+	0.1
355	+	+	0.5
250	+	+	1.5
180	+	+	6.0
125	+	+	46.0
90	+	+	83.0
63	+	+	96.5

All materials were mixed in a 10-liter Hobart planetary motion mixer, with mixing undertaken in one batch to ensure consistency. Two types of specimens were used in this investigation: 40 × 40 × 160 mm (long) prismatic specimens to monitor the influence of continued hydration (see Figure 3.1(a)), and 50 mm cuboidal specimens to determine compressive strengths (see Figure 3.1(b)). The prisms were cast into a single-use 3-gang polystyrene mould, whereas the cube specimens were cast into 3-gang cube moulds. Prior to casting, two 45 × 65 × 2 mm (thick) 316L stainless steel electrodes were positioned at opposing ends of the prismatic mould at 140 mm apart. The

electrodes had 10mm diameter perforations staggered at 15 mm pitch, allowing for the infiltration of fresh ECC during casting, thereby ensuring intimate bonding with the specimen. Immediately after casting, all specimens were covered with polyethylene sheets and left to cure for 24 hours before being demoulded and stored under saturated conditions in a water tank at $21 \pm 2^{o}C$ for 180 days. Prior to any electrical measurement, each specimen was removed from the curing tank and then wiped with a towel to dry the surface.

(a)

(b)
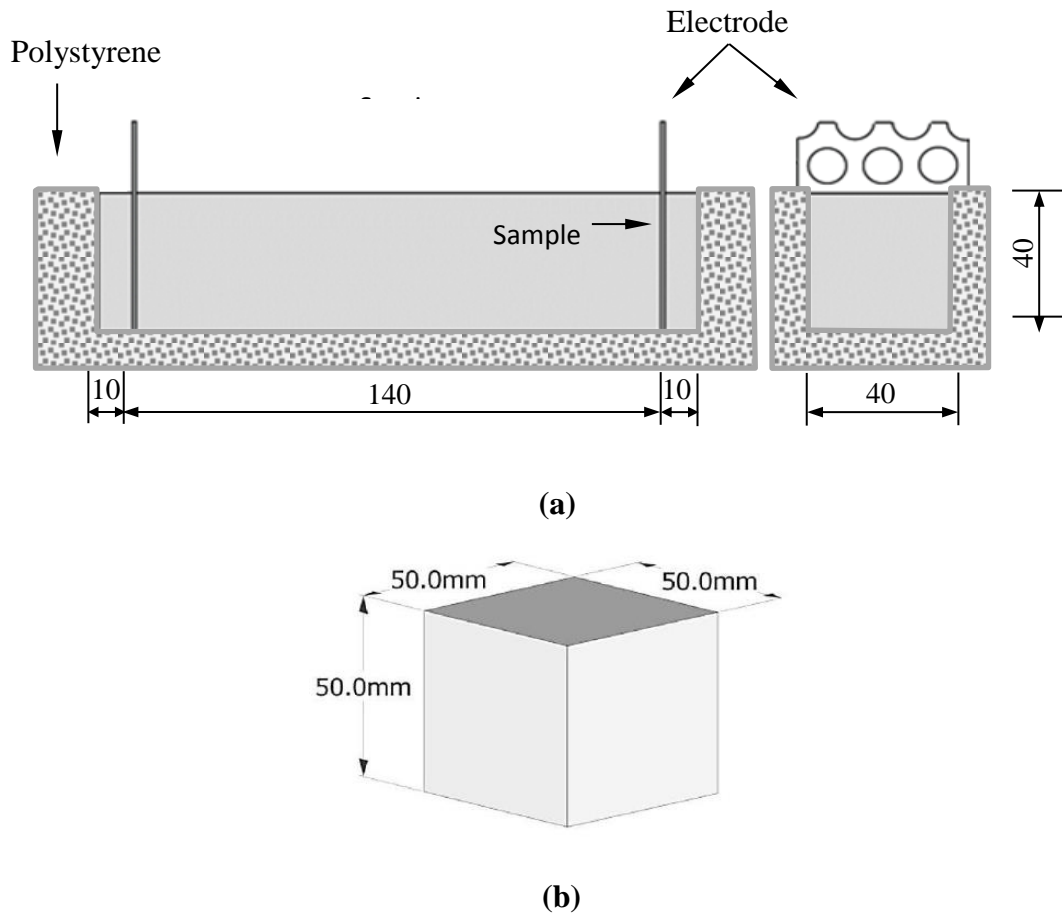
Figure 3.1: Schematic diagram showing the internal dimensions for (a) prismatic sample for the electrical measurements and (b) 50 mm cube for strength tests.

As the tensile properties of ECC are very dependent on the interaction between constituent materials, it is important to ensure that fibres and other components are thoroughly distributed during the mixing. This was achieved using a strict mixing regime, which is described below.

During the mixing process, all dry components excluding the PVA fibres (i.e., cement, fly-ash, and silica sand) were mixed manually with 80% of the water in the mixing

bowl. After that, the mixing procedure displayed in Figure 3.2 was followed, involving the adjustment of mixer speed at different times. The PVA fibres were added about 4.5 minutes after gauging to ensure that all other materials had been thoroughly mixed.
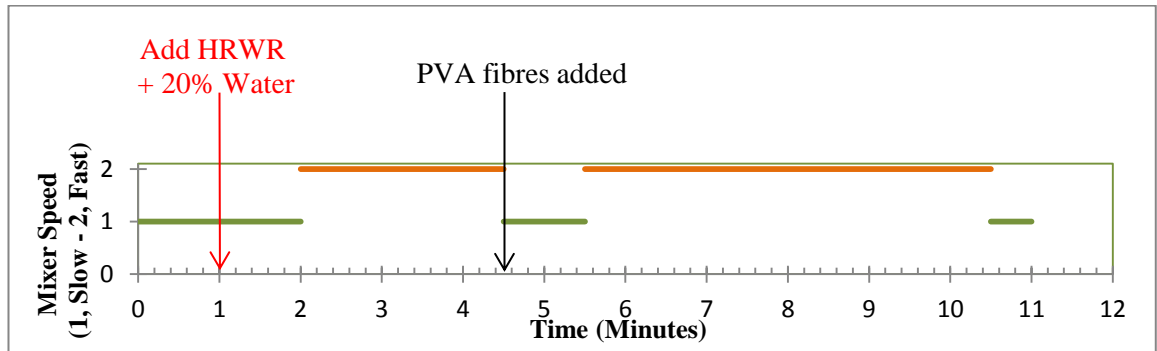
Figure 3.2: Diagram illustrating the mixing procedure.
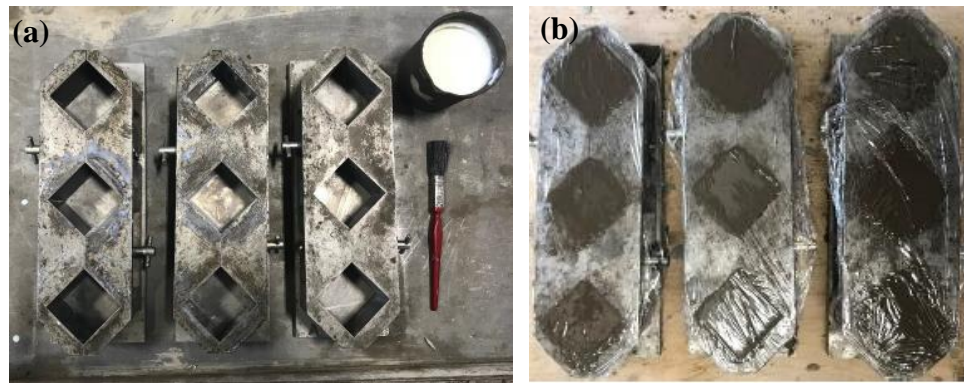
Figure 3.3: (a) Cube moulds and (b) ECC cubes after casting.

Figure 3.4: (a) Polystyrene moulds and electrodes; (b) ECC prismatic samples after casting; and (c) an example of a prismatic ECC sample after demoulding.

3.3.2 Test equipment and procedures

<u>Hydration</u>

Solartron 1260 impedance analyser was used to undertake the electrical property measurements of the prismatic samples at 14, 21, 28, 42, 63, 90, 180, and 360-days of curing over the frequency range 1 Hz–10 MHz. The signal voltage was set at 350 mV rms and the logarithmic sweep was made at 20 frequency spots per decade. The impedance analyser was connected in two-point mode to the electrodes embedded in each prismatic sample by means of four short, individually screened, coaxial cables. Two cables at one end were coupled and connected to each electrode via an alligator clip. One couple of the leads were connected to the current-generator/potential-high terminals on the analyser, whereas the other couple was connected to the current-input/potential-low terminals (see Figure 3.5).

These measurements were undertaken in a temperature-controlled laboratory environment (21 ± 2°C, $55 \pm 5\%$ RH). Prior to measurements, each specimen was removed from the curing tank (one specimen at a time). It was then wiped with an absorbent towel to dry the surface. The two alligator clips were then connected to each electrode as discussed above. One measurement took about 5 minutes in total. When the measurement was completed, the specimen was then returned to the tank, and this process was repeated for all remaining specimens.
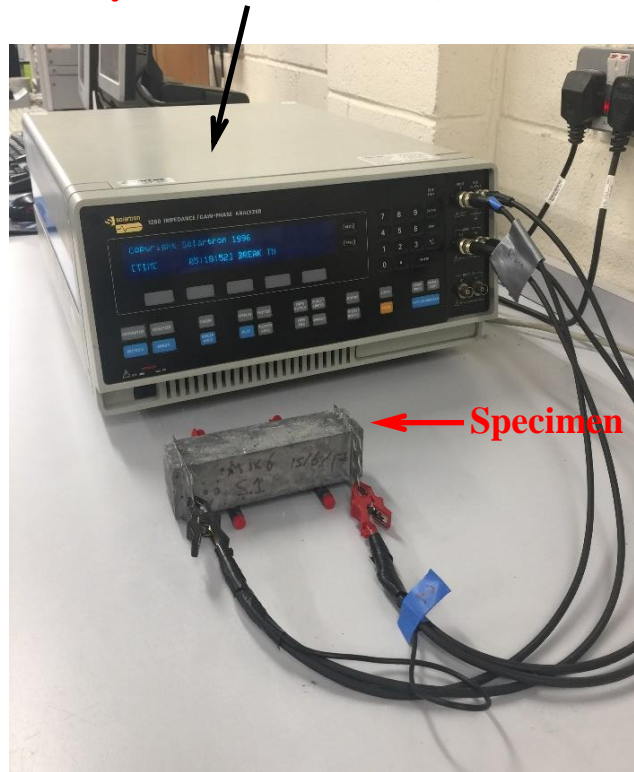
Figure 3.5: Test setup for electrical impedance measurements.

Temperature

Regarding the temperature effect study, this was done when the specimen reached 1 year to ensure that hydration and pozzolanic reactions would have virtually stopped. Prior to testing, each prism specimen was removed from the curing tank and then placed in a thermostatically controlled circulating water bath (initially at 6.5$^{\text{o}}$C) (see Figure 3.6(a)). The water was then raised to the temperature at which electrical measurements were required, which, in the case of the work presented, was 10, 15, 20, 30, 40, 50, and 60$^{\text{o}}$C. At the required temperature, the temperature was held for approximately 5 minutes before taking impedance measurements to ensure that no temperature gradients existed throughout the specimens. This was confirmed by monitoring the internal temperature within each specimen (through a thermistor which was embedded at the time of casting). Once thermal equilibrium was reached, electrical impedance measurement was then undertaken on each specimen using an E4980AL Keysight high precision LCR meter (see Figure 3.6(b)). It was decided to use this LCR meter instead of the Solartron 1260 as this meter was able to do much faster frequency sweep measurements.

As in the Solartron 1260, the LCR meter was operated at constant signal amplitude of 350mV. The meter was controlled by a desktop PC using LabVIEW virtual instrument. A logarithmic sweep was made over the frequency range 20 Hz–1 MHz, with the impedance recorded at 20 spot frequencies within this range. The connection to the LCR meter was made by means of four individually-screened (short) coaxial cables, with the electrode connected by means of alligator clips. As illustrated in Figure 3.6(b), the above measurements were undertaken in an environmental chamber with the temperature set at 6.5°C, 10°C, 15°C, 30°C, 40°C, 50°C, and 60°C.
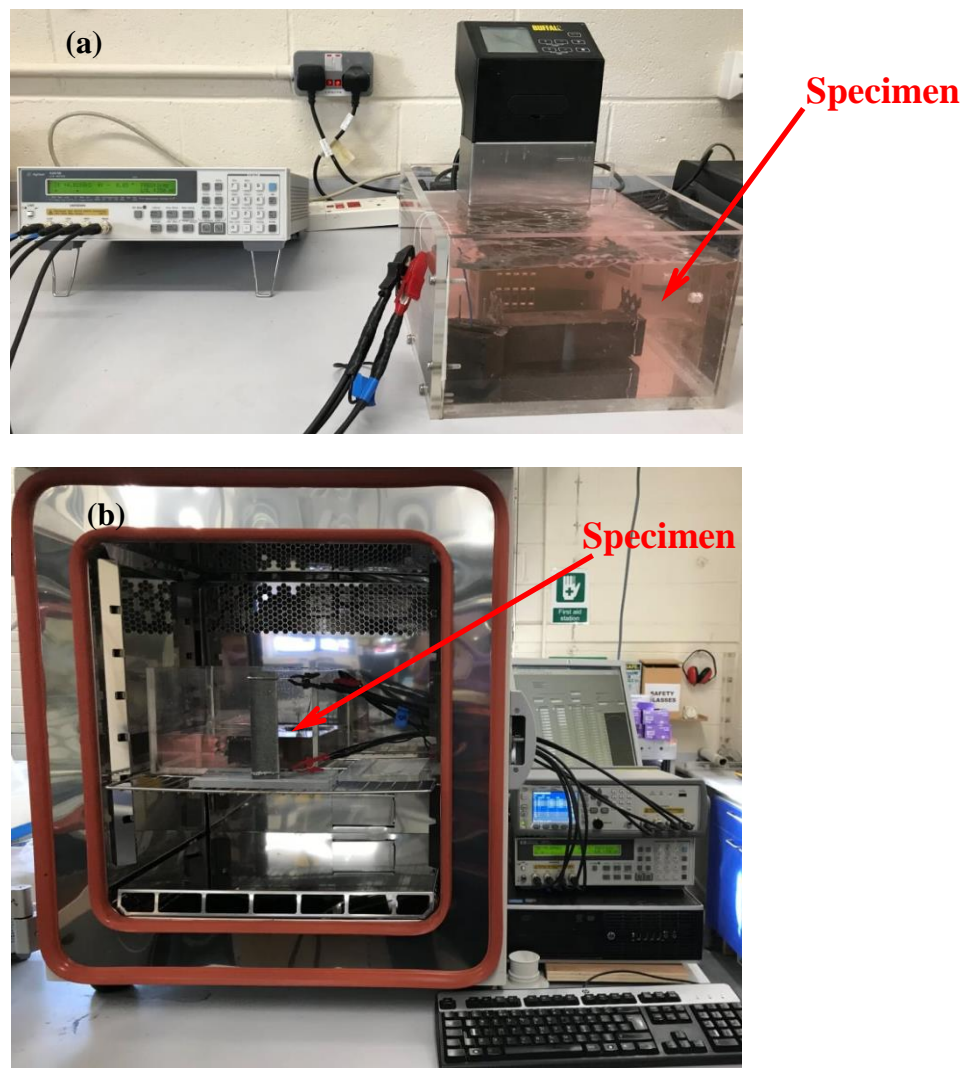
Figure 3.6: Test setup for temperature experimental study: (a) pre-conditioning stage and (b) electrical measurements.

Compressive strength

In addition to electrical measurements, it was considered appropriate to also measure the compressive strengths of the ECC mixes. This was determined by testing 50 mm cubes using a 3000 kN Avery–Dennison testing machine (see Figure 3.7), under a loading rate of 38 kN/min. This test was normally done on the 28th day of curing.

Figure 3.7: Experimental setup for the compression tests.

3.3.3   Equivalent Circuit Modelling

In order to provide an interpretation of the mechanisms underlying the impedance response obtained in this WP, the impedance data was modelled using an equivalent electrical circuit using a number of circuit elements connected in parallel and/or series. The developed electrical circuit of each mix was modelled using Z-view software, and then the results were simulated to match the impedance response.

The development of these equivalent circuits was based on possible conduction paths within the material.

3.4   WP2: Piezo-impedance study

This work package involved the testing of 8 dog-bone shaped specimens to obtain the electromechanical properties of the composite under tensile straining. The first set of the dog-bone samples, which were tested on the 28th day, had a smaller crack width

compared to the second set, which were tested on the 180th day. These specimens were produced in two different batches.

Table 3.5: Summary of the specimens in WP2

Test	Name and number of the specimens	Test age	purpose
Piezo-impedance and hydration Studies	Dog-bone samples: 8 dog-bone ECC samples E-ECC-S-(DB1-DB4) and E-ECC-L-(DB1-DB4). Prisms: -5 ECC mix E-ECC-S-(P1–P3) and E-ECC-L-(P1-P2) Cubes: 18 cubes	Dog-bone samples: 4 samples were tested on the 28th day and the other 4 samples were tested on the 180th day Prisms: -3 prisms: 7, 14, 21, 28, 42, 63, 90, days -2 prisms: 7, 14, 21, 28, 42, 63, 90, and 180 days Cubes: 28 days, 90 days, and 180 days	Dog-bone samples: To study the piezo-impedance response and understanding the effect of crack patterns on the electrical properties Prisms: To study the influence of on-going hydration on the electrical properties Cubes: To measure the compressive strength
Small Scale test	Prisms: 2 ECC prismatic samples without PVA fibres E-ECC-(P1-P2) Cubes: 3 cubes	Prisms: -E-ECC-P1 was tested at 35 days - E-ECC-P2: 7, 14, 21, 28, 42, 63, 90, and 180 days Cubes: 28 days	Prisms: -one-crack test at 35 days - To study the influence of on-going hydration Cubes: To measure the compressive strength

3.4.1 Materials and Sample preparation

A 10-litre Hobart planetary motion mixer was used to produce the ECC specimens of mixes presented in Table 3.6 including two controlled ECC tested at 28th day and 180th

day and ECC without PVA fibres. The same ECC specifications used in section 3.3.1 were also used in this section.

For the reference ECC mix, two batches of ECC specimens were produced and tested at 28 and 180 days of curing. A total of 15 specimens were produced for each batch, comprising:

i) Two prismatic samples were prepared using polystyrene moulds to study the influence of hydration over the 180 days of curing. For this, the same sample preparation stated in section 3.3.1 was used, and the same testing arrangement for the two-point measurements stated in section 3.3.2 (shown in Figure 3.5) was also used in this section; and

ii) Four dog bone samples were used to perform tensile and piezo-impedance tests. For this purpose, on the 13th day after casting, two electrodes consisting of fine metal wire were wrapped securely over the narrower portion of each dog-bone sample as presented in Figure 3.8. The fine metal wires were then covered with a layer of metallic silver paint to seal any contact gaps and thereby achieve an intimate bond with the sample surface. After allowing the paint to fully dry, the dog-bone samples were placed in the curing tank until testing; and

iii) Nine 50mm cubes, three of which were tested at 28, 90 and 180-days curing, respectively, to determine the compressive strength developments.

In addition to the above, five ECC specimens with no PVA fibre samples were fabricated to provide secondary information which was then used to validate the results conducted from the piezo-impedance tests. These specimens included two prismatic samples (E-ECC-P1 and E-ECC-P2) and three cubes, which were tested on the 28th day of curing. E-ECC-P1 was used to perform the one-crack measurements at 35 days, while E-ECC-P2 was used to take the electrical measurements up to 180 days to study the hydration effect.

Table 3.6: Summary of ECC mix design proportions

Mix	CEM I (kg/m^3)	FA (kg/m^3)	Silica sand (kg/m^3)	HRWR (kg/m^3)	PVA (kg/m^3)	F_{28} (MPa)	F_{90} (MPa)	F_{180} (MPa)
Base ECC 28th day	454	818	273	4.54	26	51.2	63.7	66.6
Base ECC 180th day	454	818	273	4.54	26	40.3	53.1	65.5
ECC without PVA	464	834	278	4.64	0	32.1	-	-
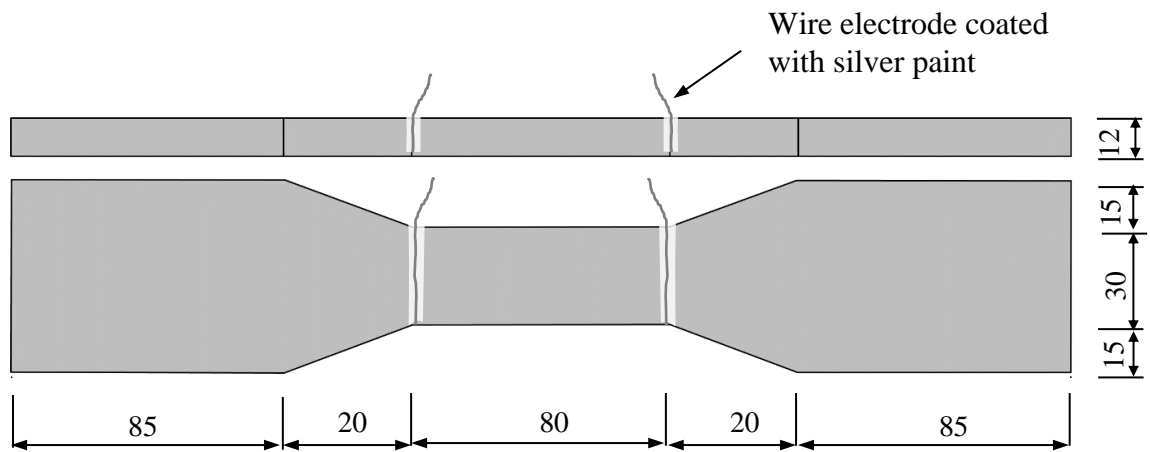
Figure 3.8: Schematic of testing arrangement for two-point measurements on dog-bone sample using surface applied (silver-coated) wire electrodes.
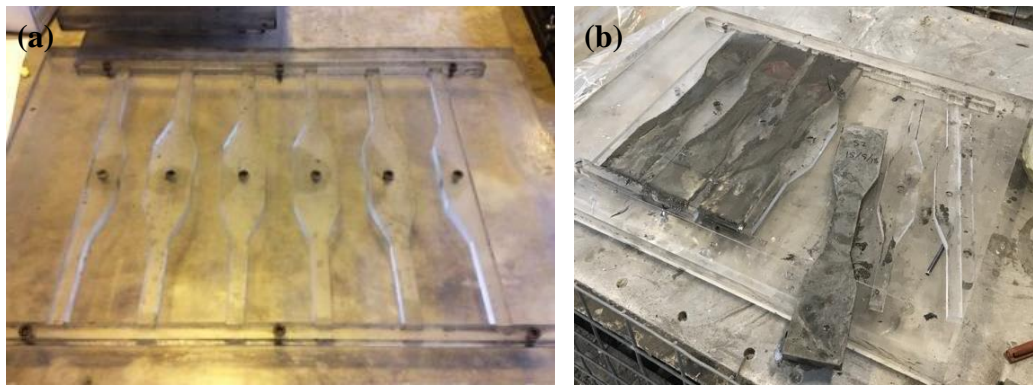
Figure 3.9: (a) Plexiglas mould; (b) demoulding process displaying the dog-bone ECC samples being removed from the mould.

During the fabrication of the test specimens, the same mixing procedure as that described in Section 3.3.1 was followed. After the fresh mix was placed into the moulds, they were allowed to cure for 24 hours in a temperature-controlled laboratory (21 ± 2°C, 55 ± 5% RH). The samples were then demoulded and stored in a curing tank until required for testing.

3.4.2 Test equipment and procedures

Hydration and compressive strength

For the first set of ECC samples which was tested on the 28th day of curing, a Keysight E4980AL precision LCR meter was employed to acquire the electrical impedance of prisms E-ECC-S-(P1-P3) over the initial 180 days after casting. The impedance was recorded at 20 spot frequencies per decade over the frequency range 20 Hz–1 MHz. The LCR meter was operated in voltage drive mode, at constant signal amplitude of 350 mV, and controlled by a desktop computer, which was also used for data acquisition. Communication with the LCR meter was established via the built-in USB interface in the LCR, which was accessed by the desktop computer through the Keysight IO Library Suite software (Version 2017.1). To manage the overall running of the experiment, a virtual instrument was developed in the LabVIEW environment (LabVIEW, 2017), which was used to trigger a full frequency sweep measurement, i.e., 20 Hz–1 MHz, present the measured impedance in both tabular and graphical formats, and save the acquired data in a CSV format for further analysis. Prior to each measurement, the high current (H$_{CUR}$) and high potential (H$_{POT}$) terminals in the LCR

meter were connected to one electrode via two, individually screened, short coaxial leads, and the low current (L_{CUR}) and low potential (L_{POT}) terminals to the other, following the two-point configuration. On the other hand, the same hydration test equipment and procedures stated in section 3.3.2 were used for the second set of the ECC samples, which were tested on the 180th day of curing.

Regarding the compressive strength, the same test equipment and procedures stated in section 3.3.2 were used in this section too.

Piezo-impedance Test

On the 28th day and 180th day of curing, tensile testing was performed on the dog-bone shaped specimens (T-ECC-S-(DB1-DB4) and (T-ECC-L-(DB1-DB4), respectively, using a 100kN 4206 Instron (see Figure 3.10) with loading applied at a constant crosshead speed of 0.5 mm/min. Prior to testing, each specimen was aligned in the machine until became symmetrical with its central axis and then clamped at both ends using pneumatic grips. Tensile stresses were determined by dividing load cell readings from the test machine by the cross-sectional area of the narrower (central) section (~30 mm × ~12 mm), whereas the longitudinal strains within this region were determined from the average of two linear variable differential transducers (LVDTs) readings over their initial distance (~60 mm). These LVDTs were attached prior to testing at the bottom end of the bone-neck region, one on each side, through two lightweight plastic mounting blocks (see Figure 3.10). All data was recorded using a 16-bit USB data acquisition system at a sampling rate of 1 second. Bluehill 2 software was used to manage the system and log load data.

In addition to the stress and strain readings, simultaneous electrical measurements were undertaken during the loading process to study the influence of multiple micro-cracking, using the same measurement system employed for testing the prisms. Prior to testing, the wire electrodes were connected to the LCR meter through individually screened coaxial leads with the connection made at the electrodes using alligator clips (see Figure 3.10). The cusp values of the specimen were checked before and after installing the sample in the Instron to make sure that there was no influence of the steel grip on the specimen impedance. During tensile loading, electrical measurements were then undertaken at thirteen selected spot frequencies covering five decades: 100 Hz, 200 Hz, 500 Hz, 1 kHz, 2 kHz, 5 kHz, 10 kHz, 20 kHz, 50 kHz, 100 kHz, 200 kHz, 500 kHz, and 1 MHz. The low frequencies (<100 Hz) were omitted from the sweep to

minimise the duration of the measurement. This sweep measurement was repeated over a 3-sec cycle, facilitating virtually continuous, real-time monitoring during loading, thus minimizing the influence of time-dependent effects on the measured impedance. Since the distance between the two electrodes is ~80 mm and the region of interest is ~60 mm (the distance between the LVDTs), the electrical measurements are expected to be proportionally overestimated due to the difference in length (~20 mm).

Figure 3.10: Piezo-impedance test setup displaying the LCR meter on the left and a specimen under testing on the right.

Digital Image Correlation (DIC)

To provide evidence of micro-crack formation, digital images of the front faces of the dog-bone specimens were taken at a 0.1 mm displacement increment using an 18.4 MP Nikon 1 J4 mirrorless digital camera, positioned approximately 300 mm from the specimen. To remove inadvertent camera movement, images were collected remotely using the Nikon wireless mobility utility smartphone application (Version 1.2.1). Prior to testing, random black dots were manually drawn on the front surface of the dog-bone specimens, which had been given a thin coat of white acrylic paint (see Figure 3.11). This was undertaken to give a random pattern with a sharp contrast, thereby facilitating automated strain mapping within the boundary indicated in Figure 3.11. The images

were then processed using the digital image correlation (DIC) freeware Ncorr (Version 1.2.1) (Blaber et al., 2015; Suryanto et al., 2017b; Tambusay et al., 2020). In addition to this automated crack mapping, more detailed crack mappings were undertaken manually using the ImageJ1 software (Schneider et al., 2012), with the aim of obtaining the number and width of each individual micro-crack under various stages of loading.
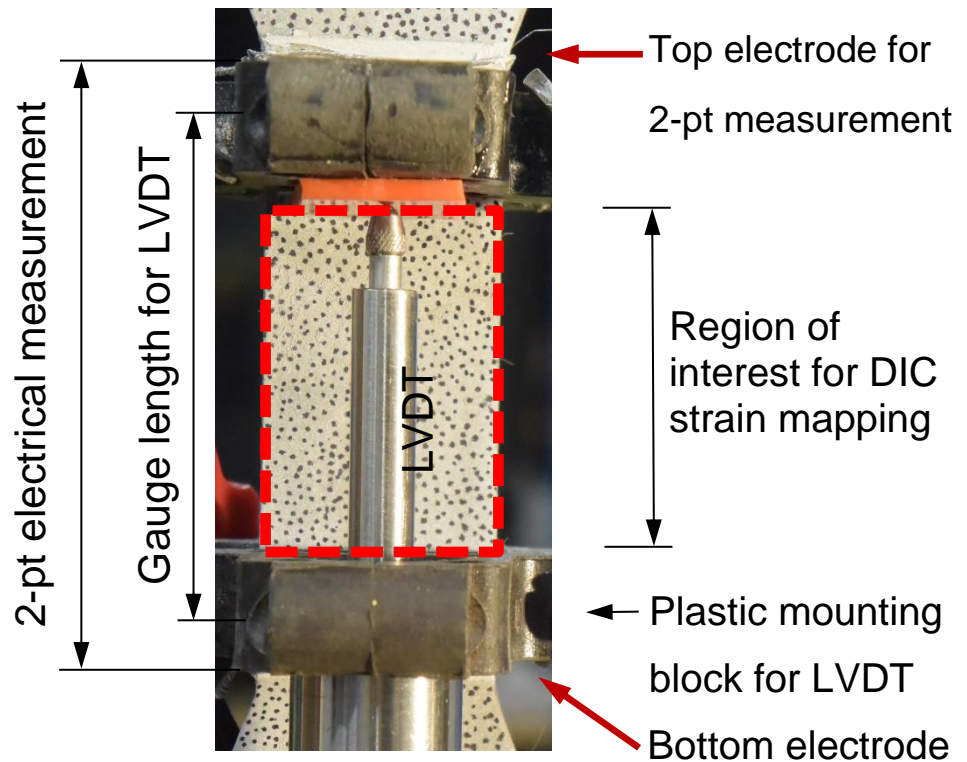
Figure 3.11: Close-up of measurement during uniaxial tensile testing.

Single Crack Experiment

Small scale test was conducted in order to help interpreting or understanding the impact of cracking to validate the outcome resulted from the piezo-impedance test. A prismatic sample was used to perform this test. At the age of 35 days, the sample was taken out of the curing tank, and then the sample surface was partially dried with wipes. After that, lines were drawn contorting the sample, the first one was placed in the middle of the sample, while the second and the third lines were drawn at 20 mm from both ends. The sample was then returned back to the curing tank in order to avoid the drying effects of the impedance. After 1 hour, the electrical measurement of the sample was conducted using the Solartron 1260 to make a comparison between the impedance response before

and after cracking. The sample was then enrolled with plastic sheet in order to protect the sample particles. A 3000 kN Avery Dennison compression machine was used to break the sample under a loading rate of 1 kN/min., before that three cylindrical bars were placed as follows: one on the top centre of the sample, while the two others were placed at the bottom of the sample far from each sample's extremities distance of 20 mm (See Figure 3.12(a)). Once the mobile plate of the compression machine entered in contact with the top surface of the cylindrical bar, the compression machine was switched off in order to end the test after obtaining one crack at the middle of the sample. The plastic sheet was removed out of the sample, while making sure to press the sample carefully to preserve the particles. The electrical measurements were then conducted by switching the sample in a vertical position and placing a non-metallic cubic rock at the top of the sample as shown in Figure 3.12(b) to compress the gap occurred from the crack and places the two alligator clips.

Figure 3.12: (a) Test setup for precracking the sample and (b) electrical measurements of the single-crack sample.

3.5 WP3: Wetting and Drying

This work package involved the testing of 7 dog-bone shaped specimens to investigate the effect of wetting and drying on the electrical properties of ECC. The first 2 dog-bone samples were tested to failure to measure the average strain of the samples. The next 3 dog-bone samples were pre-loaded up to 50% of the average strain obtained from the first 2 dog-bone samples, while the last 2 dog-bone samples were used as control samples to make a comparison between the un-cracked and cracked samples. These specimens were produced in one batch.

Table 3.7: Summary of the specimens in WP3.

Test	Name and number of the specimens	Test age	purpose
Wetting and drying cycles and hydration Studies	Dog-bone samples: 7 dog-bone ECC samples - T-ECC-TF-(DB1-DB2) tested till failure - T-ECC-PC-(DB1-DB3) pre-loaded up to 50% of the average T-ECC-TF-(DB1-DB2). - Non pre-cracked samples E-ECC-NC-(DB1-DB2).	Dog-bone samples: - T-ECC-TF-(DB1-DB2): 28th day of curing. - T-ECC-PC-(DB1-DB3) pre-loaded on the 28th day of curing. Then it is used for the wetting and drying cycles for 7 cycles. - E-ECC-NC-(DB1-DB2) was used for the wetting and drying cycles for 7 cycles.	Dog-bone samples: - T-ECC-TF-(DB1-DB2): to measure the average strain of the dog-bone samples. - T-ECC-PC-(DB1-DB3) and E-ECC-NC-(DB1-DB2) were used to investigate the wetting and drying effects on the electrical properties at the un-cracked and cracked states.
	Prisms: 2 ECC mix	Prisms: 2 prisms: 7, 14, 21, 28, 42, 63, 90, and 180 days	Prisms: To study the influence of on-going hydration on the electrical properties.
	Cubes: 3 cubes	Cubes: 28 days	Cubes: To measure the compressive strength.

3.5.1 Materials and Sample preparation

The same mix proportions used in section 3.4.1 and displayed above in Table 3.6 were also used in this section. Table 3.8 illustrates the mixes with the obtained compressive strength.

Table 3.8: Summary of ECC mix design proportions.

Mix	CEM I (kg/m^3)	FA (kg/m^3)	Silica sand (kg/m^3)	HRWR (kg/m^3)	PVA (kg/m^3)	F$_{28}$ (MPa)
ECC	454	818	273	4.54	26	42.8

A total of 12 specimens were produced to study the effect of wetting and drying, comprising:

i) Two prismatic samples to calculate the geometric factor of the dog-bone specimens. The same sample preparation stated in section 3.3.1 was used, and the testing arrangement of the prismatic samples is stated in section 3.3.2 above and displayed in Figure 3.5; and

ii) Seven dog-bone samples to determine the mechanical properties and investigate the effect of wetting and drying cycles on the electrical properties. The testing arrangement of the dog-bone samples is stated in section 3.4.2 above and displayed in Figure 3.10; and

iii) Three 50 mm cubes to determine the compressive strength at 28th day.

3.5.2 Test equipment and procedures

Hydration study and compressive strength:

The same test equipment and procedures as for the hydration study and compressive strength stated in section 3.3.2 were used in this section. The electrical measurements of the prismatic samples were conducted on the 28th day of curing using the Solartron 1260 impedance analyser. The compression test of cubes was conducted on the 28th day of curing.

Tensile Test and wetting-drying cycles study:

Seven dog-bone samples were produced to investigate the wetting and drying effects. On the 28th day of curing, tensile testing was conducted on five samples, two of which were tested until failure to obtain an indication of the strain capacity, while the other three samples were pre-cracked with 50% of the average strain capacity from the other

two samples. The two remaining samples were used as a control without being tested to be able to make a comparison with the pre-cracked samples. After tensile testing, the samples were covered with thick cling film to prevent losing the particles in the pre-cracked samples, as well as avoiding the samples to dry quickly, and then the samples were shortened using electric saw (see Figure 3.14). With reference to Figure 3.14, Table 3.8 presents the dimensions of the specimens after being cut off from the dog-bone samples. The specimens were then submerged in the water for two hours to make them fully saturated again. Subsequently, the controlled and pre-cracked samples were exposed to seven drying and wetting cycles, the first part composed a one-day drying then a one-day wetting, and the second of which consisted of a one-day drying followed by a four-day wetting (For clarity, see Figure 3.13). During the drying cycle, full electrical measurements were conducted on one sample using Solartron 1260 impedance analyser (1 Hz–10 MHz), while the measurements of other samples were conducted through data-logger at one fixed frequency 1 kHz (see Figure 3.15). The electrical measurements of all the samples were taken after each drying and wetting cycle using Solartron. In addition, the weight of the samples was also measured after these cycles using a lab scientific scale with a windshield.

DRYING (1 day) | **WETTING (1 day)**

Weight measurement   Weight measurement

Weight measurement

- Solartron on T-ECC-PC-DB1 @ every 5 min
- Data logger on Samples T-ECC-PC-DB2, T-ECC-PC-DB3, E-ECC-NC-DB1, and E-ECC-NC-DB2 @ every 2 min

Solartron measurements on all samples

Non-precracked (Samples E-ECC-NC-DB1 and E-ECC-NC-DB2):
Solartron measurements @ [30 min, 1 hr, 2 hr, 3 hr, and 4 hr of wetting (Not for all cycles)], and at the end of 1day.

Pre-cracked (Samples T-ECC-PC-DB1, T-ECC-PC-DB2, and T-ECC-PC-DB3):
Solartron measurements @ 30 min of wetting

DRYING (1 day) | **WETTING (4 days)**

Weight measurement   Weight measurement

Weight measurement

- Solartron on T-ECC-PC-DB1 @ every 5 min/ Except for the 7th cycle; Solartron on E-ECC-NC-DB2) @ every 5 min
- Data logger on Samples T-ECC-PC-DB2, T-ECC-PC-DB3, E-ECC-NC-DB1, and E-ECC-NC-DB2 @ every 2 min/ Except for the 7th cycle; Data logger on T-ECC-PC-DB1, T-ECC-PC-DB2, T-ECC-PC-DB3, and E-ECC-NC-DB1 @ every 2 min

Solartron measurements on all samples

Non-precracked (Samples E-ECC-NC-DB1 and E-ECC-NC-DB2):
Solartron measurements @ [30 min, 1 hr, 2 hr, 3 hr and 4 hr of wetting (Not for all cycles)], and at the end of 4 days.

Pre-cracked (Samples T-ECC-PC-DB1, T-ECC-PC-DB2, and T-ECC-PC-DB3):
Solartron measurements @ 30 min of wetting

Figure 3.13: Schematic diagram showing the wetting and drying cycles considered within this experimental programme.
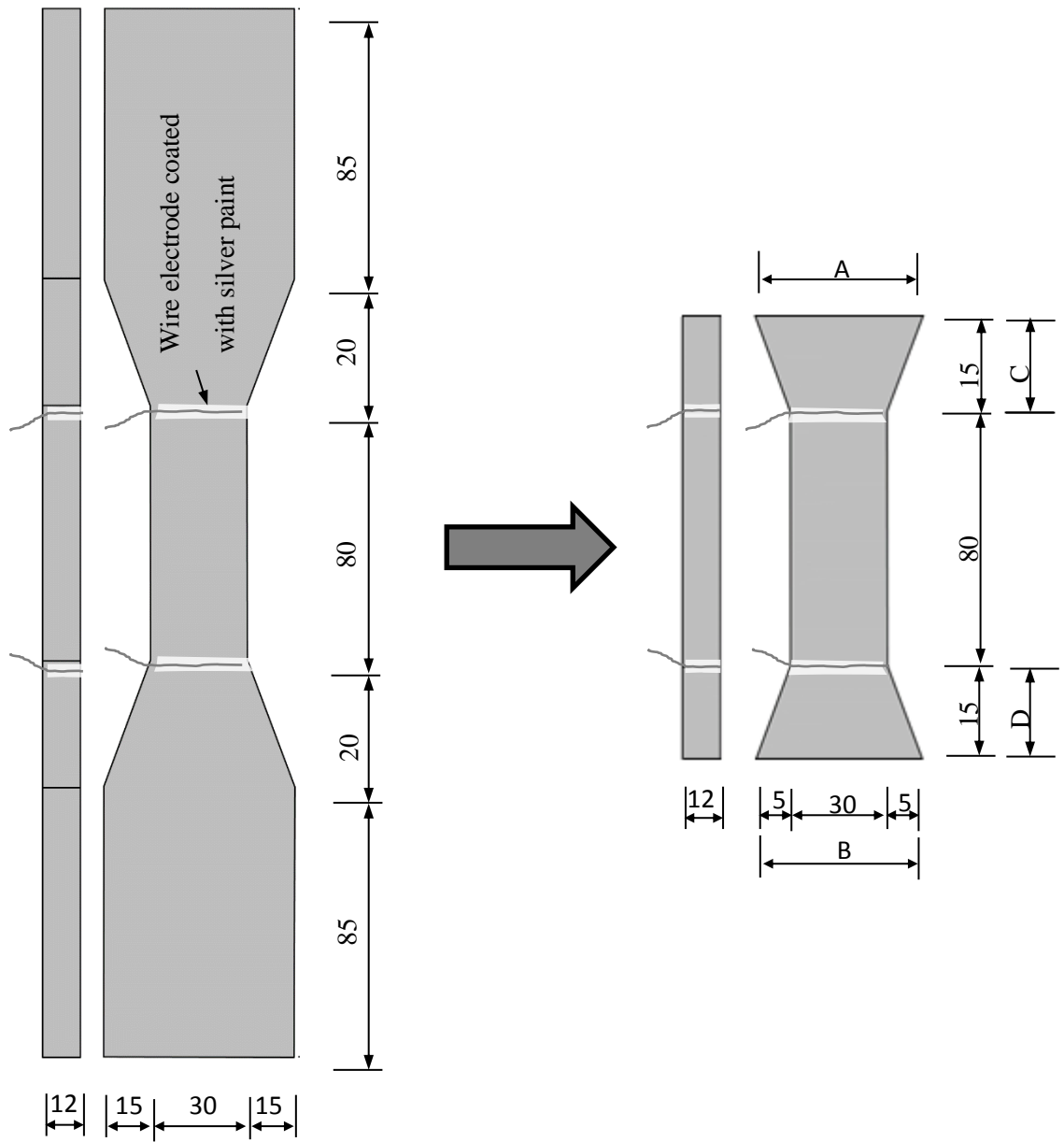
Figure 3.14: Schematic diagram showing the dimensions of dog-bone specimen before and after cutting.

Table 3.9: The dimensions of all dog-bone specimens after cutting.

Sample Number	A	B	C	D
T-ECC-PC-DB1	40	39	14.5	13
T-ECC-PC-DB2	38	38.5	14	14.5
T-ECC-PC-DB3	36	38.5	12.5	13
E-ECC-NC-DB1	38	38	13	13.5
E-ECC-NC-DB2	38	38	12.5	13
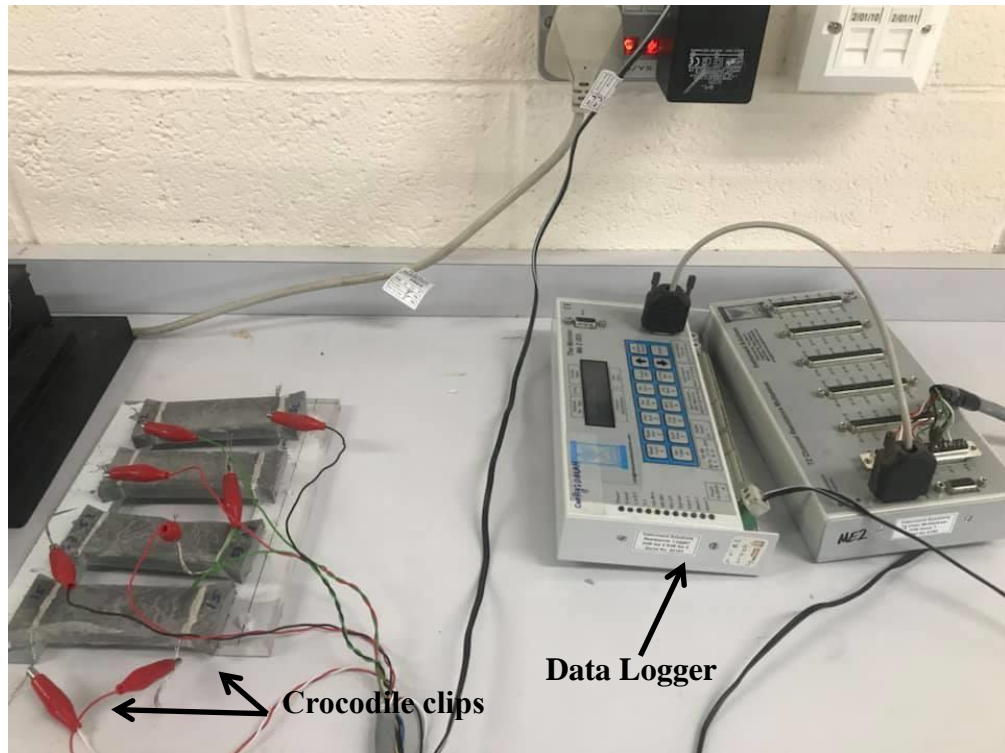
Figure 3.15: Test setup for electrical measurements during drying using a data logger.

3.6 Data analysis and presentation

The impedance of a cement-based system, $Z(\omega)$ in ohms (Ω), subjected to a small-signal sinusoidal electric field at an angular frequency, ω, can be represented in a rectangular form as (McCarter and Brousseau, 1990; Starrs and McCarter, 1998; Suryanto et al., 2016),

$$Z(\omega) = Z'(\omega) - iZ''(\omega) \tag{3.1}$$

where $Z'(\omega)$ is the resistive (real) component and $Z''(\omega)$ is the reactive (imaginary) component. These two parameters are commonly presented in the Nyquist format, with $Z''(\omega)$ plotted against $Z'(\omega)$ over a wide frequency range. At any frequency, the electrical response of a cement-based system will be produced by two superposed phenomena: conduction and the polarization phenomenon (Suryanto et al., 2016). The conductivity can be a consequence of both the direct (e.g. ionic) conduction process and the dissipation resulting from the polarization process (Hasted, 1973; McCarter et al., 1999). While the dielectric constant describes the stored energy inside the material that is derived from the polarization of charges, the dielectric loss occurs due to the dissipation of energy caused by polarization relaxation processes and direct ionic conduction processes (Hasted, 1973; Starrs and McCarter, 1998; McCarter et al., 1999). Both parameters are generally presented in the frequency domain to investigate the nature of conduction and relaxation processes. These parameters can be de-embedded from the resistive and reactive components of the impedance through the relationships (McCarter et al., 2004; Suryanto et al., 2016),

$$\sigma(\omega) = \left(\frac{Z'(\omega)}{Z'(\omega)^2 + Z''(\omega)^2} \right) g_\mathrm{p} \tag{3.2}$$

$$\kappa_r'(\omega) = \frac{1}{\kappa_\mathrm{o}\omega} \left(\frac{Z''(\omega)}{Z'(\omega)^2 + Z''(\omega)^2} \right) g_\mathrm{p} \tag{3.3}$$

with κ_o representing the permittivity of free space (8.854×10^{-12} Farads/m) and g_p representing the geometrical constant which is dependent upon the electrode geometry and spatial positioning of the electrodes within the system.

The value of g_p was obtained from a-priori experiments using solutions of known conductivity, using the same polystyrene mould and perforated stainless-steel electrodes as in the test prisms. A value of $g_\mathrm{p} = 88.48$/m was obtained.

For the dog-bone specimens, the calibration was done by converting the resistance measured from prisms E-ECC-(P1-P3) at 28-days of curing, denoted $R_{p,28}$, to resistivity, ρ_{28}, through the relationship,

$$\rho_{28} = R_{p,28} \frac{1}{g_p} \quad \text{Ohm-m} \tag{3.4}$$

Accordingly, the geometrical constant for the dog-bone specimen, g_{db}, could be calculated,

$$g_{db} = \frac{R_{db,28}}{\rho_{28}} \quad /m \tag{3.5}$$

where $R_{db,28}$ is the measured resistance for the dog-bone specimen after 28-days of curing. g_{db} was obtained as 245.28/m.

4 Influence of Cement Hydration and Temperature

4.1 Introduction

In this chapter, the electrical impedance response of engineered cementitious composite (ECC) and Portland cement (PC) mortar over a period of 180 days is presented. The first part of this chapter presents the findings of a testing programme that examines the influence of cement hydration on the bulk electrical properties of ECC. In this part, the 1 Hz–10 MHz frequency range is investigated throughout the 180-day curing period, and results are presented in both the general Nyquist format and in the frequency domain. The frequency domain presentation was particularly considered to elucidate the nature of conduction and polarization processes within the composite.

The extended period of investigation allows for the evaluation of the influence of ongoing hydration and pozzolanic reaction (and resulting pore refinement) on the electrical properties of ECC. The effect of fly-ash inclusion in the ECC is discussed. Two equivalent circuit models, each comprising a number of elements connected in parallel and in series, are then used to simulate the impedance response obtained from the specimens. At the end of this part, the developing pore structure in the ECC specimens during the extended curing period is assessed by eliminating the effect of the pore solution from the bulk electrical properties, thereby allowing for a direct comparison with the pore structure of traditional concrete.

In the second part of this chapter, the influence of temperature on the electrical properties of the composite is presented over the temperature range of 7–60$^{\text{o}}$C. Data is also presented in the Nyquist format over a slightly narrower frequency range than that used in the first part, from 20 Hz–1 MHz, due to limitations in the test equipment. The impedance data obtained is then presented in the Arrhenius format to allow for the evaluation of the activation energy for electrical conduction. An activation energy-based temperature correction protocol is then presented to develop a correction protocol which can be used to remove temperature effects from field measurements.

4.2 Effect of Cement Hydration

4.2.1 Preliminaries on Data Presentation

In this section, the general Nyquist format of data presentation is described. In this format, the imaginary component of impedance, $Z''(\omega)$, is plotted against the real component, $Z'(\omega)$, in a Cartesian coordinate system (McCarter et al., 1999; Suryanto et al., 2016). To obtain such a response, a cement-based specimen could be placed between a pair of electrodes and subjected to a small-amplitude alternating electrical current extending over several decades of frequency. Generally, the Nyquist response shown schematically in Figure 4.1(a) will result, which shows two regions comprising a spur at the right-hand (low frequency) side of the plot and a semi-circular arc at the left-hand (high frequency) side. The low-frequency spur is representative of the electrode polarization used for taking the measurement, while the semi-circular arc is associated with the bulk response (McCarter et al., 1988; McCarter and Brousseau, 1990; Suryanto et al., 2016). The intercept of the low-frequency spur with the real axis (i.e., the junction between the electrode spur and the semi-circular) arc is easily identifiable (denoted as R in Figure 4.1(a)). This is commonly referred to as the *cusp* point, which represents the bulk resistance of the material.

When fly-ash is introduced into the material, it has been reported that this causes an intermediate arc to appear between the low-frequency spur and the high-frequency arc (see Figure 4.1(b)) (McCarter et al., 2004; Suryanto et al., 2016). The prominence of this feature is dictated by the proportion of unburnt carbon in the fly-ash, which is quantified by the loss on ignition (LOI) (McCarter et al., 2004; Suryanto et al., 2016). When the LOI is low, this intermediate arc turns into a plateau region and sometimes is not an arc shape anymore (Suryanto et al., 2020b). This format of data presentation is explored in the following section.

In addition to the Nyquist formalism above, the bulk conductivity, $\sigma(\omega)$, and the relative permittivity, $\kappa_r'(\omega)$, are also de-embedded from the impedance data following equations 3.2 and 3.3, respectively, presented in Section 3.6. The results of which are normally presented in the frequency domain (see Figure 4.1(c)-(d)), with the bulk conductivity and relative permittivity plotted against the signal frequency. This format of data presentation is explored to elucidate the superposed phenomena of conduction and polarization within the ECC, when subjected to small amplitude alternating electrical current.

These two different formats of data presentation are considered to provide a fuller understanding of the electrical properties of ECC over the frequency range 1Hz–10MHz.
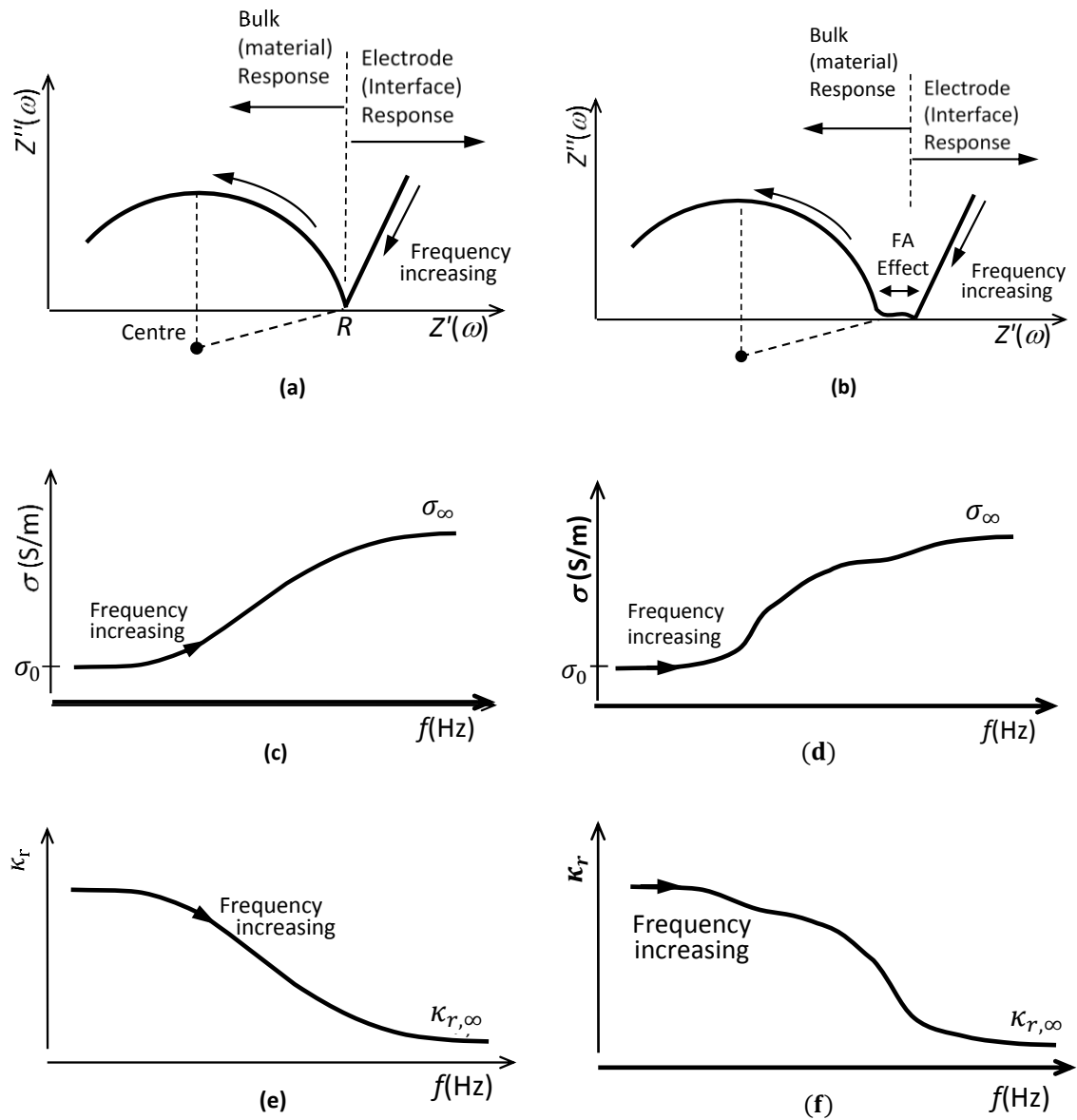
Figure 4.1: Schematic diagram of the typical electrical response of a cementitious system: (a) and (b) impedance response without and with fly-ash; (c) and (d) conductivity without and with fly-ash; (e) and (f) relative permittivity without and with fly-ash (adapted from (McCarter and Starrs, 1999; McCarter et al., 2004).

4.2.2 Impedance Response of ECC

In this section, the impedance results of ECC and mortar mixes are presented in Figure 4.2(a)-(b) are presented. The base ECC (MB) mix was used to produce two prismatic specimens (E-MB-P1 and E-MB-P2), whereas the mortar (MF0) mix was used to produce two other specimens, E-MF0-P1 and E-MF0-P2. Note that MF0 mix is a neat Portland cement mix (it does not contain fly-ash).

The complex impedance plots ($Z'(\omega)$ vs $Z''(\omega)$) for specimens E-ECC-P1 and -P2 over the 180-day period are presented in Figure 4.2(a), with the solid lines representing the response of P1 specimen and the dashed lines representing the response of P2 specimen. In this figure, frequency increases from right-to-left across the curve, from 1 Hz to 10 MHz range at 20 points per decade. For comparative purposes, the complex impedance plots for specimens E-MF0-P1 and -P2 are presented in Figure 4.2(b), with the same line style (dash type) for specimens P1 and P2, respectively.

With reference to the Nyquist diagram shown in Figure 4.2(b), it is evident that the mortar displays a typical impedance response with two distinct regions: a 'V'-shaped plot on the right-hand-side of the spectrum and the bulk-arc on the left-hand-side of the plot, following closely the schematic diagram presented earlier in Figure 4.1(a). The presence of the V-shaped plot is due to the formation of the low-frequency spur resulting from polarization phenomena that occur at the electrode/sample interface (McCarter et al., 1988; McCarter and Brousseau, 1990; Suryanto et al., 2016). It has been suggested that the spur actually constitutes a part of a larger arc that would only be detectable at much lower frequencies, i.e., <<1 Hz (Suryanto et al., 2016).

Regarding the impedance spectra of ECC presented in Figure 4.2(a), it is interesting to note that they are, in many respects, similar to the respective mortar specimens presented in Figure 4.2(b). However, a closer inspection at the base of the V-plot reveals the emergence of a very weak intermediate 'plateau' region, although the extent of which is not that visible in this case. As demonstrated by Suryanto et al. (2016), this intermediate region is attributed to the presence of unburnt carbon in the fly-ash (traceable from the value of loss on ignition (LOI)) (McCarter et al., 2004; Suryanto et al., 2016). The weak formation of the plateau region would suggest that the amount of unburnt carbon could be smaller than that used by Suryanto et al. (2016). This difference in the extent of the plateau region would highlight the natural variation of unburnt carbon content in the fly-ash. McCarter et al. (2004) stated that the

prominence of this intermediate region is dictated by the unburnt carbon proportion in the fly-ash (loss on ignition (LOI) during production), as the intermediate region becomes more noticeable with the increase in LOI.

Further comparisons of Figures 4.2 (a) and (b) reveal that the impedance spectra of ECC display a more noticeable progressive displacement to the right-hand-side and a more marked increase in size than those of the mortar. This can be associated with the slower pozzolanic reaction of the fly-ash in the ECC (MB) mix. Although cement hydration is also present in this mix, its contribution is noticeably limited due to the high replacement level of the fly-ash (1.8 by mass). This can be seen from the gradual increase of the bulk resistance, from approximately 1 kOhm at 7 days of curing to over 10 kOhm at 180 days of curing (or a tenfold increase). On the other hand, the mortar (MF0) mix did not contain any fly-ash and hence would only experience a hydration process that is a lot faster than pozzolanic reactions. This explains the high initial value of the bulk resistance at 7 days, which is approximately 3 kOhm (or a twofold increase).

It is interesting to note from Figures 4.2(a) and (b) that the bulk arc for ECC and mortar becomes more discernible with increasing curing age when measured within the same frequency range 1 Hz–10 MHz. This could be associated with the reduction in the cusp-point frequency (or reduction in relaxation time) with time. A cusp-point is generally defined as the junction between the electrode spur and the arc; in this work, this was taken at the minimum point within the intermediate plateau/valley region. Accordingly, the cusp-point frequency is related to the signal frequency that corresponds to this minimum point. Another salient feature relates to the peak point at which the bulk arc maximizes.

Figures 4.2(c) and (d) present the temporal change in cusp-point and peak frequencies (f_c and f_p) for both ECC (MB) and mortar (MF0) mixes over the 180-day curing period, with the error bars representing $\pm$ one standard deviation. It is apparent from these figures that there is a rapid reduction in the cusp-point frequency, f_c, over the initial 28 days, which is then followed by a more gradual decrease in value over the remainder of the test period. Consider, for example, the f_c values at 7 days, which attained values of ~1.3 kHz for the ECC and ~1.0 kHz for mortar. At 28 days, these values rapidly decreased to ~0.5 kHz for both mixes, which is in good agreement with the range of frequencies reported earlier by Suryanto et al. (2016), who found a reduction in the f_c of a different ECC mix from ~1.4 kHz at 7 days of curing to ~0.4 kHz at 28 days. The rate

of change of frequency was noticeably reduced at the curing-time thereafter, attaining values of ~0.3 kHz and ~0.4 kHz at 90 days for ECC and mortar mixes, respectively, and ~0.2 kHz (ECC) and ~0.3 kHz (mortar) at 180 days. This reduction in the cusp-point frequency reflects the change in the conduction and polarization operative within the composite due to the on-going hydration and pozzolanic reaction (resulting microstructural changes) within the cement matrix. With reference to the corresponding peak frequency, f_p, values for the two mixes, it evident from Figure 4.2(c)-(d) that at 7 days of curing, f_p attained values of ~8.9 MHz for the ECC mix and ~6.3 MHz for the mortar mix, and these values decreased to ~5.7 MHz at 28 days of curing (values are similar for both mixes). These values are in the same order as the peak frequency values measured from a different ECC mix reported in Suryanto et al. (2016), in which values of 6.3 MHz at 7 days and 3.5 MHz at 28 days were observed. Thereafter, the ECC mix displayed a continuous reduction in f_p values, attaining values of ~3.5 MHz at 90 days and ~1.6 MHz at 180 days, whereas the mortar mix exhibited a constant f_p, ~4.5 MHz. The trend observed in these salient frequencies represents the expected rates of hydration and pozzolanic reaction and could potentially be used to estimate the rate of hydration and pozzolanic reaction. However, given that no specific measurements of the degree of hydration and pozzolanic reaction were undertaken, this couldn't be achieved.
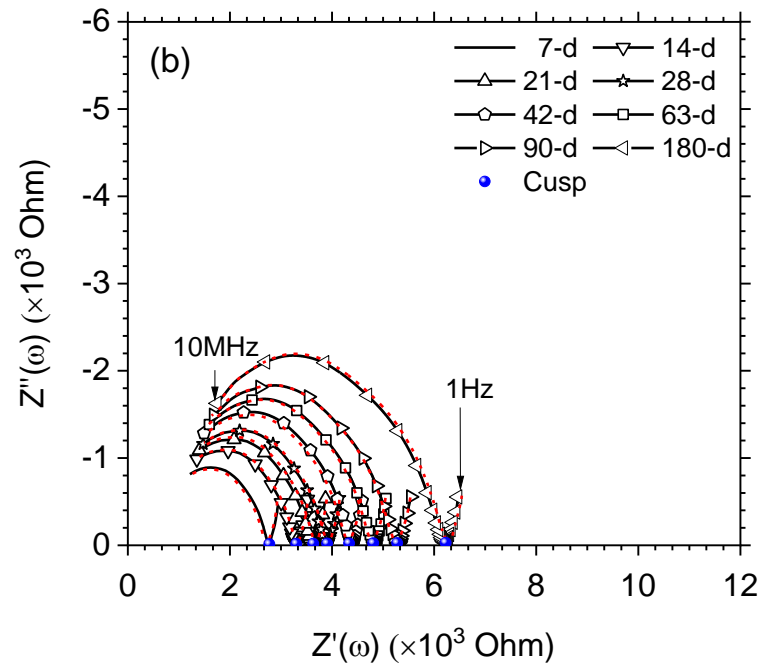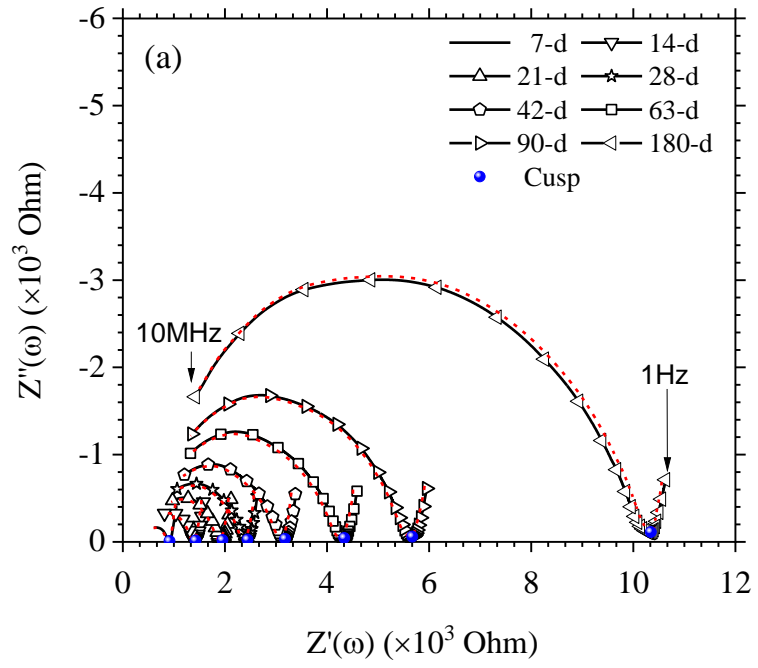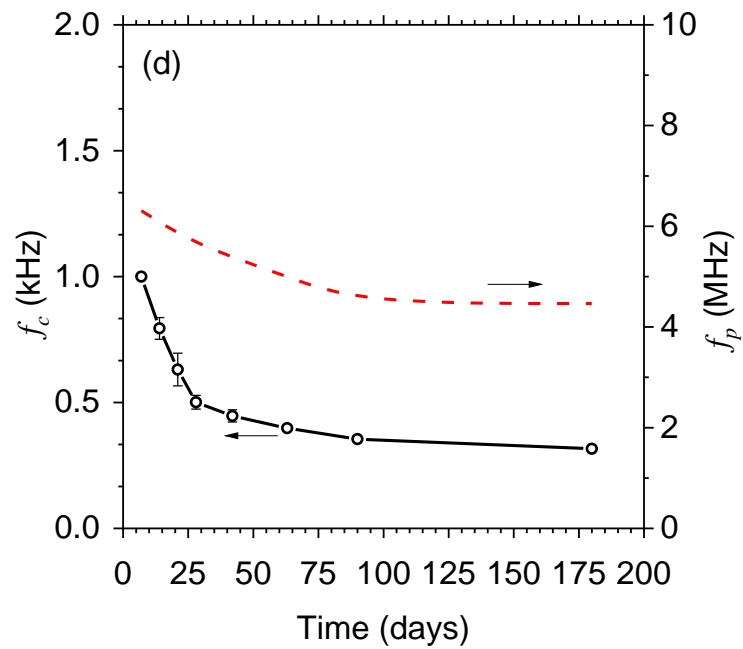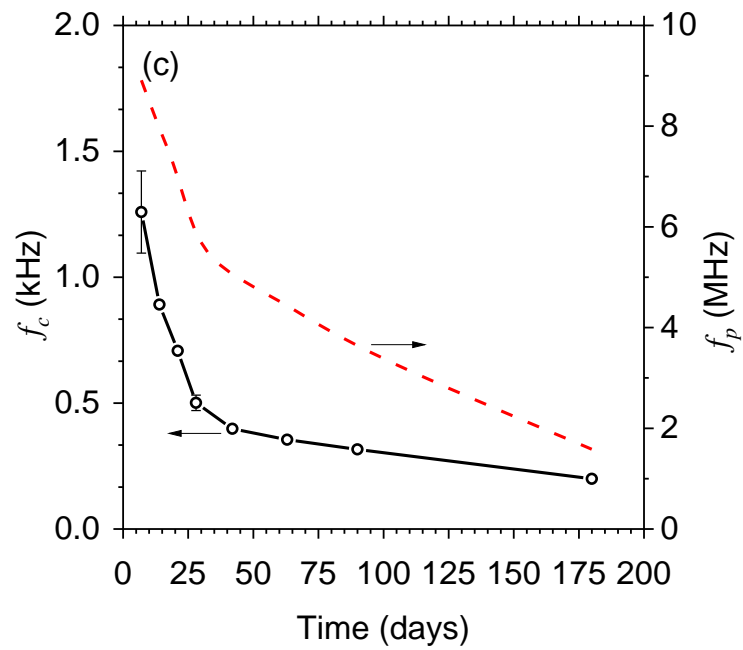
Figure 4.2: Summary of the impedance response progression over 180-day cuing duration for prismatic samples of: a) ECC (MB) mix; and (b) PC (MF0) mix. The effect of curing-time on the cusp (f_c) and peak (f_p) frequencies for: c) ECC (MB) mix; and (d) PC (MF0) mix.

To provide better insights into the effect of hydration, the conductivity (reciprocal of resistivity) for ECC (MB) and PC (MF0) mixes is displayed in Figures 4.3(a) and (b).

This was done by first obtaining the bulk resistance of the test sample, R (Ω), from the cusp point; the inverse of which was then multiplied by the electrode geometrical factor to give the bulk conductivity, σ (S/m), as given in equation 3.2 stated in section 3.6. The geometrical constant for the electrode pair used in this specimen was 88.5 S/m.

It is evident from Figures 4.3(a) and (b) that both mixes display a continual decrease in conductivity across the entire curing period, which reflects on-going hydration and pozzolanic reaction. The influence of fly-ash on conductivity is evident and clearly affects the conductivity values of the ECC mix. At 7 days, for example, the ECC was approximately three times more conductive than the PC mortar (i.e., 0.097 S/m vs 0.032 S/m). At 180 days, however, the ECC attained a value of 0.009 S/m, which was approximately 50% less conductive than the PC mortar, which attained a value of 0.014 S/m. The higher initial conductivity of the ECC (MB) mix is expected due to the slower reaction of fly-ash during the initial stage of hydration, which is well documented (Aggarwal et al., 2015; Hemalatha and Ramaswamy, 2017; Fakih et al., 2021). On the other hand, the lower conductivity of the ECC at the longer timescale would reflect the beneficial effects of the fly-ash in reducing the connectivity of the capillary pore network with time (pore refinement effects (Yio et al., 2017; Liu et al., 2020). However, it is worth noting that the bulk conductivity is also affected by the pore-solution conductivity, which depends on the ionic concentrations within the pore solution, which are affected by the presence of fly-ash. A lower conductivity may not necessarily be indicative of a lower porosity (a more detailed discussion of this is presented in Section 4.2.6).
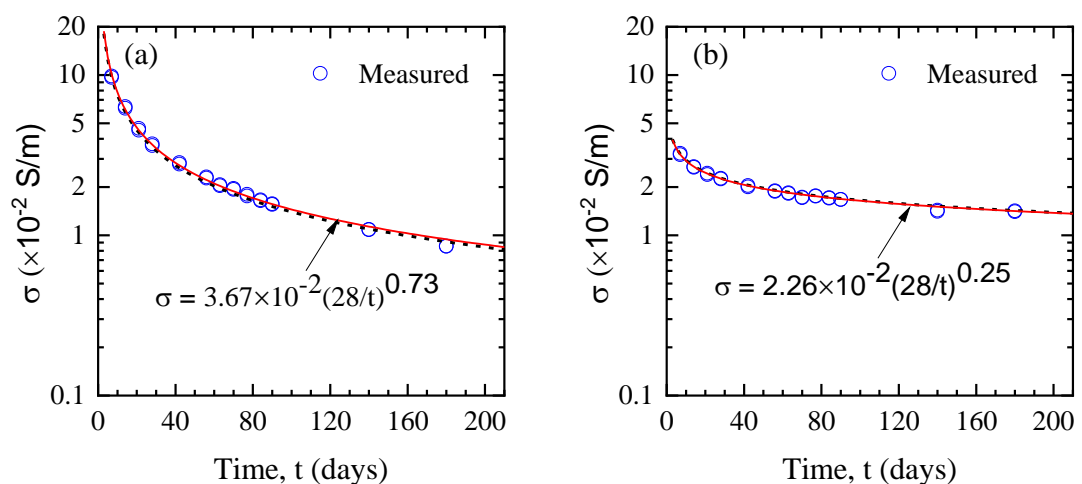
Figure 4.3: Variation in conductivity during the 180-day curing period for: (a) ECC (MB) mix and (b) PC (MF0) mix.

113

The temporal decrease in conductivity for the two mixes shown in Figures 4.3(a) and (b) can be represented by the equation:

$$\sigma_{\mathrm{t}} = \sigma_{\mathrm{ref}} \left(\frac{t_{\mathrm{ref}}}{t}\right)^{N} \tag{4.1}$$

where, σ_{t} (S/m), is the predicted conductivity at time t (in days); σ_{ref} is the reference conductivity at a reference time, t_{ref}, which is taken as 28 days (hence, σ_{28} and t_{28}, respectively); N is an aging (or hydration) exponent, which can be related to hydration and pozzolanic reaction. Best-fit curves to the data are displayed in Figures 4.3(a) and (b) in a solid line through the circular data markers (measured conductivity); the fitting equations are plotted on these figures as well. It is evident that this equation could be used to fit the two datasets well, with the exponent n obtained as 0.73 for the ECC mix (See Appendix A, Table A-1) and 0.25 for the PC mix, which was also observed by McCarter et al. (2015).

4.2.3 Relative permittivity and conductivity of ECC

In a heterogeneous system such as the ECC, a number of polarization processes can operate simultaneously within the system within an overlapping frequency range. Each process may relax according to its own time constant, which makes it difficult to accurately determine the contribution of each individual mechanism to the polarizability of the system. Polarization can be defined as the displacement of opposite charges from their equilibrium (zero-field) position in the presence of an externally applied electrical field (MCcarter et al., 2002; Taha et al., 2017). The main parameter discussed in this section (the relative permittivity) provides a relative measure of the polarizability of a heterogeneous system and, at any particular frequency of applied electrical field, quantifies the sum of all polarization mechanisms operative at that frequency (MCcarter et al., 2002; Suryanto et al., 2016; Taha et al., 2017). It may be possible to reveal the dominant polarization mechanisms (and the frequency range over which they operate) by plotting the permittivity in the frequency domain and by analysing its dispersive behaviour over a wide frequency range (McCarter and Starrs, 1999; Suryanto et al., 2016).

The relative permittivity, $\kappa'_{r}(\omega)$, which has been de-embedded from the impedance data presented in Figures 4.2(a) and (b) using equation 3.3 (see section 3.6), is presented in

the frequency domain in Figures 4.4(a) and (b). In general terms, it is evident that there is a reduction in permittivity with increasing frequency, and this can be associated with the relaxation of polarization mechanisms within the cementitious system. The high permittivity at low frequencies is a direct result of the contribution of all polarization mechanisms operating within the cementitious system to the overall polarizability. As the frequency of the electrical field increases, the low-frequency polarization mechanisms are unable to follow the alternations of the electrical field, and hence no longer contribute to the overall polarizability of the system (relaxation). This is seen as a gradual reduction in permittivity across the entire frequency range. Apart from the value of the permittivity, there is also a distinct change in the rate of relaxation across the entire frequency range. Most notably is the rapid reduction in value at frequencies less than ~1 kHz, regardless of the binder type. Consider, for example, the permittivity of the ECC (MB mix) at 7 days, which has attained a value of ~5.2×10^8 at 1 Hz, this decreases by more than four orders of magnitude to ~1.9×10^4 at 1 kHz. The same order of reduction was observed from the PC (MF0 mix), from ~8.8×10^7 at 1 Hz to ~2.8×10^3 at 1 kHz, although the values were consistently smaller in this case. The rate of change of permittivity reduces at this frequency thereafter, with the ECC attaining values of ~3.6×10^2 at 100 kHz and ~64.1 at 10 MHz (five orders of magnitude) and the PC attaining values of ~1.5×10^2 at 100 kHz and ~60.5 at 10 MHz.

With reference to Figures 4.4(a) and (b), it is interesting to note that over the frequency range 1 Hz-1 kHz, it is apparent that the permittivity of ECC is also influenced by curing time, with a progressive reduction observed with increasing curing time thereby displaying a large spread in value. This is in contrast with the permittivity of the PC, which shows a similar value throughout the entire 180-day curing period. The same trend can be observed from both the ECC and the PC over the intermediate (1 kHz to 100 kHz) frequency range, although from the ECC, it could be inferred that the influence of curing time becomes less evident with increasing frequency as all the curves merge to almost the same value (approximately ~2×10^2) at frequencies close to 100 kHz regardless of the material type. With regard to the response over the high (100 kHz to 10 MHz) frequency range, there is a gradual decrease in permittivity with increasing frequency, which would indicate that relaxation is still operative within this frequency range. As before, the permittivity is not notably influenced by curing time, and similar responses were obtained from both mixes, with all the curves shown to superimpose on each other. This similarity in response is interesting and could,

potentially, be exploited as a feature of electrical measurement which is independent of cement hydration and pozzolanic reactions, as well as the type of cementitious binder.
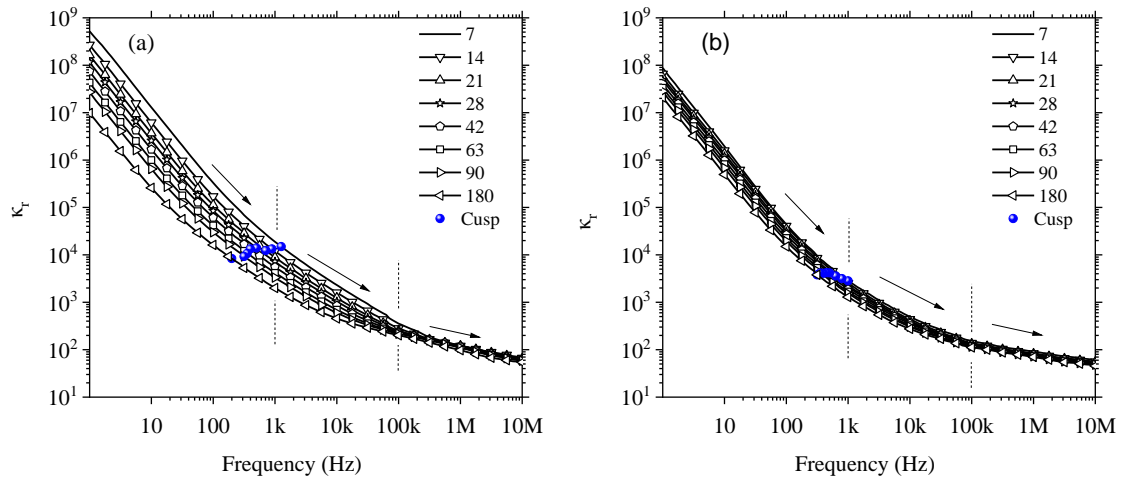
Figure 4.4: Influence of frequency and curing on the relative permittivity of: (a) ECC (MB) mix and (b) PC (MF0) mix. *Note: circular (solid) data marker represents the response at the cusp-point frequency.

Within the frequency range 1 Hz–10 MHz, it is postulated that three dominant mechanisms of polarization are operative:

(i) Polarization processes at the electrode/sample interface, are referred to commonly as the electrode polarization (McCarter et al., 2009; Ishai et al., 2013; McCarter et al., 2015) and can result in anomalously high permittivity values. This is generally a low-frequency mechanism, typically relaxing at frequencies <kHz;

(ii) Double-layer polarization occurs due to charges electrostatically held on the surfaces of the cement gel and other particles such as fly-ash and fine sand (Schwan et al., 1962; Schwarz, 1962; McCarter et al., 2002) (see Figure 4.5(a)). This is a low/medium frequency mechanism and may operate up to ~100 kHz region; and

(iii) Interfacial or space charge polarization resulting from the accumulation of charges at the interface of two dissimilar materials with different relaxation times, also known as the Maxwell-Wagner polarization (Hasted, 1973; Prodromakis and Papavassiliou, 2009; Iwamoto, 2012) (see Figure 4.5(b)). In a cement-based system including ECCs, this can arise from translating charges which are blocked inside isolated pores and accumulate at pore water/hydrate

interfaces. Interfacial polarization is an intermediate-frequency mechanism, operating typically over high kHz into the MHz region.

No Field (E = 0)   Applied Field (E ≠ 0)

(a)

No Field (E = 0)   Applied Field (E ≠ 0)

(b)
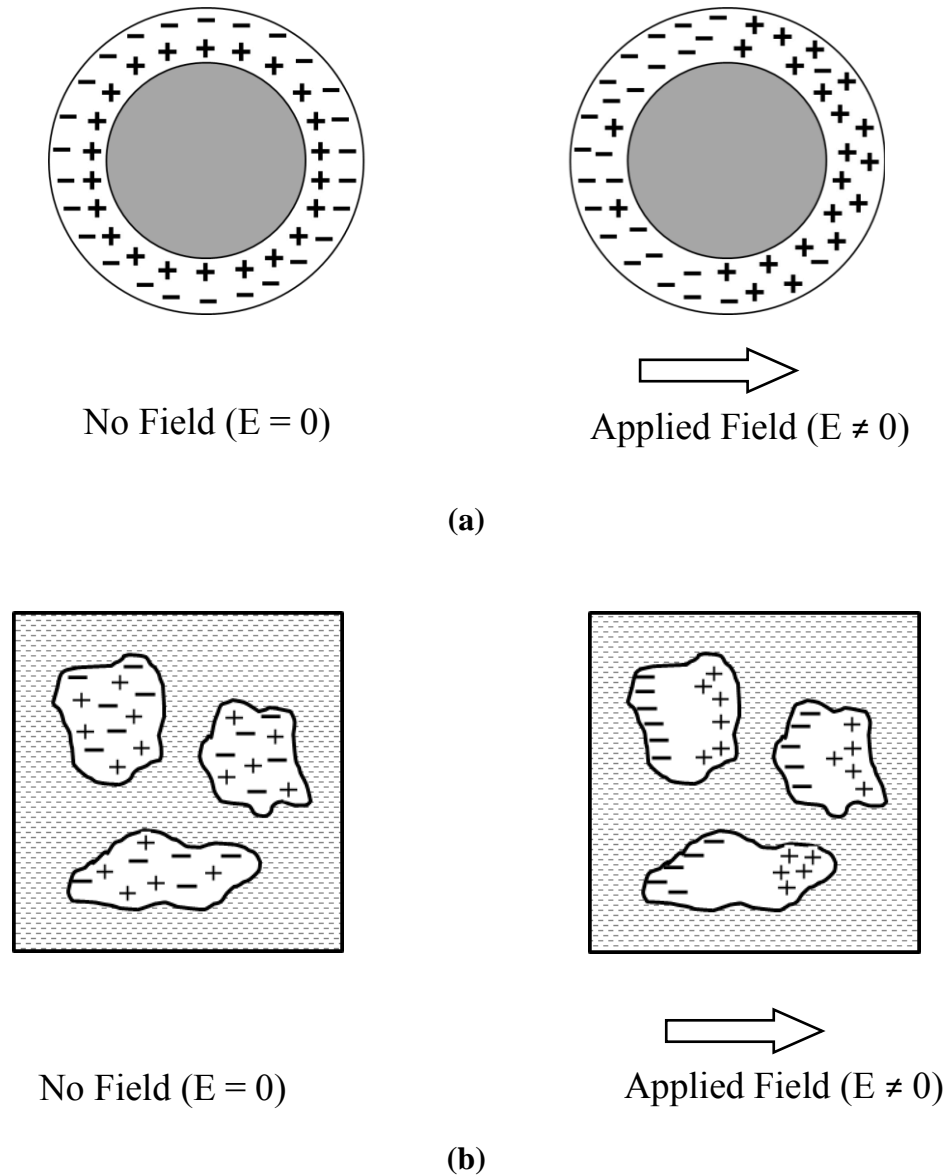
Figure 4.5: Schematic diagram of polarization mechanisms operative within a cementitious system: (a) double-layer polarization; and (b) Maxwell-Wagner (interfacial) polarization.

With reference to Figures 4.4(a) and (b), it is proposed that the mechanism responsible for the decrease in permittivity at frequencies <1 kHz is the relaxation of polarization processes at the electrode/sample interface, possibly overlapping with relaxation of double-layer process within the composite itself. Within the frequency range 1 kHz–1 MHz, it is proposed that the continuing decrease in permittivity is as a direct result of two superimposed mechanisms: the relaxation of double-layer processes, operating

primarily within this frequency range, and the relaxation of interfacial (Maxwell-Wagner) processes, which have a more dominant influence at frequencies >100 kHz.

It is also interesting to note from the results presented in Figures 4.4(a) and (b) that there is a reduction in the magnitude of the dispersion/relaxation with increasing curing time. For both the mixes, this decreases from approximately six orders of magnitude at 7 days of age to five orders of magnitude at 180 days. This reduction is attributed, in part, to the reduction in relaxation time discussed above and to the change in the dispersive polarization processes with time.

To further investigate the dispersive behaviour of the material, Figures 4.6(a) and (b) present the bulk conductivity in the frequency domain, with the conductivity de-embedded from the impedance measured using equation (3.2) in section 3.6. Conductivity gives a measure of both ionic conductions through the movement of ions within the continuous capillary pore network, which is a low-frequency feature, and a dispersive conduction contribution resulting from the relaxation of polarization processes which is dependent upon the frequency of the applied field. The cumulative effect of the latter mechanism would result in an increase in conductivity with increasing frequency, hence the conductivity, $\sigma(\omega)$, at angular frequency, ω, can be written as,

$$\sigma(\omega) = \sigma_d(\omega) + \sigma(0) \tag{4.2}$$

where $\sigma(0)$ represents the ionic conduction process via the percolated capillary pore network and $\sigma_d(\omega)$ represents the conductivity resulting from dissipative polarization processes.

Regarding the conductivity over the entire frequency range presented in Figures 4.6(a) and (b), it can be inferred that dispersion results in an increase in conductivity across the entire frequency range, indicating the existence of relaxation of polarization processes over the entire range, as discussed above. The progressive increase over the entire frequency range would indicate that the polarization mechanisms operate at an overlapping frequency range, resulting in a spread of relaxation time. Due to this progressive increase, it would be difficult to separate the underlying mechanisms from this presentation formalism. However, three general regions can be delineated:

(i) a low-frequency dispersive region of increasing conductivity resulting from relaxation of electrode polarisation;

(ii)   an intermediate plateau region indicated by a marginal increase in conductivity; and,

(iii)   an extended, high-frequency dispersive region of rapidly increasing conductivity. This can be associated with the relaxation of double-layer polarisation and a stronger contribution resulting from the relaxation of Maxwell-Wagner interfacial polarisation processes at frequencies (Hasted, 1973).

Apart from the consistent increase in conductivity with increasing frequency, it is apparent from Figures 4.6(a) and (b) that there is also a gradual decrease in conductivity with increasing curing time. This is attributed to continual refinement of the pore-structure resulting from the on-going hydration (both mixes) and pozzolanic reaction (ECC only). In these figures, the cusp-point frequencies are indicated with circular data markers, and the conductivity values at this specific frequency would reflect the bulk conductivities presented earlier in Figures 4.3(a) and (b) (ionic conductivity). It is interesting to note that there is a frequency shift towards the lower frequencies with increasing curing time, thereby causing the cusp-point frequency to shift to the left-hand side. It is also evident from the figures that this frequency shift occurs over the entire frequency range under study (1 Hz–10 MHz), with region (i) gradually disappearing with increasing curing time and region (iii) becoming more visible (and prominent). Regardless of the frequency shift, however, it is interesting to see that the cusp-point (all data markers) always falls within the plateau region of the frequency domain responses, generally within the range 100 Hz–1 kHz. The bulk electrical conductivity of both cement-based systems can therefore be determined within this frequency range without the need for taking the full frequency response, and plotting and locating the cusp point, either in the Nyquist or in the frequency domain format. Given that all the data markers are within the plateau region, a single-frequency measurement could, therefore, be taken within this optimal frequency range without compromising measurement accuracy. This approach could be applied to a regular/frequent testing regime more effectively. A-priori (multi-frequency) measurements, as described in this section, should be, however, undertaken when different electrode configurations are used.
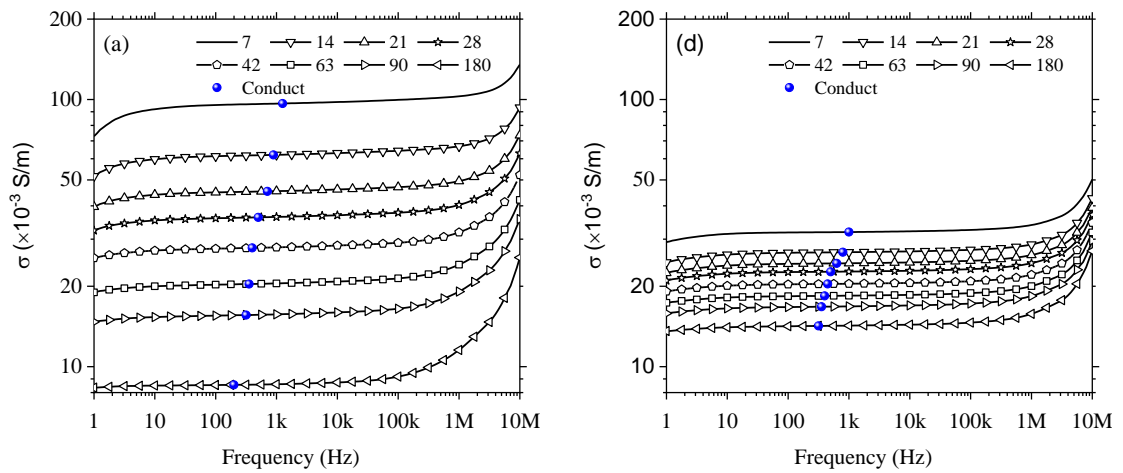
Figure 4.6: Influence of frequency and curing on the relative permittivity of:
(a) ECC (MB) mix and (b) PC (MF0) mix. *Note: the circular (solid) data marker
represents the response at the cusp-point frequency.

4.2.4 Influence of fly-ash on the electrical properties of ECC

In this section, the influence of fly-ash on the electrical impedance of ECC is discussed. Three replacement levels were considered: 15%, 30%, and 64%, denoted MF15, MF30, and MF64.

Figures 4.7(a)-(c) present the impedance response for all these mixes over a 360-day curing period. It can be clearly seen that increasing the fly-ash amount increases the width of the V-shaped valley, although marginally (see Figure 4.7(d) for the response at 2 days of curing). As discussed in Section 4.2.1, the amount of un-burnt carbon in a fly-ash (see Figure 4.8), as quantified by the loss on ignition (LOI), was found to exert an influence on the impedance characteristics of a cement-based system (McCarter et al., 1999). Given that fly-ash is a by-product, it could be expected that there would be a significant variation in LOI from different batches. However, given that the fly-ash used in the three mixes was taken from the same bag of fly-ash, it could be expected that there would be more un-burnt carbon in the mix as fly-ash dosage is increased, and this may exert a more significant influence on the various electrical properties of the overall system. From the results presented, however, although a generally wider valley was found from the higher fly-ash amount mixes, the difference is not as prominent as those reported in (Suryanto et al., 2017c). In all cases, no emergence of a new secondary arc or an extensive plateau region is evident. The extent of the plateau regions is seen to increase with curing time but remains in the same proportion as the size of the arc.
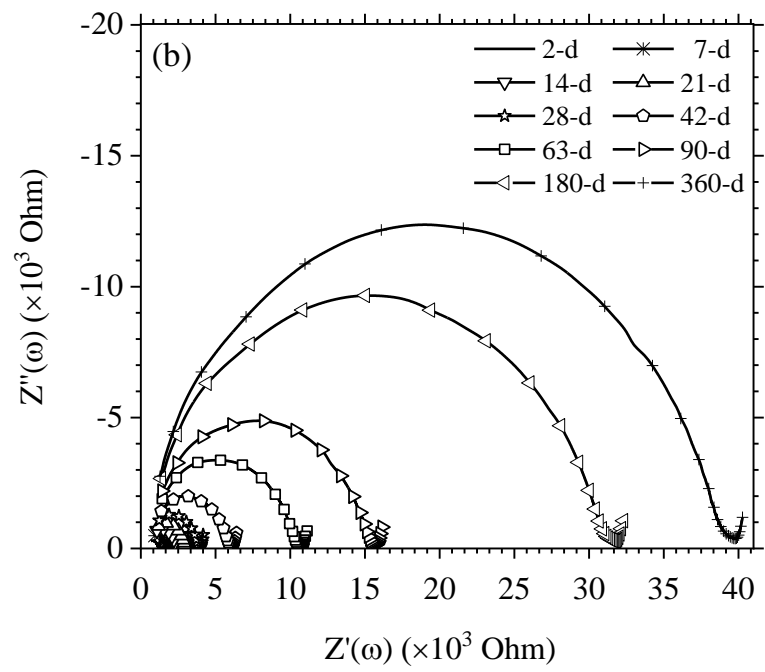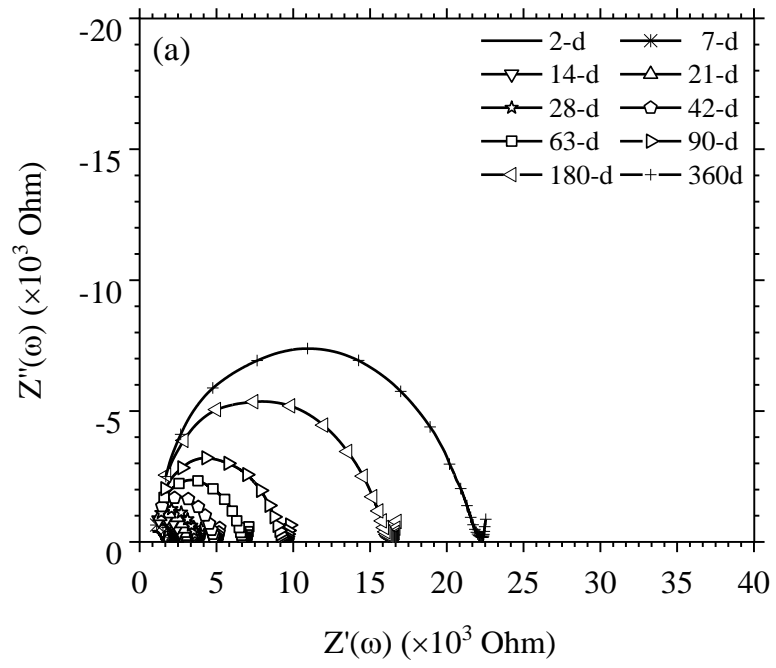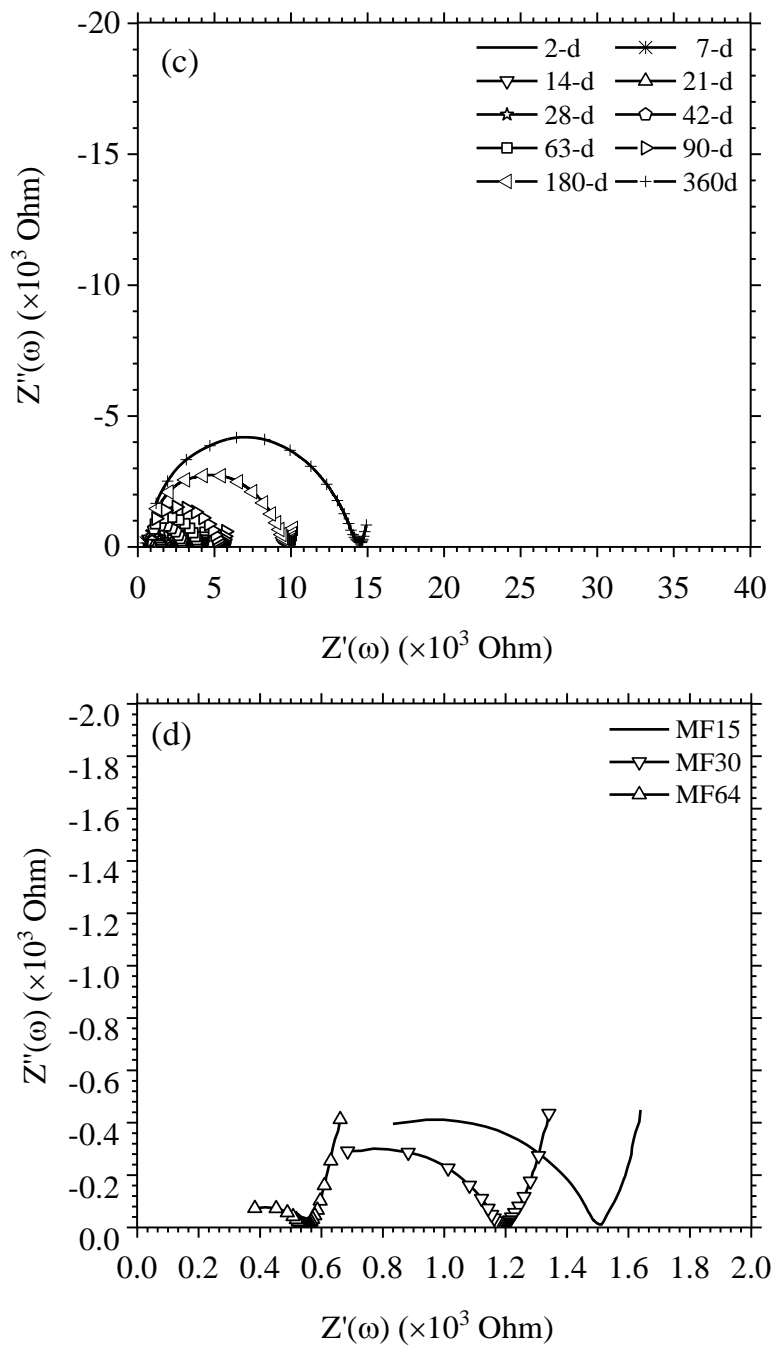
Figure 4.7: Impedance response for Mixes (a) MF15; (b) MF30; and (c) MF64 over the period 360 days. (d) The corresponding impedance responses at 2 days of curing.
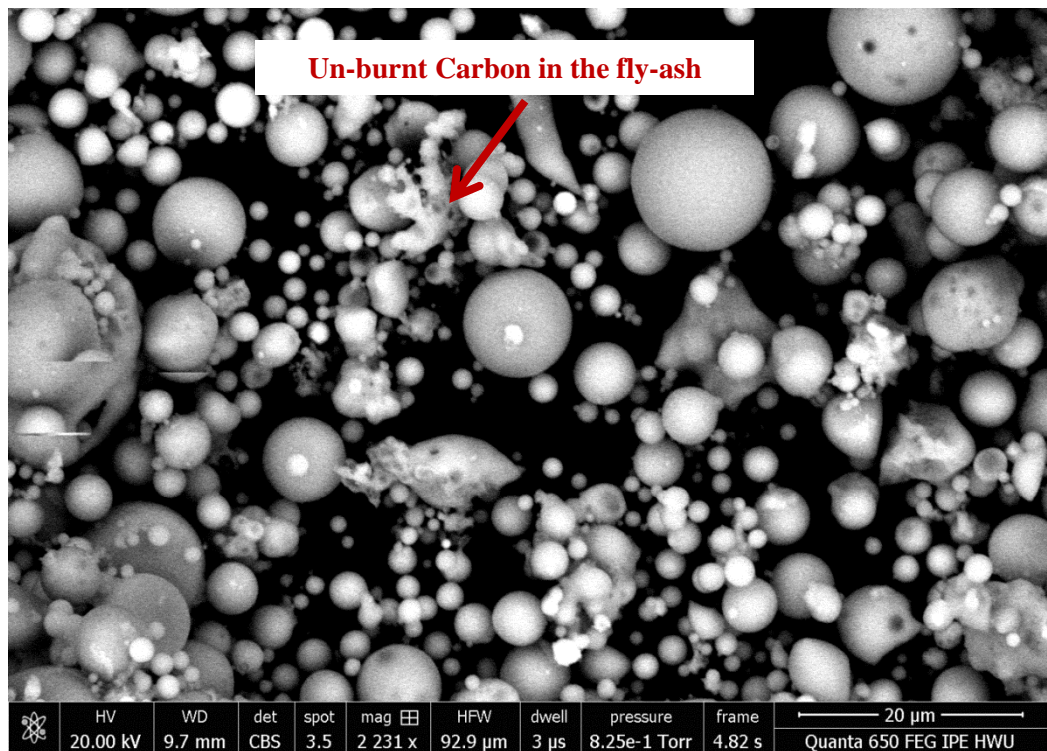
Figure 4.8: ESEM image shows the fly-ash particles (in spherical forms) and the very limited presence of un-burnt carbon (in cellular forms).

To investigate the influence of fly-ash on pore-structure development, the impedance values at the cusp point (i.e., the lowest point at the junction between the low-frequency spur and the bulk arc) from all impedance responses of Mixes MF0, MF15, MF30, and MF64 displayed, respectively, in Figures 4.2(b) and 4.7(a)-(c) were converted to the bulk conductivity and plotted in Figure 4.9(a).

It can be clearly seen from Figure 4.9(a) that at initial stages of curing (<21 days), fly-ash has the effect of increasing the bulk conductivity; the extent of which is almost directly proportional to the level of replacement. Consider, for example, the bulk conductivity at 2 days of curing. Increasing the fly-ash replacement from 0% to 64%, results in a ~3 fold (linear) increase in conductivity, from ~0.05 S/m for the MF0 mix to ~0.16 S/m for the MF64 mix. This linearity was found to remain in place up to approximately 21 days of curing, where a linear increase in conductivity is still evident, from ~0.03 S/m for the MF0 mix to ~0.05 S/m for the MF64 mix. However, this is not the case with the progression of the curing age (>28 days). It can be clearly seen that at 28 days, the conductivity values of MF15 and MF30 are getting close to MF0. At 42 days of curing, it is clearly noticeable that the conductivity value of MF30 becomes less conductive than all mixes, followed by MF15, MF0, and then MF64. This change in the

trend can be associated with the added presence of pozzolanic reaction in mixes M15, M30, and M64. This trend remains the same until 90 days after curing. After that, the MF64 started to decrease considerably, and the MF64 became less conductive compared with MF0. This trend is affected firstly by the conductivity of the MF0, which decreases gradually with increasing curing age due to the on-going hydration compared with the rest of the mixes (with fly-ash); secondly, there has been a decrease in the conductivity of the MF15, MF30 and MF64 due to the presence of fly-ash in the ECC which enhances the pozzolanic reaction after 28 days. However, the Conductivity of MF64 was higher than MF15, and MF30 due to the high presence of fly-ash which involves a reduction of the hydration products, thus a reduction of the pozzolanic reactions.

In order to have a better insight into the effect of hydration and pozzolanic reaction, the bulk conductivity values for all mixes presented in Figure 4.9(a) were normalized to the corresponding value at 2 days of curing. Figure 4.9(b) displays the normalized bulk conductivity for all mixes. It is apparent that all mixes display a continual decrease in bulk conductivity over the 360-day curing period, with MF0 (with no fly-ash) displaying the lowest decrease among the mixes. Once the fly-ash was introduced into the system, there was a significant decrease in conductivity over the first 28 days of curing, indicating the effect of hydration at an early age. The results also obviously show that the hydration and pozzolanic reactions have a prominent effect on the bulk conductivity of the material, which is seen as a gradual decrease in the bulk conductivity over the test period.
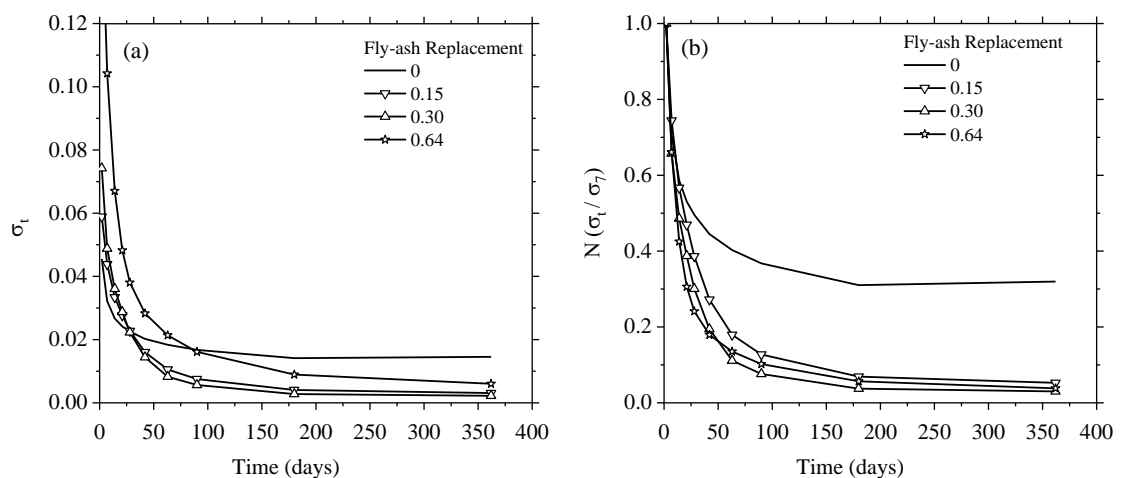
Figure 4.9: a) Conductivity versus FA replacement of (MF0, MF15, MF30, and MF64); b) the corresponding normalized bulk conductivity over the 360-day curing period.

4.2.5 Equivalent circuit modelling

In this section, the impedance responses at different curing times presented earlier in Figures 4.2(a) and (b) were modelled using equivalent electrical circuits, comprising a number of circuit elements connected in parallel and/or series. The formulation of these equivalent circuits was based on the potential electrical pathways within the cementitious system. Figures 4.10(a) and (b) illustrate a schematic diagram representing possible electrical pathways within the plain PC (MF0) and ECC (MB) mixes.

With reference to Figure 4.10(a), two electrical pathways were considered for the PC to represent (McCarter et al., 2015):

(i) the continuous capillary pore network (ionic conduction); and

(ii) the solid cement matrix comprising products of hydration, sand particles, isolated pore-water, and un-hydrated cement particles.

Regarding the ECC, three electrical pathways as displayed in Figure 4.10(b) was considered, which includes paths (i) and (ii), and a new path (iii) to represent the conduction through the unburnt carbon particles in the fly-ash and the continuous capillary pore in the cement matrix in series, following the equivalent circuits for ECC containing conductive steel fibres reported in Suryanto et al. (2016). These potential pathways are represented by the following circuit elements (see Figures 4.10(a) and (b)):

- a circuit comprising a resistor, R_{cp}, and a constant phase element, CPE_{sm}, both are connected in parallel. This is to represent the pathways (i) and (ii) described above. The parallel connection was considered to take into account the superimposed phenomena of the conductive and capacitive effects within the system; and

- a circuit comprising

  ➢ a resistor, R_{c-f}, for representing the electronic conduction through the unburnt carbon;

  ➢ a parallel circuit, R_{ci}, and, CPE_{ci}, for describing the resistance at the interface of the carbon particle and the cement matrix, and the capacitive component of the interface, respectively; and

  ➢ a parallel circuit, R_{c-cp}, and, CPE_{c-cp}, for representing the ECC matrix between carbon particles (similar to Pathways (i) and (ii) above).

In addition to these main circuit elements, the following circuit components were also considered:

- a resistor, R_s, for describing the projected intercept of the high-frequency arc with the real-axis at the high-frequency end; and

- a circuit comprising, R_{el}/CPE_{el}, connected in parallel, to represent the response from the electrode/sample interface.

These two circuit components operate in series with the bulk response.

(a)

(b)
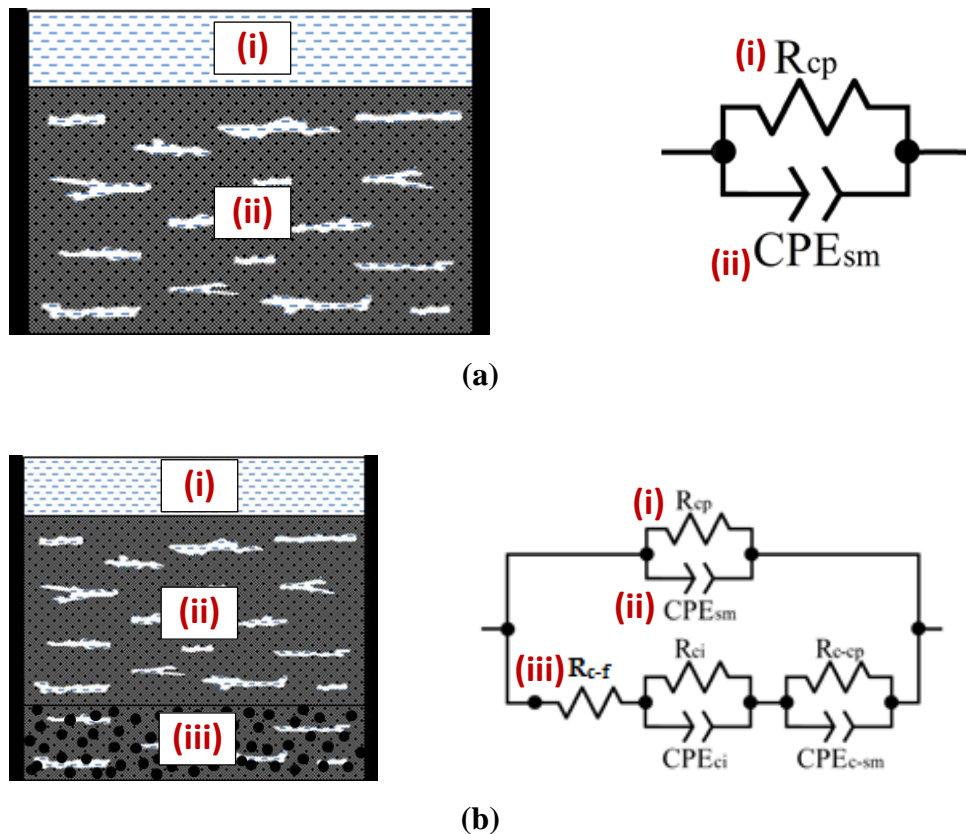
Figure 4.10: Diagrammatic representation of the electrical pathways (denoted by (i) to (iii)) and the corresponding electrical models used for (a) plain PC mix and (b) ECC mix.

The simulated impedance responses for the ECC and PC mixes are presented in Figures 4.11(a) and (b) in solid lines, together with the measured data (shown in red dashed lines). Good agreement can be seen between the measured and simulated responses indicating, that the electrical models can offer a good phenomenological representation of the two cement systems. For reasons of clarity, the parameter values used in the simulation for both mixes are presented in Appendix A (Tables A-2 and A-3) over the entire 180-day test period (viz., 14, 21, 28, 42, 63, 90, and 180 days). It is

shown that the values of the bulk resistance R_{cp} for both mixes increase as curing time increases due to the ongoing hydration as discussed above. Regarding the CPE, which is used to represent the semicircle arc depressed below the real axis, there are two components involved: the pseudo-capacitance (CPE-T) and the exponent (CPE-P) (see Section 2.5.2). From the simulated response presented, an increase in CPE-T$_{sm}$ values was evident with increasing curing time, from 1.5×10^{-10} to 1.9×10^{-10} for the PC mix, and from 3.2×10^{-10} to 9.8×10^{-10} for the ECC mix over the entire 180-day period. This could be attributed to the increase of isolated pores in the system (McCarter et al., 2015; Suryanto et al., 2016). On the other hand, as curing time increases, the values of the exponent (CPE-P$_{sm}$) are shown to decrease, thereby causing the centre of the semicircle arc to further depress below the real axis (see Figure 4.12(a) and (b)).
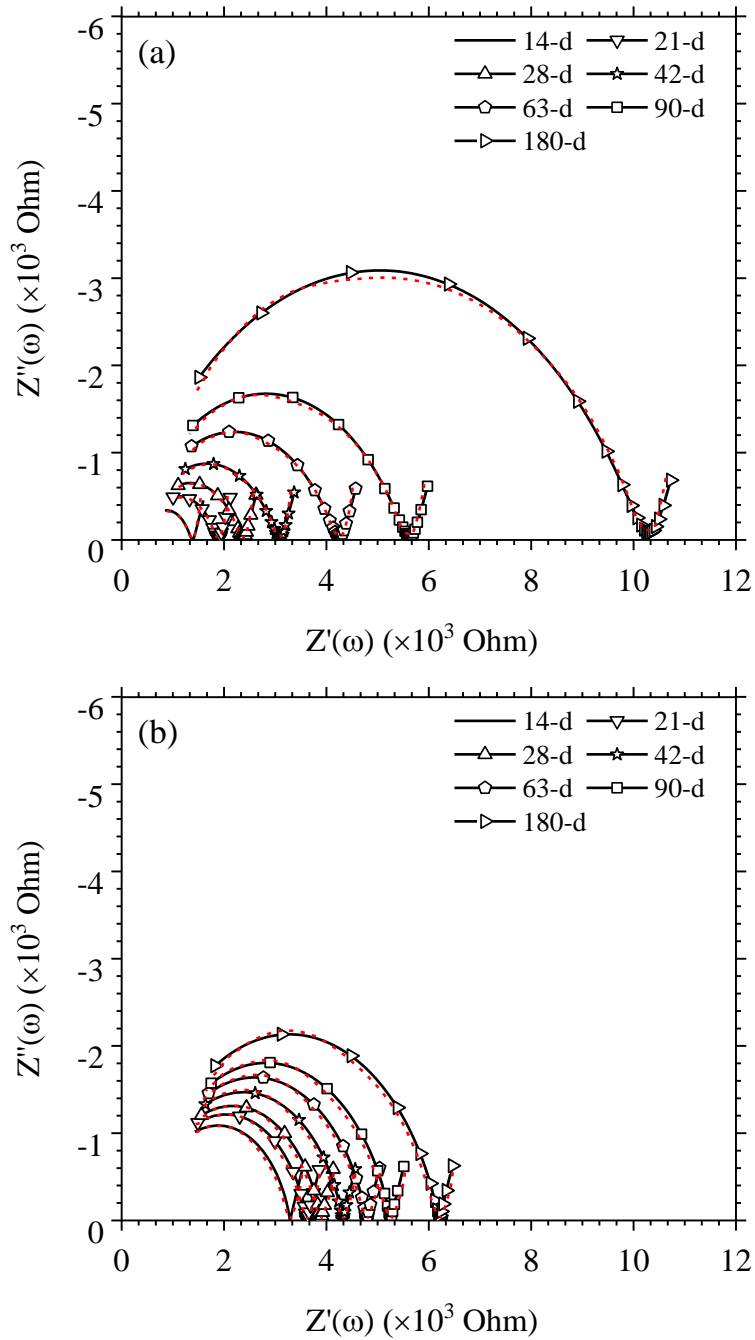
Figure 4.11: Measured and simulated impedance responses for:
(a) ECC (MB) mix and (b) PC (MF0) mix.

The simulation outputs of the equivalent circuit's elements of ECC are presented in Appendix A, Table A-3. It was assumed that the R_{cp}/ CPE_{sm} and R_{c-cp}/CPE_{c-cp} were the same because of the low LOI in the fly-ash (<2%). It can be clearly seen that the ECC and mortar show a similar trend with an increase in the R_{cp} and CPE-P_{sm} and a decrease in the CPE-T_{sm} values. However, when the mortar and ECC trends are compared in detail (see Figure 4.12(a) and (b)), it can be seen that on day 14 of curing, the R_{cp} value of mortar was 2800, while ECC resistance was 1050 (less than half of the mortar

resistance value). After 63 days of curing, the trend evolved with quite similar resistance values for both specimens. At 180 days of curing, it is interestingly noticeable that the R_{cp} value of ECC was approximately twofold compared to the R_{cp} value of mortar. This phenomenon is attributed to the on-going hydration in both specimens and, in addition, the presence of fly-ash in the ECC, which enhances the pozzolanic reaction.

The additional pozzonalnc reaction will refine the pore structure and make the pores less interconnected. This is evidenced by the CPE-T_{sm} values of the ECC specimens presented in Figure 4.12(b) and Table A-3 in Appendix A. In addition, the presence of isolated pores is greater in the ECC than in the mortar (See CPE-T_{sm} values in Figure 4.12(a) and (b) or Table A-2 and A-3 in Appendix A). Moreover, the semi-circuit arc of ECC became more depressed below the Real axis compared to the mortar specimen after the 14-days (See the exponent (CPE-P_{sm}) values in Figure 4.12(a) and (b) or Table A-2 and A-3 in Appendix A).

The most important outcome extracted from simulations of the ECC is that the un-burnt carbon/matrix interface plays a primary role in the response. It can be clearly notice that the R_{ci} increases with increasing the curing age (see Figure 4.12(c)). Consider for example, the interface resistance at 14-days was 20×10^3 Ω, this increased to almost seven-folds ($\sim 144 \times 10^3$ Ω) at 180days. This increase in R_{ci} with time is associated with the decrease of the interface size between the capillary pore and the un-burnt carbon, which forces the same current to flow through a tinier area. It can also be noticed that the interface capacitive component 'CPE-T_{ci}' decreases with time. For example, the interface capacitance decreased from $\sim 8 \times 10^{-6}$ at 14-days to approximately half at 180 days with $\sim 4 \times 10^{-6}$. This decrease could be due to: i) some of the un-burnt carbon no longer contributing to the capacitance, suggesting it has become isolated; and/or ii) the interface size between the capillary pore and the un-burnt carbon decreasing with time, which causes less capacitance of the un-burnt carbon. In addition, the exponent 'CPE-P_{ci}' is a very small value, and it decreases with time.
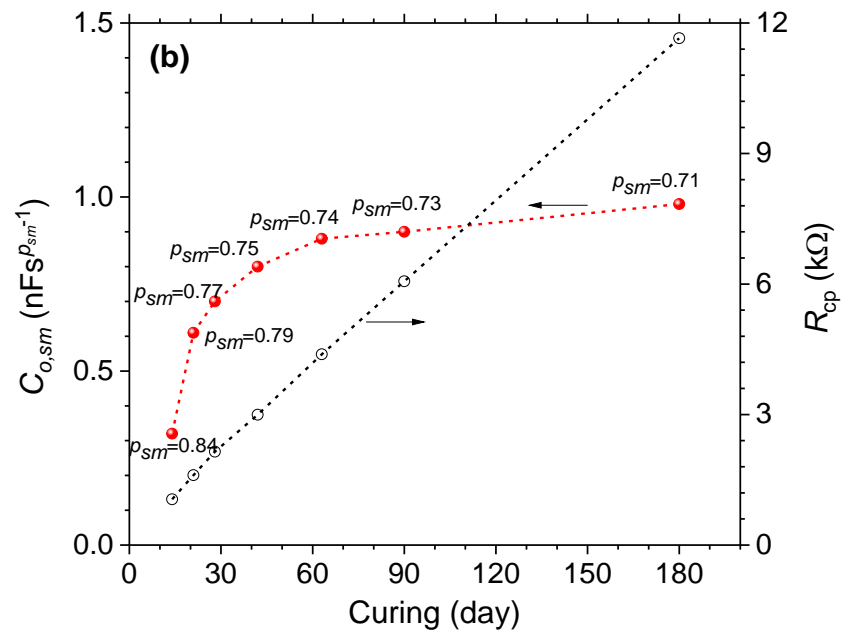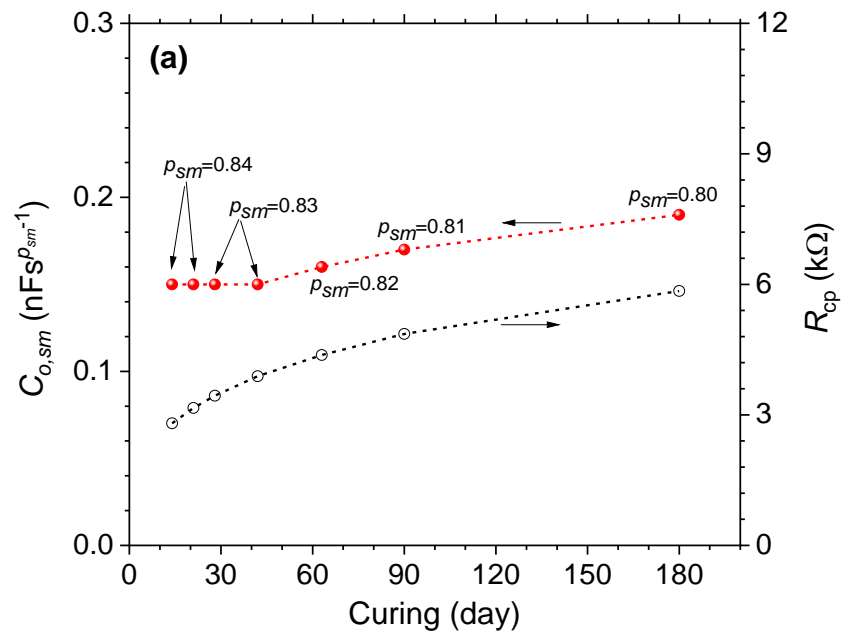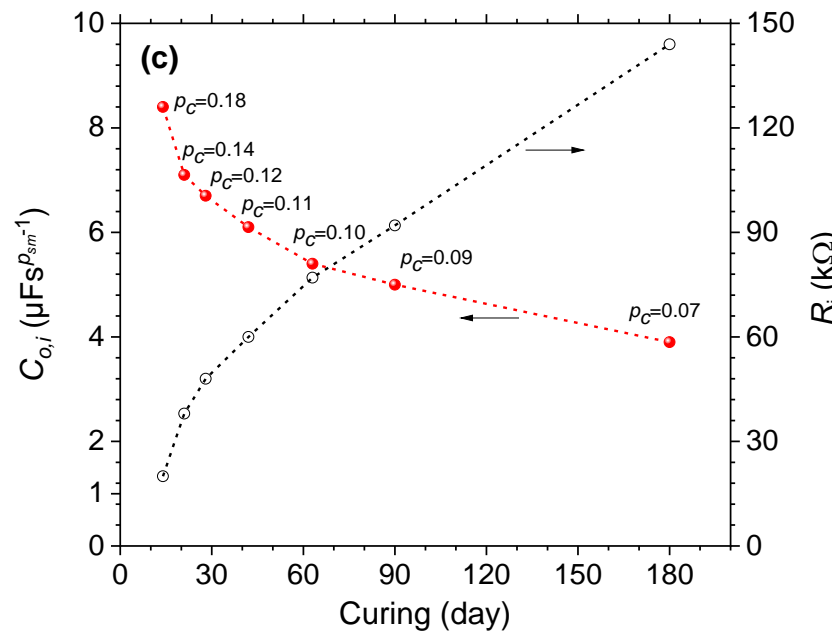
Figure 4.12: The corresponding variations in circuit parameters represent: (a) PC (MF0); (b) ECC; and (c) the un-burnt carbon/matrix interface in the ECC.

4.2.6 Formation factor and pore solution resistivity

To understand the effect of microstructural changes in mortar and ECC, the influence of pore-solution resistivity must be taken into account. With regard to the traditional treatment of rock resistivity data, the term Formation Factor (F) has been used, which is defined as the ratio of the bulk electrical resistivity of a fully water-saturated rock-sample, ρ_r (Ωm), to the electrical resistivity of the water saturating the pores (i.e., pore solution), ρ_f (Ωm). This parameter is associated to the rock porosity, φ, through the Archie's law relationship,

$$F = \frac{\rho_r}{\rho_f} = a \, \varphi^{-M} \qquad \qquad (4.3)$$

Where a represents the correction factor, which is applicable to a certain range of porosities, φ, with a value range from 0.4 to 2.5, while M represents the cementation exponent, which is associated with the connectivity and tortuosity in the network of pores within the rock-sample. M values are generally in the range of 1.2 to 2.5 (Suryanto et al., 2020b).

The pore solution resistivity is an essential factor in measuring the formation factor, which can be determined experimentally and/or theoretically. As discussed by Barneyback and Diamond (1981), the pore solution expression technique could be used, which requires placing a sample into a high-pressure die system to squeeze the sample and obtain its pore solution. A small pore solution cell could then be used to measure the expressed pore solution resistivity (Spragg et al., 2016). However, such a technique is complex to implement due to the need for special skills and equipment (Spragg et al., 2016), and is more applicable to cement paste and mortar. Concrete, especially that cured for an extended period of time, is much harder to process (Suryanto et al., 2020b).

The theoretical way to obtain the pore solution resistivity could be done through the Virtual Cement and Concrete Testing Laboratory (VCCTL) software (NIST 2019). It is software that can be used for modelling the microstructural development, physical properties, and hydration of cementitious materials (Suryanto et al., 2020b).

The major contributions to the approximate pore solution resistivity in the cementitious materials are the pore structure produced by the VCCTL (see Figure 4.13(a)) and the pore solution chemistry, which can be automatically determined through VCCTL through the concentration of three major ions (sodium [Na^+], potassium [K^+] and

hydroxide [OH$^-$]) in the pore water and their equivalent conductivity through the use of a simple model proposed by Snyder et al. (2003), known as the NIST model. This model was then implemented into the VCCTL by Bentz (2007). The ionic concentrations are determined based on both the binder composition and the alkali content (total and soluble) in the cementitious materials. According to Brouwers and vanEijk (2003), it was presumed that upon measurement, a proportion of 55% and 35% of the K$_2$O and Na$_2$O are released into the pore-water upon gauging.

Figures 4.13(b) and (c) present the pore solution resistivity and porosity for mortar and ECC over the 180-day period, respectively. With reference to Figure 4.13(b), it can be clearly seen that there is a gradual reduction in the pore solution resistivity for both mixes, resulting from the continuous dissolution of ions into the pore water. The plots also display that the pore solution resistivity of mortar is higher than that of ECC. Figure 4.13(c) shows that there is a rapid decrease in porosity over the initial few weeks of curing, which is then followed by a gradual decrease over the remaining test period. It can also be noticed that the porosity of the ECC is higher than the porosity of the mortar.
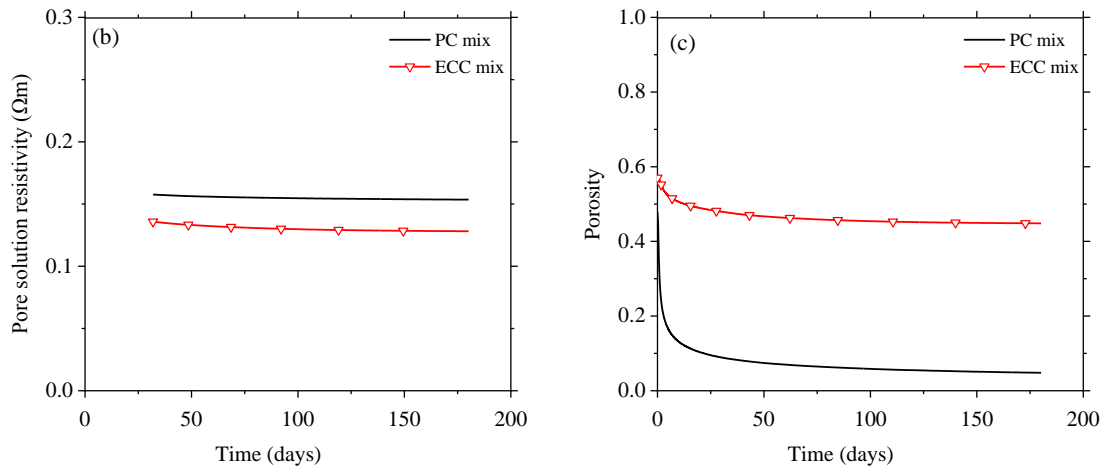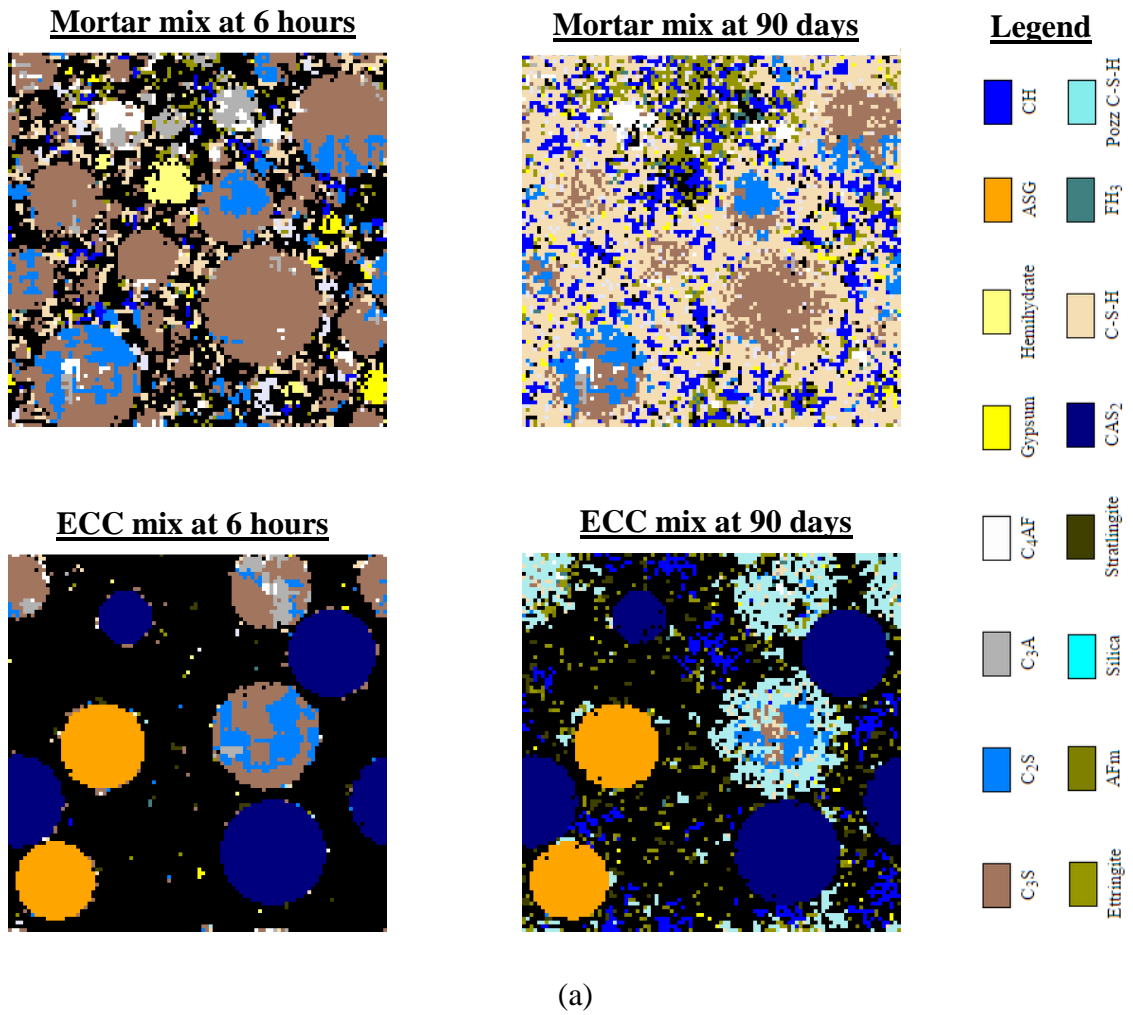
Figure 4.13: (a) Pore structure generated at 6 hours and 90 days of hydration for MF0 and ECC mixes; (b) computed pore solution resistivity; and c) total porosity.

Once the pore-solution resistivity is obtained, the formation factor can be determined using equation (4.3) above. Figure 4.14 shows the measured formation factor over the 180-day of curing of mortar and ECC. It is evident that the formation factor plots of both the mortar and ECC show a continuous increase over the 180-day period of curing. This is attributed to the on-going pore structure refinement. It is also apparent that the formation factor of mortar mix increases gradually after 28 days of curing. On the other hand, the formation factor of the ECC mix increases significantly and reaches higher values compared to the mortar mix after 42 days of curing. This higher value of the formation factor of the ECC is attributed to the replacement of Portland cement with fly-ash, which leads to further pore structure refinement in the long run. This is desirable in durability considerations as the capillary pore network is more tortuous and disconnected, which results in slower transport through the pore system. Suryanto et al. (2020b) investigated the formation factor for Portland cement concrete and concrete mixes, including different levels of GGBS, over a period of 360 days. It was found that all mixes exhibit an increase in the formation factor over the entire test period. For example, the formation factor increases from $\pm$ 5 to 315 for the PC, 545 for the GGBS/35, 835 for the GGBS/50, and 1040 for the GGBS/65 at the end of the test period. This increase is related to the on-going hydration and pozzolanic reaction, which cause pore structure refinement, which was more obvious with slag concrete. Moradllo et al. (2018) calculated the porosity and the formation factor for mortar samples with different w/c. They found that increasing the porosity through increasing the w/c of the mixture leads to a decrease in the formation factor. It was found that the formation factor was ~750 for w/c of 0.30, ~400 for w/c of 0.40, ~250 for w/c of 0.50, and ~150 for w/c of 0.60. The higher rate of the formation factor increase was found when the w/c was reduced from 0.40 to 0.30. This significant increase is associated with high tortuosity and a refined pore network.
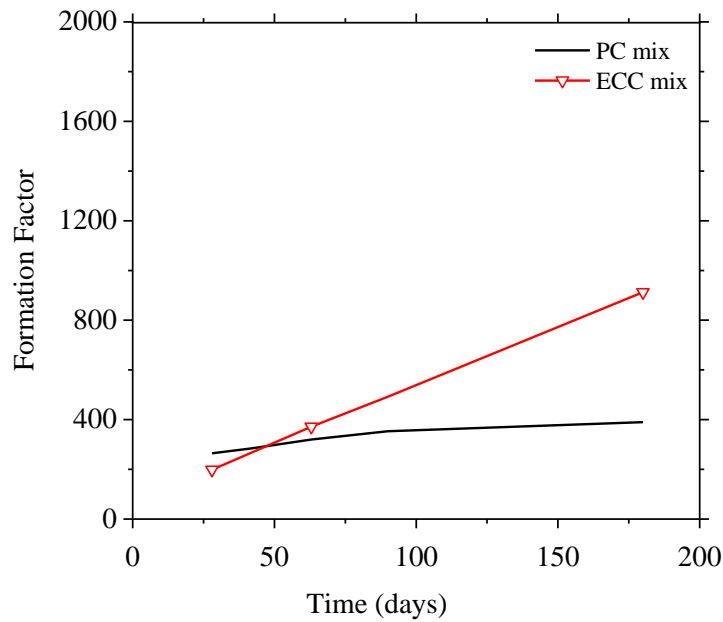
Figure 4.14: Computed formation factor of PC mix and ECC mix.

4.3 Effect of temperature

4.3.1 Complex impedance and bulk resistance

To understand the influence of temperature, the complex impedance spectra for Mix ECC (MB) under varying temperatures are displayed in Nyquist format in Figure 4.15, with frequency increasing from right-to-left across the curve over the frequency range 20Hz–1MHz. It should be noted that measurements were taken on mature samples (365 days of curing) as hydration and the pozzolanic reaction could be expected to have ceased at this stage. This is done to ensure that the measured response accurately reflects the effect of temperature on ionic conduction in a fully developed pore structure with minimal interference from hydration effects. It should also be noted that the frequency range is slightly smaller in this case than the range presented in the previous section (1 Hz–10 MHz), due to the limitation of the working frequency range of the LCR meter. Also, as before, although measurements were obtained at 20 spot frequencies per decade, for clarity, only selected frequencies are highlighted in Figure 4.15 with data markers.

With regard to the results presented in Figure 4.15, a similar overall response to the schematic shown earlier in Figure 4.1(b) is evident, comprising a depressed semi-circular arc and a weakly developed spur at the low-frequency end. The full extent of the spur would only become apparent at frequencies considerably smaller than the lower

frequency limit considered in this study (i.e., << 20 Hz) (Suryanto et al., 2016). The data clearly shows that the real and imaginary components of the impedance are both affected by temperature at all test frequencies. As the specimen temperature increases, there is a progressive displacement of the entire impedance response to the left-hand side toward the origin, together with a reduction in the radius of the bulk arc, which indicates an overall reduction in specimen impedance. Increasing the specimen temperature has the effect of shortening the length of the bulk arc, with the end of the arc shifting toward the cusp-point.

Taking the cusp-point as the bulk resistance of the ECC specimen, Figure 4.15(b) displays the variation in resistance as the sample temperature is increased from approximately 7°C to 60°C. The best-fit line to the test data is plotted in the figure as a solid line through the measurement points, with the resulting fitting equation displayed on the figure. The results obtained from the two prismatic specimens indicate good repeatability, and it is evident that over the temperature range considered, the bulk resistance exhibits an inverse relationship with temperature, with resistance decreasing with increasing temperature, although the changes in resistance at higher temperatures are not as sensitive to changes in temperature as those at lower temperatures. This natural temperature dependence is well-documented and could be attributed primarily to the changes in ionic mobility within the pore network (hence changes in pore-fluid resistance) (McCarter, 1995). In this work, it is anticipated that the influence of other factors, such as dissolution of ions and microstructural changes (McCarter et al., 2000), is more limited in extent.

(a)

$R = 4.3\times10^3\,e^{-0.028T}$ (Ω)

$r^2 = 1.0$
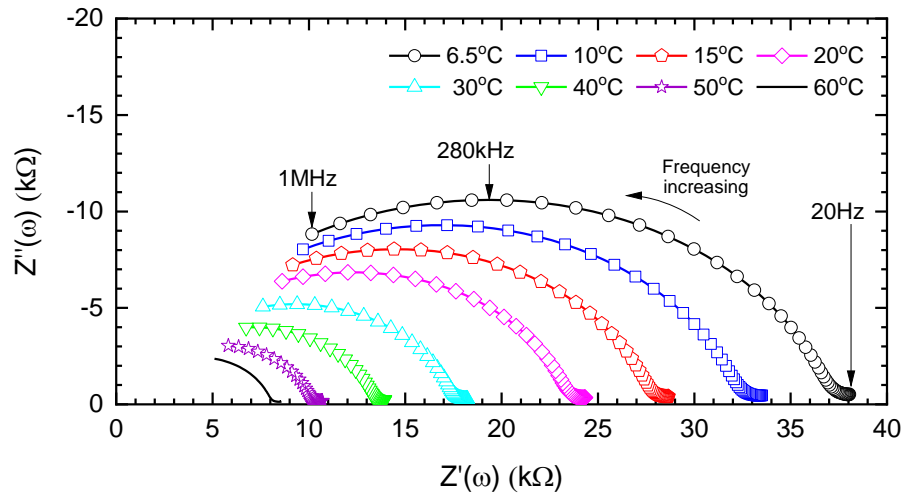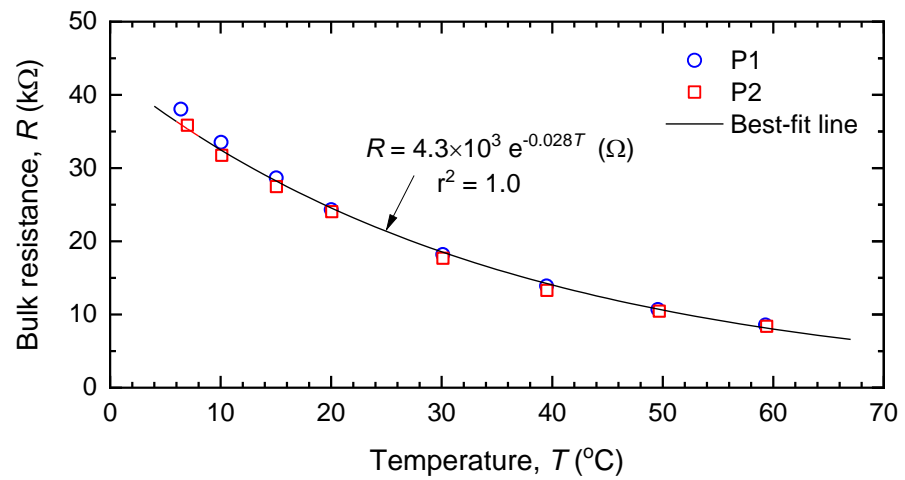
(b)

Figure 4.15: Variations in (a) impedance and (b) bulk resistance with temperature.

4.3.2 Arrhenius presentation

Given that ionic conduction in ECC is a thermally activated process, the Arrhenius relationship can be applied (McCarter et al., 2000; Chrisp et al., 2001),

$$R = R_o e^{\left[\frac{E_a}{R_g T_k}\right]} \tag{4.4}$$

where R is the bulk resistance (Ω) at temperature T_k (Kelvin); R_o is the pre-exponential constant and represents the nominal resistance at infinite temperature (Ω); E_a is the activation energy for the conduction process (J mol^{-1}); R_g is universal gas constant (8.3141 J mol^{-1}K^{-1}). Figure 4.16 presents the natural logarithm of bulk resistance, $ln(R)$, plotted against $1000/T$. In this format of presentation, the sample temperature increases

from right-to-left along the horizontal axis and the data markers represent the measured resistance; while the solid line represents the linear fit from which the slope could be used to obtain the apparent activation energy (i.e., multiplying the slope by R_g will obtain E_a in kJ mol^{-1}). From the data presented, the activation energy for conduction processes over the temperature range of 6.5–60°C was obtained as 21.7 kJ mol^{-1} (0.22 eV per ion), which is in agreement with the value reported in (Suryanto et al., 2017a).

Published data on the activation energy for electrical conduction in engineered cementitious composite are very limited; comparisons are, therefore, made with test data obtained from plain Portland cement mortar (water/cement ratio = 0.45), which was evaluated as 19.4 kJ/mol over the range 10–50°C (McCarter, 1995), and Portland cement mortars containing various supplementary cementitious materials (with a constant water/binder ratio = 0.55), which were reported in the range 16–30 kJ/mol (McCarter, 2000). The activation energy obtained in this study could therefore be considered to lie within the range of the anticipated values.
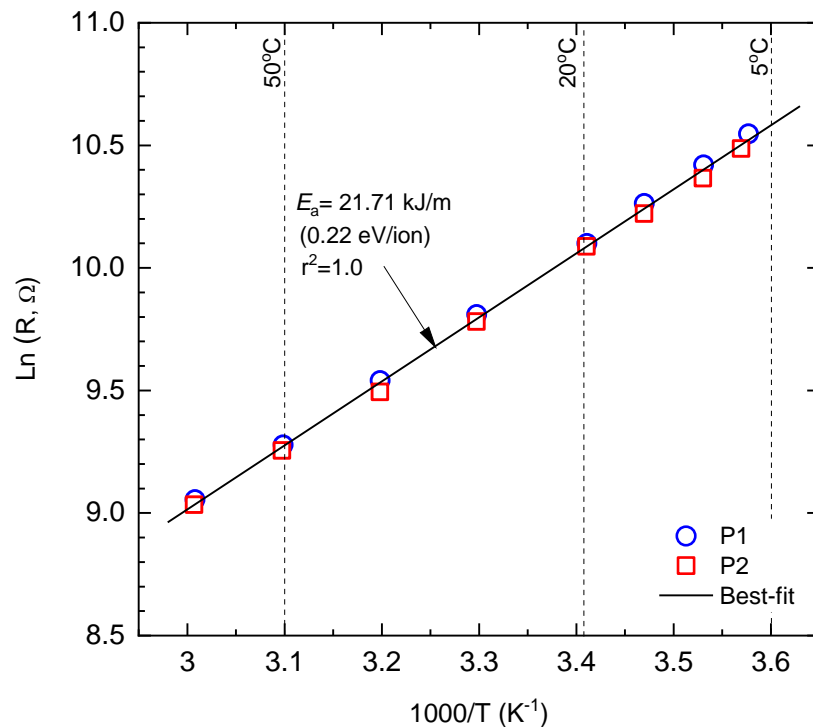
Figure 4.16: Variations in bulk resistance displayed in Figure 4.15(b) plotted in an Arrhenius format.

4.3.3 Temperature correction protocol

To demonstrate the value of this work package, the bulk resistance at different temperatures was used in equation 4.5 to correct the temperature effects.

$$R_x = R_y \, e^{\frac{E_a}{R_g}\left[\frac{1}{T_{k,x}} - \frac{1}{T_{k,y}}\right]} \qquad (4.5)$$

where R_x and R_y represent the bulk resistance at temperatures $T_{k,x}$ and $T_{k,y}$, respectively; E_a represents the activation energy for the conduction process (in this case = 21.7 kJ/mole); and R_g represents the gas constant (8.3141×10^{-3} kJ/mole/K).

From this equation, the bulk resistance value (R_y) of the ECC mix measured at a temperature $T_{k,y}$ was used to acquire an equivalent resistance (R_x) of the mix at temperature $T_{k,x}$. Since the E_a/R_g ratio is known, this allows for the measurements to be standardized to a reference temperature (in this case, taken as 25°C (298.15 K)).

Table 4.1 presents the measured bulk resistance (R_y) under varying temperatures and the equivalent resistance (R_x), which is displayed in Figure 4.17. It can be clearly seen that this temperature correction protocol can remove the temperature effect, from a fivefold difference over the temperature range of 6.5–60°C to a relatively constant equivalent resistance (approximately 10% difference).

Table 4.1: Measured and equivalent bulk resistance to correct the temperature effects.

$T_{k,y}$ (°C)	$T_{k,x}$ (°C)	R_y (kΩ)	R_x (kΩ)
6.5	25	51.04	28.60
10	25	44.63	28.07
15	25	39.11	28.86
20	25	32.93	28.36
30	25	24.26	28.03
40	25	19.64	29.88
50	25	15.29	30.10
60	25	12.44	31.21

Notes: 25°C = 298.15 K (for conversion, 0°C = 273.15 K).
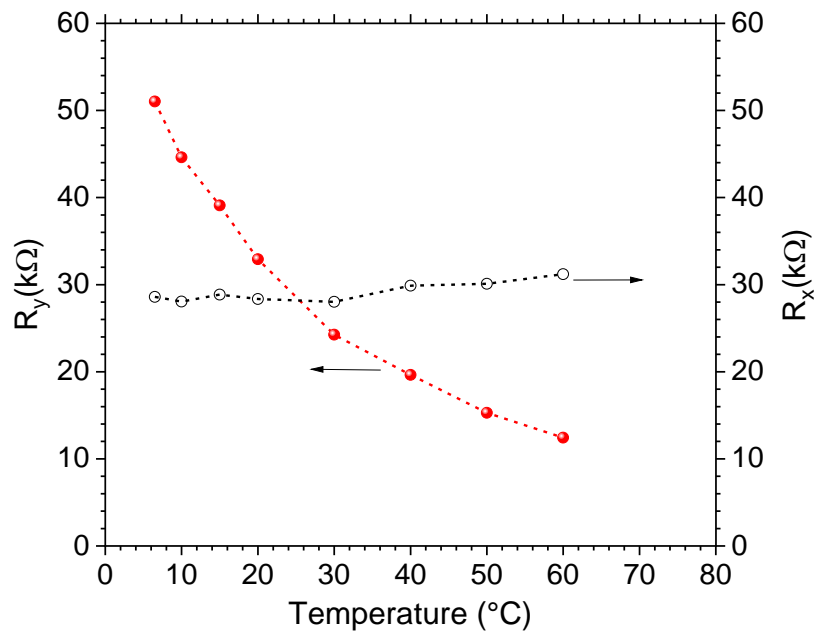
Figure 4.17: Comparison of measured bulk resistance (R_y) and equivalent resistance (R_x) after the removal of the temperature effects.

4.3.4 Equivalent circuit modelling

The impedance response obtained in Figure 4.15(a) was modelled using equivalent electrical circuits. The equivalent electrical circuits for the ECC mix displayed in Figure 4.10(b) were simplified by not taking into consideration the electronic conduction through the unburnt carbon. Therefore, the equivalent electrical circuits displayed in Figure 4.10(a) were used in this section.

Figure 4.18(a) displays the measured and simulated impedance response of specimen P1 under varying temperatures (6.5–60°C), with the modelled circuit parameters at different temperatures displayed in Figure 4.18(b). The solid lines represent the simulated curves while the markers represent the measured response, with the frequency increasing from right-to-left across the curves. The measured and simulated plots illustrate good agreement. It is evident from Figures 4.18(a) and (b) that an increasing the temperature causes a decrease in the bulk impedance, thereby resulting in a reduction in the diameter of the bulk arc. Consider for example, the resistance, R_{cp}, of specimen P1 which decreases from 50 kΩ at 6.5°C to 12 kΩ at 60°C. It is also obvious that the $C_{o,sm}$ and p_{sm} slightly increases with increasing the temperature (See Figure 4.18(b) or Table A-4 in Appendix A).
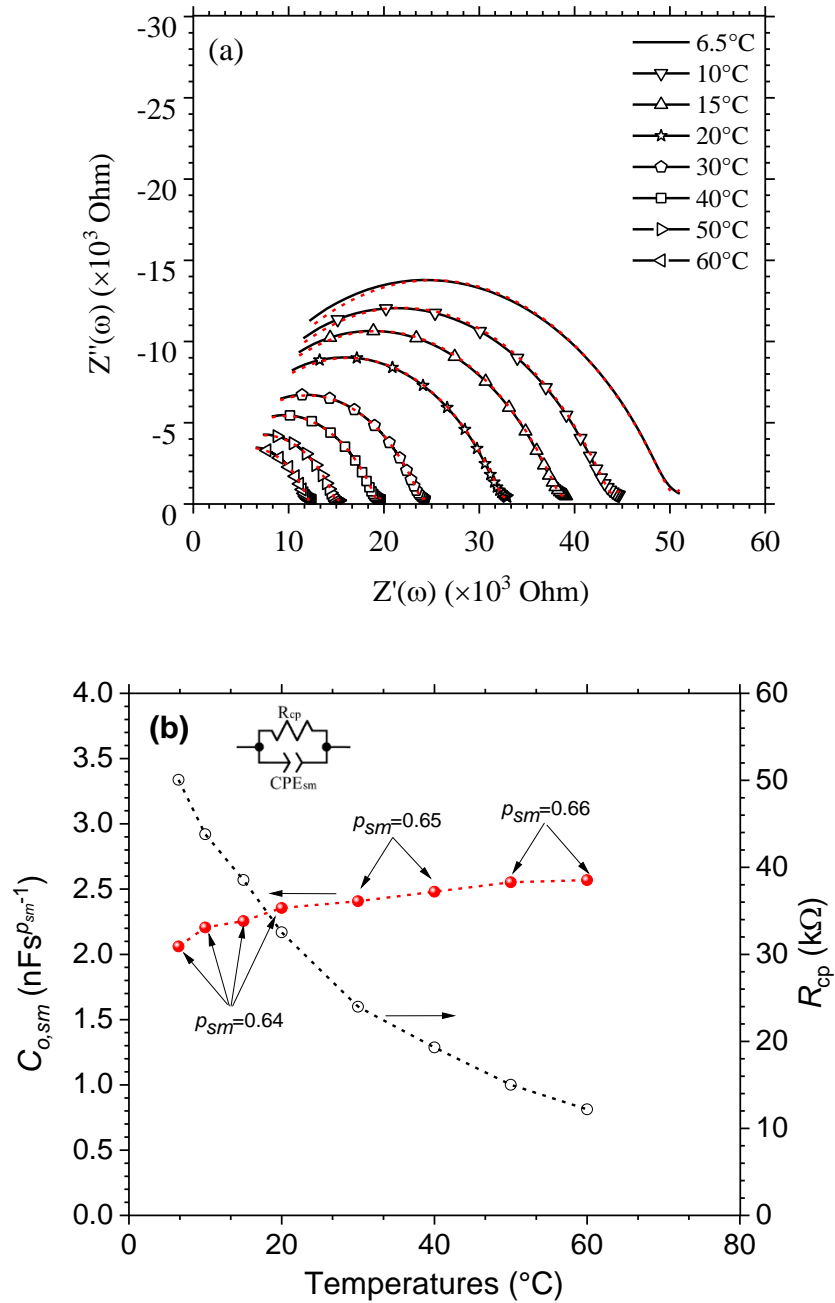
Figure 4.18: (a) Measured and simulated representative responses for specimen P1 under varying temperatures; and (b) the variations in circuit parameters for specimen P1.

4.4 Conclusions

This chapter provides complementary information on the influence of on-going hydration and temperature on the electrical properties of an Engineered Cementitious Composite (ECC) in relation to the use of the ECC as a sensor for monitoring purposes. The following conclusions can be drawn from the work presented:

- A distinct impedance response was observed at all stages during the hydration process, comprising a low-frequency spur, a weak intermediate "plateau" region and a high-frequency bulk arc. Increasing hydration is shown to result in an overall increase in impedance and a better definition of the high-frequency arc, which reflects the development of the pore structure with time. A progressive increase in bulk resistance is evident during the entire curing period, with almost a tenfold increase from 7 days to 180 days of curing, which reflects on-going hydration and pozzolanic reaction.

- Dispersion in polarization is shown to result in a reduction in relative permittivity with increasing frequency and a corresponding increase in conductivity. Ongoing hydration and pozzolanic reactions are shown to have a negligible influence on the relative permittivity at the upper frequency limit (i.e., 1MHz).

- A frequency domain presentation highlighted the dispersive behaviour of the composite. It is postulated that the dominant mechanisms responsible for the dispersion are electrode polarization processes operating at frequencies <1kHz, double-layer polarization, and Maxwell-Wagner interfacial polarization, operating mainly at higher frequencies.

- The temporal decrease in conductivity was modelled using a general equation. An aging factor was provided to calculate conductivity versus time response. The aging value (exponent N) of the ECC was obtained as 0.73 compared with the PC mix, which was 0.25.

- An electrical model involving resistive and constant phase circuit (CPE) elements was developed which could simulate the ECC matrix (the bulk response and the electrode/sample interface). The CPE was used instead of the capacitor to take into consideration the dispersion in capacitance with frequency.

- The electrical model of ECC shows that the resistance 'R_{cp}' representing the continuous capillary pore network increases with an increase in curing age, increasing from ~1 kΩ at 14 days of curing to ~6 kΩ at 90 days (a sixfold increase) and ~12 kΩ at 180 days (a twelvefold increase) due to the ongoing hydration and pozzolanic reaction. The '$CPE-T_{sm}$' parameter is shown to display an almost threefold increase from 14 days to 180 days of curing, whereas the exponent '$CPE-P_{sm}$' parameter is shown to decrease with time, from 0.84 at 14 days to 0.71 at 180 days of curing, causing further depression of the semicircle arc below the real ($Z'(\omega)$) axis with time.

- It was observed that the un-burnt carbon/matrix interface plays a vital role in the response. The resistance at the interface of the carbon particle and the cement matrix 'R_{ci}' increases with increasing curing age and increases almost seven-folds from 14 days to 180 days of curing. This is due to a decrease in interface size between the capillary pore and the un-burnt carbon, forcing the same current to flow through a smaller area. Furthermore, the capacitive component of the interface 'CPE-T_{ci}' decreases with time. This decrease could be attributed to some of the isolated un-burnt carbon, which no longer contributes to the capacitance, and/or the decrease in the interface size between the capillary pore and the un-burnt carbon with time, which causes less capacitance of the un-burnt carbon.

- The ECC mix displayed a higher formation factor than the equivalent mortar mix for periods > 42 days. The formation factor of the ECC mix at 180 days was approximately twice that of the mortar mix.

- Based on the durability considerations using the formation factor, it is interesting to note that whilst the mortar mix displays a higher value, it is out-ranked by the ECC mix in the longer term (i.e., > 42 days).

- The work has highlighted that the resistive and reactive components of the complex impedance both display an inverse relationship with temperature. When presented in an Arrhenius format, the bulk resistance displayed a linear response over the entire temperature range studied, and the activation energy, E_a for electrical conduction was evaluated as 21.7 kJ/mol (0.22 eV/ion). In addition, a temperature correction protocol was used to remove the temperature effects by standardizing the resistance values to a reference temperature.

- Equivalent circuit modelling was also used to simulate the temperature effects on the ECC matrix. It was found that the resistance 'R_{cp}' decreases with increasing temperature. It was also found that increasing the temperature causes an increase in the values of the two CPE parameters ('$C_{o,sm}$' and 'p_{sm}').

5 Potential of ECC for Strain and Damage Sensing

5.1 Introduction

This chapter presents the mechanical and electrical properties of two series of Engineered Cementitious Composite (ECC) dog-bone shaped specimens under direct tensile tests. The two series of specimens were fabricated from different batches of the same mix composition. Despite the similarity, the crack widths of these two series of specimens were notably different (the first series generally exhibiting smaller crack widths than the second series). Attention is thus focused on studying the influence of crack widths on the piezo-impedance electrical response of the composite, with an outlook on how to exploit this cement composite for strain/damage sensing. As in Chapter 4, the obtained impedance data over the frequency range 20 Hz–1 MHz are presented in various formats of data presentation (i.e., Nyquist format and both the time and frequency domains) to provide details on the underlying mechanisms and to elucidate the nature of conduction and polarization processes. The results of which are also modelled using equivalent electric circuits to elucidate the underlying mechanisms. The crack patterns obtained from each specimen, from both visual observations and digital image correlation, are presented and discussed to provide explanations for the piezo-impedance response of the composite. It is worth noting that the influence of cement hydration was also investigated in parallel. Due to significant overlaps with those presented in Chapter 4, the results of this part are thus presented in Appendix B (Figures B-1 and B-2).

5.2 Mechanical properties: tensile stress-strain response

5.2.1 Preliminaries

In this work, tensile tests were performed on two series of ECC samples of the same mix composition. The samples were produced from a different batch and tested at different curing times (the first series was tested on the 28th day of curing while the second was tested on the 180th day). Four dog-bone samples named T-ECC-S-DB1/DB2/DB3/DB4 were tested for the 1st series, and four dog-bone samples named T-ECC-L-DB1/DB2/DB3/DB4 were used for the 2nd series. Despite the similarity, it was noted that these two series of samples exhibited different crack patterns. The set that was tested on the 28th day has a smaller crack width compared to the set that was tested

on the 180th day, with a mean crack width of 56 µm for the 1st set and 81 µm for the 2nd set.
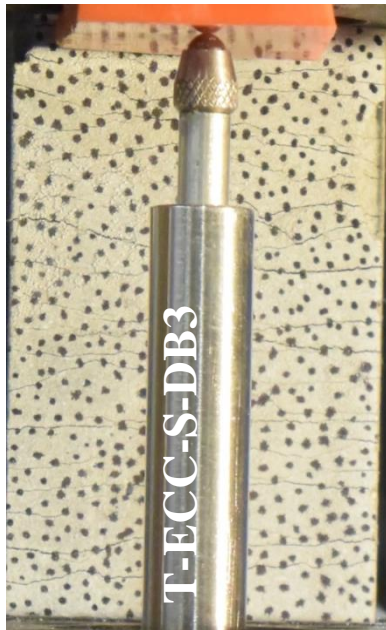
(a) 4.9% strain
Crack number = 16
Mean crack width = 65 µm
Max crack width = 120 µm
Min crack width = 40 µm

(b) 4% strain
Crack number = 15
Mean crack width = 47 µm
Max crack width = 150 µm
Min crack width = 20 µm

(c) 4% strain
Crack number = 11
Mean crack width = 60 µm
Max crack width = 110 µm
Min crack width = 20 µm

(d) 4.4% strain
Crack number = 12
Mean crack width = 103 µm
Max crack width = 160 µm
Min crack width = 70 µm

Figure 5.1: Crack images at failure of a) T-ECC-S-DB3; b) T-ECC-S-DB4; c) T-ECC-L-DB2; and d) T-ECC-L-DB3.

The tensile stresses and strains (f_t and ε_t, respectively) were calculated using the following equations:

$$f_t = \frac{P}{A} \tag{5.1}$$

$$\varepsilon_t = \frac{\Delta L}{L_0} \tag{5.2}$$

where P is the load recorded from the load cell mounted on the Instron test machine (in N); A is the cross-sectional area of the narrower (central) section of the dog-bone shape specimens (approximately 30×12 mm^2); ΔL is the length change of the sample during testing (in mm) and was determined from the average of two linear variable differential transducers (LVDTs) readings; and L_0 is the initial centre-to-centre distance of two lightweight plastic mounting blocks which were used to attach the two LVDTs (one on each side) at both ends of the bone-neck region (approximately 60 mm).

5.2.2 General Test Observations

Figures 5.2(a) and (b) display the tensile stress-strain responses for the two series of samples, with a summary of the results presented in Tables 5.1 and 5.2. It is evident from the figures that the ECC displays highly ductile tensile strain hardening behaviour, with individual curves of both series exhibiting notable fluctuations in stress with increasing strain. These fluctuations can be attributed primarily to the progressive development of micro-cracks when subjected to tensile stresses beyond the elastic range. The two series of specimens produce comparable mean tensile strain capacities and strengths, with Series 1 specimens producing 4.2% and 4.4 MPa, and Series 2 specimens displaying 4.6% and 4.7 MPa. This insignificant difference would indicate that curing time does not exert any appreciable influence on the tensile properties, although this could be masked by the variation between the two batches.
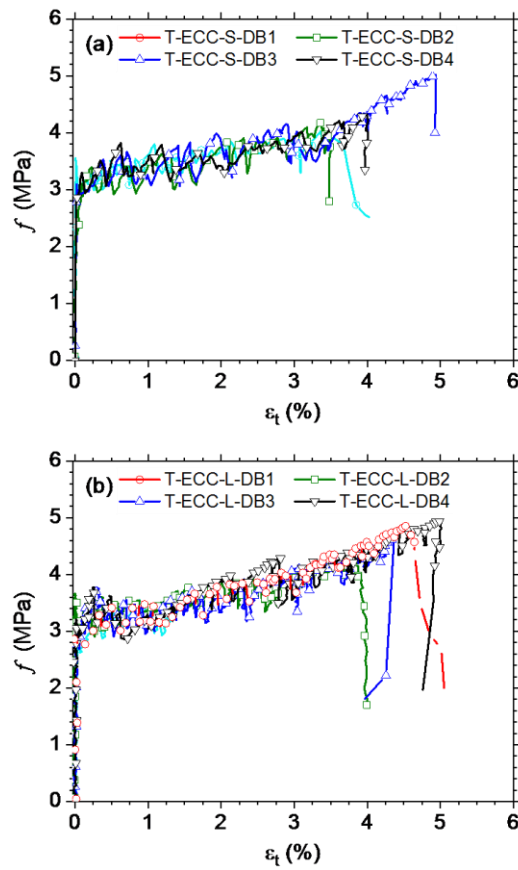
Figure 5.2: Tensile stress-strain responses from (a) Series 1; and (b) Series 2.

Table 5.1: Tensile properties from Series 1 (SD: standard deviation and CoV: coefficient of variation).

Specimen	Tensile strain capacity ε_{tu} (%)	Ultimate tensile strength, f_{tu} (MPa)	First crack strength, f_{tcr} (MPa)
T-ECC-S-DB1	4.5	4.0	3.6
T-ECC-S-DB2	3.5	4.1	2.7
T-ECC-S-DB3	4.9	5.0	3.3
T-ECC-S-DB4	4.0	4.3	3.0
Mean	4.2	4.4	3.2
SD	0.53	0.38	0.34
CoV (%)	14.4	10.4	12.3

Table 5.2: Tensile properties from Series 2 (SD: standard deviation and CoV: coefficient of variation)

Specimen	Tensile strain capacity ε_{tu} (%)	Ultimate tensile strength, f_{tu} (MPa)	First crack strength, f_{tcr} (MPa)
T-ECC-S-DB1	5.0	4.9	2.9
T-ECC-S-DB2	4.0	4.2	3.7
T-ECC-S-DB3	4.4	4.6	3.1
T-ECC-S-DB4	5.0	4.9	3.1
Mean	4.6	4.7	3.2
SD	0.42	0.29	0.3
CoV (%)	9.2	7.1	10.8

With reference to the failure crack patterns presented in Figures 5.1(a)–(d), detailed post-mortem crack analyses were undertaken using the ImageJ1 software to obtain the number and width of each individual micro-crack. To allow comparison, the crack width distributions measured at 4% strain and the corresponding best-fit lognormal distribution curves for T-ECC-S-DB3, T-ECC-S-DB4, T-ECC-L-DB2, and T-ECC-L-DB3 specimens are plotted in Figures 5.3(a–d), respectively. Figures 5.3(a) and (b) show that T-ECC-S-DB3 and T-ECC-S-DB4 had roughly the same number of cracks (15 cracks), with an average crack width of 50 µm at 4% strain, whereas T-ECC-L-DB2 and T-ECC-L-DB3 had 12 cracks, with average crack widths of 60 µm and 90 µm at 4% strain, respectively.
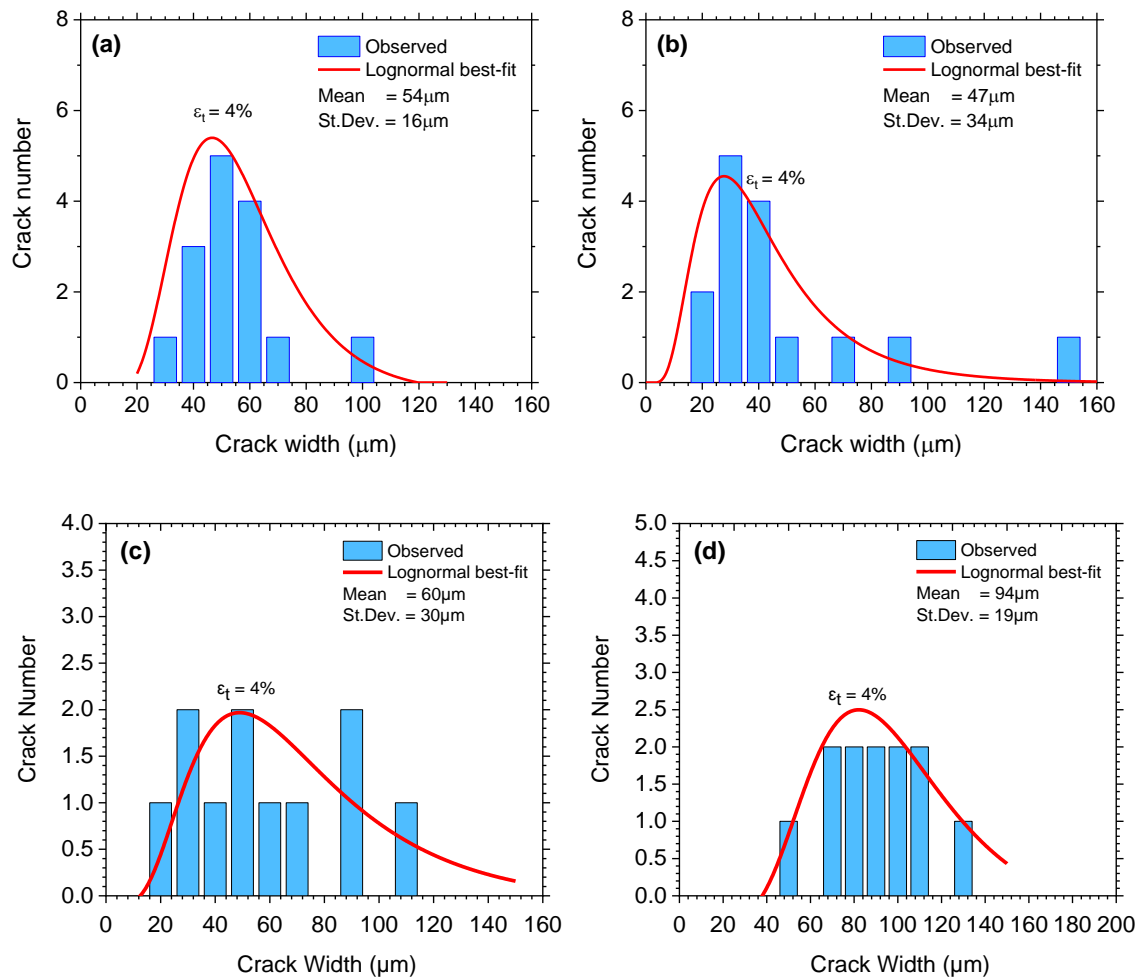
Figure 5.3: Observed and fitted crack width distribution at 4% strain for samples:
(a) T-ECC-S-DB3; (b) T-ECC-S-DB4; (c) T-ECC-L-DB2; and (d) T-ECC-L-DB3.

5.3 Results of Series 1 specimens

5.3.1 Complex impedance response

The complex impedance plots for Series 1 specimens during tensile loading conducted on the 28th day of curing are presented in Figures 5.4(a)–(d). Owing to the number of data points in each curve (i.e., measurements at 13 spot frequencies), the data markers have been connected with B-Splines and, for reasons of clarity, only the response at 1% strain increment is presented. At any stage of loading, cracked ECC displayed a classic response comprising an arc forming the left-hand-side of the plot and a spur forming the right-hand side, which is not dissimilar to the response observed in the hydration study (see Figure 4.2(a) and Figure B-1(a) in Appendix B). It is apparent from Figures 5.4(a)–(d) that tensile straining causes the entire response being gradually displaced to the right, indicating an overall increase in impedance with increasing strain. With reference

to Figures 5.5(a)–(b), this gradual increase is as a direct result of successive formation and widening of multiple micro-cracks (Wansom and Kanokkanchana, 2017), which have the effect of altering the conduction pathway within the composite, from a relatively straight (Figure 5.5(a)) to a more tortuous pathway (Figure 5.5(b)). Accordingly, as the tensile strain increases, this has the effect of reducing the continuity and increasing the circuitous path length, which increases the overall impedance of the ECC. Regarding Figure 5.5(b), conduction will occur via several possible mechanisms across the micro-crack comprising:

i. Conduction via a wavy un-cracked portion within the ECC matrix, occurring only when the micro-cracks have not fully developed;

ii. Conduction through ECC matrices in series, either through direct contact or through broken particles bridging the micro-cracks; and

iii. Conduction through the ECC matrix and PVA fibres in series. Whilst PVA fibres which, as a polymeric material, can be considered as non-conductive, surface conduction might still occur through the fibres bridging the microcracks as they could be coated with leached pore water or covered with broken fragments which were more conductive than the fibres themselves.

As illustrated in Figure 5.5(b), it is postulated that (i) had an effect of increasing the circuitous path length, while (ii) and (iii) had the effect of decreasing the available cross-sectional area for conduction at crack locations, all of which would have the effect of decreasing the conductivity and hence increasing the overall impedance with increasing strain. As depicted in the figure; at this stage, however, it is difficult to delineate the contribution from each pathway.

Another interesting feature which is apparent from Figures 5.4(a)–(d) relates to the definition of the high-frequency arc associated with the bulk response of the material including the micro-cracks. It is observed that the arc becomes more pronounced as the strain increases, indicating a shift in time constant to the frequency range under investigation as in the hydration study. Furthermore, Figures 5.4(a)–(d) also show that there is notable variation in impedance response during the loading process. Consider, for example, the impedance at the minimum point within the V-shaped valley at 2% strain, which were found to be: 15.5 kΩ for Sample 1, 21.7 kΩ for Sample 2, 21.9 kΩ for Sample 3, and 13.8 kΩ for Sample 4. This variation was expected and

would indicate the spatial difference in the distribution and width of micro-cracks; this will be discussed in section 5.3.4.
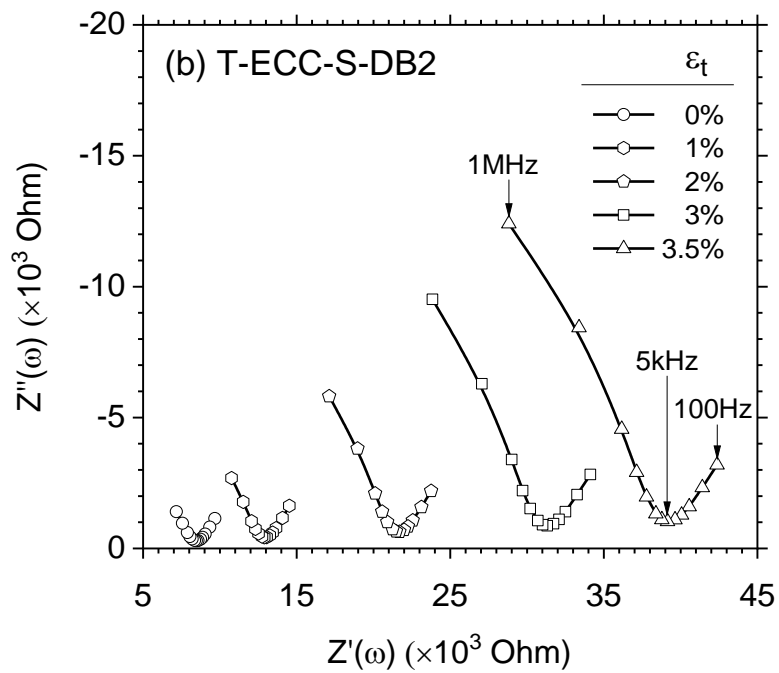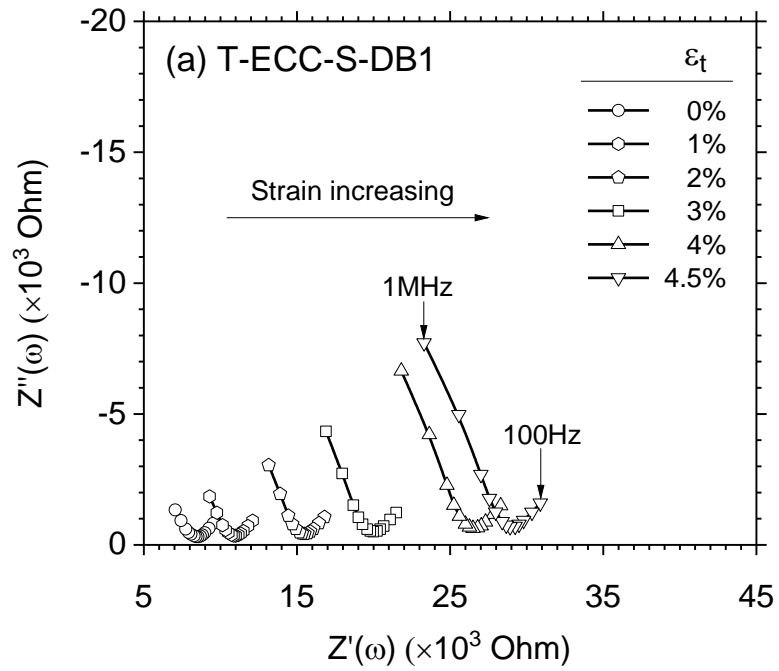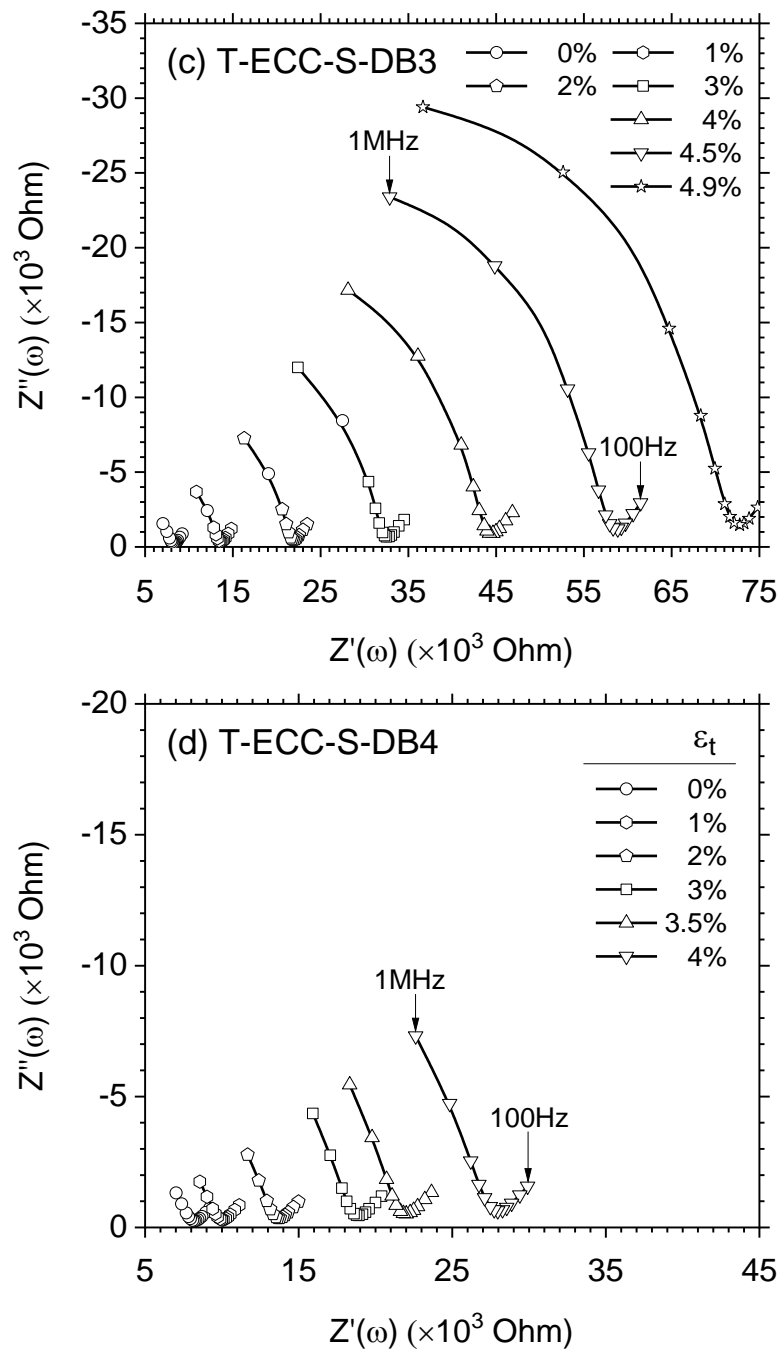
Figure 5.4: Variation in impedance response with tensile strain for specimens: (a) T-ECC-S-DB1; (b) T-ECC-S-DB2; (c) T-ECC-S-DB3; and (d) T-ECC-S-DB4.

Un-cracked matrix

$(\varepsilon_t = 0)$

Water-filled capillary pores

(a)

Matrix with partially
developed micro-cracks

Matrix with fully
developed micro-cracks

Direct contact

Fractured particles

Pore water
in crack

PVA fibres coated
by pore water

(b)
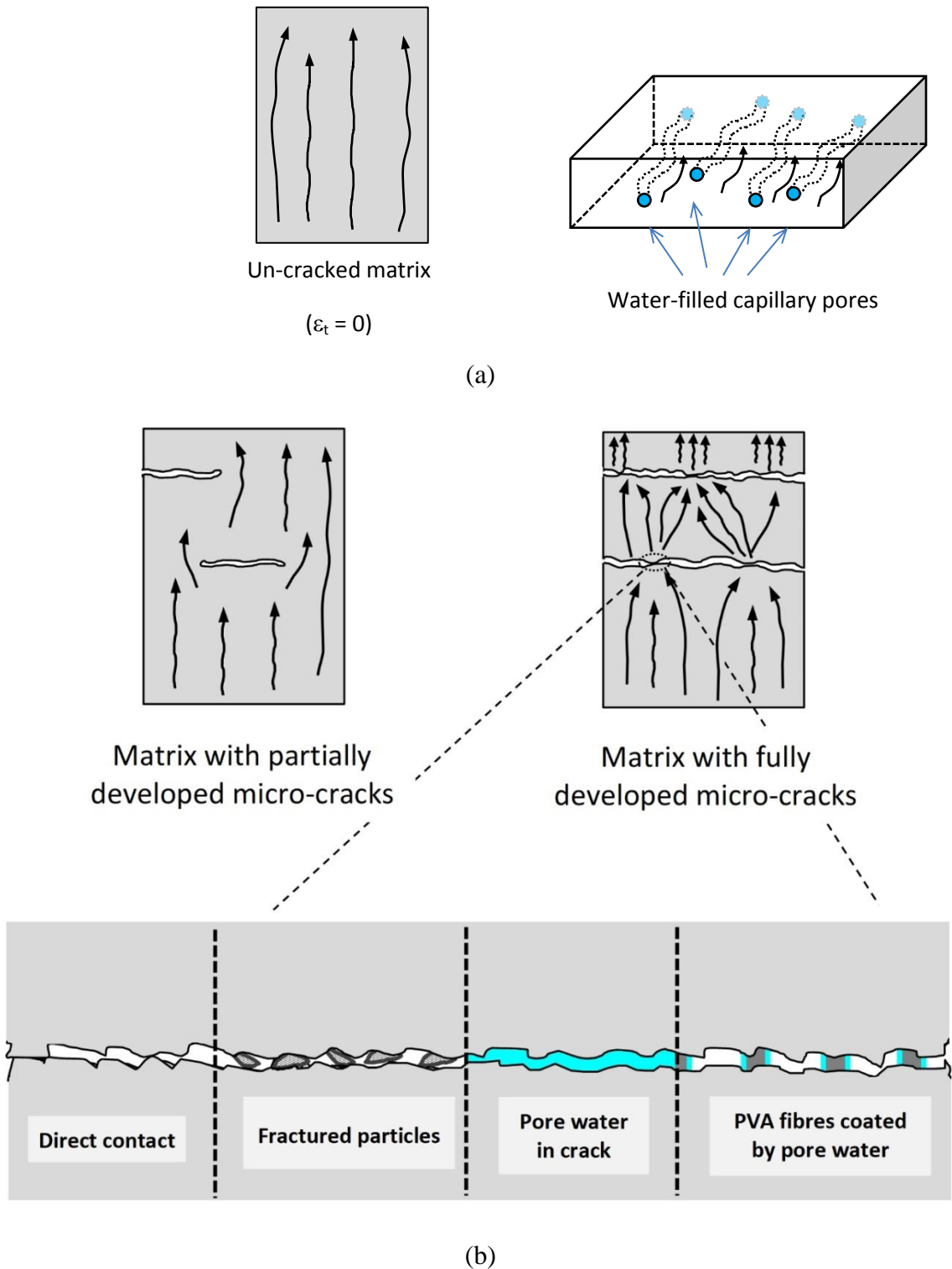
Figure 5.5: Schematic of possible conduction pathways in (a) un-cracked and
(b) cracked ECC matrix showing possible bridging pathways.

5.3.2 Relative permittivity and bulk conductivity

Figures 5.6(a)–(d) present the relative permittivity, which has been de-embedded from the impedance data using equation (3.3) stated in section 3.6, in the frequency domain with varying tensile strains and marked at every 1% increment of strain. In general terms, the trend in the relative permittivity plots is, in many respects, similar to the respective specimens in the hydration study (see Figure 4.4(a) and Figure B-1(c) in Appendix B), characterized by a reduction in relative permittivity with increasing frequency across the entire frequency range. As before, this is due to the relaxation of superimposed polarization mechanisms operative within the composite and the shift in time constant with increasing strain, which has the effect of shifting the relative permittivity curve to the left along the Z' axis toward the origin.

It is interesting to note that whilst the relative permittivity plots presented in Figure 4.4(a) and Figure B-1(c) in Appendix B all merge at frequencies >~200kHz, this is not the case for the plots presented in Figures 5.6(a)–(d) which display a progressive downward displacement with increasing strain across the entire frequency range, including high frequencies (i.e. > 200kHz). This can be associated with the progressive formation of micro-cracks within the ECC matrix; as the relative permittivity of the air-gap between two opposite cracked surfaces is ~1, multiple crack formation would have the effect of decreasing the overall polarizability of the system. To understand this aspect, consider the idealised system presented in Figure 5.7(a) comprising the saturated ECC matrix, and a crack comprising an air-gap and a crack-bridging pathway. The bridging pathway would represent all the possible pathways presented in Figure 5.5(b), so could be regarded as a *smeared* contribution. Given that the micro-cracks are, in essence, connected in series with the bulk ECC matrix, the permittivity of the micro-cracks could be estimated by the mathematical mixing law (Reynolds and Hough, 1957),

$$\frac{\phi_{\mathrm{r,t}}}{\kappa_{\mathrm{r,t}}} = \frac{\phi_{\mathrm{cr}}}{\kappa_{\mathrm{cr}}} + \frac{\phi_{\mathrm{r,i}}}{\kappa_{\mathrm{r,i}}} \tag{5.3}$$

with $\kappa_{\mathrm{r,t}}$ representing the bulk relative permittivity of the composite at strain ε_{t} after the start of the test, κ_{cr} representing the average relative permittivity of the micro-cracks, and $\kappa_{\mathrm{r,i}}$ is the bulk relative permittivity of the composite at the start of the test (i.e., $\varepsilon_{\mathrm{t}} = 0$). Both $\kappa_{\mathrm{r,t}}$ and $\kappa_{\mathrm{r,i}}$ were evaluated at the upper frequency limit which, in the present study, is 1MHz. With reference to the system displayed in Figure 5.7(a), the

total volume at strain ε_t after the start of the test is given by $\phi_{r,t} = \phi_{r,i} + \phi_{cr}$, where $\phi_{r,i}$ is the initial volume at the start of the test and ϕ_{cr} is volume fraction of the micro-cracks at strain, ε_t.

Figure 5.7(b) presents the average permittivity of the micro-cracks computed using Equation 5.3 at discrete tensile strain levels. The results show that the value of the apparent permittivity of the micro-cracks is consistently higher than that of air ($\approx$1), indicating the presence of other materials within the space between two micro-crack surfaces. The plots also display variations in calculated permittivity values, with a general decreasing trend with increasing tensile strain up to ~4% where the permittivity plateaus at ~4. The best-fit power equation was added to provide an alternative means of predicting the tensile strain in a fully saturated system from permittivity measurements. The variation in permittivity would indicate the spatial distribution in the number of physical pathways across the crack (see Figure 5.5(b)), whilst the reduction in permittivity with increasing strain is indicative of their temporal change during the loading process.
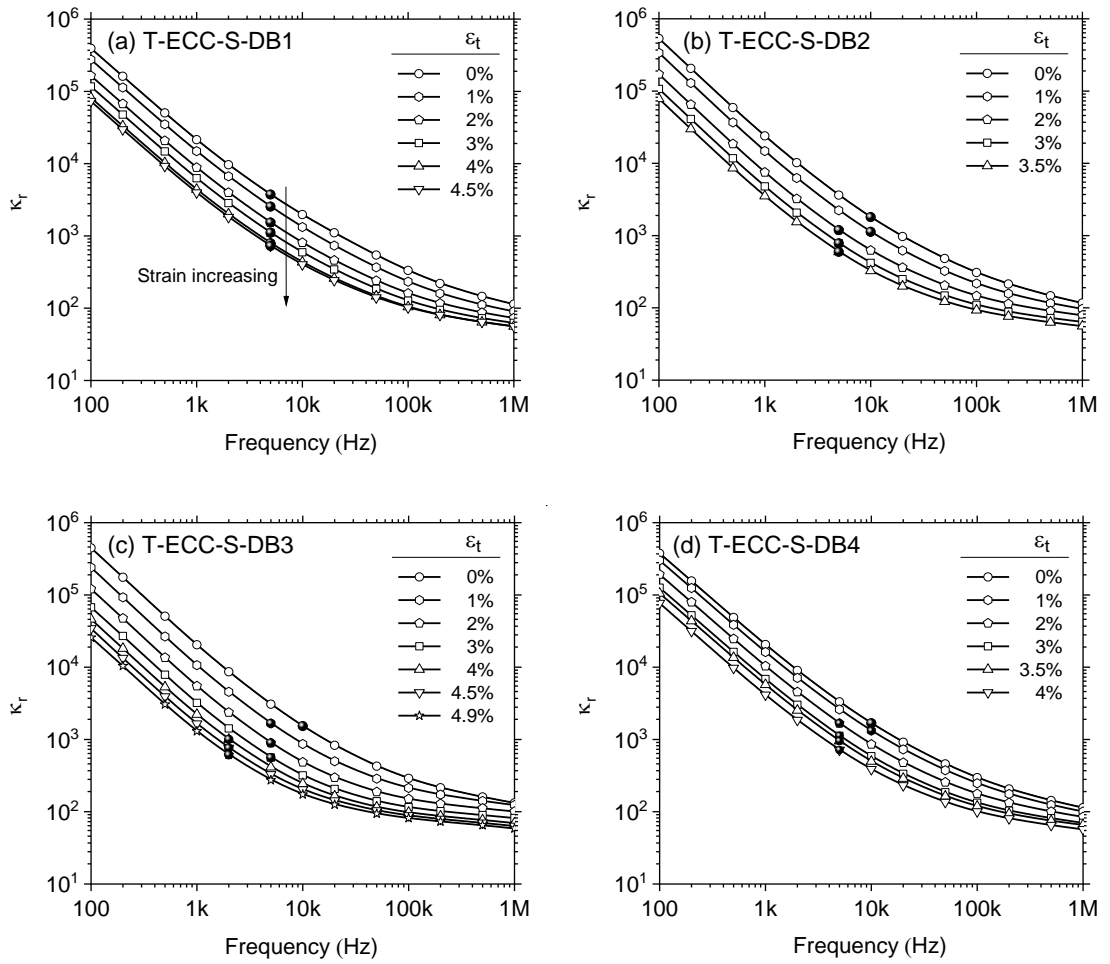
Figure 5.6: Relative permittivity versus frequency at selected strain levels for specimens: (a) T-ECC-S-DB1; (b) T-ECC-S-DB2; (c) T-ECC-S-DB3; and (d) T-ECC-S-DB4. *Note: The cusp frequency is presented in solid marker.
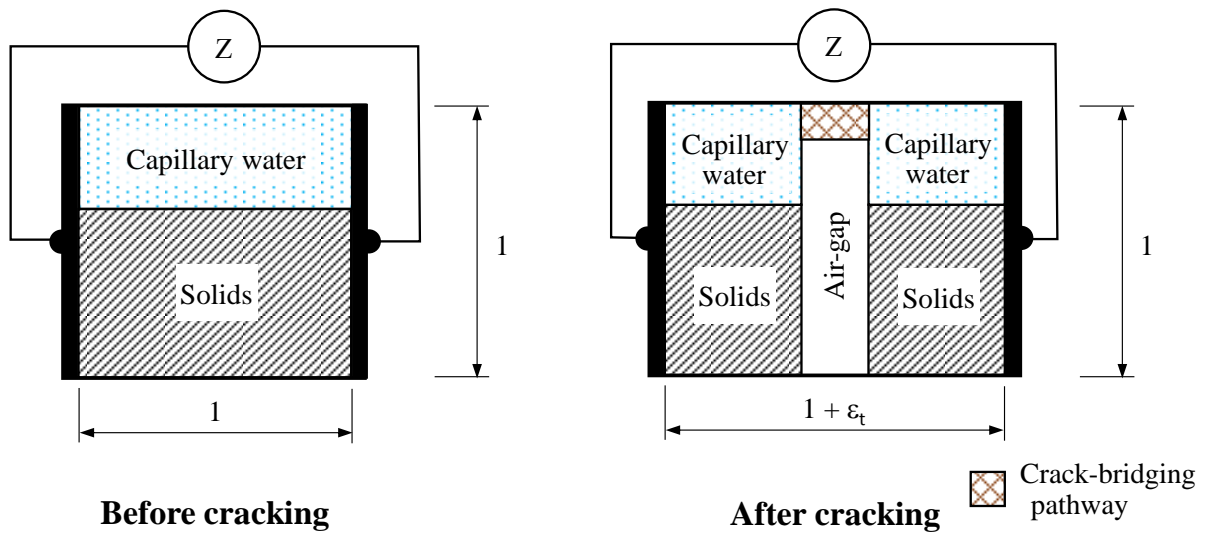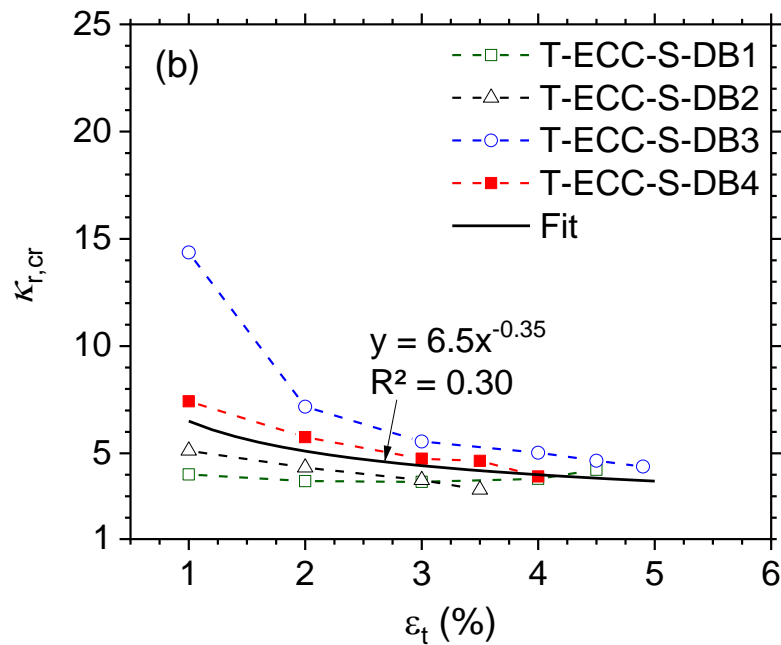
Figure 5.7: (a) Idealized representation of ECC before and after cracking; and (b) variation in relative permittivity of the micro-cracks assuming a series mixing law (equation (5.3)).

To further highlight the influence of crack formation on the bulk electrical properties of cracked ECC, the bulk conductivity of specimens T-ECC-S-(DB1-DB4) at varying strains is presented in the frequency domain in Figures 5.8(a)–(d). As before, owing to the relaxation of the polarisation mechanisms operative within the ECC matrix, the conductivity gradually increases with frequency across the entire frequency range.

Tensile straining is shown to result in a downward, parallel displacement of the bulk conductivity curves, resembling the trend displayed in Figure 4.6(a) and Figure B-1(d) in Appendix B. This is as a direct result of the formation of micro-cracks with increasing load rather than pore refinement due to hydration, as the duration of the tensile test is short (less than 10 min). As tensile strain increases, micro-cracks form progressively within the ECC matrix and cause a reduction in conductivity with increasing strain.
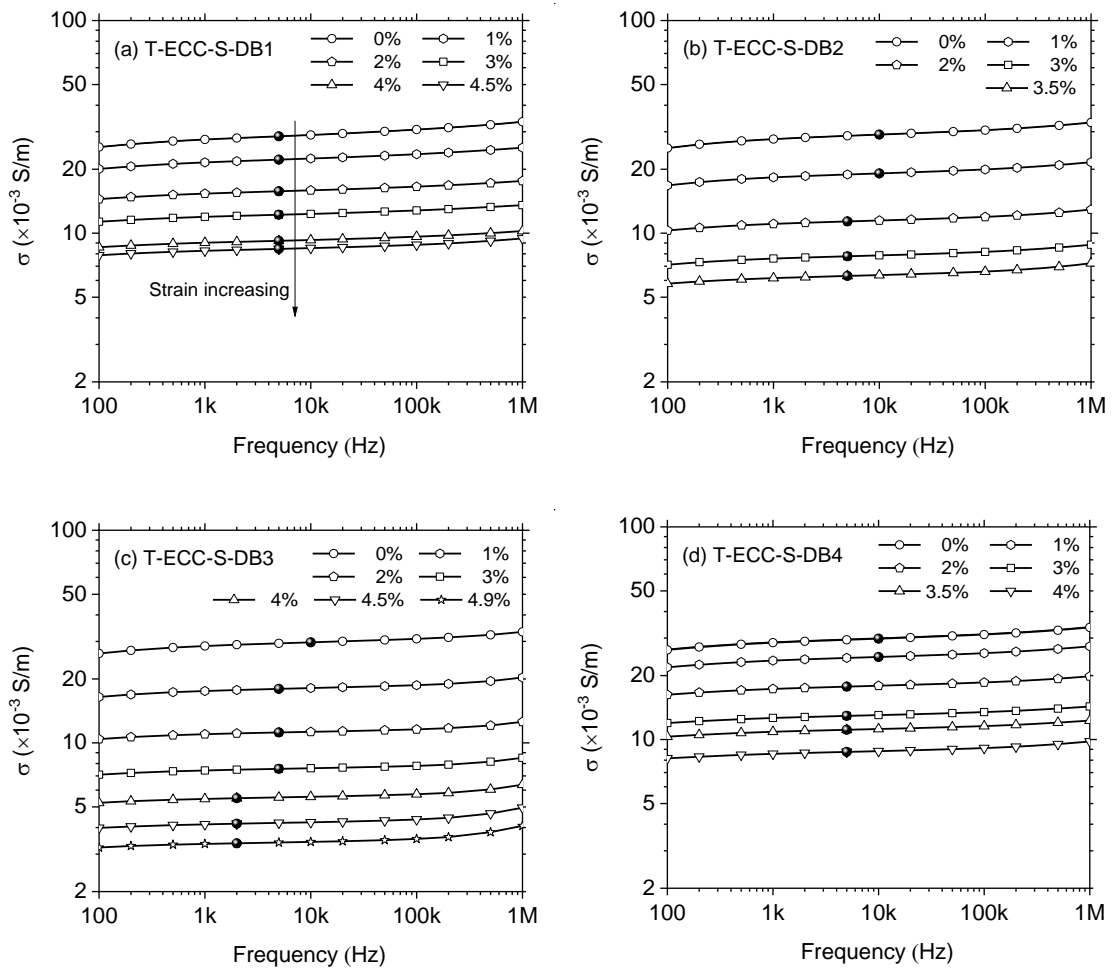
Figure 5.8: Conductivity versus frequency response under tensile load for specimens: (a) T-ECC-S-DB1; (b) T-ECC-S-DB2; (c) T-ECC-S-DB3; and (d) T-ECC-S-DB4. *Note: The cusp frequency is highlighted by a solid marker.

5.3.3 Fractional Change in Resistivity and Gauge Factor

To highlight the sensing capability of the composite, the conductivity of specimen T-ECC-S-DB2 is, for illustrative purposes, plotted against the tensile strain in Figure 5.9(a) together with the corresponding stress-strain relation. The conductivity is

presented at 13 spot frequencies (i.e., 100 Hz, 200 Hz, 500 Hz, 1 kHz, 2 kHz, 5 kHz, 10 kHz, 20 kHz, 50 kHz, 100 kHz, 200 kHz, 500 kHz, and 1 MHz) and the response near to the cusp point frequency, f_c, (5 kHz) is highlighted with data markers. In all curves, only every 10th data marker is highlighted for reasons of clarity. This figure clearly shows the dependence of bulk conductivity on both tensile strain and test frequency. As the strain increases to ~0.15%, a reduction in conductivity is evident as micro-cracks begin to develop within the ECC matrix, and the dominant conduction path at this stage would be via the un-cracked portion. This is then followed by a rapid reduction in conductivity with increasing strain, resulting in approximately a fivefold decrease in value. To investigate the sensitivity of the composite to mechanical strain, the bulk conductivity, $\sigma(\omega)$, is converted to its reciprocal (bulk resistivity, $\rho(\omega)$) and then used to calculate the fractional change in resistivity (FCR), which is defined as (Wen and Chung, 2003; Ranade *et al.*, 2014; Han *et al.*, 2015; Chia and Huang, 2017; Ozbulut *et al.*, 2018; Yang *et al.*, 2018; Yoo *et al.*, 2019),

$$FCR = \frac{\rho_t - \rho_i}{\rho_i} \tag{5.4}$$

where, ρ_t is the bulk resistivity at strain ε_t after the start of the test and ρ_i is the initial bulk resistivity (i.e., at zero strain).

Figure 5.9(b) presents the FCR values for the four dog-bone specimens over the entire frequency range, plotted against the fractional change in dimension (or strain), together with the stress-strain response measured from individual dog-bone specimens. As before, for reasons of clarity, only the 10th data marker is highlighted in all curves, and the FCR is presented to highlight its sensitivity to frequency. It is interesting to note from the figure that by presenting the resistivity data in a dimensionless format (viz., the fractional change in resistivity versus the fractional change in dimension), this virtually removes the dependence of FCR on frequency and all the resistivity curves collapse onto a unique curve. It is evident that all specimens exhibit a quasi-linear increase in FCR with strain, with a notable increase in slope with increasing strain. The slope in specimen T-ECC-S-DB3 is shown to increase more appreciably at strain levels > ~3%, which coincides with the increase in the post-cracking stiffness shown in the figure reflecting the slip hardening behaviour resulting from abrasion damage on the fibre surfaces as the fibres are pulled out from the ECC matrix (Redon et al., 2001). This figure also indicates that the FCR of specimens T-ECC-S-DB2 and T-ECC-S-DB3 is very similar and consistently greater than the other two counterparts, which also display

similarity in response. The FCR values at 4% strain range between 2.4 and 4.2, which are comparable to the values reported by Ranade et al. (2014) for the high-volume fly-ash ECC mix and are lower than those for the moderate-volume fly-ash ECC mix reported in the same paper.

By plotting the FCR against the strain as in Figure 5.9(b), distinct regions can be delineated in Figure 5.9(c) and denoted I–IV: (I) up to ~0.3%; (II): 0.3%-1%; (III): 1%-3%; and (IV): >3%, with the slope values highlighted. Considering the variations in FCR during the strain-hardening discussed above, it is interesting to note that this is not evident in the stress-strain responses of the four dog-bone specimens presented in Figure 5.9(b), with all specimens displaying a comparable overall stiffness during the strain-hardening. As the electrical response of the specimens is affected by the presence of the micro-cracks, the apparent difference may thus originate from the distribution of the micro-cracks during loading. Attention is thus focused on the number and width of the individual micro-cracks during loading.
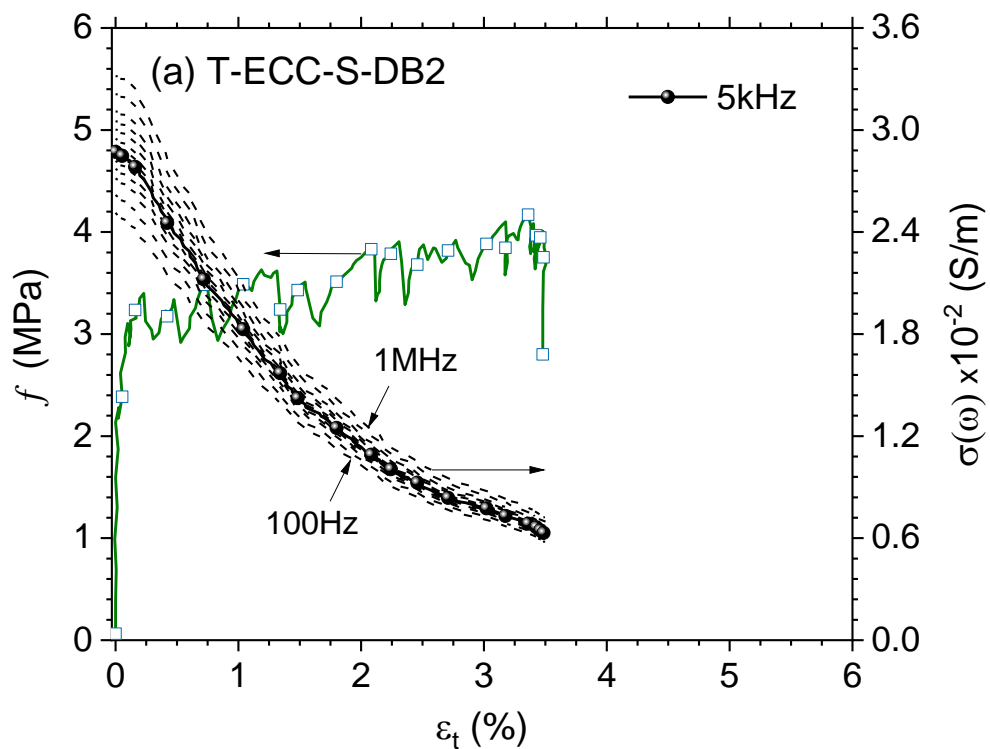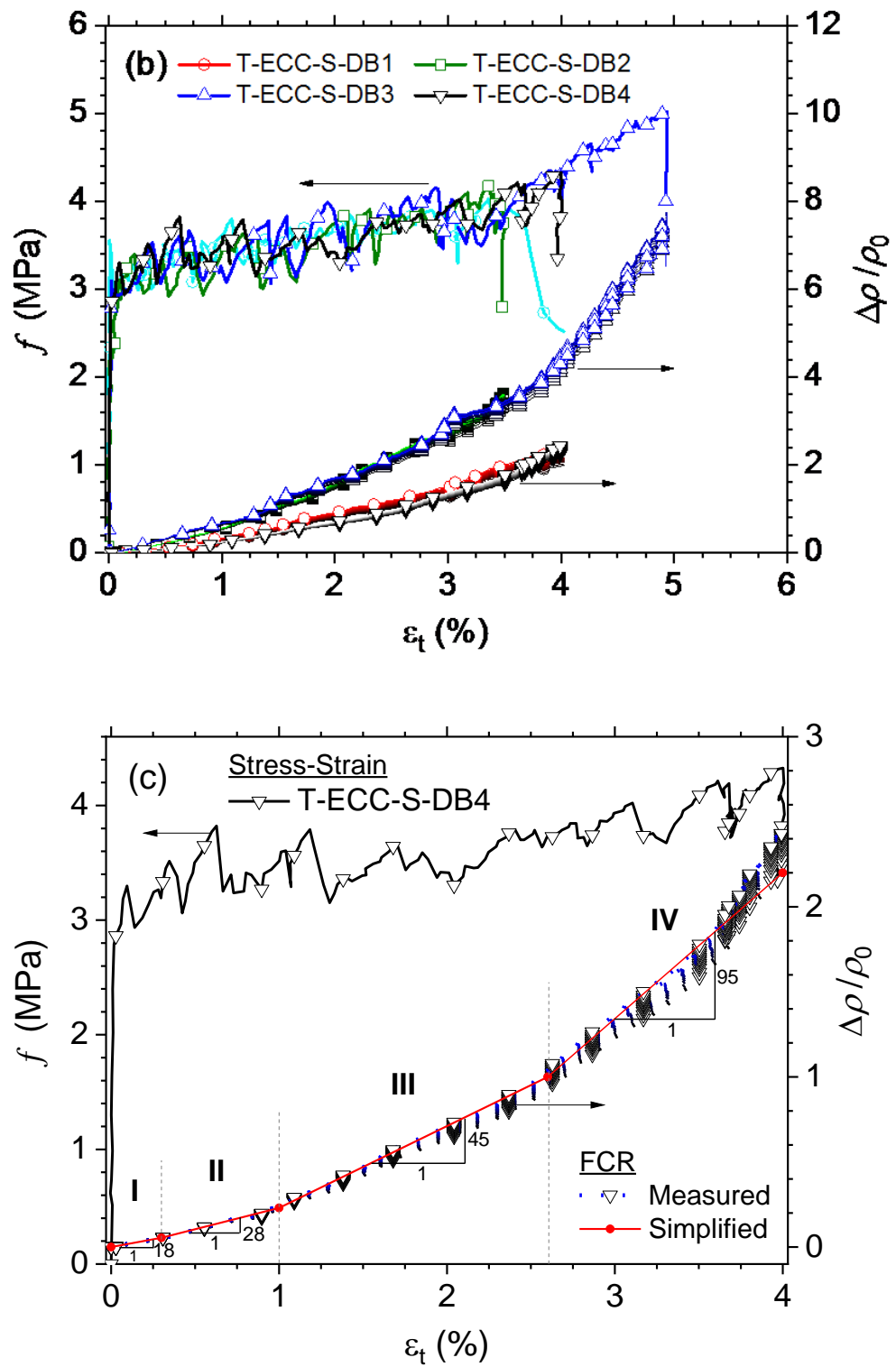
Figure 5.9: (a) Variation in the bulk conductivity of specimen T-ECC-S-DB2 under varying tensile strains; (b) the fractional change in resistivity for specimens T-ECC-S-(DB1–DB4) under varying tensile strains; and (c) representation of the fractional change in resistivity of specimen T-ECC-S-DB4 into contiguous linear segments. All curves are plotted alongside the stress-strain response.

Table 5.3: Calculated gauge factors (GF) at various strain levels for Series 1 specimens.

Specimen	Bulk resistivity at $\varepsilon = 0\%$, ρ (Ω-m)	GF_I $\varepsilon_t<0.3\%$	GF_{II} $0.3\%<\varepsilon_t<1\%$	GF_{III} $1\%<\varepsilon_t<3\%$	GF_{IV} $\varepsilon_t > 3\%$
T-ECC-S-DB1	8535	15	36	53	92
T-ECC-S-DB2	8467	30	68	102	203
T-ECC-S-DB3	8256	50	72	103	$141^{\&}$, $313^{\#}$
T-ECC-S-DB4$	8203	18	28	45^{*}	95
Mean	8365	28	51	76	133
SD	139.5	15.9	22.2	31.1	51.9
CoV (%)	1.9	56.2	43.6	41.0	39.1

Notes: $: see Figure 5.10(c); *: ε_t between 1% and 2.6%; &: ε_t between 3% and 4% and marks the quantity used in the statistical calculation; #$\varepsilon_t > 4\%$. SD: standard deviation and CoV: coefficient of variation.

5.3.4 Crack Mapping during Tensile Loading

To corroborate electrical measurements regarding micro-cracking, Figures 5.10(a) and 5.11(a) present the representative longitudinal strain maps for, respectively, specimens T-ECC-S-DB3 and T-ECC-S-DB4 obtained using the DIC technique at every 0.5% strain increment. The best-fit lognormal distribution curves at 1% strain increment for both specimens are plotted in Figures 5.10(b) and 5.11(b), respectively to aid data interpretation.

Figure 5.10(a) displays an increasing number of near-parallel bands of localized strain with a relatively constant colour range over the initial 3% strain, followed by a similar pattern of strain maps but with a notable increase in value. It could be inferred from the evolution of the crack pattern obtained that the increase in FCR for specimen T-ECC-DB3 over the initial 3% strain is attributed primarily to micro-crack formation, whereas

the increase in both values thereafter is due to the widening of existing micro-cracks. This trend agrees well with the crack width distribution shown in Figure 5.10(b).

With reference to the evolution of the crack pattern of specimen T-ECC-DB4 (see Figures 5.11 (a)), it is evident that micro-crack formation occurs constantly throughout the loading, from 2 fully-developed micro-cracks at 1% strain to 15 cracks at 4% strain, which is also accompanied by a notable increase in the average crack width. This would indicate that the predominant mechanism responsible for the increase in FCR presented previously in Figure 5.9(b) is due to progressive crack formation, with a significant contribution of crack width increase at strain levels >3%. It is interesting to note from both specimens that although they had more or less the same crack number (~15 cracks), with an average crack width of ~50 μm at 4% strain, these two specimens attained different FCR values, with those of specimen T-ECC-S-DB3 being approximately twice that of specimen T-ECC-S-DB4.
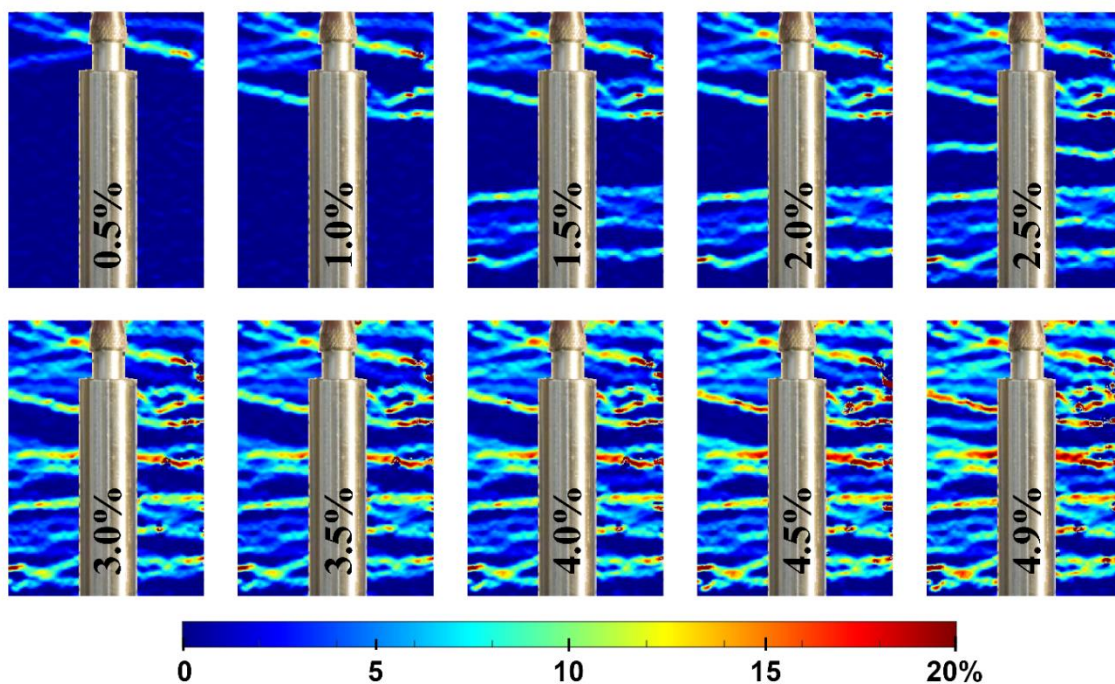
(a)
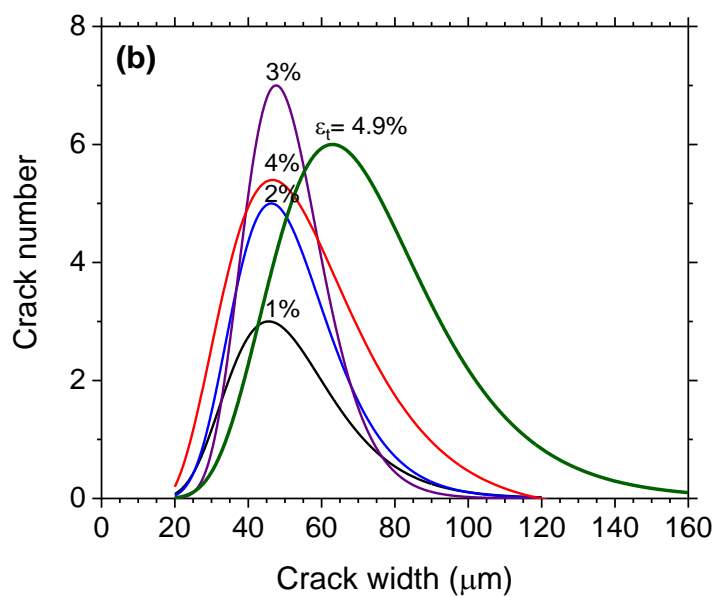
Figure 5.10: (a) Progressive development of longitudinal strains on the front face of specimen T-ECC-S-DB3; (b) The best-fit lognormal distribution curves at 1% strain increment for specimen T-ECC-S-DB3.
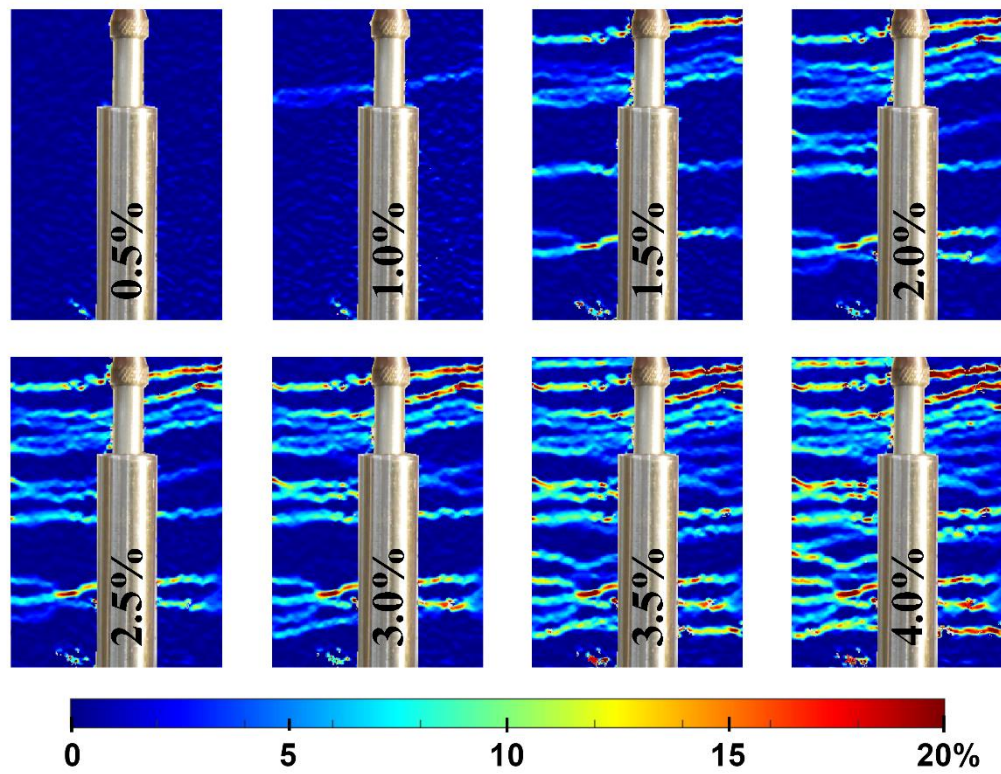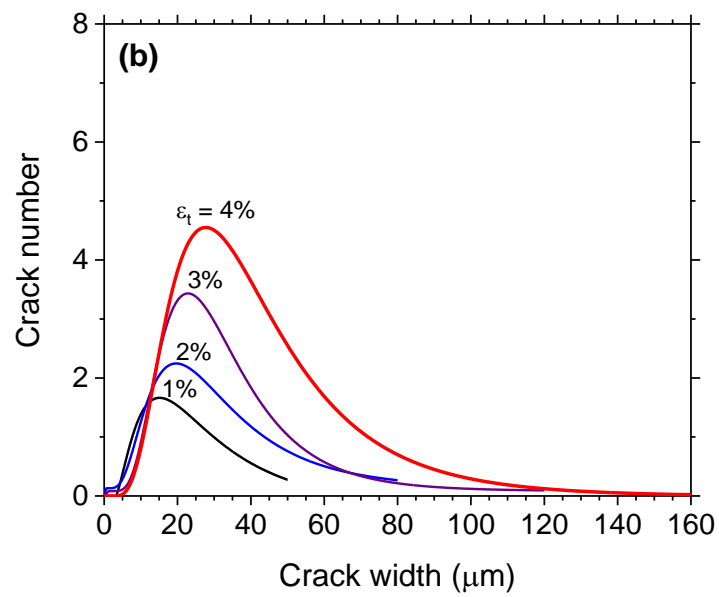
Figure 5.11: (a) Progressive development of longitudinal strains on the front face of specimen T-ECC-S-DB4; (b) The best-fit lognormal distribution curves at 1% strain increment for specimen T-ECC-S-DB4.

5.4 Results of Series 2 specimens

5.4.1 Complex impedance response

The complex impedance responses for Series 2 specimens during tensile testing on the 180th day of curing are presented in Figures 5.12(a)–(d). As before, the response at 1% increment has been presented for reasons of clarity. It can be clearly seen that the ECC during the tensile loading displayed a similar response to that observed in the piezo-impedance response presented in Figures 5.4(a)–(d) with a gradual displacement of the impedance response to the right-hand-side with increasing strain across the entire frequency range. However, the displacement here was higher in the 2nd set of the ECC results with a mean increase from ~22 kΩ at 0% strain to ~187 kΩ at failure compared to the 1st set of the ECC results presented in Figures 5.4(a)–(d), with a mean increase from ~8 kΩ at 0% strain to ~56 kΩ at failure. This could be attributed to the formation of larger crack width and a reduction in water bridging the micro-cracks, due to the prolonged curing period in this series of specimens. Moreover, tensile straining also resulted in a better definition of the bulk response arc of the 2nd set of the ECC compared to 1st set of the ECC presented in Figures 5.4(a)–(d) due to the higher shift in time constant.

It is obvious from Figures 5.12(a)–(d) that there has been a variation in the impedance response during loading process. Consider for example, the bulk resistance at 2% strain, which was found to be: ~95.2 kΩ for Sample 1, ~70.8 kΩ for Sample 2, ~64.9 kΩ for Sample 3, and ~93.8 kΩ for Sample 4. It is also obvious that the impedance at failure for T-EE-L-DB2 attains ~120 kΩ, while the rest of the samples attain higher values with ~457 kΩ, ~151 kΩ, and ~221 kΩ for T-EE-L-DB1, T-EE-L-DB3, and T-EE-L-DB4, respectively. This is attributed to a smaller crack width (~60 μm at failure).

(a) T-ECC-L-DB1
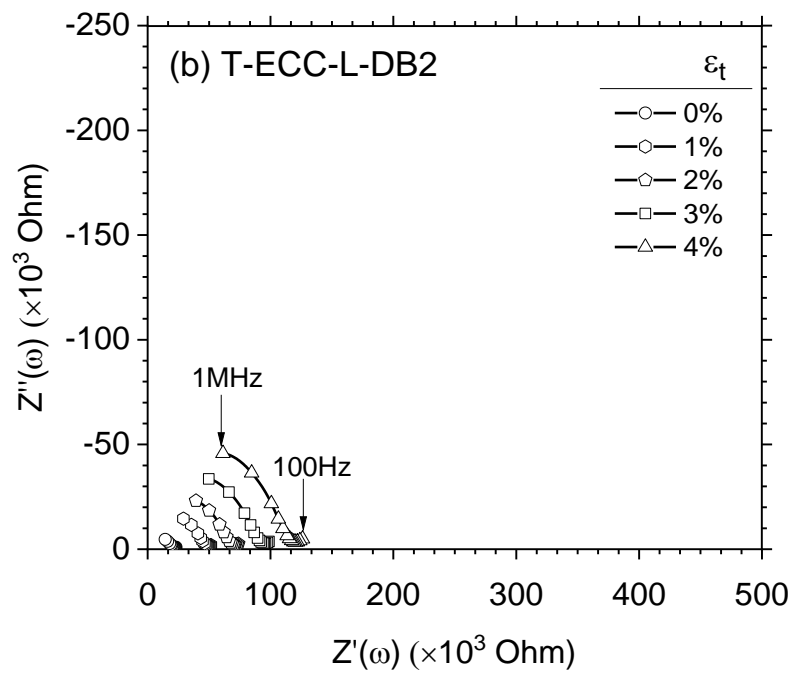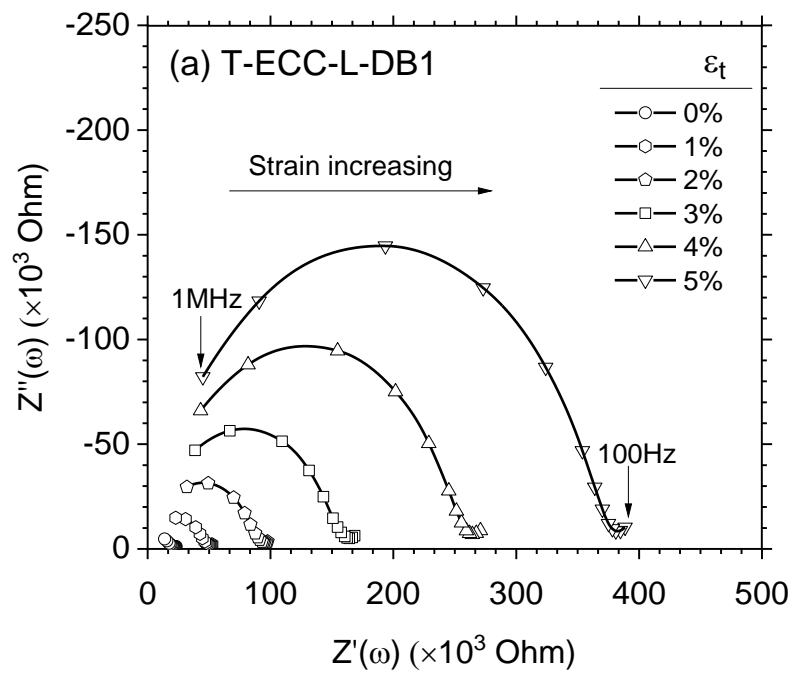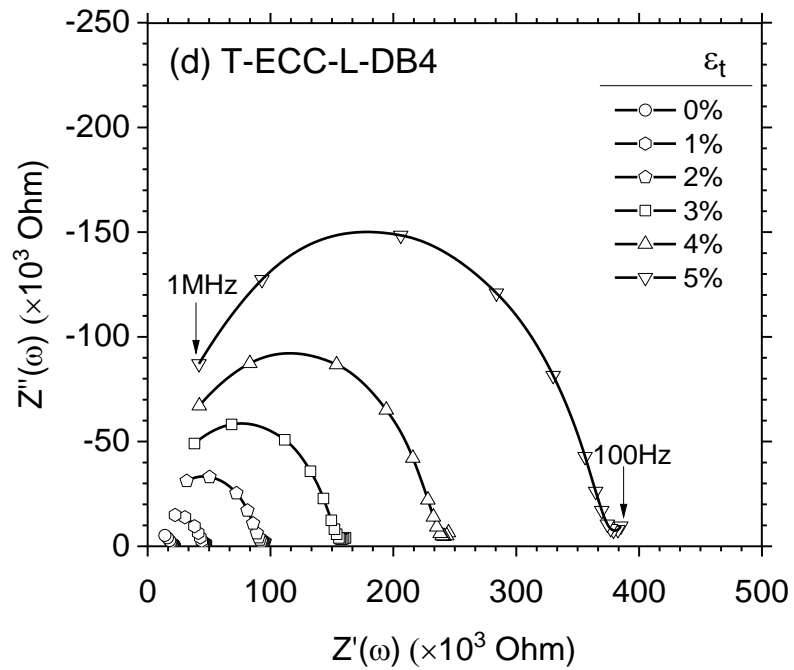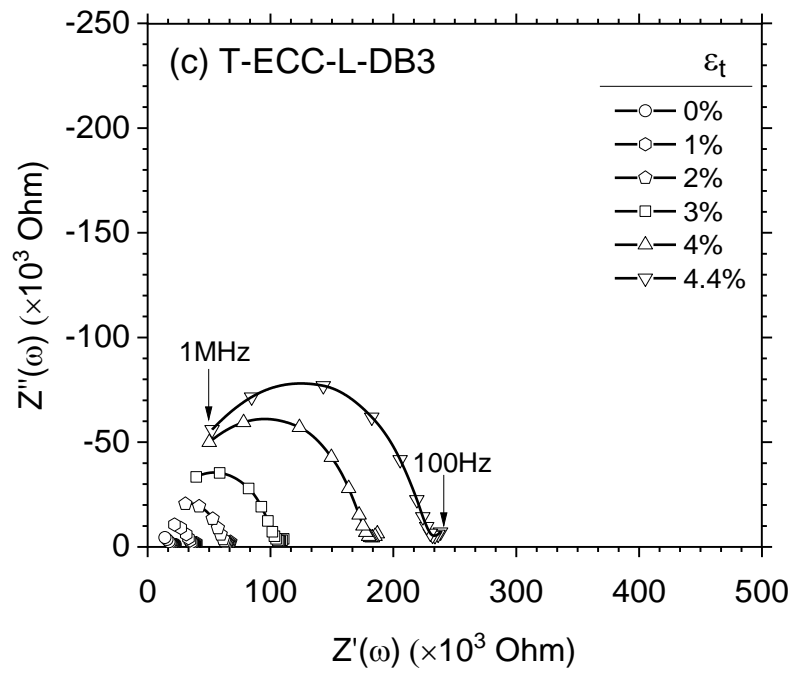
(b) T-ECC-L-DB2

Figure 5.12: (a) Variation in impedance response with tensile strain for specimens: (a) T-ECC-L-DB1; (b) T-ECC-L-DB2; (c) T-ECC-L-DB3; and (d) T-ECC-L-DB4.

5.4.2 Relative permittivity and bulk conductivity

Figures 5.13(a)–(d) show the relative permittivity versus frequency at various strain levels, with each 1% increment of strain shown for clarity. The relative permittivity plots for specimen T-ECC-L-DB2 (Figure 5.13(b)) displays a similar trend to those observed earlier in Figures 5.6(a)–(d), with a downward displacement of relative permittivity plots with increasing stain across the entire frequency range. From other

specimens (T-ECC-L-DB1, T-ECC-L-DB3, and T-ECC-L-DB4), however, it is interesting to see from Figures 5.13(a), (c) and (d) that despite the same downward displacement, there is an enhancement in relative permittivity in the high frequency range at high strain levels. This results in the emergence of a shoulder in the frequency-domain response (this feature was not present in specimen T-ECC-L-DB2, nor in all Series 1 specimens). This enhancement of the relative permittivity would reflect that a new polarization mechanism is operative within the system. Figure 5.14 presents the relative permittivity of ECC after conducting the one-single crack test. It is evident that micro-cracking results in a significant enhancement in relative permittivity due to the polarization at the matrix/crack interface, which is prominent over >10 kHz into the ~low MHz. Based on the polarization mechanism, it is proposed that within the frequency range >kHz into the ~low MHz, there are two superimposed mechanisms: the relaxation of the matrix/crack interfacial polarization, together with the relaxation of Maxwell-Wanger polarization, which have a more dominant influence up to the high MHz region.

In order to explain this added feature in this series of specimens, which has a larger crack width, the ECC specimen could be considered to have two parts, comprising a non-cracked part and a cracked part connected in series. On application of an alternating electrical field, electric current must pass across the specimen, including the fibre bridging across the micro-cracks. Due to the larger crack widths, however, charges can accumulate at the interface and result in the development of an electrochemical over-potential. This may result in polarization build-up at the end of the un-cracked matrix, which is quantified by the enhancement of capacitance, hence permittivity, of the composite. This effect is shown schematically in Figure 5.15. This enhancement in relative permittivity dispersion was not observed in specimen T-ECC-L-DB2 due to its small crack width (mean value of ~60 μm at failure), thereby allowing the crack-bridging pathway to form more easily within the micro-cracks (see Figure 5.5(b)). As the curing age increases, the free-water within the ECC matrix gradually declines because of the ongoing cement hydration results from the refinement of the pore (Wu et al., 2017). Therefore, there will be less leached pore water when cracking occurs.
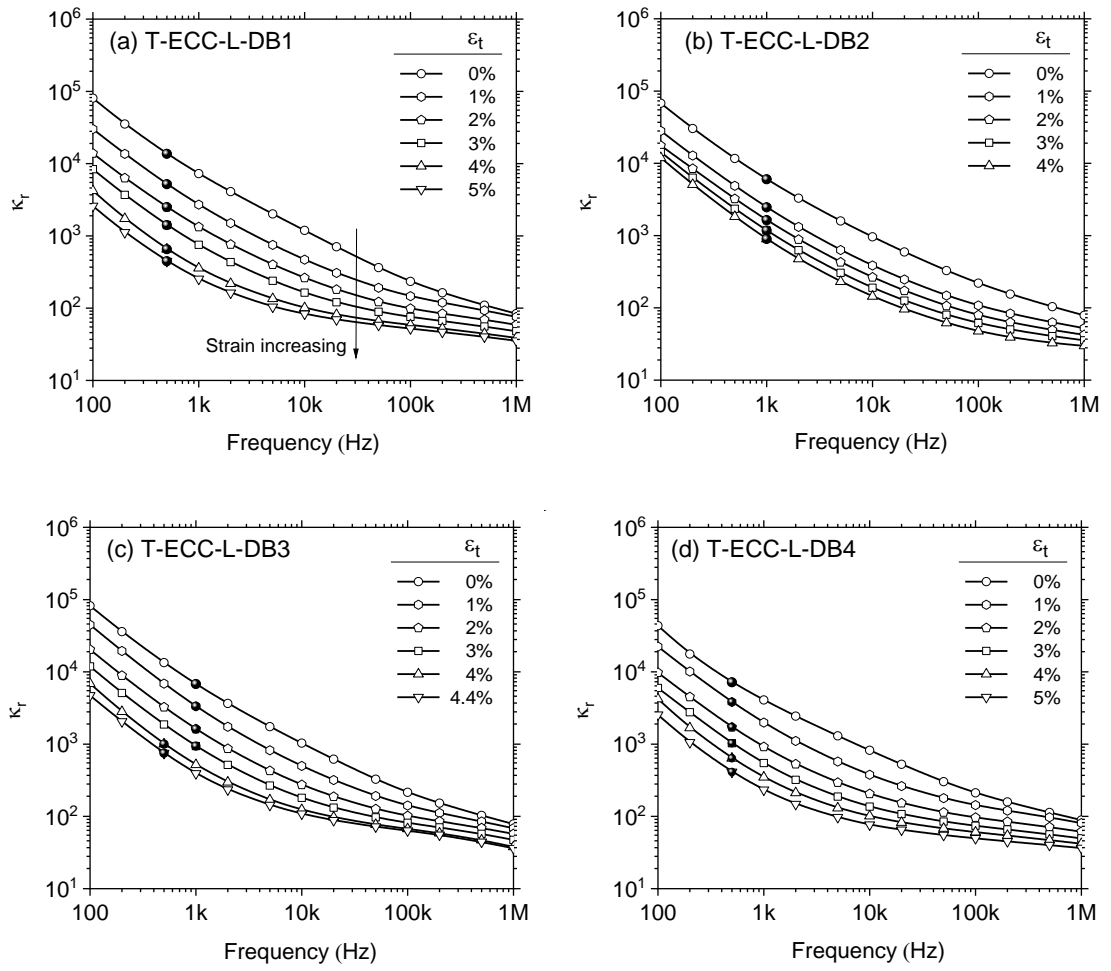
Figure 5.13: Relative permittivity versus frequency at various strain levels for specimens: (a) T-ECC-L-DB1; (b) T-ECC-L-DB2; (c) T-ECC-L-DB3; and (d) T-ECC-L-DB4.
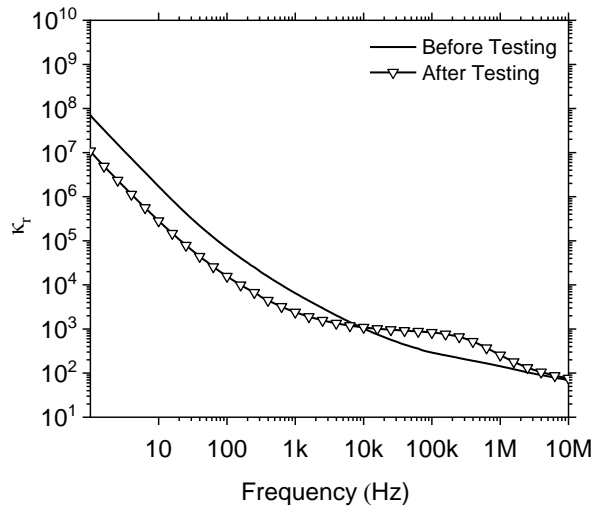
Figure 5.14: Relative permittivity of ECC before and after cracking (one discrete crack).

Applied Field (E ≠ 0)
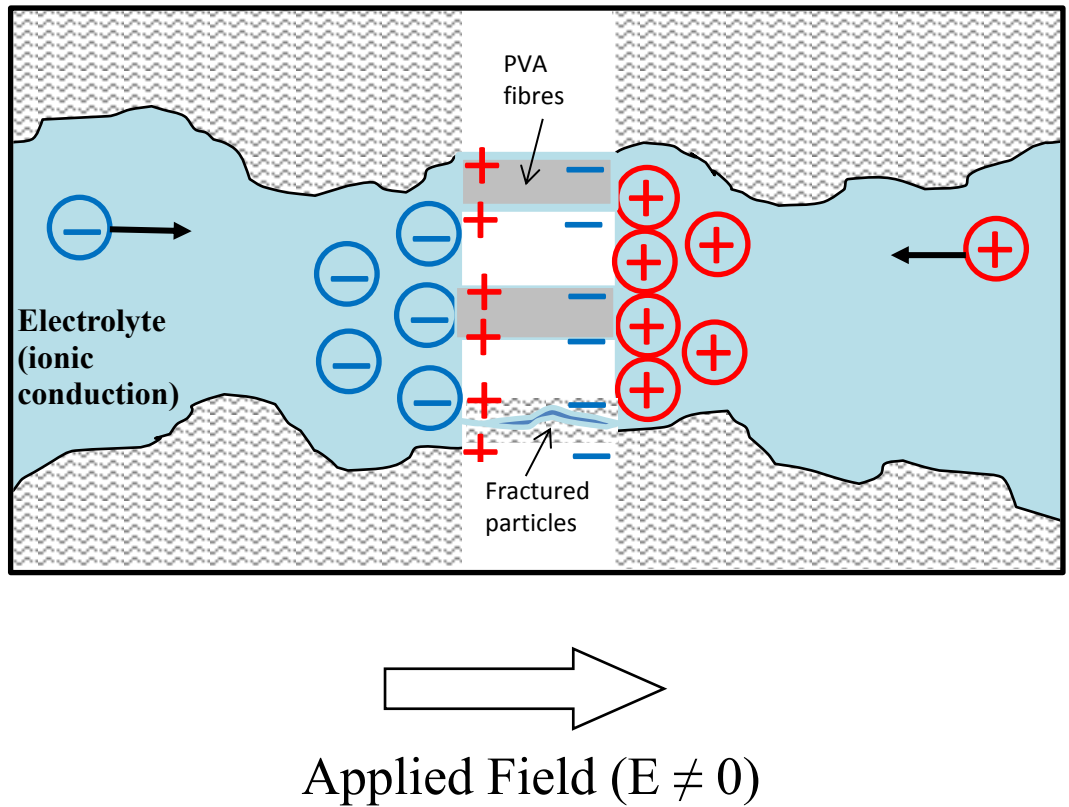
Figure 5.15: Schematic showing induced polarisation at cracks–pore solution interface.

The bulk conductivity plots for Series 2 specimens are presented in Figures 5.16(a)–(d) in the frequency domain, with the frequency at the cusp-point highlighted using solid data markers as before. In general, the same trend to Series 1 specimens displayed

earlier in Figures 5.8(a)–(d) is evident, as shown by the progressive downward displacement of the bulk conductivity curves with increasing strain. However, it is interesting to observe that the conductivity at high frequencies displays a greater increase in value (particularly at high strain levels), which was not evident in Series 1 of results presented earlier in Figures 5.8(a)–(d). Figure 5.17 displays the conductivity of ECC after conducting the one-single crack test. It can be clearly seen that there is an enhancement in conductivity at high frequencies of the cracked sample. This can be attributed to the relaxation of the matrix/crack interface and Maxwell-Wagner polarisation processes.
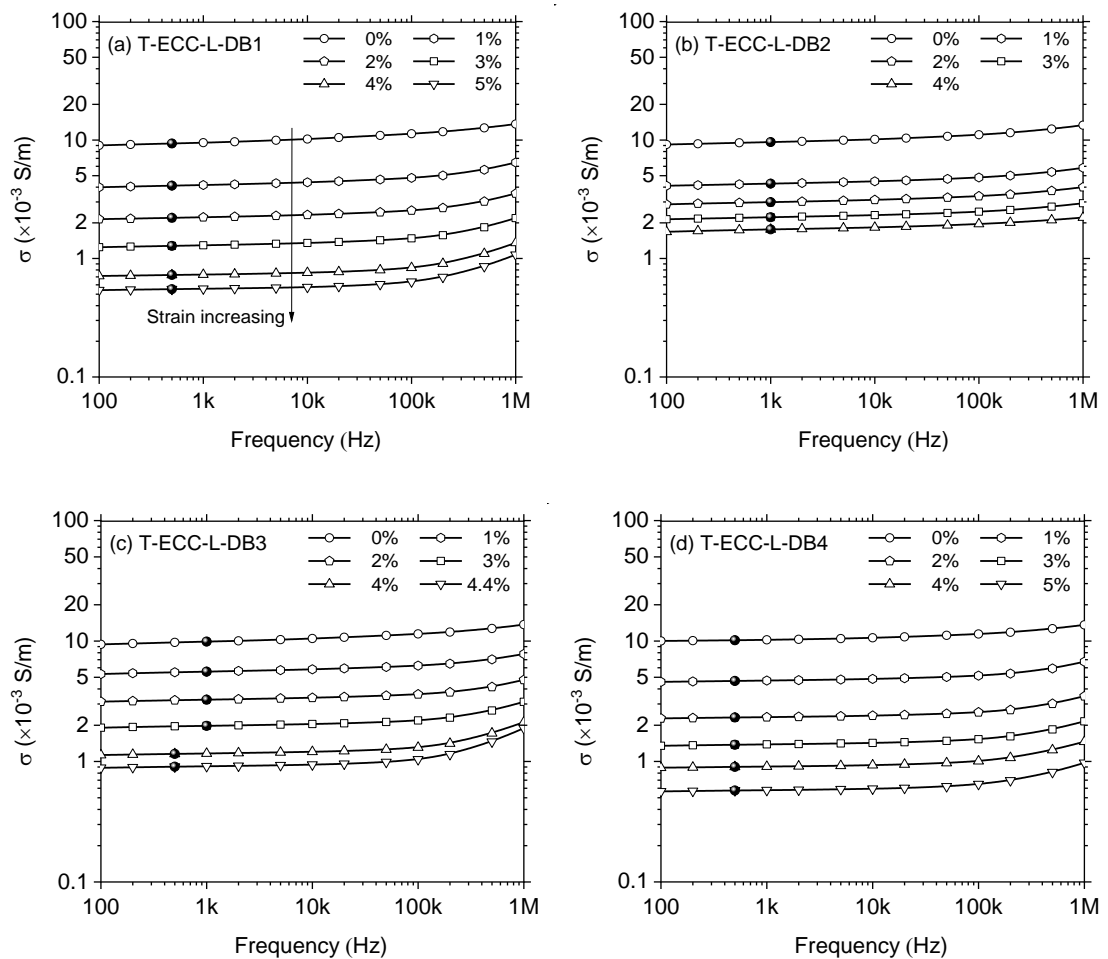
Figure 5.16: Conductivity versus frequency at various strain levels for specimens: (a) T-ECC-L-DB1; (b) T-ECC-L-DB2; (c) T-ECC-L-DB3; and (d) T-ECC-L-DB4.
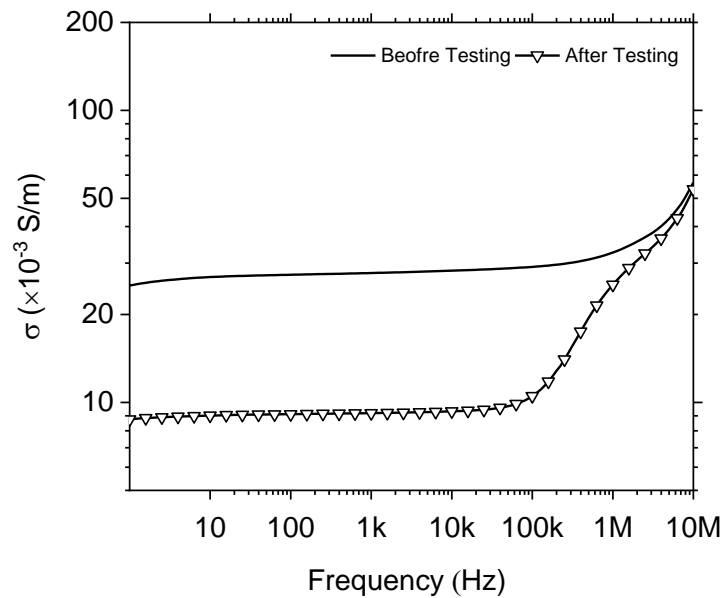
Figure 5.17: Conductivity before and after cracking (one discrete crack).

5.4.3 Fractional change in resistivity (FCR) and crack mapping

The FCR over a wide frequency band together with the stress-strain response is presented in Figures 5.18(a)–(d). It is evident that the FCR plots exhibit a nonlinear increase with strain, with the mean FCR value at failure of 19.7, 4.6, 9.7, and 17.2 for T-ECC-L-DB1/DB2/DB3/DB4 samples, respectively. The increase in FRC is associated with the progressive development of micro-cracks during the strain-hardening phase. It is interesting to note that the FCR values for the T-ECC-L-DB2 sample at 4% strain are comparable to the 1st series and to those reported earlier by Ranade et al. (2014) and Deng and Li (2018) who conducted similar tests on relatively young specimens (28 days of curing). However, the rest of the samples all attained much higher values of FCR, which would indicate higher sensitivity to tensile straining (or crack formation). This could be associated with the process of micro-crack development and the distribution of the micro-cracks during loading. As the capillary pores within the ECC matrix break down as being intercepted by a micro-crack, the crack space may be partially filled by pore-water, thereby creating a water-bridging conduction path across the micro-crack. With increasing time, however, the amount of free water within the ECC matrix could be expected to decrease due to the reduction in overall porosity resulting from on-going cement hydration and pozzolanic reaction. As a result, fewer water bridg effects could be expected in a mature ECC sample, as in the samples tested in this study. In addition to this aspect, it was observed that the crack widths were

relatively large, and this aspect could also contribute to the enhancement in sensitivity. With regard to the influence of test frequency, it is interesting to notice that the variation between T-ECC-L-DB2 where the FCR plots lie close to one another compared to T-ECC-L-DB1, T-ECC-L-DB3, and T-ECC-L-DB4 with the slope of the FCR plots decreases with increasing frequency. This could be attributed to the enhancement in the relative permittivity (the precence of the shoulder) at high frequencies and the larger increase in the conductivity. Since the FCR is frequency-dependent and shows a large spread, it is suggested to use the cusp-point frequency (in this case, 500 Hz). For clarity, Figure 5.18(e) provides the FCR plots of all samples at the cusp-point frequency of 500 Hz. Table 5.4 presents the gauge factors (GF) at various strain levels for Series 2, and compares them with the GF for Series 1. It can be clearly seen that the mean GF when $\varepsilon_t < 0.3\%$ is ~3 fold higher in Series 2 (~100) compared with Series 1. While the mean GF when $\varepsilon_t > 0.3\%$ is almost ~2 fold higher in Series 2 compared with Series 1.

In order to interpret the variation of the FCR values between the samples, the observation of crack development during loading was calculated through the Digital Image Correlation (DIC) technique and visually. Figures 5.19(a) and 5.20(a) illustrate the representative longitudinal strain maps using the DIC technique with every 0.5% increment of strain for T-ECC-L-DB2 and T-ECC-L-DB3, respectively. In addition, the best-fit lognormal distribution curves at 1% strain increment for ECC-L-DB2 and T-ECC-L-DB3 are plotted in Figures 5.19(b) and 5.20(b), respectively. Figure 5.19(a) displays a similar trend to that observed in Figure 5.10(a), with an increasing number of micro-crack formations up to 3% strain, followed by an increase in the average crack width. While Figure 5.18(a) which also followed a similar trend to that observed in Figure 5.11(a) displays a continuous increase in micro-crack formation together with an increase in the average crack width. These strain maps depicted in Figures 5.19(a) and Figure 5.20(a) agree well with the observations found in Figures 5.19(b) and Figures 5.20(b).

Although ECC-L-DB2 and T-ECC-L-DB3 had nearly the same number of cracks (~12 cracks). However, the FCR in T-ECC-L-DB3 was found to be higher than that of ECC-L-DB2. This is attributed to the crack width; it is obvious from Figures 5.19(b) and 5.20(b) that the mean crack width of T-ECC-L-DB2 at 4% strain is ~60 μm, while T-ECC-L-DB3 is ~90 μm, signifying that a larger crack width causes a higher FCR. These crack width values at 4% strain of the 2nd set are higher than those observed in

the 1st set (See Figures 5.10(b) and 5.11(b)) with 54 μm of T-ECC-L-DB3 and 47 μm of T-ECC-L-DB4.
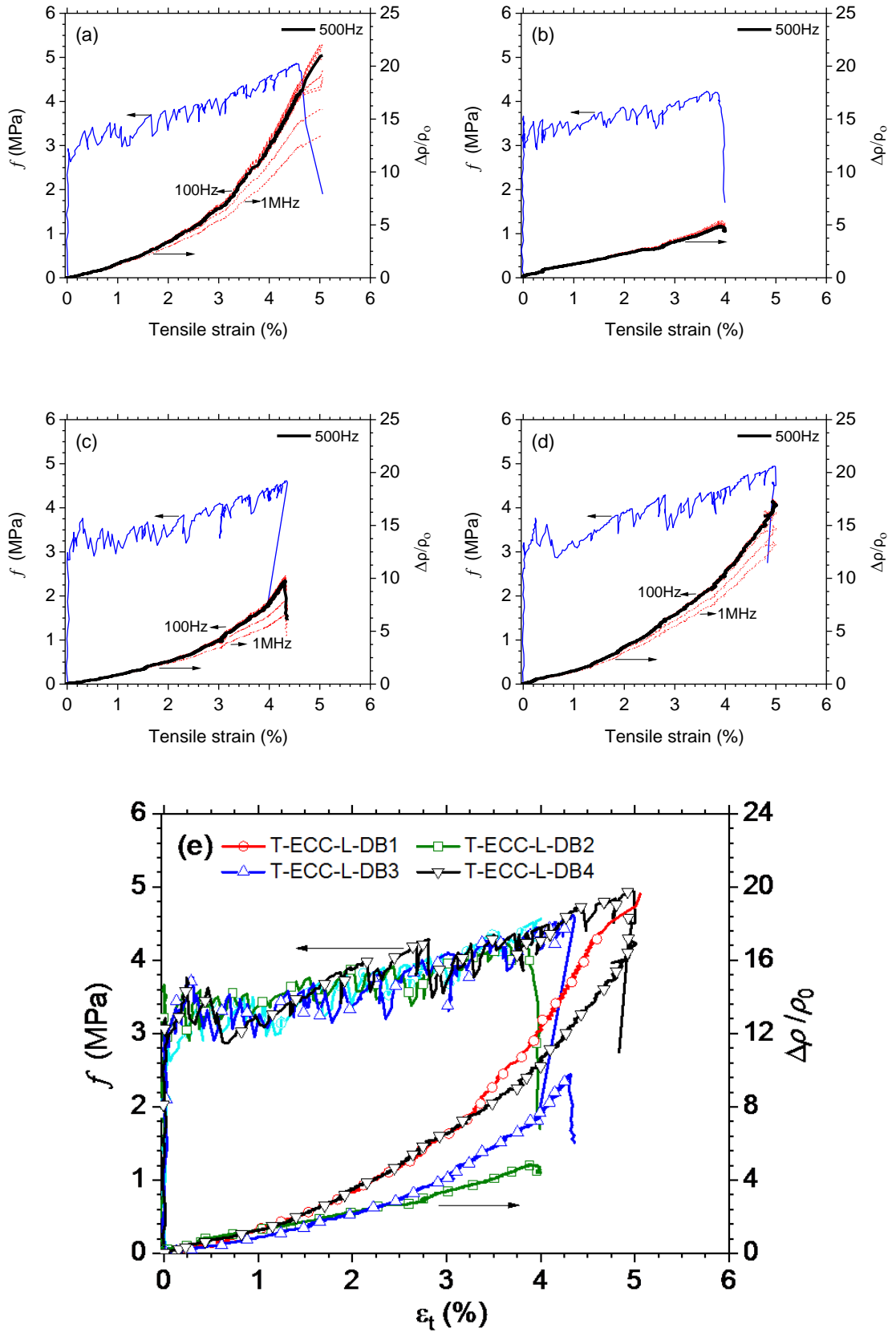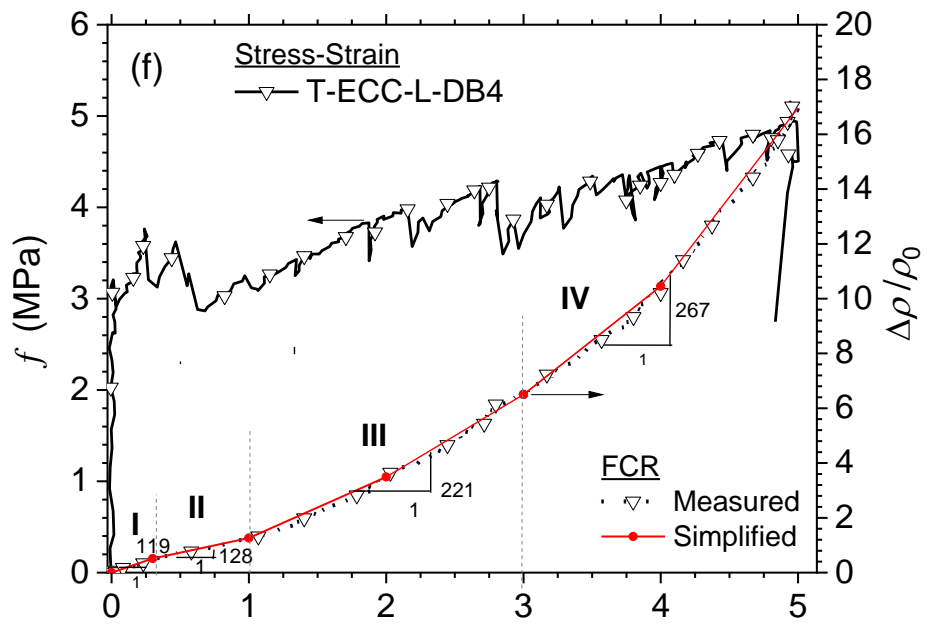
Figure 5.18: The fractional change in resistivity (FCR) for specimens: (a) T-ECC-L-DB1; (b) T-ECC-L-DB2; (c) T-ECC-L-DB3; and (d) T-ECC-L-DB4. (e) The FCR for specimens T-ECC-L-(DB1–DB4) at the cusp-point frequency (500 Hz). (f) Representation of the fractional change in resistivity of specimen T-ECC-L-DB4 into piecewise linear segments at 500 Hz. All curves are plotted alongside their stress-strain response.

Table 5.4: Calculated gauge factors (GF) at various strain levels for Series 2. Value in brackets is from Series 1 testing.

Specimen	Bulk resistivity at $\varepsilon = 0\%$, ρ (kΩ-m)	GF$_I$ ε_t<0.3%	GF$_{II}$ 0.3%<ε_t<1%	GF$_{III}$ 1%<ε_t<3%	GF$_{IV}$ ε_t > 3%
T-ECC-L-DB1	22.42	103	141	226	325[&], 440[#]
T-ECC-L-DB2	22.35	110	117	122	138
T-ECC-L-DB3	21.38	66	91	144	161
T-ECC-L-DB4	21.43	119	128	221	267[&], 344[#]
Mean	21.90 (8.4)	99.5 (28)	119.3 (51)	178.3 (76)	222.8 (133)
SD	0.49 (139.5)	20.2 (15.9)	18.4 (22.2)	45.9 (31.1)	76.5 (51.9)
CoV (%)	2.58 (1.9)	23.4 (56.2)	17.8 (43.6)	29.8 (41.0)	39.7 39.1)

Notes: [&]: ε_t between 3% and 4% and marks the quantity used in the statistical calculation; [#]ε_t > 4%. SD: standard deviation and CoV: coefficient of variation.

(a)

(b)
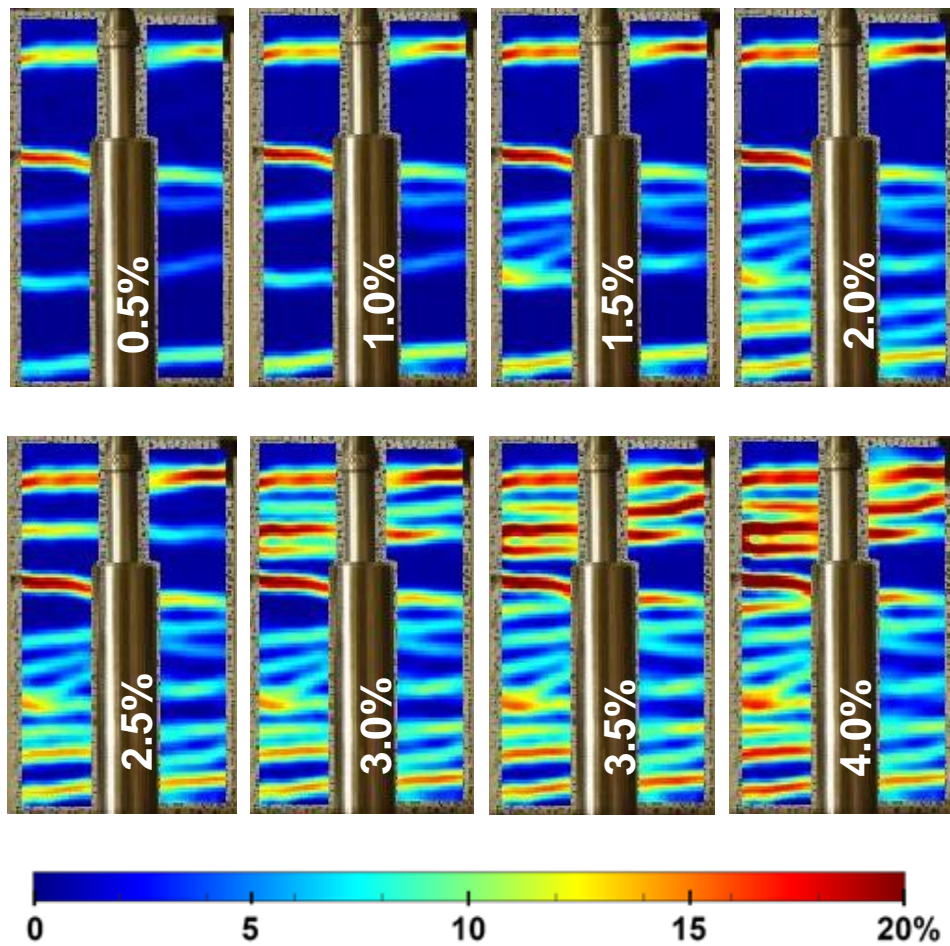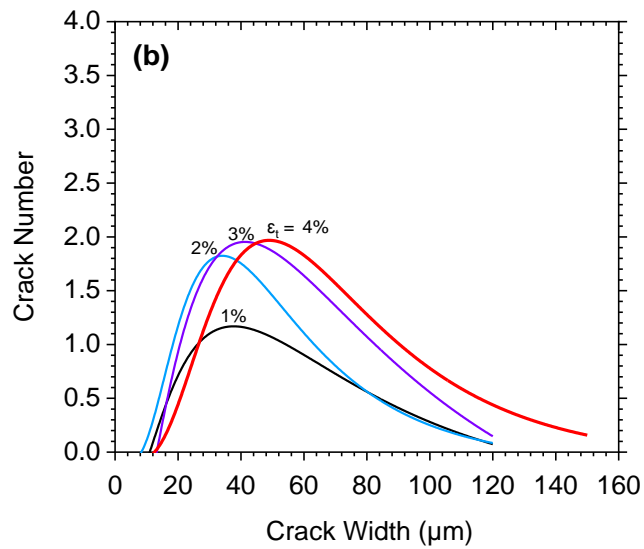
Figure 5.19: (a) Progressive development of longitudinal strains maps using DIC technique with every 0.5% increment of strain for T-ECC-L-DB2; and (b) The best-fit lognormal distribution curves at 1% strain increment of T-ECC-L-DB2.
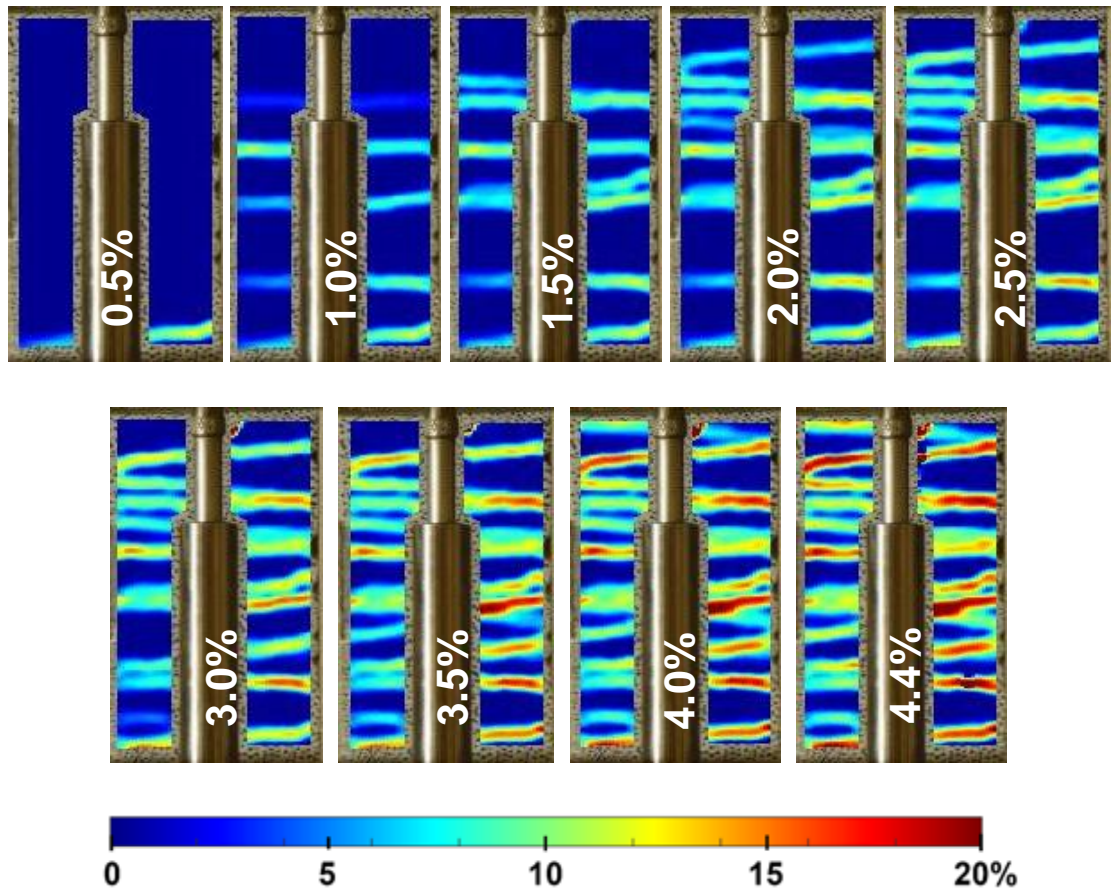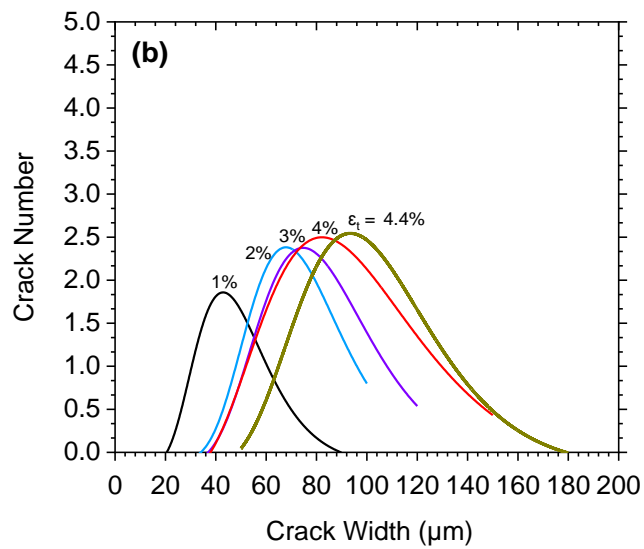
Figure 5.20: (a) Progressive development of longitudinal strains maps using DIC technique with every 0.5% increment of strain for T-ECC-L-DB3; and (b) The best-fit lognormal distribution curves at 1% strain increment of T-ECC-L-DB3.

5.5 Comparison of FCRs with previous data

Figure 5.21 provides a summary of the FCR values of different versions of ECCs obtained from the literature (Hou and Lynch, 2005; Hou, 2008; Lin et al., 2011; Ranade et al., 2014; Suryanto et al., 2015; Huang et al., 2018; Deng and Li, 2018; Yıldırım et al., 2020) (see Figure 2.16 in section 2.4.2.4), together with the FCR values obtained from this study (1st series and 2nd series).

It is interesting to see that there has been a large scatter in FCR values, which could be attributed to the various ECC mixtures used by different researchers and different test methodology. Regarding the FCR at 1% strain, this varies from 8 as reported by Deng and Li (2018), 15 as reported by Huang et al. (2018), to higher values such as 170 as reported by Ranade et al. (2014), 200 as reported by Suryanto et al. (2015), and 260 as reported by Lin et al. (2011). It is also interesting to note that the higher slope between the FCR and strain indicates higher sensitivity to crack formation. It is noteworthy that when the FCR value is comparatively low, the ECC mix consists of a higher volume of fly-ash and such a mixture display a smaller crack width, as reported in Ranade et al. (2014), Huang et al. (2018), and Deng and Li (2018). Therefore, it can be suggested that the large variations in FRC values are related to the distribution of the micro-cracks during loading. In addition, it is interesting to note that there have been a few data published at strain levels greater than about 4%, and the data from Series 1 and 2 could be useful in this regard. It is obvious that the values obtained in Series 1 and 2 are within the published values' range. The FCR values obtained from Series 1 are similar to those reported by Ranade et al. (2014), while the FCR of Series 2 is similar to Deng and Li (2018). A summary of key aspects is presented in Table 5.5.

Table 5.5: Summary of the mechanical and electrical properties and crack patterns of different versions of ECCs presented in the literature.

Name/Reference	Mix name	FA/C ratio	Tensile Strain Capacity	GF	Strain level	Crack width	Crack number
Hou and Lynch (2005)	ECC mix	_	3%	100	_	_	_
Hou (2008)	M45-ECC	_	2.3%	(10-20) in the elastic region (30-80) in the strain-hardening region	_	_	_
Lin et al. (2011)	M45-ECC	1.2	2.2%	32 in the elastic region 283 in the strain-hardening region	_	_	_
Ranade et al. (2014)	M45-ECC	1.2	4.2%	24 -232	1.4%	75 μm	19
	HFA-ECC	2.8	3.3%	13-78	4.2%	57 μm	70
Suryanto et al. (2015)	ECC mix	1.8	2.0%	200-340	_	_	_
Liu et al. (2016)	ECC mix	2.2	2.0%	_	0.5%	33 μm	8
					1.0%	48 μm	13
					1.5%	53 μm	18
					1.8%	54 μm	20
					2.0%	55 μm	24
Huang et al. (2018)	ECC mix	1.2	2.6%	75-235	2.6%	65 μm	19
	HFA-ECC	3.0	3.8%	17-50	3.8%	7 μm	100
Deng and Li (2018)	ECC mix	1.5	3.8%	130-257	3.8%	44 μm	14
	HFA-ECC	3.0	4.5%	50-94	4.5%	14 μm	38

Table 5.5: Summary of the mechanical and electrical properties and crack patterns of different versions of ECCs presented in the literature (Continued).							
Yıldırım et al. (2020)	ECC mix	1.2	3.6mm deformation	60-150	–	–	–
This Study	ECC mix (1st series)	1.8	4.5%	15-92	–	–	–
			3.5%	30-203	–	–	–
			4.9%	50-313	1.0%	46 μm	5
					2.0%	46 μm	9
					3.0%	46 μm	14
					4.0%	54 μm	15
					4.9%	65 μm	16
			4.0%	18-95	1.0%	25 μm	4
					2.0%	32 μm	6
					3.0%	40 μm	11
					4.0%	47 μm	15
	ECC mix (2nd series)	1.8	5.0%	103-440	5.0%	–	–
			4.0%	110-138	1.0%	40 μm	6
					2.0%	40 μm	8
					3.0%	48 μm	11
					4.0%	60 μm	11
			4.4%	66-161	1.0%	46 μm	5
					2.0%	66 μm	9
					3.0%	79 μm	10
					4.0%	94 μm	12
					4.4%	103 μm	12
			4.9%	119-344	4.9%	–	–
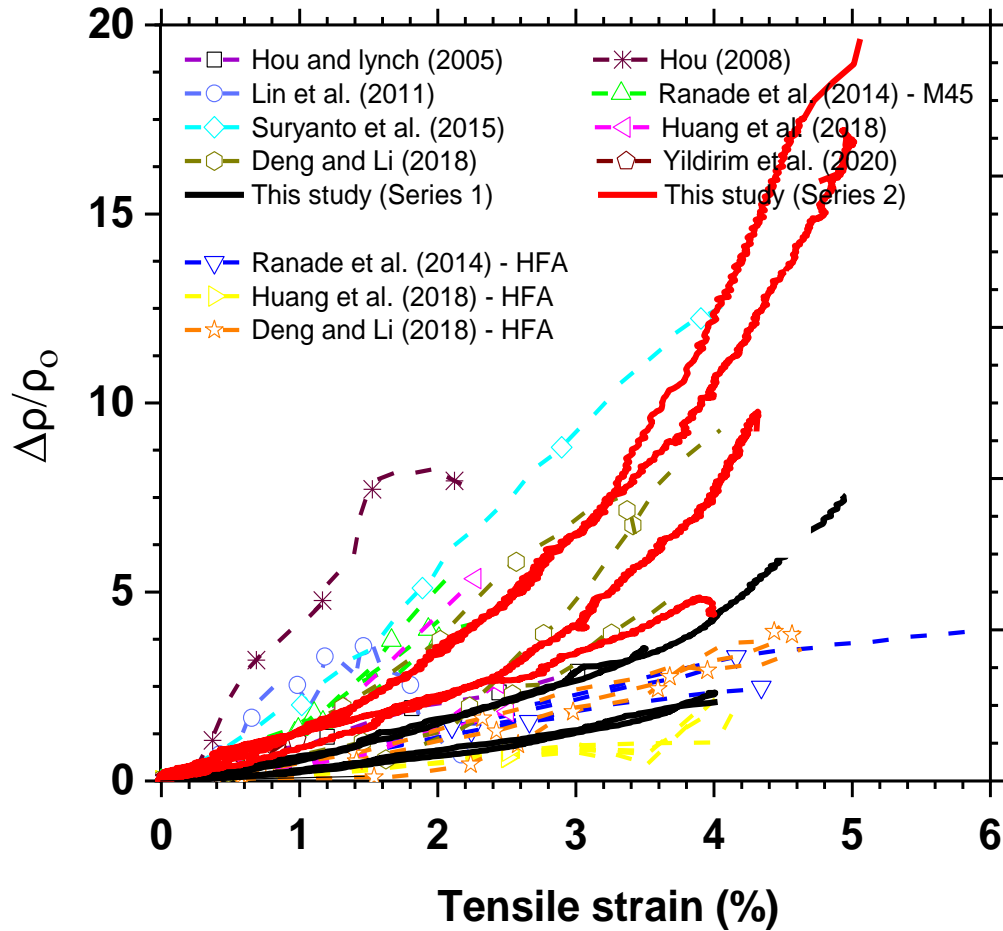
Figure 5.21: Comparison of the obtained FCR values with data reported in previous studies (Hou, 2008; Hou and Lynch, 2005; Lin et al., 2011; Ranade et al., 2014; Suryanto et al., 2015; Huang et al., 2018; Deng and Li, 2018; and Yıldırım et al., 2020).

5.6 Equivalent Circuit Modelling

The impedance responses obtained in Figures 5.4 and 5.12 from the cracked results of the 1st and 2nd set of ECC, respectively, together with the impedance responses of the 1st and the 2nd set of ECC in the un-cracked stage displayed in Appendix (B) in Figures B-1(a) and B-2(a), were modelled using equivalent electrical circuits. The equivalent electrical circuits when the un-cracked ECC specimen is placed between two parallel electrodes is shown in Figure 4.10(b) in section (4.2.5) were simplified by not taken into account the electronic conduction through the unburnt carbon. The simplified potential paths were represented as circuit elements, as can be seen in Figure 5.22(a),

- The resistor 'Rs' describes the projected intercept of the high-frequency arc with

the real-axis at the high-frequency end.

- The parallel element, R_{cp}–CPE_{sm}, is used to represent the bulk response.
- The parallel element, R_{el}–CPE_{el}, is used to describe the response of the electrode/sample interface. This parallel element operates in series with the bulk response.

When micro-cracks introduce to the system, the following is also present,

- A circuit compresses a resistor, 'R_c', in parallel with a constant phase element 'CPE_c'. 'R_c' is employed to represent the conduction through the micro-cracks (viz., direct contact between the cement matrix across the micro-cracks or any broken particles bridging the micro-cracks). For normal ECC, PVA fibres coated with pore solution from broken capillaries/cavities should also be considered (not in this test). While, 'CPE_c' to describe the capacitive effect resulting from the physical separation between two opposite un-cracked surfaces caused by the micro-cracks, this parallel circuit, R_c–CPE_c, is added in series with the bulk and electrode circuits.
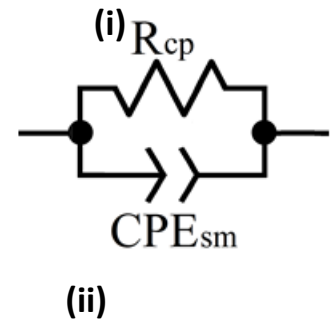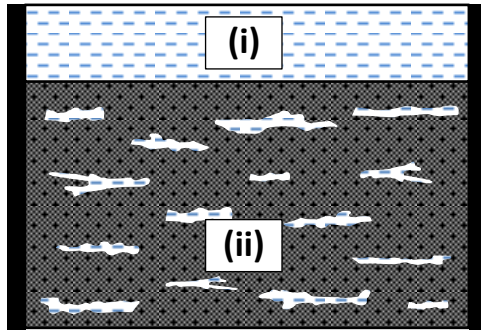
(a)
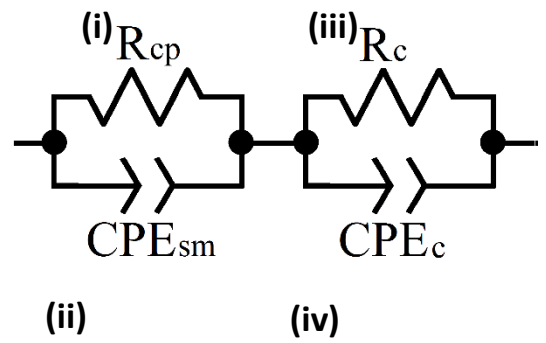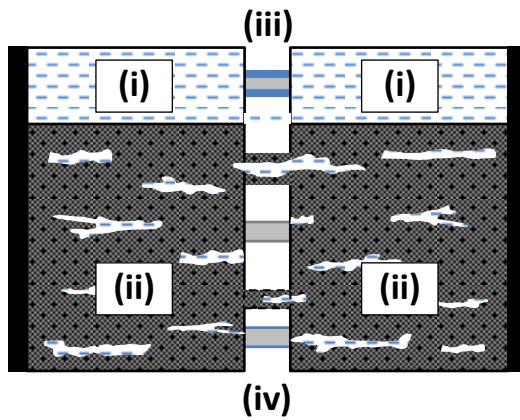
(b)

Figure 5.22: Simplified electrical models were used in the simulation and the diagrammatic representation of the electrical pathways for (a) the un-cracked ECC matrix and (b) the cracked ECC matrix.

Figure 5.23(a) and Figure 5.24(a) present representative simulated and measured impedance responses of specimens E-ECC-S-(P1–P3) and E-ECC-L-(P1–P2) at different curing ages, with the modelled circuit parameters at selected times presented in Figure 5.23(b) and Figure 5.24(b). The solid lines in Figure 5.23(a) and Figure 5.24(a) represent the simulated curves, whereas the markers represent the measured response, with the frequency increasing from right-to-left across the curves. Good agreement can

be seen between the measured and simulated responses, indicating that the simplified electrical circuit is a good representation of the composite system. Regarding the temporal changes in R_{cp}, $C_{o,sm}$ and p_{sm} presented in Figure 5.23(b) and Figure 5.24(b), it is evident that R_{cp} increases with increasing curing time, reflecting microstructural refinement due to the ongoing hydration and pozzolanic activity. As the hydration progresses, it could be expected that the capillary pore network becomes more tortuous, constricted, and disconnected, which manifests as an overall increase in $C_{o,sm}$ with time and an overall slight reduction in p_{sm}, with the latter indicative of an increasing spread of time constants and an increased depression angle, α, with time, which is very well explained previously in section (4.2.5) in chapter (4).
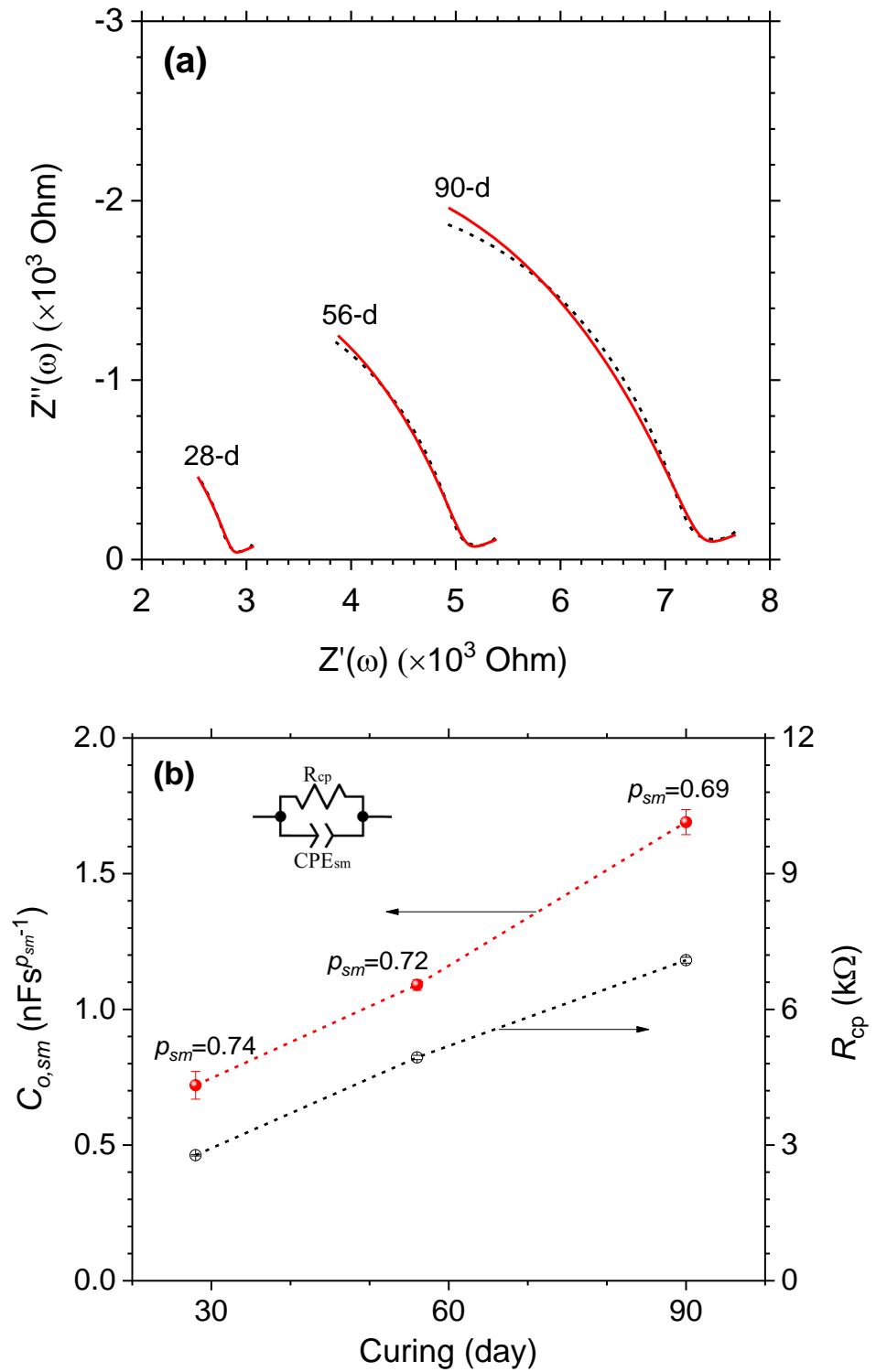
Figure 5.23: (a) Measured and simulated representative responses for specimen E-ECC-S-P1 at 28-, 56-, and 90-day curing; and (b) variations in circuit parameters for all three specimens E-ECC-S-(P1–P3).
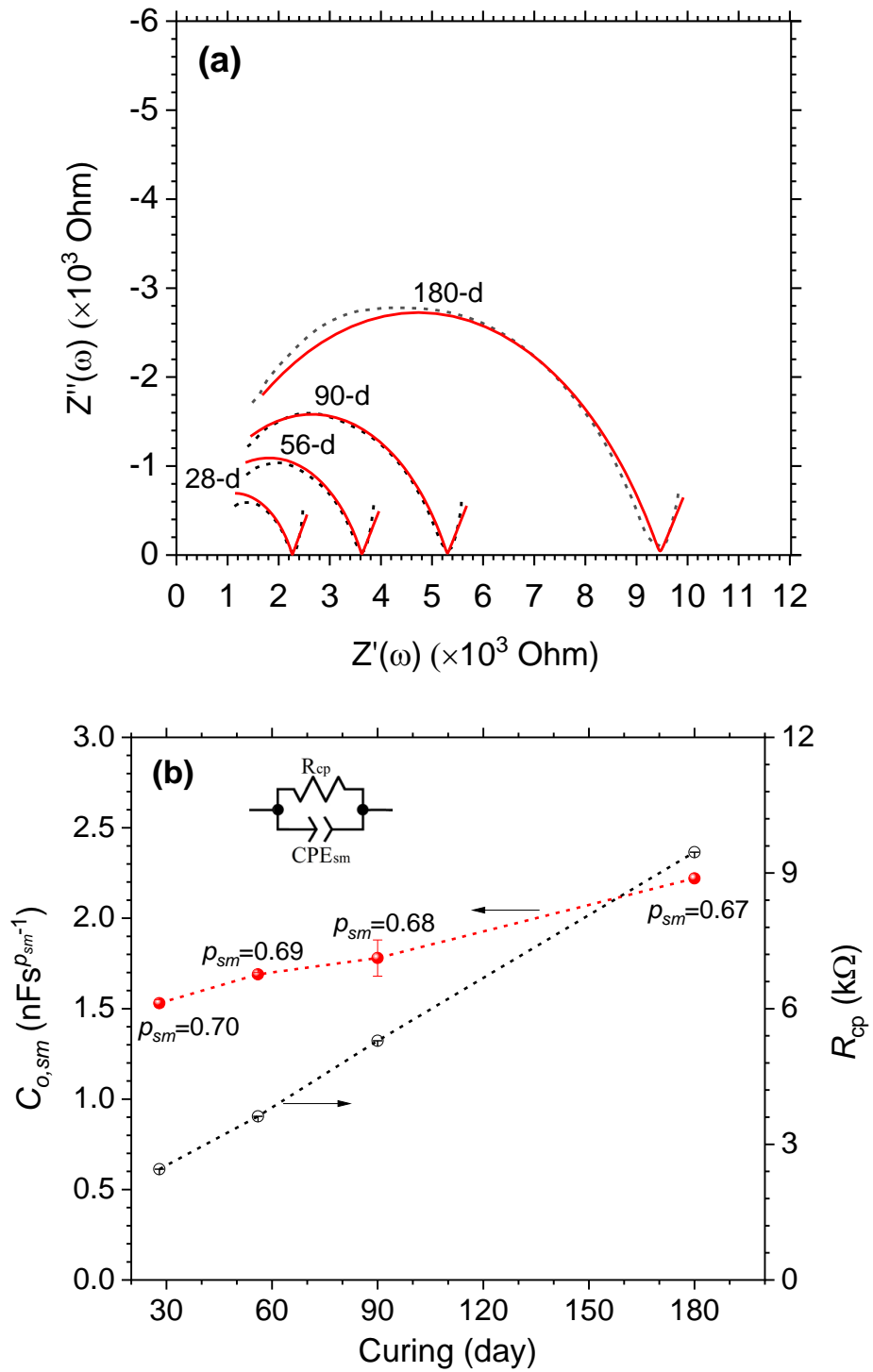
Figure 5.24: (a) Measured and simulated representative responses for specimen E-ECC-L-P1 at 28-, 56-, 90-, and 180-day curing; and (b) variations in circuit parameters for both specimens E-ECC-L-(P1-P2).

The simulated impedance responses of specimen E-ECC-S-DB4 and E-ECC-L-DB2 at every 1% increment of strain are presented in Figure 5.25(a) and Figure 5.26(a) alongside with the measured responses, respectively, with the frequency increasing from right-to-left across the curves and the parameters obtained from the fitting process are presented in Figure 5.25(b) and Figure 5.26(b), respectively. The solid lines, as before, represent the simulated curves while the markers represent the measured response. A good agreement between the measured and simulated responses is evident in Figure 5.25(b). However, due to the limitations of spot frequencies (measurements were taken at 13 spot frequencies) and the LCR meter (the higher frequency is 1 MHz), it was difficult to obtain a good agreement between the measured and simulated responses in Figure 5.26(b). With regards to the parameters obtained from the fitting process, it is immediately apparent that the new parallel circuit, R_c–CPE_c, has an important role to play. With reference to Figure 5.25(a), The R_c is shown to increase almost linearly with increasing strain, from 1.7 kΩ at 1% strain, to 5.4 kΩ at 2% strain, and further to 10.4 kΩ at 3% strain (or a total of a 6-fold increase). This is due to the physical separation resulting from micro-crack formation within the ECC matrix discussed earlier. Also, as before, owing to notable crack widening beyond the 3% strain, the R_c increases more markedly to 19.2 kΩ at 4% strain, reaffirming the additional contribution of micro-crack widening. The E-ECC-L-DB2 behaved similarly to E-ECC-S-DB3, and it was found that the R_c values of E-ECC-L-DB2 were close to the E-ECC-S-DB3 values, which increased from 18.5 kΩ at 1% strain to 39.9 kΩ at 2% strain, 63.9 kΩ at 3%, and reached 86.7 kΩ at 4% strain.

Apart from understanding the influence of micro-crack on the resistive component, it would be informative to understand its influence on the capacitive behaviour throughout the loading process. This is done by plotting the temporal variations in $C_{o,c}$ and p_c in Figure 5.25(b) and Figure 5.26(b), respectively. If the micro-cracks can be considered as a *variable* capacitor, then it may be desirable to relate these parameters with (i) the effective surface area of the micro-cracks; (ii) the effective permittivity of the micro-cracks, as presented in Figure 5.5(b); and (iii) total crack opening. During the loading process, (i) can be considered to remain virtually constant, and hence only (ii) and (iii) would make a greater contribution. It is evident from Figure 5.25(b) and Figure 5.26(b) that the $C_{o,c}$ decreases markedly with strain. Consider for example, the $C_{o,c}$ of E-ECC-S-DB4 which decreases from 139 pFs$^{-0.10}$ at 1% strain to 48.2 pFs$^{-0.10}$ at 2% strain, followed by a gradual decrease to 31.4 pFs$^{-0.14}$ at 4% strain. This reduction can be

associated with the decrease in the effective permittivity of the micro-cracks with increasing strain resulting from an increase in the total crack opening due to new crack formation with increasing strain.
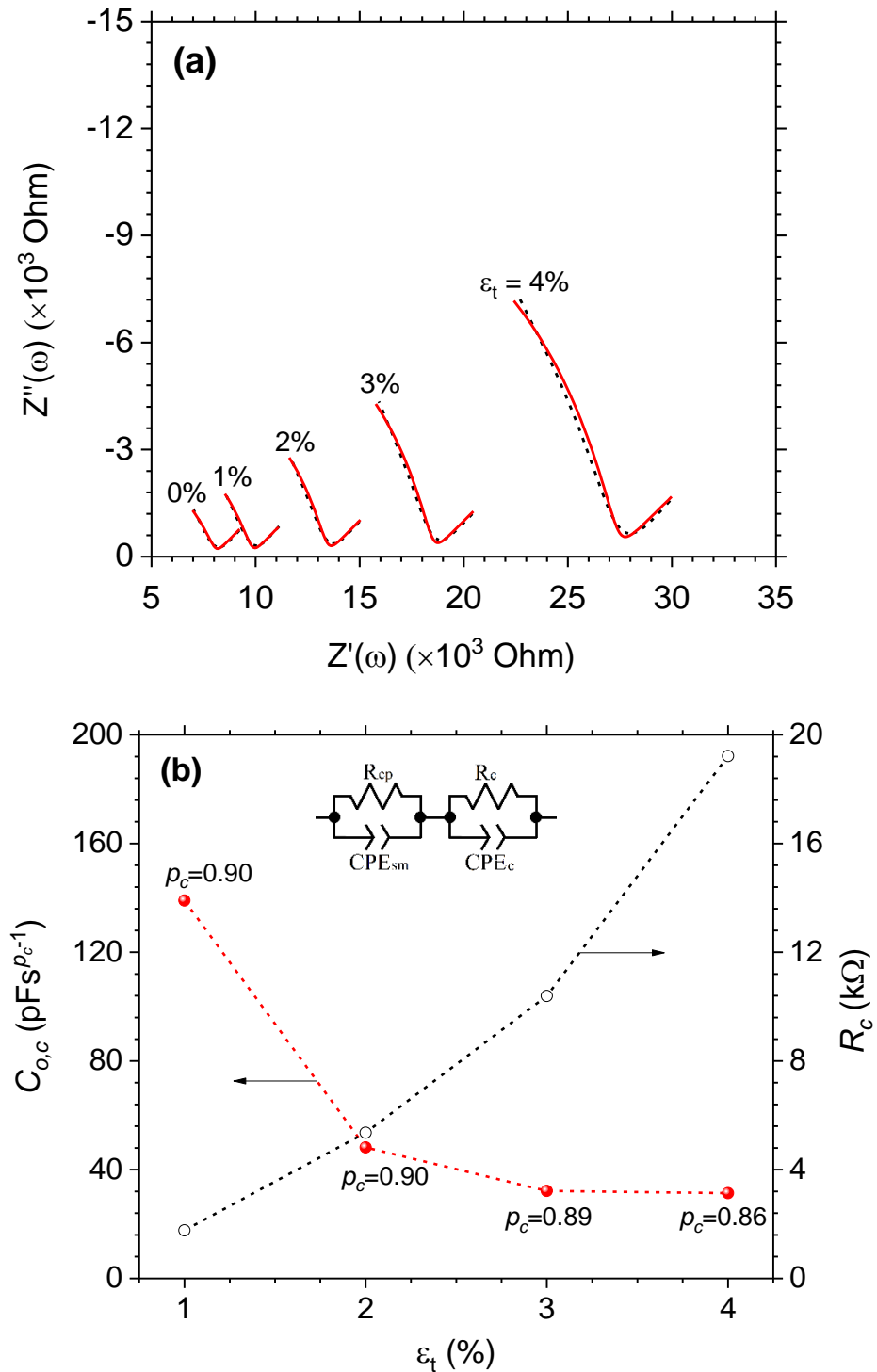
Figure 5.25: (a) Measured and simulated representative responses for specimens E-ECC-S-DB4 at 1% strain increment; and (b) the corresponding variations in circuit parameters representing the micro-cracks. Parameters representing the ECC matrix were taken as constant: $R_{cp} = 8$ kΩ, $C_{o,sm} = 7.93$ nFs$^{-0.33}$, and $p_{sm} = 0.67$.
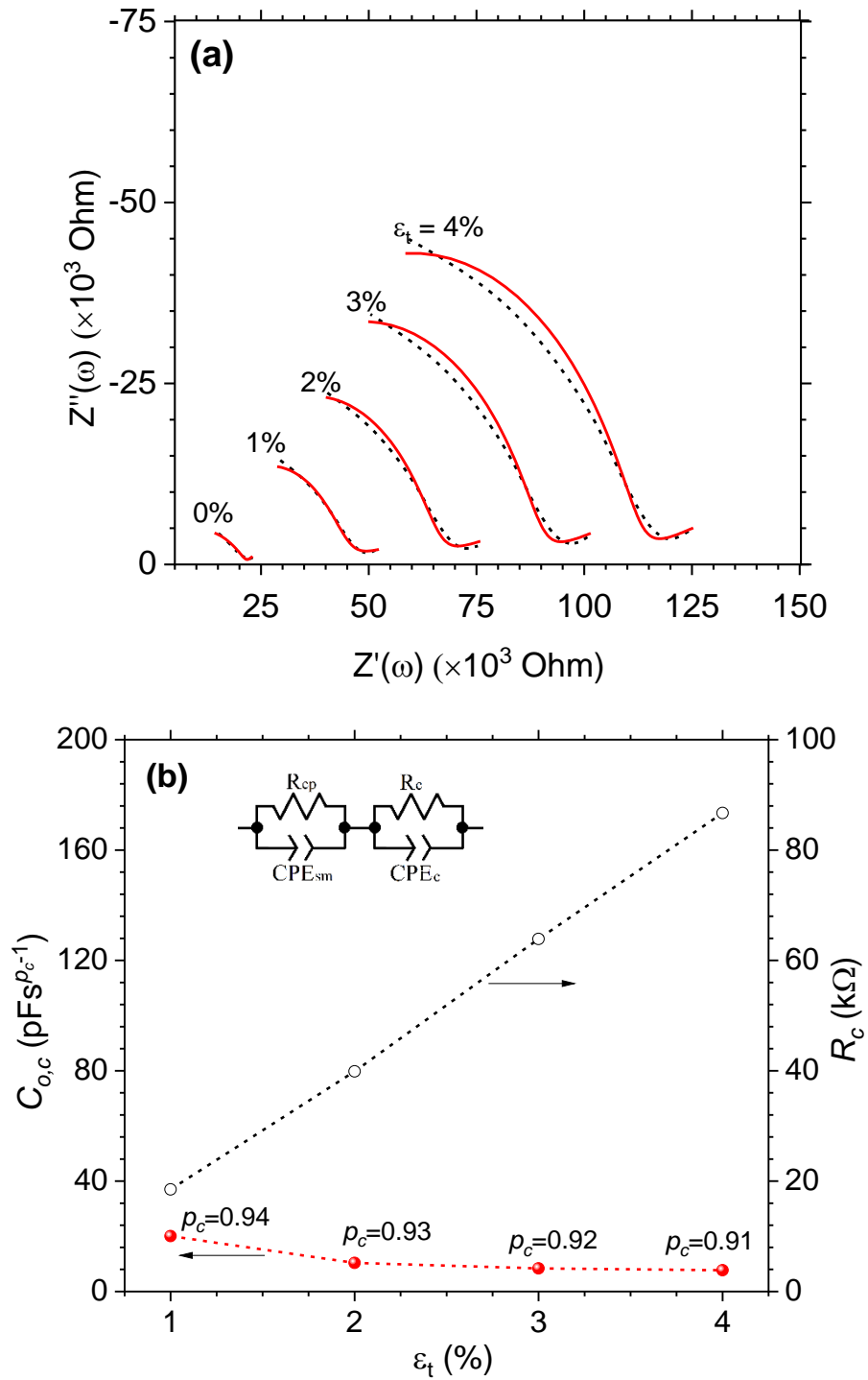
Figure 5.26: (a) Measured and simulated representative responses for specimens E-ECC-L-DB2 at 1% strain increment; and (b) the corresponding variations in circuit parameters representing the micro-cracks. Parameters representing the ECC matrix were taken as constant: $R_{cp} = 21$ kΩ; CPE-$C_{o,sm} = 6.7$ nFs$^{-0.47}$, and $p_{sm} = 0.53$.

5.7 Conclusions

Multiple testing methodology utilising electrical impedance measurements, mechanical testing, and detailed image analysis have been employed to investigate the piezo-resistive properties of an engineered cementitious composite under direct tension, with the impedance measurements also employed to provide complementary information on the influence of on-going hydration. The following can be drawn from the work presented:

- The complex impedance response of cracked ECC during tensile loading displayed a classic impedance response comprising an arc at the high-frequency end, a short intermediate plateau and a low-frequency spur (only weakly developed).

- Tensile straining was found to increase the sample impedance markedly, characterized by a progressive displacement of the impedance curves when presented in a Nyquist format. This marked increase in the impedance is attributed to the micro-cracks formation and widening during the tensile testing. Micro-cracks were found to influence the bulk resistance. The mean bulk resistance of samples with average crack widths of 56 μm increases from ~8 kΩ to ~56 kΩ (or a sevenfold increase), while the mean bulk resistance of samples with average crack widths of 81μm increases from ~22 kΩ to ~187 kΩ (or almost a ninefold increase).

- The relative permittivity of cracked ECC with smaller average crack widths displays a downward *vertical* displacement across the entire frequency range, while the relative permittivity of cracked ECC with larger crack widths displays the same downward displacement together with an enhancement of the relative permittivity at high frequencies (>10kHz to ~1MHz) at high strain levels. This downward displacement and/or the enhancement of the relative permittivity at high frequencies is related to the polarization at the matrix/crack interface.

- It is shown that there is a nonlinear relationship between tensile strain and the fractional change in resistivity. Micro-cracks were found to alter the fractional change in resistivity, with the sensitivity of the material to tensile straining increasing with increasing crack width. It was found that the mean fractional change in resistivity of samples with average crack widths of 56 μm is ~3 at the strain level of 4.2%; while for samples with a larger crack width of 81 μm is ~13 (four-fold increase) at the strain level of 4.6%.

- An electrical model involving resistive and constant phase circuit elements was developed which could simulate the effect of cracking on the ECC matrix. It was observed that the crack/matrix interface plays a vital role in the impedance response. The interface resistance 'R_c' increases with strain, reflecting the physical separation caused by the micro-crack formation, while the capacitance 'CPE-$C_{o,c}$' decreases with increasing strain due to the increase in the total crack opening.

6 Potential ECC for Monitoring Moisture Ingress and Drying

6.1 Introduction

In this chapter, the influence of wetting and drying on the electrical properties of non-pre-cracked (E-ECC-NC) and pre-cracked (T-ECC-PC) ECC samples is presented. This chapter contains two parts: (i) the pre-cracking stage, which includes testing two specimens to failure and pre-cracking three specimens (T-ECC-PC) from which test samples were obtained; and (ii) wetting and drying cycles, which include measurements of mass changes and electrical properties. Regarding the latter, electrical properties measurements were conducted using Solartron over the frequency range 1 Hz–10 MHz and the data logger only at 1 kHz for seven drying and wetting cycles. Each cycle contains two parts: (i) one day of drying and one day of wetting; and (ii) one day of drying and four days of wetting (see Figure 6.1). In this chapter, the results of the relative percentage change in mass during the wetting and drying cycles for the E-ECC-NC and T-ECC-PC samples are also presented. In addition, the normalized bulk resistivity over all the wetting and drying cycles, sorptivity, degree of saturation, and the electrical response for the E-ECC-NC and T-ECC-PC samples during the drying and wetting process are presented. The impedance results during the wetting and drying are modelled using equivalent electric circuits to elucidate the underlying mechanisms.
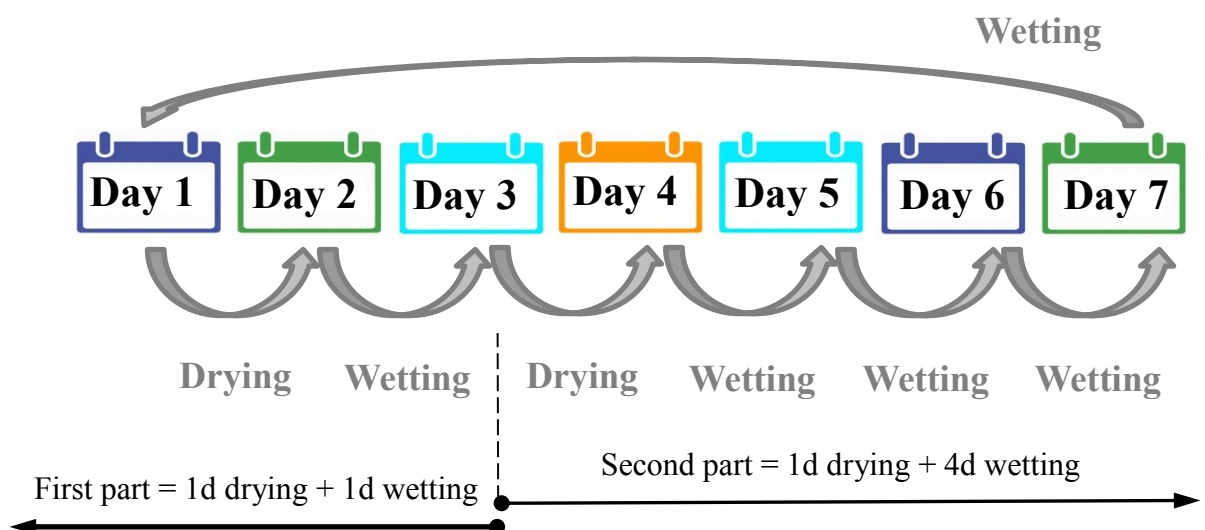
Figure 6.1: Schematic diagram showing the wetting and drying cycles.

6.2 Test Results: Stage 1

6.2.1 Pre-cracking

The stress-strain diagram of two dog-bone reference samples which were tested to failure is presented in Figure 6.2(a). The average tensile strain capacity was found to be 5.8%. The other three samples were then pre-cracked to 50% of the average tensile strain capacity obtained from the reference samples (= 3.0%), the results of which are presented in Figure 6.2(b). No premature failure was observed. These specimens were fully unloaded and then observed under a portable digital microscope, in order to document the residual widths of the micro-cracks. Figure 6.3 presents the digital micrograph images at three different positions on the precracked (T-ECC-PC-DB1/DB2/DB3) specimens, showing the variation in crack widths even within the same sample.
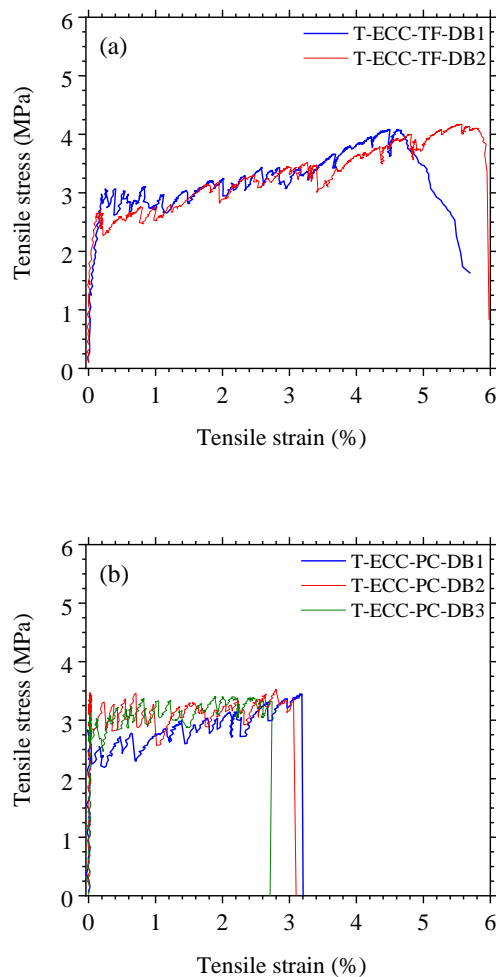
Figure 6.2: Tensile stress-strain response for (a) reference specimens which were tested to failure; and (b) other specimens which were loaded to 50% of the average tensile strain capacity of the reference specimens displayed in (a).
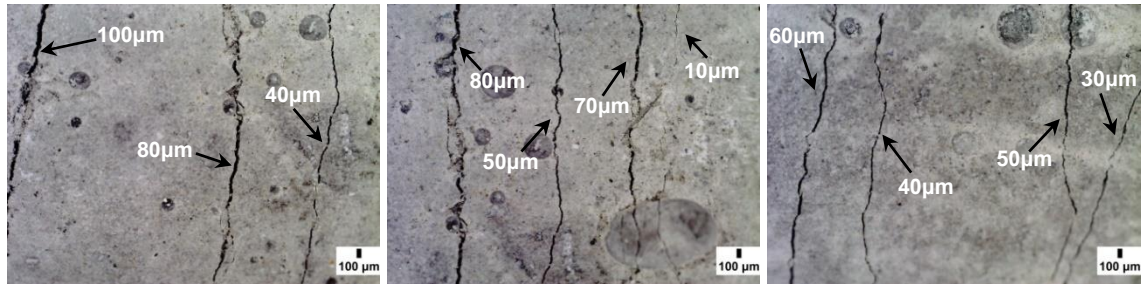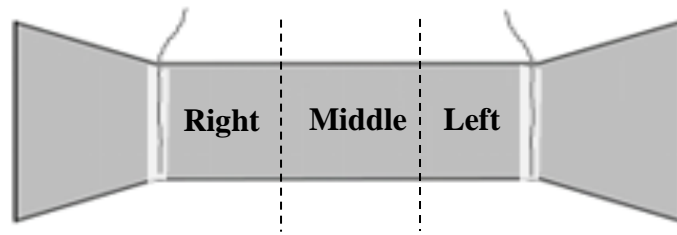
(a)
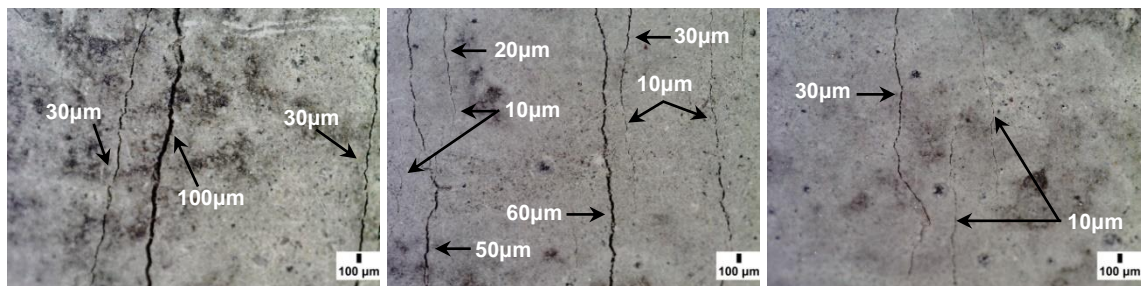
(b)
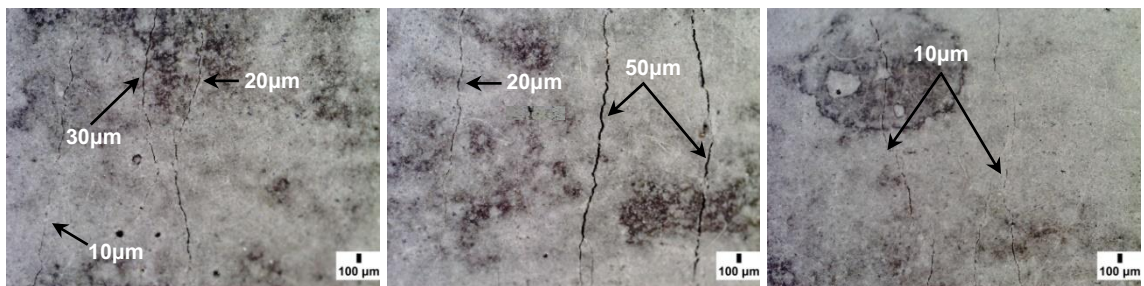
(c)

Figure 6.3: Micrograph images taken at three different locations (right, middle and left) of specimens (a) T-ECC-PC-DB1; (b) T-ECC-PC-DB2; and (c) T-ECC-PC-DB3. Images were taken using a portable digital microscope equipped with a 12MP digital camera (Veho VMS).

6.3 Test Results: Stage 2

6.3.1 Mass change during the wetting and drying cycles

The relative percentage change in mass (%) versus time is presented in Figure 6.4. It can be seen that the relative percentage change in mass for all samples decreases after 24 hr of drying and then increases when immersed in water due to evaporation and filling of water into the micro-cracks and capillary pores. The pre-cracked (T-ECC-PC) samples displayed a larger relative mass change during the 24 hr drying than the non-precracked (E-ECC-NC) samples, indicating the added contribution of the microcracks in increasing the evaporation process.

The relative percentage change in mass after water immersion of all the precracked (T-ECC-PC) samples increased more significantly than the un-cracked (E-ECC-NC) samples despite the loss of some particles in the T-ECC-PC samples (see Figure 6.5(c)). The difference in mass gain between the E-ECC-NC and T-ECC-PC sample was less significant in the early cycles. With time, the relative percentage change in mass after water immersion of the pre-cracked sample increased approximately two-fold compared with the non-pre-cracked ECC. This two-fold increase could be attributed to the new hydration products along the cracks.
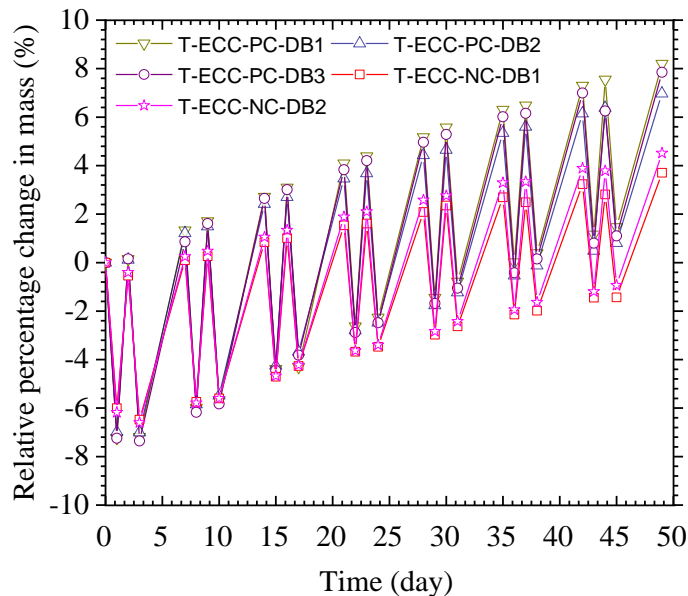
Figure 6.4: The relative percentage change in mass versus time.
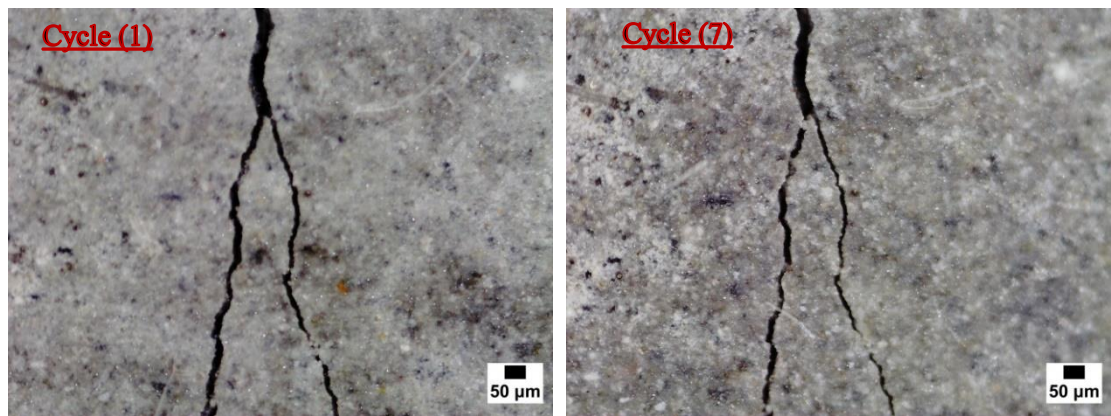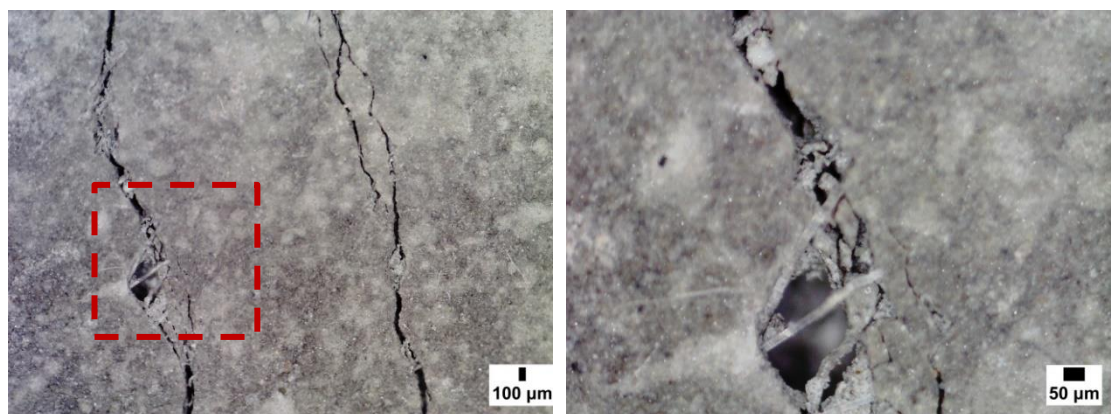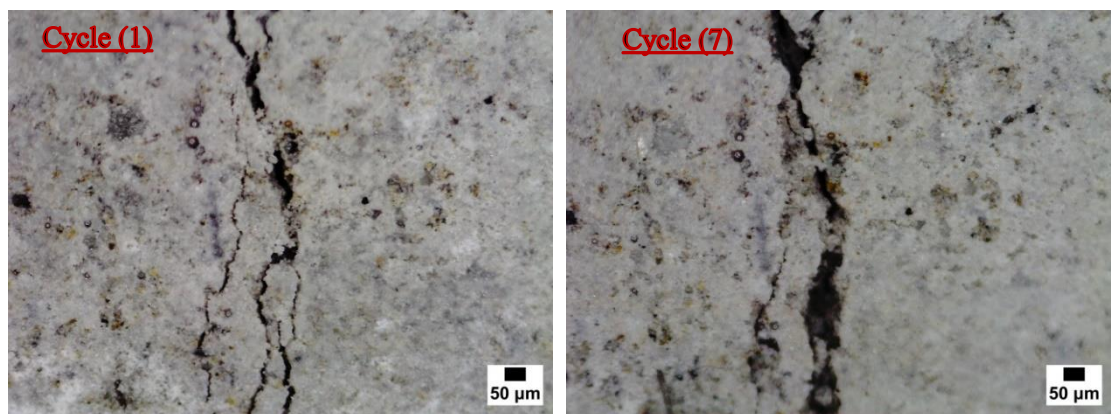
Figure 6.5: Micrograph digital images in sample T-ECC-PC-DB2 display: (a) a reduction in crack width between cycles 1 and 7; (b) a slight formation of calcium carbonate inside the micro-cracks; and (c) missing particles in cycle 7 (compared to cycle 1).

6.3.2 Results of bulk resistivity measurements

The bulk resistivity values during the wetting and drying cycles for the NC and PC samples are presented in Figures 6.6(a) and (b). It is obvious that the bulk resistivity increases during the drying process and decreases during the wetting. It is also obvious that the average bulk resistivity after one day of drying increases from ~40 kΩ at cycle 1 to ~60 kΩ at cycle 7 for the NC samples. This increase is attributed to the pore structure refinement, which was explained in chapter (4), and the leaching of pore solution into the water. On the other hand, the average bulk resistivity for the PC samples exhibits a higher increase compared with the NC samples. For example, the T-ECC-PC-DB1 sample increased from ~330 kΩ after one day of drying at cycle 1 to ~1MΩ at cycle 7 (~17 fold higher than the NC sample), while the T-ECC-PC-DB2 and T-ECC-PC-DB3 samples increased from ~200 kΩ at cycle 1 to ~580 kΩ at cycle 7 (~10 fold higher than the NC value). This significant increase in the bulk resistivity is due to the presence of the micro-cracks, which accelerate the drying process (the evaporation of the water from the pores). It is interestingly noticeable that this increase was approximately two-fold higher in the T-ECC-PC-DB1 sample compared with T-ECC-PC-DB2 and T-ECC-PC-DB3. This variation between the PC samples is attributed to the differences in the crack pattern.
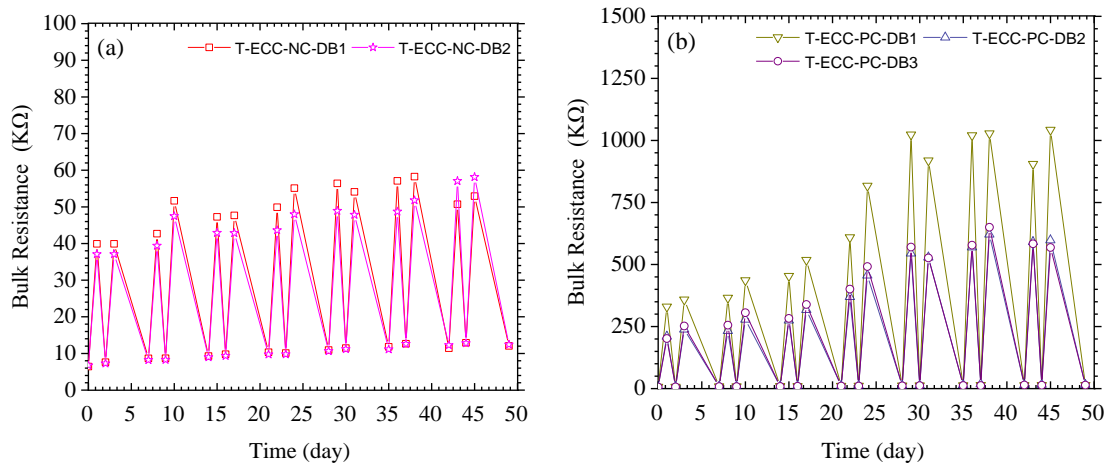
Figure 6.6: The bulk resistivity of during the wetting and drying cycles of a) NC samples and b) PC samples.

The bulk resistivity values were normalized to the bulk resistivity at the first measurement. Figure 6.7(a) and (b) present the normalized bulk resistivity for the E-ECC-NC and T-ECC-PC samples. It is evident that there is a significant variation

between the fluctuation of the E-ECC-NC and T-ECC-PC samples. The peak values within the fluctuation of the E-ECC-NC samples were almost constant for all cycles (~7). While the peak values of the T-ECC-PC samples were significantly higher than the E-ECC-NC samples, the peak values of T-ECC-PC-DB1 was (~50) at the beginning (cycle 1) and increased to (~160) at cycle 7, while both T-ECC-PC-DB2 and T-ECC-PC-DB3 were (~30) and increased to (~95) at cycle 7. This significant increase from cycle 1 to cycle 7 of the PC samples is attributed to the formation of the new hydration products along the crack.
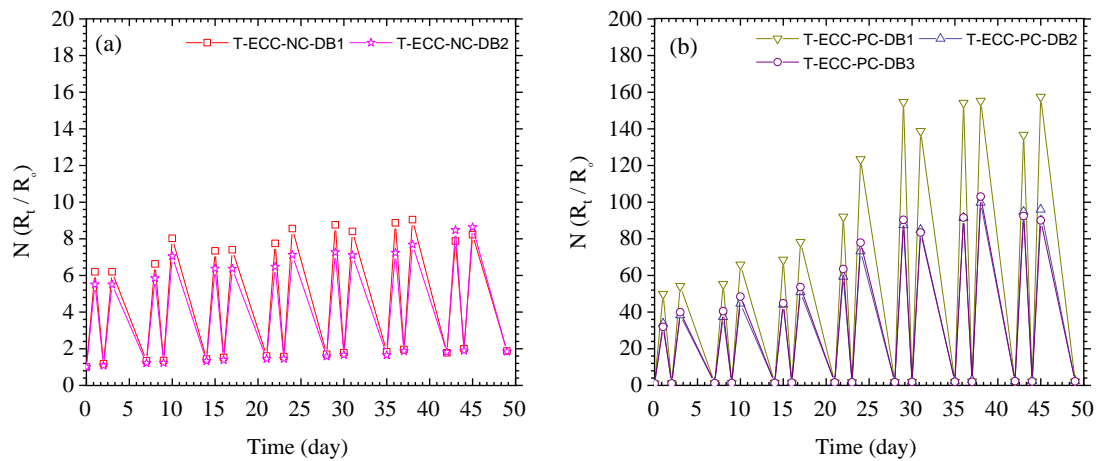
Figure 6.7: The corresponding normalized bulk resistivity over the wetting and drying cycles for a) NC samples and b) PC samples.

6.3.3 Sorptivity

In order to show the effects of micro-cracks on the capillary suction (absorption) of ECC, Figure 6.8 presents the average cumulative water absorption (cumulative volumetric gain per unit area) against square root time of PC and NC samples. It can be clearly seen that the cumulative volumetric gain per unit surface area (mm^3/mm^2) in the PC and NC samples increased with the square root of time. It was found that there was a linear relationship between the cumulative water absorption of NC samples and the square root of time. It is obvious from Figure 6.8 that the presence of micro-cracks within the matrix leads to a significant increase in the cumulative water absorption. When the ECC matrix is damaged, the initial rate of capillary suction (absorption) is very quick; this implies that the capillary pores and cracks become saturated in a short period of time. It can also be observe from Figure 6.8 that there is a non-linear relationship between the cumulative water absorption of PC samples and the square root of time. Hall and Hoff (2002) explained that this non-linear increase of the micro-

cracked ECC samples with the square root of time was most likely because of the capillary absorption into the crack, which is considered weak, and reaches capillary rise equilibrium against gravity during the sorptivity test.

The cumulative absorption of water by the PC samples originates from two processes: i) the absorption into the un-cracked part and ii) the absorption into the cracked part. In (i), the capillary forces are strong compared with the opposing gravitational forces, while in (ii), the absorption reaches a limiting equilibrium value (Sahmaran and Li, 2009). Sahmaran and Li (2009) provided another reason for the non-linear increase, which could be due to the quick filling of the micro-cracks in the water because of the high capillary suction. Thus the absorption may happen from the crack plane, and that the exposed cross-sectional area used to calculate the cumulative absorption of water of the PC samples is incorrect.
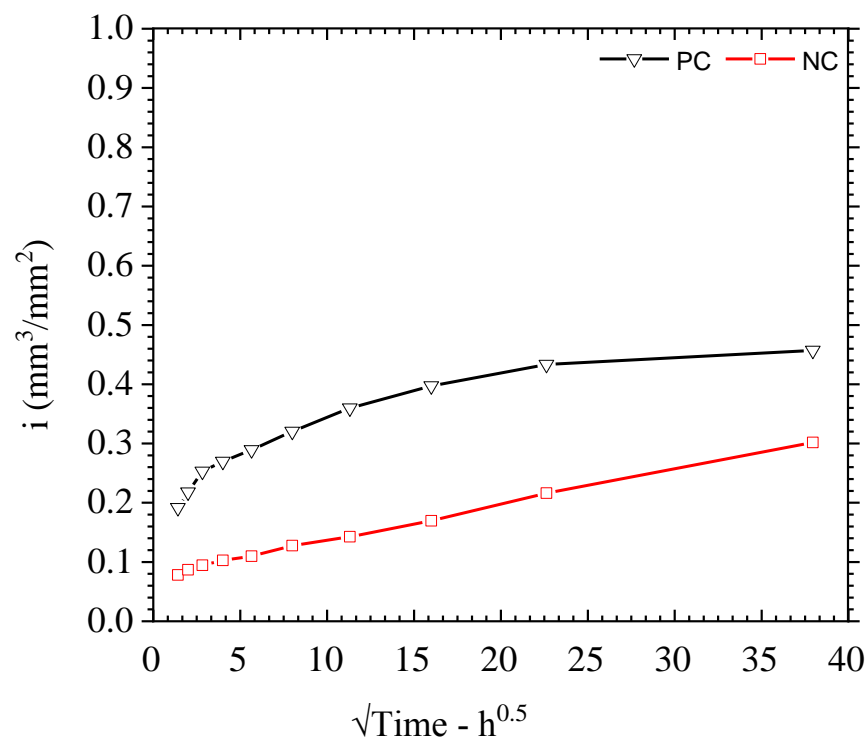
Figure 6.8: Typical cumulative water absorption result as a function of square root of time for PC and NC samples.

Figures 6.9 present the average cumulative volumetric gain per unit area against square root time of PC and NC samples during the wetting and drying at different cycles, with the best-fit-line taking the form. It was found that the cumulative volumetric gain per

unit area increases with the square root of time during the wetting and drying cycles. It was also discovered that the cumulative volumetric gain per unit area for both NC and PC samples decreases with time during the wetting and drying cycles. This can be attributed to two reasons: i) the hardness effect, with increasing the samples' age making the water penetration and water evaporation from the pores more difficult; and ii) pore refinement effects due to the on-going hydration and pozzolanic reaction, making the size of the pore smaller, causing a reduction in the pore capacity.
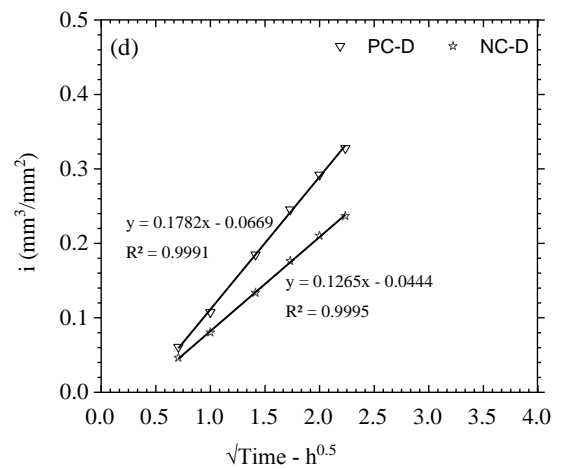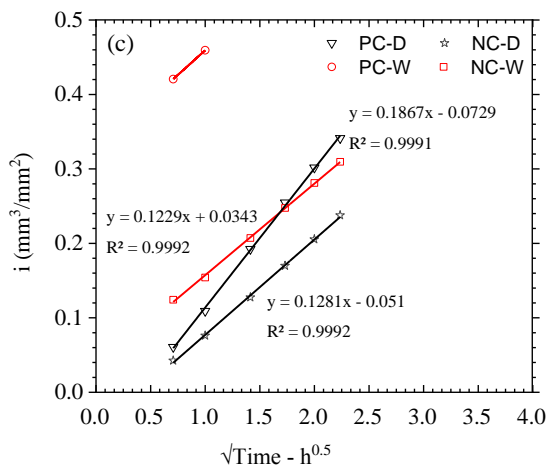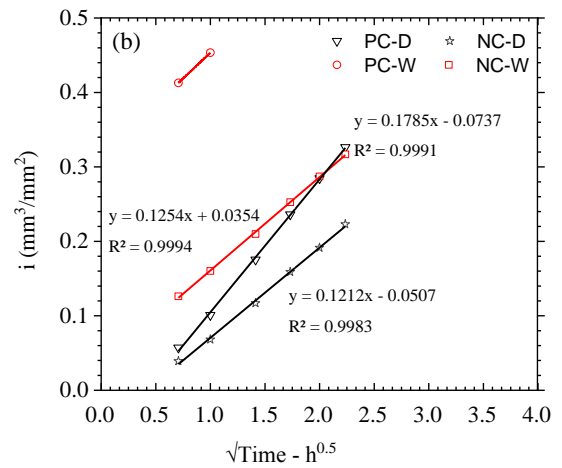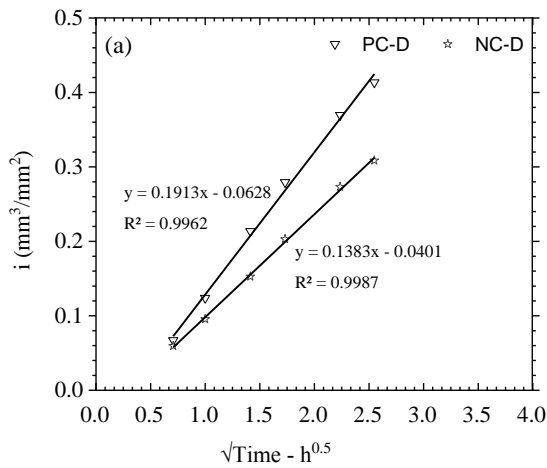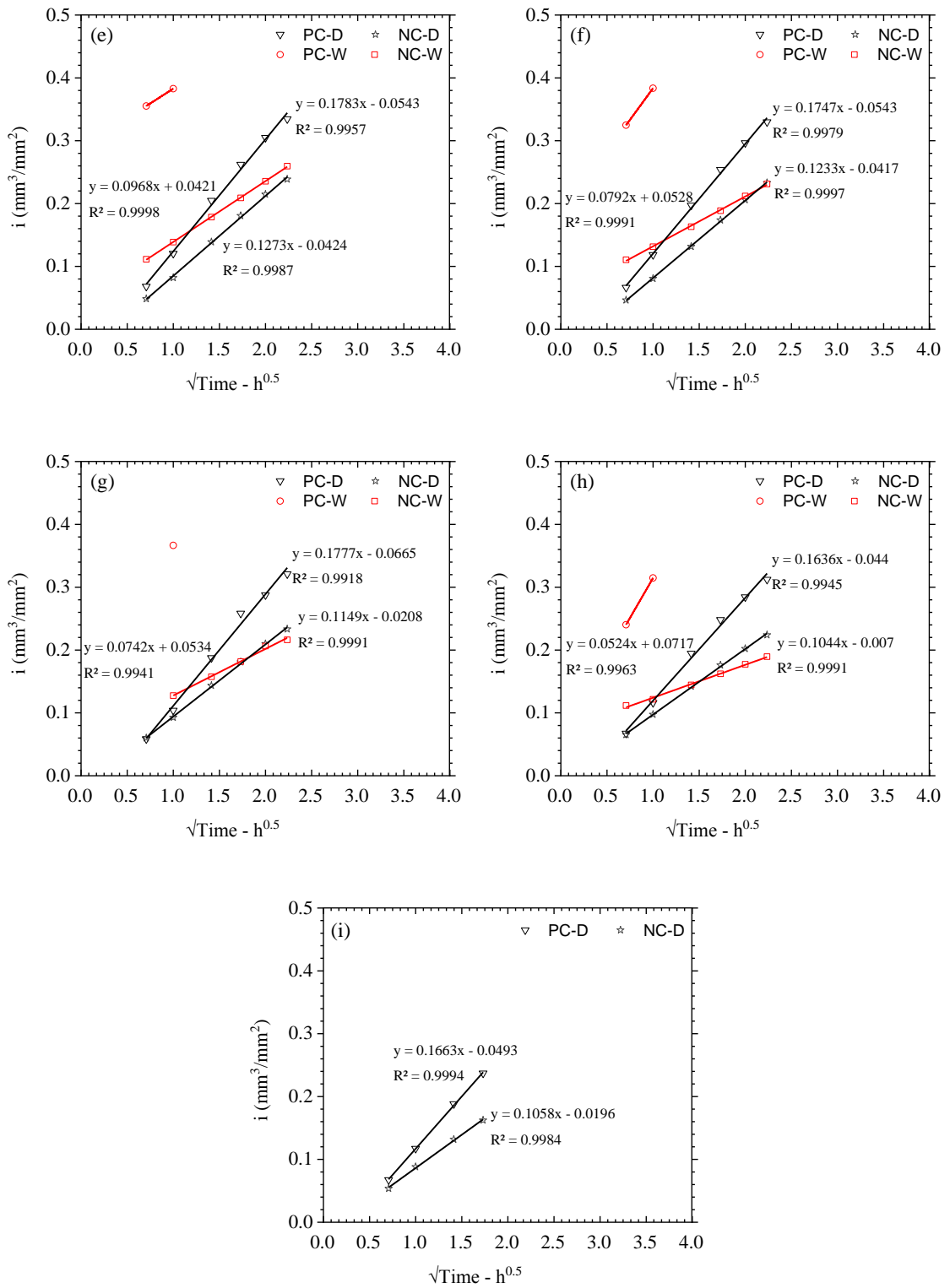
Figure 6.9: Cumulative water gain per unit area (mm^3/mm^2) vs square root of time for PC and NC samples during; a) drying for C2-second part b) wetting and drying for C3-first part; c) wetting and drying for C3-second part; d) drying for C4-first part; e) wetting and drying for C4-second part; f) wetting and drying for C5-first part; g) wetting and drying for C5-second part; h) wetting and drying for C7-first part; and i) drying for C7-second part.

6.3.4 Degree of saturation

Regarding the resistivity between two electrodes, Figure 6.10 displays schematic diagrams of an idealized representation of cementitious material when the cementitious material specimen is saturated and partially-saturated. The saturated cementitious material (i.e., prior preconditioning) is characterized by a system in two phases including solids and pore water (un-hydrated cement and gel), whilst partially-saturated concrete (i.e., after preconditioning) is characterized by a model of three phases including solids, pore water, and air (or solvent of high resistivity). Based on an electrical point of view, the main conduction path of current is the pore water (resistivity defined as ρ_w) because both air and solids are considered non-conductive. Assuming that a material unit cube is taken for each model, the electrical resistance, named R_o, for the saturated cementitious material (See Figure 6.10) can be defined by:

$$R_o = \frac{\rho_w}{\phi^m} \tag{6.1}$$
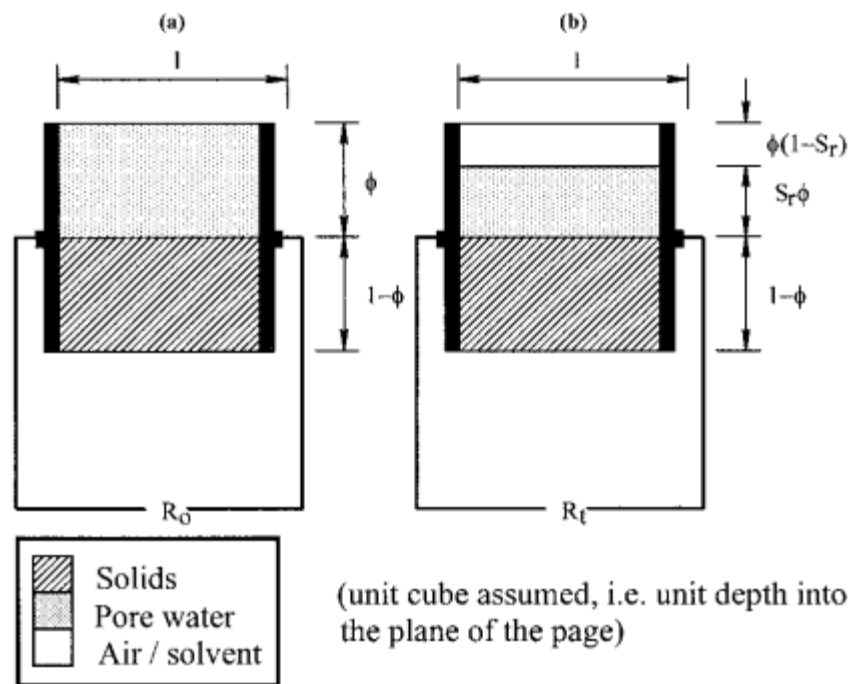
Figure 6.10: Schematic diagrams that display the idealized representation of cementitious material (Basheer et al., 2000).

Where ϕ is numerically equivalent to the capillaries' porosity, which represents in the model illustrated the cross-sectional area of the conduction path (the available conduction area), and ρ_w is the pore water resistivity. The available conduction area by the pore network is ϕ^m not, ϕ, as the exponent m which is also named as cementation factor, takes into consideration the capillary pores' tortuosity between the electrodes. The cementation factor values for hardened cement pastes (Christensen et al. 1994) and rocks (Dullien 1992) are in the range of 1.5–3.0.

The measured resistance at any time t during the preconditioning, which is termed as R_t can be represented as:

$$R_t = \frac{\rho_w}{(S_r \, \phi)^m} \tag{6.2}$$

Where, S_r represents the degree of saturation of the pore networks, therefore:

$$\frac{R_t}{R_o} = \left(\frac{1}{S_r}\right)^m \tag{6.3}$$

Thus:

$$S_r = \left(\frac{R_t}{R_o}\right)^{(1/m)} \times 100\% \tag{6.4}$$

Consequently, the change in the R_t/R_o ratio represents the change in the degree of saturation of the cementitious material. Figures 6.11(b) and (c) display the R_t/R_o ratio for the PC and NC samples for cycle 1-second part and cycle 7-second part, with m value was approximated as a value of 2. Figure 6.11(a) displays the location of the first cycle (1-second part) and the last cycle (7-second part) during the drying process. It is obvious that the initial resistance value is equal to 1, and it increases with increasing the drying process (time), reflecting a reduction of the pore saturation level in the ECC. It can be clearly seen that the NC samples exhibit a gradual increase in the ratio with time, from 1 at the initial time (t = 0) to approximately ~2 after one day of drying for the cycle 1-second part and the cycle 7-second part. On the other hand, the PC samples increased significantly compared with the NC samples. For example, the average ratio after one day of drying of the PC samples increased to ~6.5 in the cycle 1-second part and ~7 in the cycle 7-second part, which is almost 3 times higher than the NC samples. This indicates that the presence of micro-cracks accelerates the decreasing level of pore saturation.
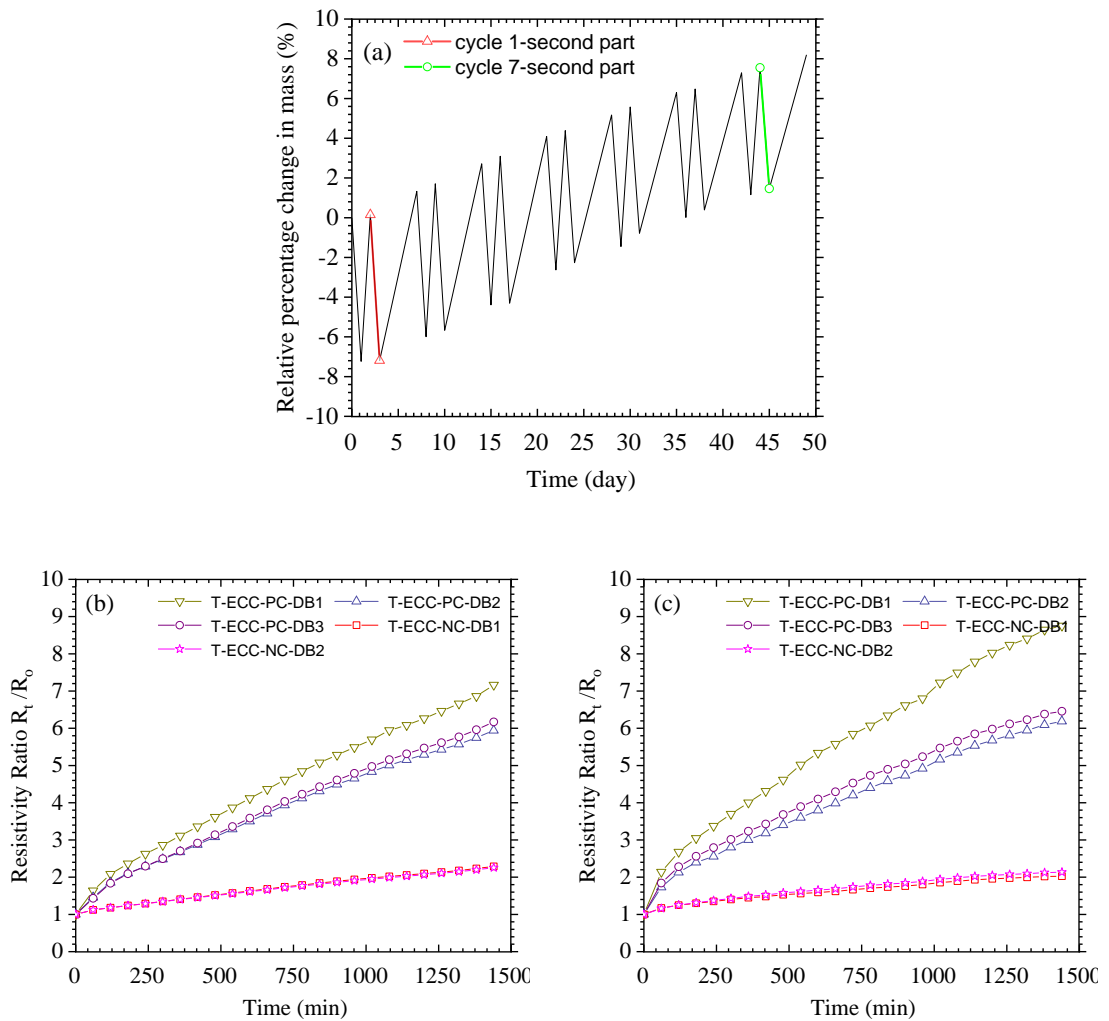
Figure 6.11: a) The location of the cycle 1-second part and the cycle 7-second part during the drying process. The changes in the degree of saturation for Nc and PC samples in b) cycle 1-second part; and c) cycle 7-second part.

6.3.5 Drying cycle results

6.3.5.1 *Impedance response during the drying process*

During the drying process, Solartron was used to take the electrical measurements during 24hrs of T-ECC-PC-DB1 sample for all cycles, except for cycle 7 (first part), the electrical measurements were taken for E-ECC-NC-DB2 sample to have 24 hr data for E-ECC-NC sample. Since the Solartron equipment can take the electrical measurements during 24 hr of drying for only one sample, the electrical measurements of all the samples were only taken before and after each drying cycle using this equipment. Therefore, Figures 6.12(b) and (c) present the impedance response during the 24 hr drying for E-ECC-NC-DB2 in Cycle (7-first part) and T-ECC-PC-DB1 in cycle (6-first part), respectively. For reasons of clarity, only the response every 1 hr is presented.

Figure 6.12(a) illustrates the definition of cycle 6 (first part) and cycle 7 (first part) throughout the drying/wetting process. With reference to Figures 6.12(b) and (c), it is clear that both samples showed an increase in resistance and reactance values as drying time increased. This increase is considerably higher for the T-ECC-PC-DB1 sample (attaining a value of ~1 MΩ after 24 hr of drying, or a 17-times increase) than for the E-ECC-NC-DB2 sample (attaining a value of ~60 kΩ after 24 hr of drying). It can also be clearly seen that the impedance response for all E-ECC-NC and T-ECC-PC samples at all stages during the drying process displayed the typical impedance response consisting of a low-frequency spur, an intermediate "plateau" region, and a high-frequency bulk arc.
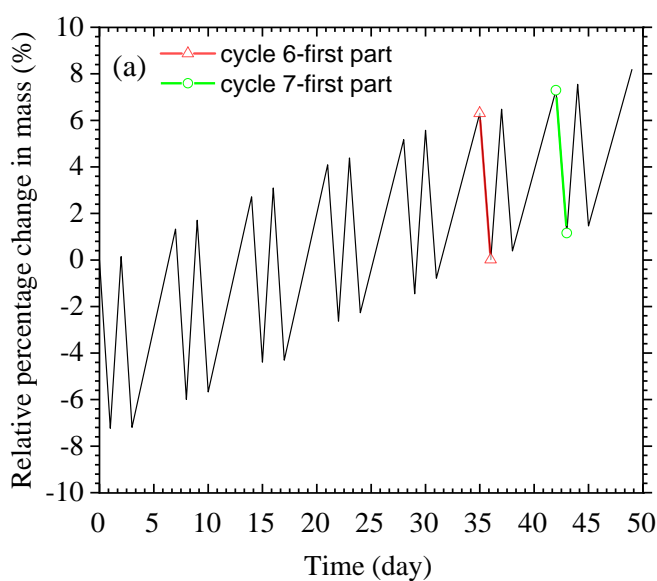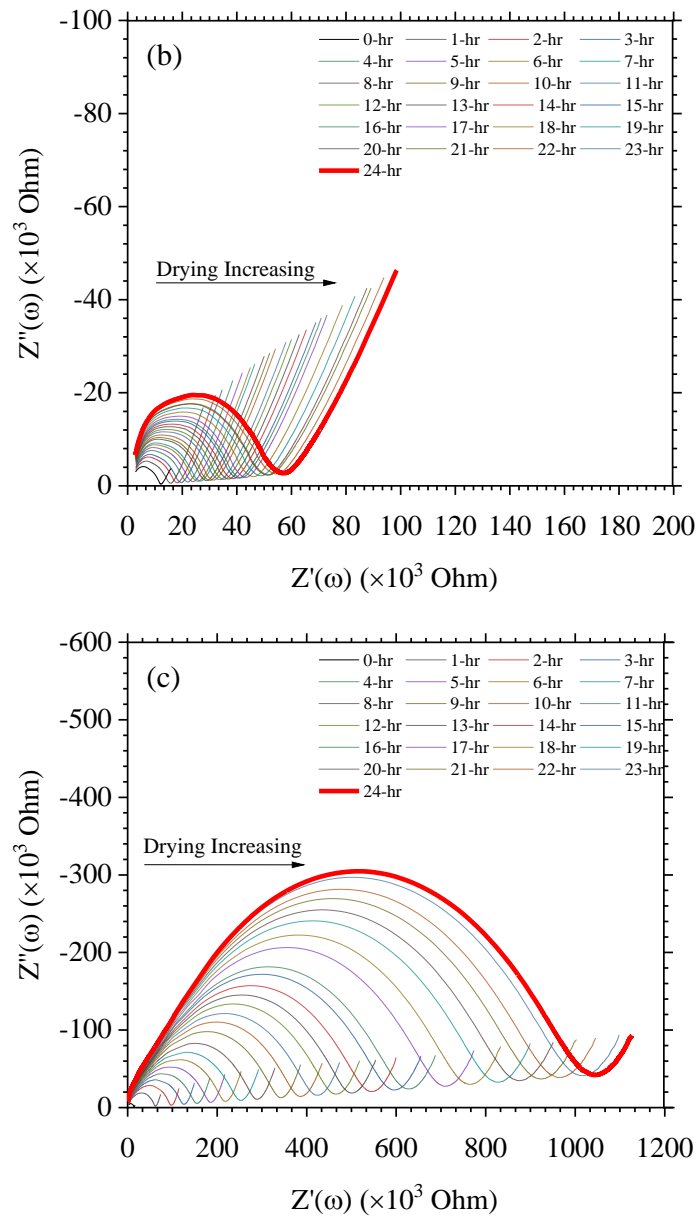
Figure 6.12: (a) The definition of cycle 6 (first part) and cycle 7 (first part) during the drying/wetting process. Impedance response during 24 hr of drying for specimen (b) E-ECC-NC-DB2 during cycle 7 (first part); and (c) T-ECC-PC-DB1 during cycle 6 (first part).

To demonstrate the effect of drying on the electrical properties, the impedance responses of the first cycle (1-second part) and the last cycle (7-second part) of the E-ECC-NC and T-ECC-PC ECC samples before and after drying for 24 hr are presented in Figures 6.13(a)–(d). With reference to Figures 6.13(a) and (b), it can be clearly seen that the average bulk resistivity before starting the drying process was ~7 kΩ at the cycle 1-second part and increased to ~13.5 kΩ at cycle 7-second part. This increase is

due to the ongoing hydration and pozzolanic reaction, which is explained well in chapter (4), and possibly due to the leaching of pore solution into the water.

In addition, it is noticeable that the crack pattern has a significant impact on the impedance response during the drying process, as the evaporation process will increase with increasing crack width. Consider, for example, the bulk impedance values of the T-ECC-PC samples in cycle (1-second part), which increased from ~6 kΩ before drying to ~350 kΩ for T-ECC-PC-DB1, ~230 kΩ for T-ECC-PC-DB2 and ~250 kΩ for T-ECC-PC-DB3 after one day of drying. See Figure 6.3 for further clarity on the variation of the crack width that causes this difference in the bulk impedance values. On the other hand, the bulk impedance values in cycle (7-second part) increased from ~13.5 kΩ before drying to ~1000 kΩ for T-ECC-PC-DB1, ~630 kΩ for T-ECC-PC-DB2 and ~630 kΩ for T-ECC-PC-DB3 after one day of drying. Interestingly, T-ECC-PC-DB1 and T-ECC-PC-DB2 show almost similar bulk impedance values in the cycle (7-second part), although they behaved differently in the cycle (1-second part). This could be associated with the reduction in the crack width of some of the samples, the slight formation of calcium carbonate (See Figure 6.5(a) and 6.5(b), or the loss of some particles (See Figure 6.5(c)). On the other hand, the bulk impedance values of the E-ECC-NC samples were close to each other with an increase from $~6\times10^3\Omega$ before drying to ~33 kΩ of E-ECC-NC-DB1 and ~37 kΩ of E-ECC-NC-DB2 in cycle (1-second part) and ~47 kΩ of E-ECC-NC-DB1 and ~55 kΩ of E-ECC-NC-DB2 in cycle (7-second part) after one day of drying.
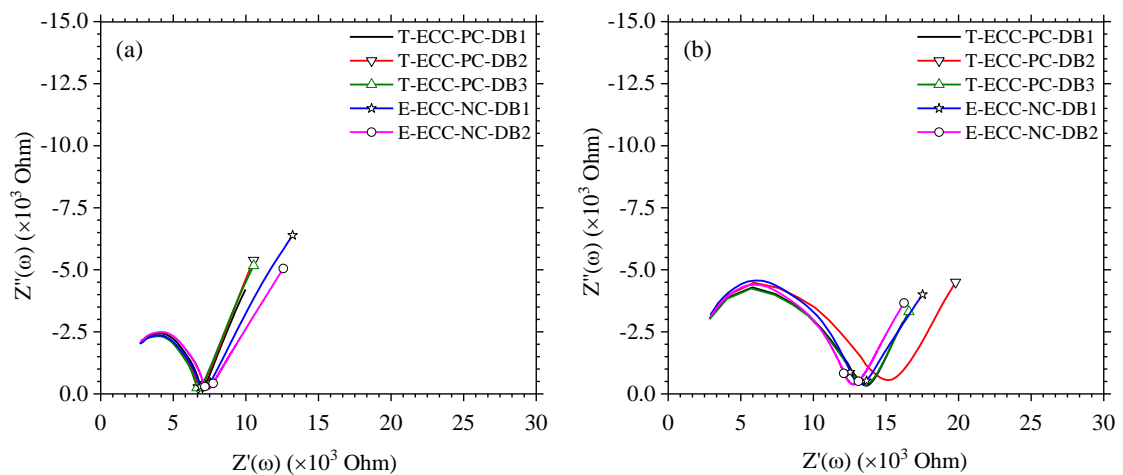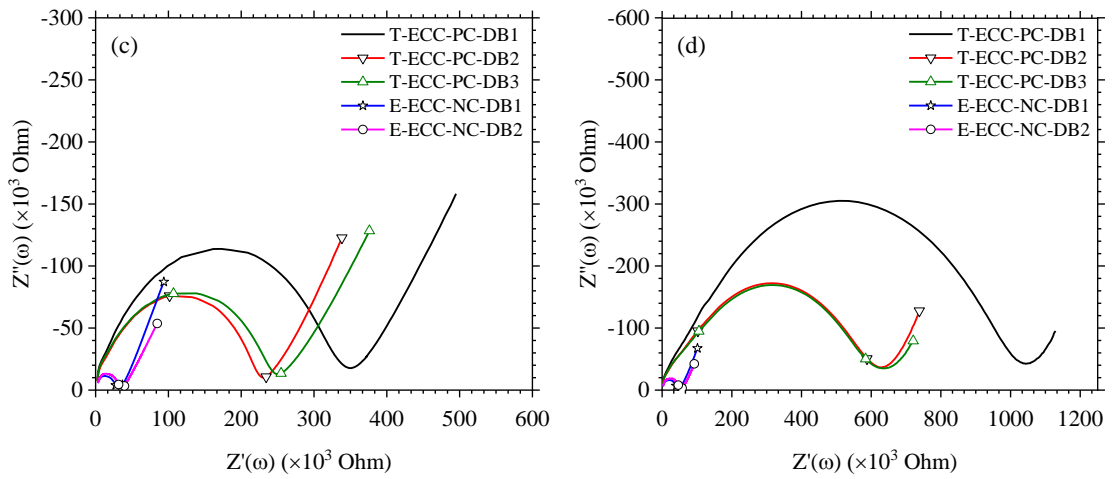
Figure 6.13: Impedance response of all samples before starting the drying process during (a) cycle 1 (second part) and (b) cycle 7 (second part). Impedance response of all samples after 24 hr of drying for (c) cycle 1 (second part) and (d) cycle 7 (second part).

6.3.5.2 *Relative Permittivity and Conductivity during the drying process*

The relative permittivity of E-ECC-NC-DB2 during cycle 7 (first part) and T-ECC-PC-DB1 in cycle (6-first part) during 24 hr of drying is displayed in Figure 6.14(a) and (b), respectively. For reasons of clarity, only the response every 1 hr is presented. It can be clearly noted that the relative permittivity plots of both samples decrease with increasing frequency because of the relaxation of superimposed polarization mechanisms that operate within the mixture. It can also be noted that the relative permittivity plots for both samples decrease with increasing the drying process. This decrease was considerable in T-ECC-PC-DB1 compared with E-ECC-NC-DB2. It is obvious that the relative permittivity of T-ECC-PC-DB1 at low frequency is very sensitive to drying. It is interesting to note that the relative permittivity plots of the T-ECC-PC-DB1 display an enhancement in relative permittivity at high frequencies, which lead to the emergence of a shoulder compared to the controlled samples due to the new polarization mechanism that appeared from the micro-cracks/matrix interface.
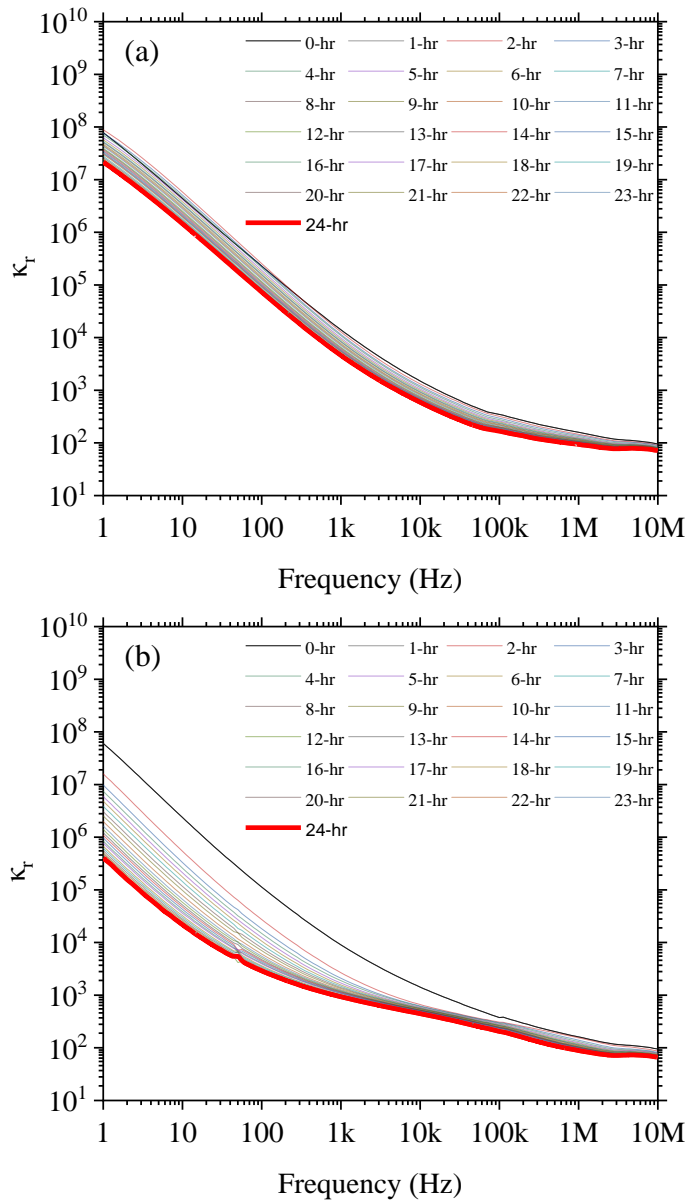
Figure 6.14: Relative permittivity for a) E-ECC-NC-DB2 in cycle (7-first part) and
b) T-ECC-PC-DB1 in cycle (6-first part) after 24 hr of drying.

Figure 6.15(a) and 6.15(b) show the relative permittivity versus frequency of cycle (1-second part) and cycle (7-second part), respectively for the E-ECC-NC and T-ECC-PC ECC samples after 24 hr of drying. It is also noticeable that the relative permittivity plots vary between the E-ECC-NC and T-ECC-PC samples. For example, the relative permittivity in cycle (1-second part) of both E-ECC-NC samples was $\sim 3.0 \times 10^7$ at 1 Hz, while the relative permittivity of the T-ECC-PC samples was $\sim 3.0 \times 10^6$ of T-ECC-PC-DB1, $\sim 5.0 \times 10^6$ of T-ECC-PC-DB2 and $\sim 4.0 \times 10^6$ of T-ECC-PC-DB3 at 1 Hz. There is a ~ 1.0 order of magnitude difference between them. This difference is

associated with a decrease in relaxation time with increased evaporation and a change in the dispersive polarization process with drying. Furthermore, it is interesting to note that in cycle (7-second part), the enhancement of the relative permittivity shifted to the left along the Z' axis toward the origin, as in cycle (7-second part), there has been a shift in the time constant due to the wetting cycles (on-going hydration), together with the shift in time constant with increasing the evaporation.
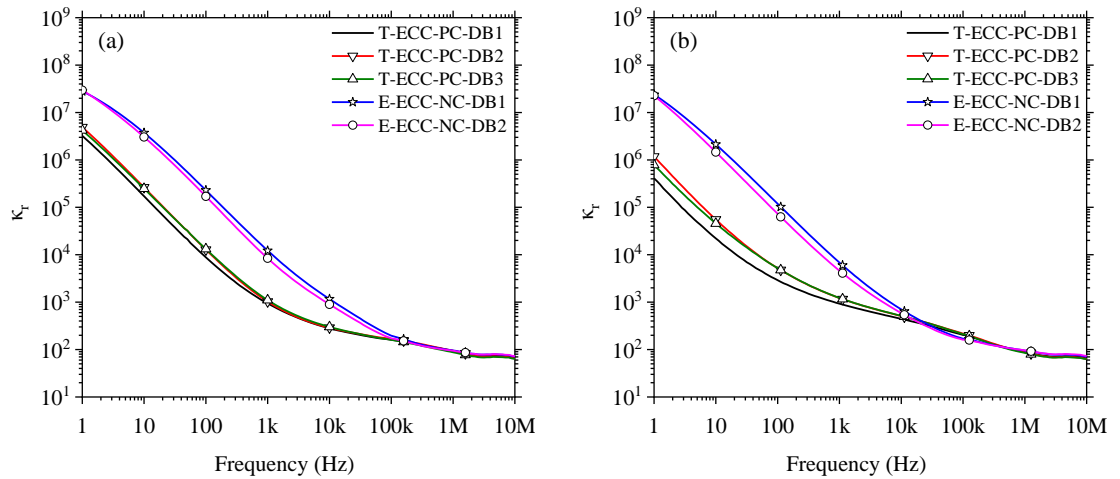
Figure 6.15: Relative permittivity of all samples after 24 hr of drying for a) cycle (1-second part); and b) cycle (7-second part).

Figures 6.16(a) and 6.16(b) show the conductivity responses of E-ECC-NC-DB2 in cycle (7-first part) and T-ECC-PC-DB1 in cycle (7-second part) during the first 24 hours of drying. For reasons of clarity, only the response every 1 hr is presented. It can be clearly seen that the conductivity decreases with the increasing evaporation process. This decrease was more significant in T-ECC-PC-DB1 compared with E-ECC-NC-DB2. In addition, it is very interesting to observe the sharp contrast in conductivity between the E-ECC-NC-DB2 and T-ECC-PC-DB1, where an enhancement in the conductivity was found at high frequencies of T-ECC-PC-DB1. This enhancement in conductivity is attributed to the relaxation of the new polarization mechanism that emerged from the cracks/matrix interface together with the relaxation of the interfacial processes.
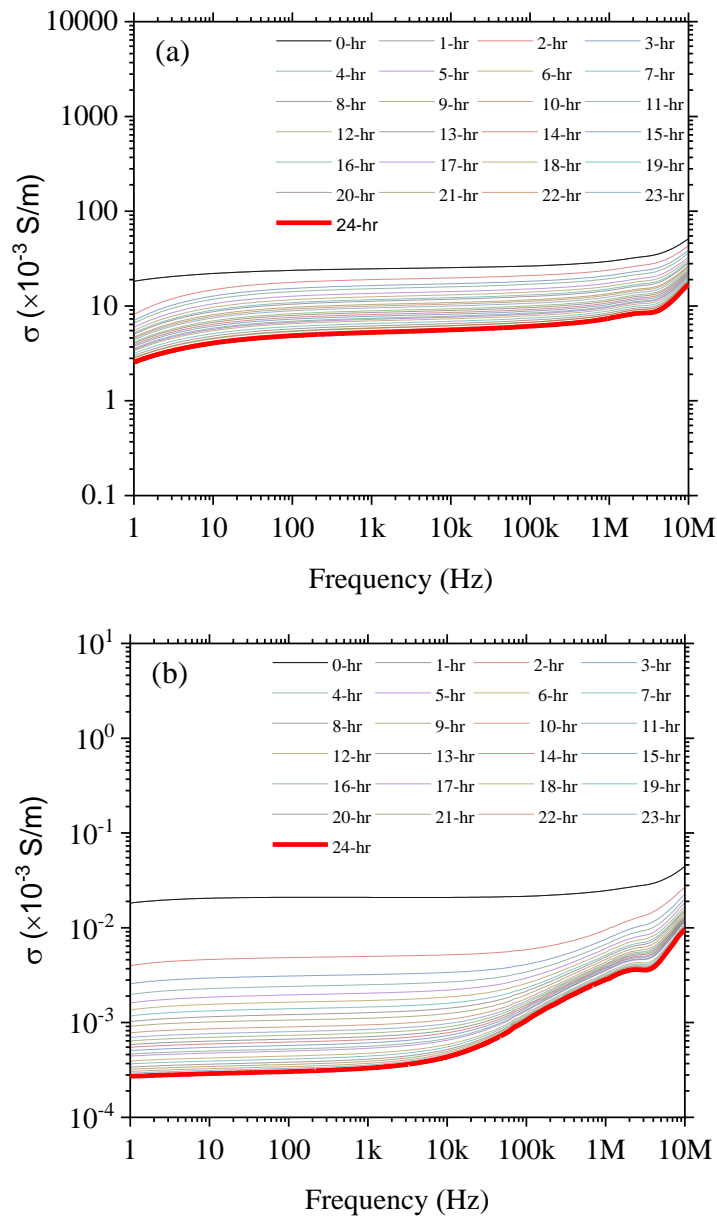
Figure 6.14: Conductivity for a) E-ECC-NC-DB2 in cycle (7-first part) and b) T-ECC-PC-DB1 in cycle (6-first part) after 24 hours of drying.

Figures 6.17(a) and 6.17(b) depict the conductivity versus frequency of cycle (1-second part) and cycle (7-second part) for the E-ECC-NC and T-ECC-PC samples after 24 hours of drying. It can be clearly seen that the conductivity of all samples increases with increasing frequency due to the relaxation/dispersion of the polarization process, together with the movement of the ions in the capillary pore network. Consider, for example, the conductivity of the controlled samples E-ECC-NC-DB1 and E-ECC-NC-DB2 has attained values of ~2×10^{-3} S/m and ~3×10^{-3} S/m at 1 Hz, respectively, which increases for both of them to ~2×10^{-2} S/m at 10 MHz. On the other hand, the

conductivity of the T-ECC-PC samples was found ~6×10^{-4} S/m of T-ECC-PC-DB1, ~8×10^{-4} S/m of T-ECC-PC-DB2, and ~7×10^{-4} S/m of T-ECC-PC-DB3 at 1 Hz, which all increases to ~1×10^{-2} S/m at 10 MHz. This significant decrease in conductivity in the T-ECC-PC samples compared to the E-ECC-NC samples is associated with the increase in evaporation in the T-ECC-PC samples because of the cracks caused by water reduction in conduction paths within the matrix. Moreover, it is interesting to observe the increase of the conductivity enhancement in cycle (7-second part) due to the cut-off frequency (reduction of the relaxation time), which causes a shift of the conductivity plot to the left.
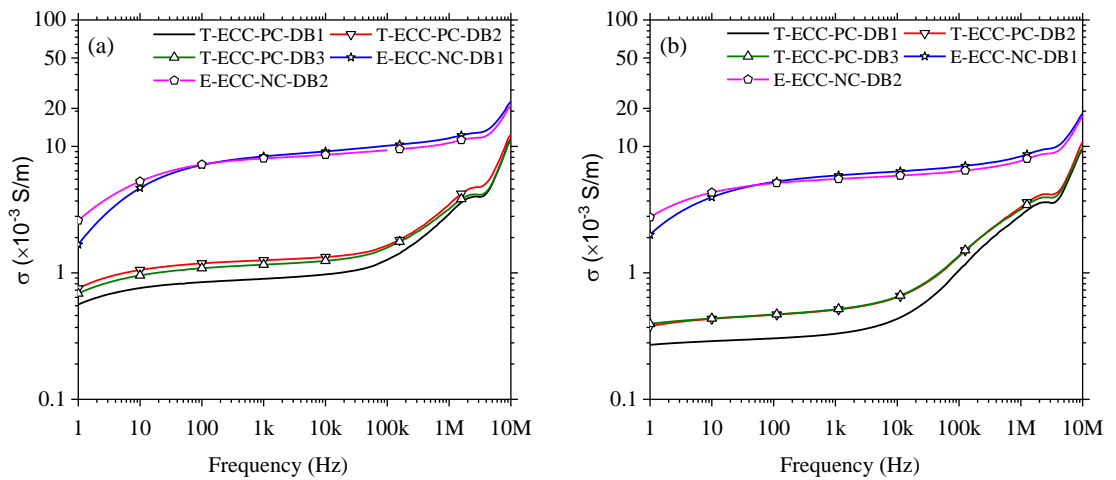
Figure 6.15: Conductivity of all samples after 24 hr of drying for a) cycle (7-first part); and b) cycle (7-second part).

6.3.6 Results of wetting cycle

6.3.6.1 Impedance response during wetting

In order to show the effect of wetting on E-ECC-NC and T-ECC-PC samples after a short period of time (30 minutes) (Note: the time (30 minutes) was chosen based on the ability to complete a full sweep measurement (13 spot frequencies) without measuring the evaporation of the water from the cracks) and a longer period of time (4 days) (Note: this is done at the end of each cycle and when the sample is fully saturated); the results of the first cycle (1-second part) and the last cycle (7-second part) of the E-ECC-NC and T-ECC-PC after 30 minutes and 4 days wetting in the water are presented in Figures 6.18(b)–(e). The location of the cycle 1-second part and the cycle 7-second part during the wetting process is presented in Figure 6.18 (a). It was found that all samples displayed a decrease in impedance after their exposure to water due to the filling of capillary pores. This phenomenon is caused by the filling of water in the micro-cracks,

which acts as a bridge to the conducting path (a pre-cracked sample behaves as if it is un-cracked). With reference to Figure 6.18(b), it was found that after the samples first exposure to water for a small duration of time (30 minutes) in cycle (1-second part), the decrease in impedance operated faster for the T-ECC-PC samples compared for the E-ECC-NC samples. This is attributed to the water intrusion from all directions through the cracks to fill the capillary pores. Subsequently, the samples that have a bigger crack width and/or a greater number of cracks have the biggest decrease in impedance. Meanwhile, based on the results shown in Figure 6.18(b), the bulk impedance of both controlled samples is approximately the same. It is distinctive that the impedance response of cycle (7-second part) for the E-ECC-NC and T-ECC-PC samples after 30 minutes of wetting in the water exhibits the same cycle (1-second part) findings shown in Figure 6.18(d), with a decrease in the impedance values when the samples are exposed to water, with the exception of the E-ECC-NC samples, which showed a variation in bulk impedance. This is due to a hardness effect of the samples which causes difficulties with water intrusion at exactly same time into the isolated pores. After 4 days of submersion (see Figure 6.18(c)) for cycle (1-second part), it was found that the impedance of all samples matched approximately at the same point at ~8 kΩ. While, regarding cycle (7-second part) shown in Figure 6.18e), the bulk impedance values for all samples after 4 days of wetting did not match in the same point as in cycle (1-second part) displayed in Figure 6.18(c). It was found that the impedance response of the T-ECC-PC samples was higher than that of the E-ECC-NC samples. This is related to the healing of some of the micro-cracks or the loss of some particles, as explained above.
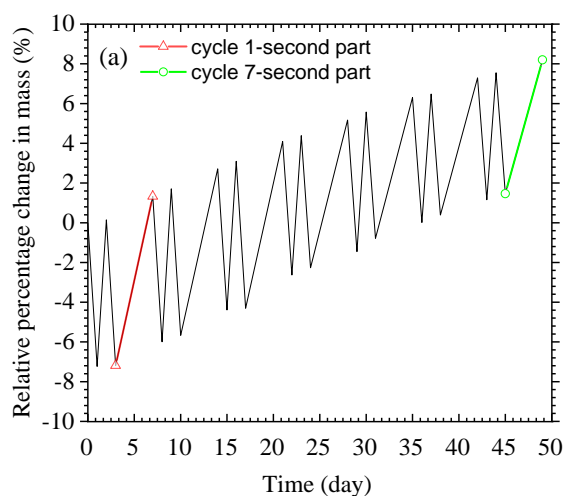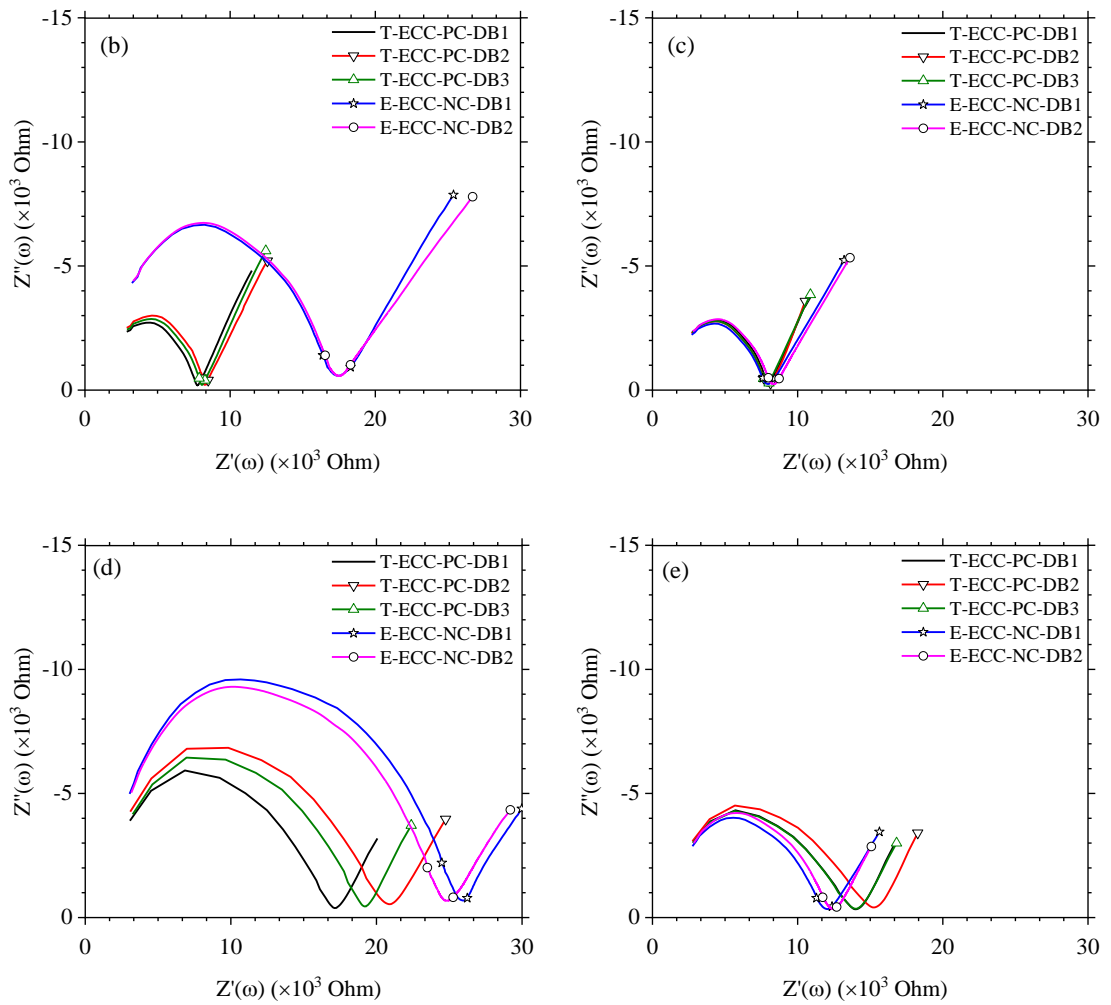
Figure 6.18: a) the location of cycle 1-second part and cycle 7-second part during the wetting process. The impedance response for the controlled and pre-cracked ECC samples after b) 30 min of wetting in cycle (1-second part); c) 4 days of wetting in cycle (1-second part); d) 30 min of wetting in cycle (7-second part); and e) 4 days of wetting in cycle (7-second part).

Figures 6.19(a) and 6.19(b) show the impedance response of E-ECC-NC-DB2 at various timings ranging from 30 minutes to 4 hours of wetting for a) cycle (1-second part) and b) cycle (7-second part). It can be clearly seen that the bulk impedance response and then bulk arc of all plots for both cycle (1-second part) and cycle (7-second part) decrease as the wetting time increases. With reference to Figure 6.19(a), it is clear that the decrease in bulk impedance was significant at the start of the submersion (particularly between the first 30 minutes and 1 hour), and then gradually decreased. This is due to the sample's behaviour, which acts as a sponge when it is first exposed to water. As the pores near the external surface are filled with water, the

penetration of water into the pores becomes harder. While there was no difference in the impedance decrease between the first 30 minutes and 1 hour in cycle (7-second part) shown in Figure 6.19(b), after a longer submersion in water, a decrease in impedance was noticeable due to the sample's hardness. The range of impedance decrease was higher in the cycle (1-second part) than in the cycle (7-second part). Consider that the bulk impedance of cycle (1-second part) decreased from (~17.5 × 10³ Ω) after 30 min of submersion to (~8 × 10³ Ω) after 4 hr, whilst it decreased from (~25 × 10³ Ω) at 30 min to (~21 × 10³ Ω) at 4 hr in cycle (7-second part).
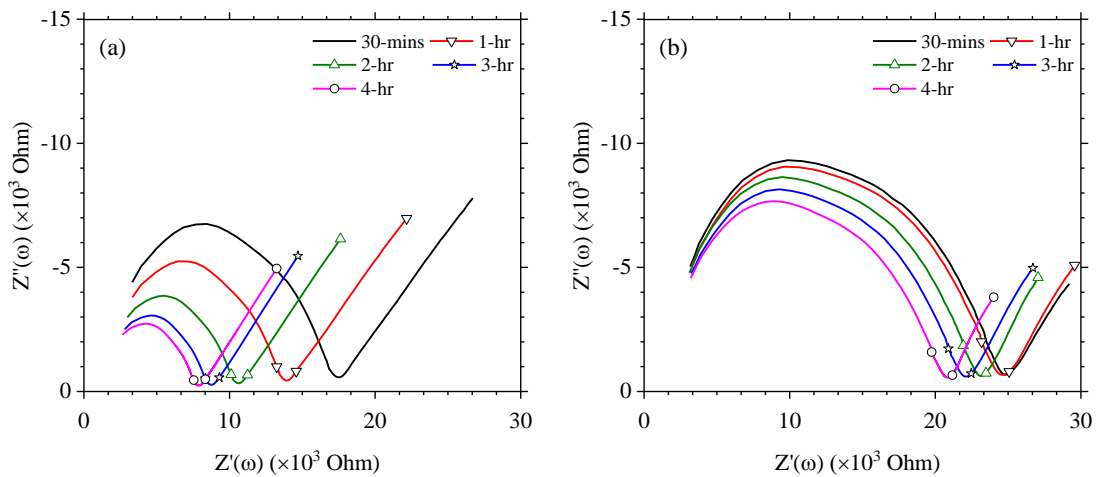
Figure 6.19: Impedance response staged at various timings from 30 min up to 4 hr of wetting for E-ECC-NC-DB2 of a) cycle (1-second part) and b) cycle (7-second part).

6.3.6.2 *Relative permittivity and Conductivity during the wetting process*

The relative permittivity versus frequency for the E-ECC-NC and T-ECC-PC samples after 30 minutes and 4 days wetting in the water of cycle (1-second part) and cycle (7-second part) is presented in Figures 6.20(a)–(d). With reference to Figure 6.20(a), it can be clearly seen that the relative permittivity plots of all samples increased after 30 min of wetting compared to the 24 hours of drying process (See Figure 6.15(a)). Consider, for example, the average relative permittivity in cycle (1-second part) at 1 Hz of the T-ECC-PC samples was evaluated as (~4 × 10⁶) after 24 hours of drying, increasing to (~2 × 10⁸) after 30 minutes of wetting. While the average relative permittivity at 1 Hz of the controlled samples was obtained at a value of (~3 × 10⁷) after 24 hours of drying, it increased to (~6 × 10⁷) after 30 minutes of wetting. It's interesting to notice that although the relative permittivity of the T-ECC-PC samples dropped dramatically during the 24 hours of drying compared to the E-ECC-NC samples, it came even higher

than the E-ECC-NC samples after 30 minutes of wetting. This increase in the relative permittivity plots is related to the shift in time constant (raise of cusp-point frequency), which causes a shift in the relative permittivity plot to the right along the Z' axis toward the origin. It's also interesting to see that the enhancement in relative permittivity at high frequencies of the T-ECC-PC samples disappeared after the sample was submerged in water, and the relative permittivity plots of the T-ECC-PC samples became similar to the E-ECC-NC samples due to the water that bridged the micro-cracks and allowed the current to follow through them. While the relative permittivity plots after 30 minutes of wetting of cycle (7-second part) displayed in Figure 6.20(c) almost merged from 1 Hz up to ~1 kHz then the plots show a slight variation at high frequencies from ~1 kHz to ~1 MHz between the E-ECC-NC and T-ECC-PC samples and then they merged again at 10 MHz. It's also interesting to notice that the relative permittivity of all plots displayed in Figure 6.20(a) shows very close values. This is not the case for the plots displayed in Figure 6.20(c), which display a significant variation across the entire frequency range. This can be attributed to the hardness effect of the samples with increasing age, which prevents the water from penetrating easily into the sample.

After the samples became fully saturated (after 4 days of wetting) as can be seen in Figure 6.20(b), it can be clearly seen that the average relative permittivity value of all samples reached nearly the same value at 1 Hz with ($\sim 1.5 \times 10^8$) and (~96) at 10 MHz with, a slight difference in the relative permittivity between the samples in middle range frequencies. With reference to Figure 6.20(d), the relative permittivity plots after 4 days of wetting displayed a slight variation from 1 Hz to ~10 kHz then the plots merged together up to 10 MHz. This slight variation in the relative permittivity plots between the E-ECC-NC and T-ECC-PC samples after 30 minutes or 4 days of wetting is related to the differences in the relaxation of polarization mechanisms, and the shift in time constant.
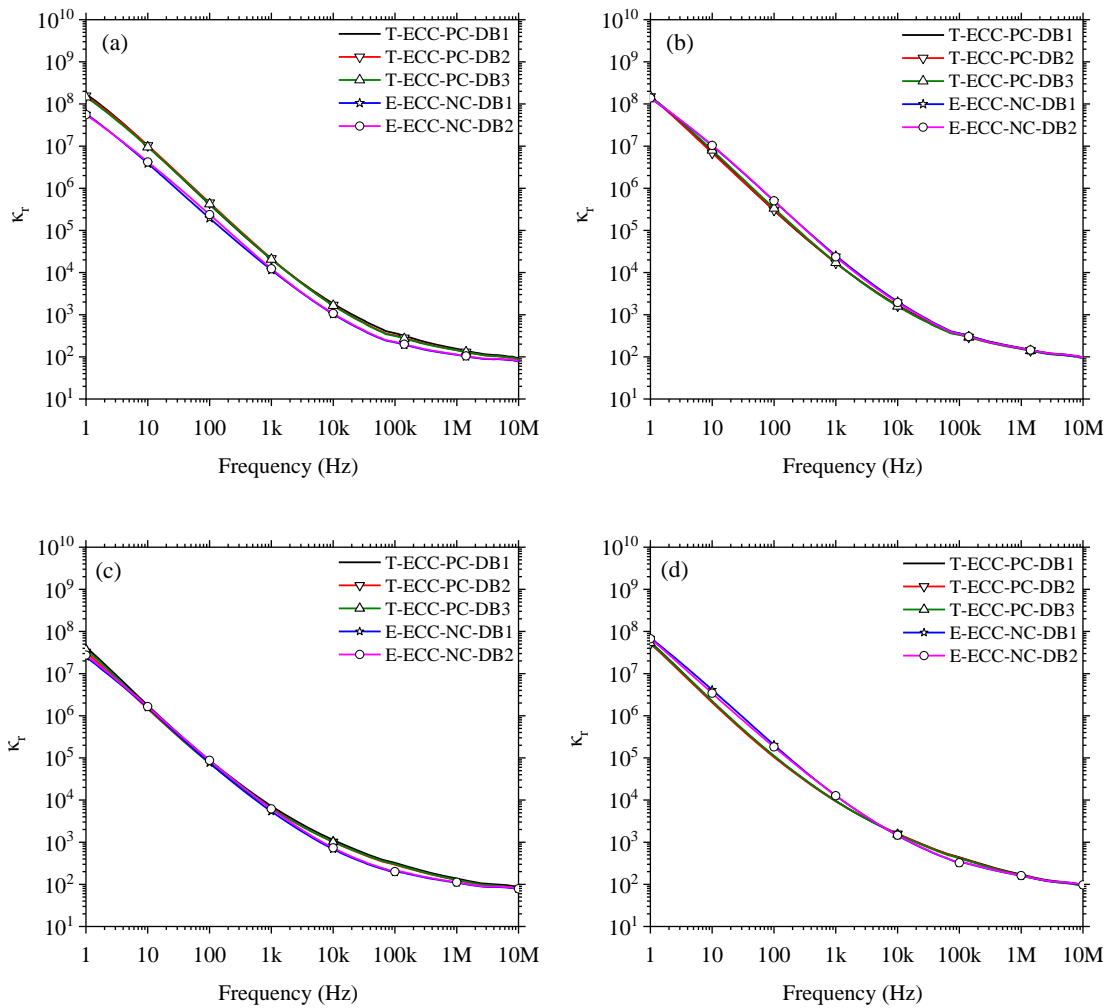
Figure 6.20: The relative permittivity for the controlled and pre-cracked ECC samples after a) 30 minutes of wetting in the cycle (1-second part); b) 4 days of wetting in the cycle (1-second part); c) 30 minutes of wetting in the cycle (7-second part); and d) 4 days of wetting in the cycle (7-second part).

Figures 6.21(a) and 6.23(b) show the relative permittivity of E-ECC-NC-DB2 at various wetting times ranging from 30 minutes to 4 hours for cycle (1-second part) and cycle (7-second part), respectively. With reference to Figure 6.21(a), it is clear that the relative permittivity plots increase as the submerging timing increases. For example, the relative permittivity of E-ECC-NC-DB2 at 1 Hz was ~5.5×10^7 after 30 minutes of submersion in water, ~7×10^7 after 1 hr, ~9.8×10^7 after 2 hr, ~1.2×10^8 after 3 hr and ~1.4×10^8 after 4 hr. This increase in the relative permittivity plots is due to the increase in the polarization process within the mixture. However, in cycle (7-second part) of Figure 6.21(b), the increase in relative permittivity was not clearly visible. It was found that the relative permittivity at 1 Hz increased from ~2.8×10^7 after 30 min of

submersion to $\sim 3.6 \times 10^7$ after 4 hr of submersion. This neglected increase in the relative permittivity indicates that there was no significant water absorption between the 30 min and 4 hr of submersion due to the hardness of the sample.
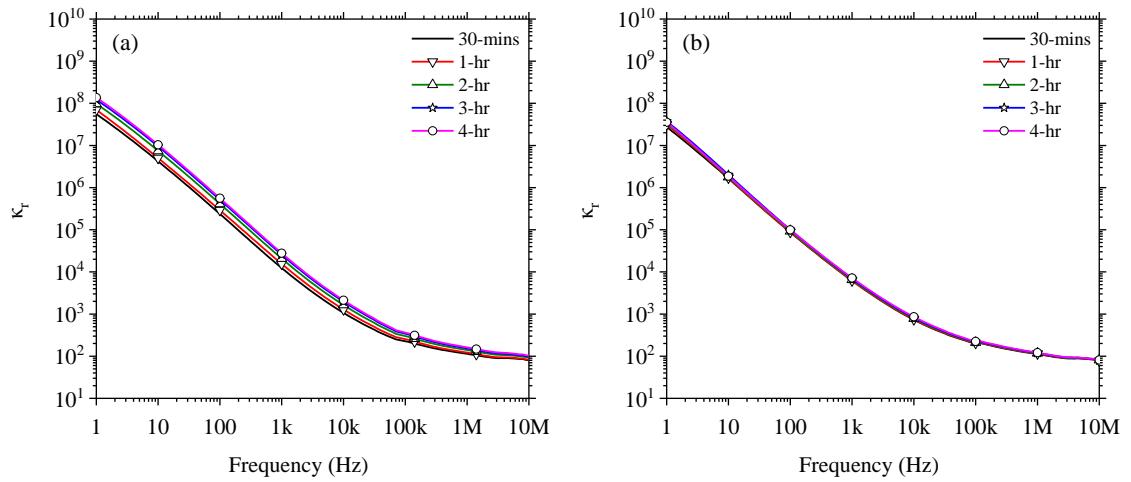
Figure 6.16: Relative permittivity staged at various timings from 30 min up to 4 hr of wetting for E-ECC-NC-DB2 of a) cycle (1-second part) and b) cycle (7-second part).

Figures 6.22(a)–(d) display the conductivity versus frequency for the E-ECC-NC and T-ECC-PC samples after 30 minutes and 4 days of wetting in the water of cycle (1-second part) and cycle (7-second part), respectively. It can be clearly seen that the conductivity plots of all samples increased significantly after being submerged in water when compared to the conductivity plots shown in Figure 6.17(a) after 24 hours of drying. This increase in conductivity is related to the filling of water in the continuous capillary pore network. It is also interesting to see that the increase of conductivity plots in cycle (1-second part) in the T-ECC-PC samples is higher than that in the E-ECC-NC samples, with an average conductivity of the E-ECC-NC samples was $\sim 1 \times 10^{-2}$ S/m at 1Hz increased to $\sim 3 \times 10^{-2}$ S/m at 10 MHz, while the average conductivity of the T-ECC-PC samples was $\sim 2 \times 10^{-2}$ S/m at 1 Hz increased to $\sim 6 \times 10^{-2}$ S/m at 10 MHz. This is due to the quick filling of the capillary pores caused by the presence of cracks. It is also interesting to see the conductivity plots of all samples after 4 days of wetting merged and displayed the same trend with slight differences at low frequencies, indicating that when the sample is fully saturated, the micro-cracks in the T-ECC-PC samples act as short circuits, which allow the current to flow without feeling the physical separation. Regarding the cycle (7-second part) conductivity results, it is clear that the conductivity plots after 30 minutes of wetting show a similar behaviour as in

cycle (1-second part) shown in Figure 6.22(a), with an increase in conductivity after submerging in water compared to the conductivity results after 24 hours of drying (See Figure 6.17(b)), and that the conductivity of the T-ECC-PC samples was higher than the controlled samples. However, there is some variation in conductivity compared to the cycle (1-second part). Cycle (1-second part) shows a significant variation between the E-ECC-NC and T-ECC-PC samples, whereas this variation has dramatically decreased in cycle (7-second part) with very close conductivity values. For example, the average conductivity of the E-ECC-NC samples attained ~1×10^{-2} S/m at 1 Hz increased to ~3×10^{-2} S/m at 10 MHz, whereas that of the T-ECC-PC samples attained ~1×10^{-2} S/m at 1Hz increased to ~3.5×10^{-2} S/m at 10 MHz. This decrease in the variation between the controlled and pre-cracked samples is related to the hardness effect due to the increase in the sample's age, which makes it harder for the water to penetrate the samples easily. There is also another difference between the cycle (1-second part) and the cycle (7-second part) after the samples are submerged in the water for 4 days. It's noticeable that in cycle (7-second part), the conductivity plots don't merge as displayed in cycle (1-second part) presented in Figure 6.22(b), and that the conductivity of the E-ECC-NC samples was higher than the T-ECC-PC samples. This is associated with the formation of new hydration products along the cracks, which causes the healing of some of the cracks, thus reducing their size. However, these new hydration products have different properties which make it even harder for the current to flow compared to the cycle (1-second part) where the current has to flow from the matrix to the water only.
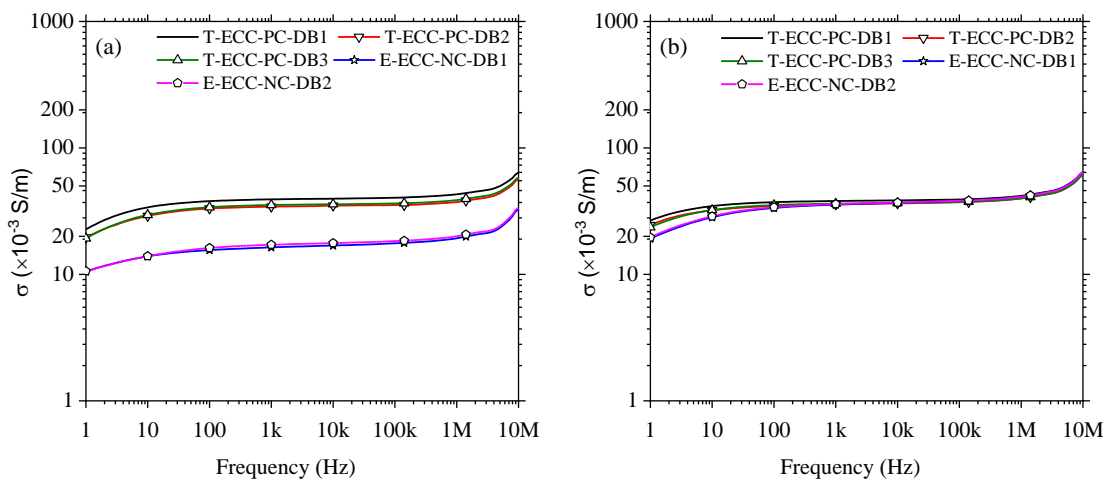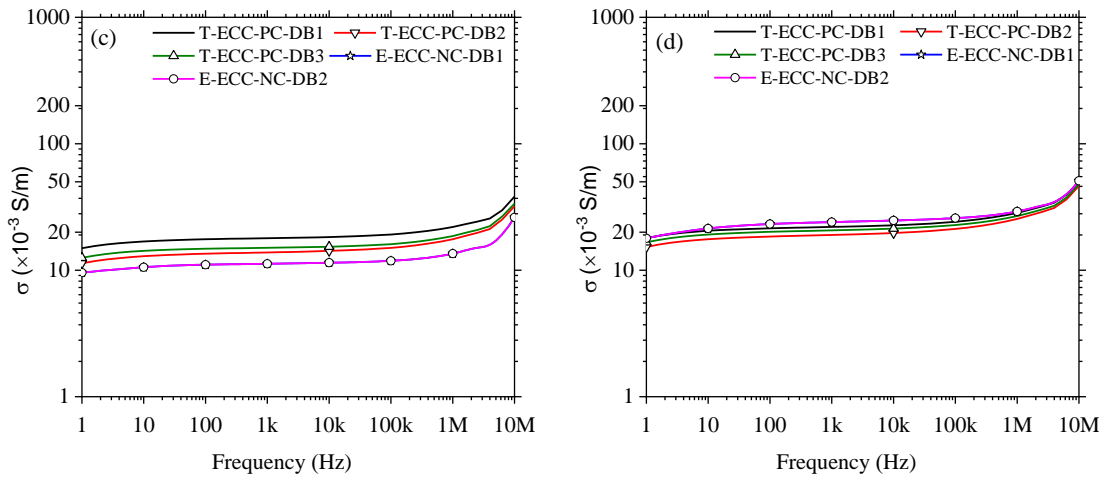
Figure 6.22: The conductivity for the controlled and pre-cracked ECC samples after a) 30 min of wetting in cycle (1-second part); b) 4 days of wetting in cycle (1-second part); c) 30 min of wetting in cycle (7-second part); and d) 4 days of wetting in cycle (7-second part).

For further clarification of the effect of wetting with increasing curing age, Figures 6.23(a) and 6.23(b) display the conductivity staged at various timings from 30 minutes to 4 hours of wetting for E-ECC-NC-DB2 of cycle 1-second part and cycle 7-second part. It can be clearly seen that increasing the submerging time causes an increase in the conductivity plots due to the re-filling of the ionic conductive paths with water. It can be clearly seen that the hardness of the sample has a significant impact on the conductivity. Consider, for example, the conductivity of the sample in the cycle 1-second part, where the conductivity at 1 Hz increased from $\sim 1 \times 10^{-2}$ S/m after 30 min of submersion to $\sim 2 \times 10^{-2}$ S/m after 4 hr of submersion, whilst in the cycle (7-second part), it increased from $\sim 1.0 \times 10^{-2}$ S/m after 30 min of submersion to $\sim 1.3 \times 10^{-2}$ S/m after 4 hr of submersion.
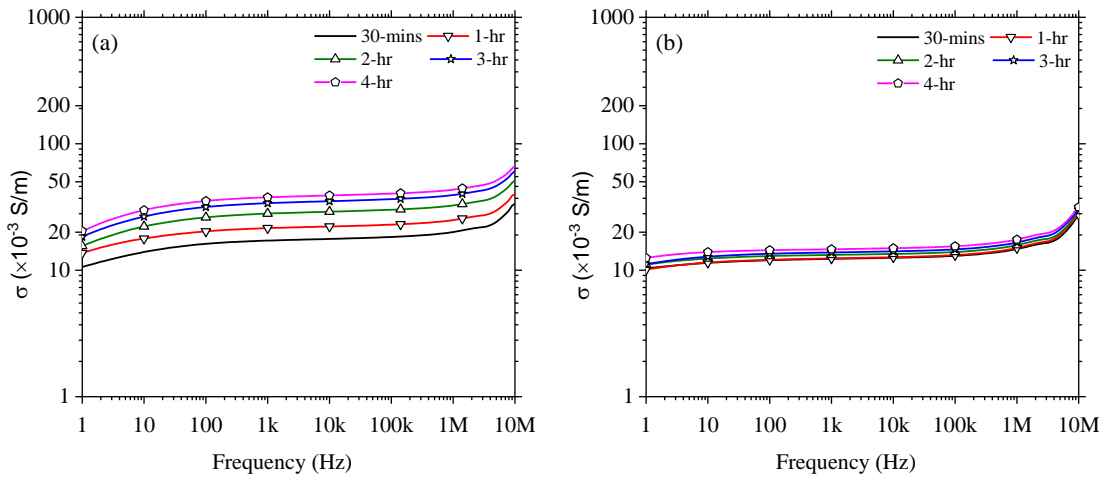
Figure 6.17: Conductivity staged **at** various timings from 30 min to 4 hr of wetting for E-ECC-NC-DB2 of a) cycle (1-second part) and b) cycle (7-second part).

6.3.7 The change in cusp-point frequency for cycle (1-second part) and cycle (7-second part)

It is also interesting to observe that in all cycles, the bulk arc becomes more discernible with increasing evaporation. On the contrary, as soon as the sample is exposed to water, the bulk arc becomes smaller. This relies on the increase or decrease of cusp-point frequency. For clarification purposes, Figures 6.24(a) and (b) show the change in cusp-point frequency (f_c) which represents the lowest point within the V-shaped valley region during 24 hr of drying and after 30 min of wetting of T-ECC-PC-DB1 for cycle (1-second part) and cycle (7-second part), respectively. It can be clearly seen that there was a sharp reduction in frequency at the first 2 hr of the cycle (1-second part) and at the 1 hr of the cycle (7-second part), and then the reduction became more gradual over the rest of the evaporation period of 1440 min (24 hr). Interestingly, the frequency came back to its initial value (~5 kHz) after 30 min of submersion in water. The remaining cusp-point frequency values for all samples of cycle (1-second part) and cycle (7-second part) are displayed in Table 6.1. The variation in the sharp reduction in frequency presented above is associated with the hardening of the sample, which makes the water evaporation process slower with increasing age of the sample. While the gradual decrease in frequency reflects the changes resulting from the evaporation, which causes a reduction in polarization and conductive processes operative within the matrix, on the contrary, an increase in polarization and conductive processes happened when the sample was exposed to water.
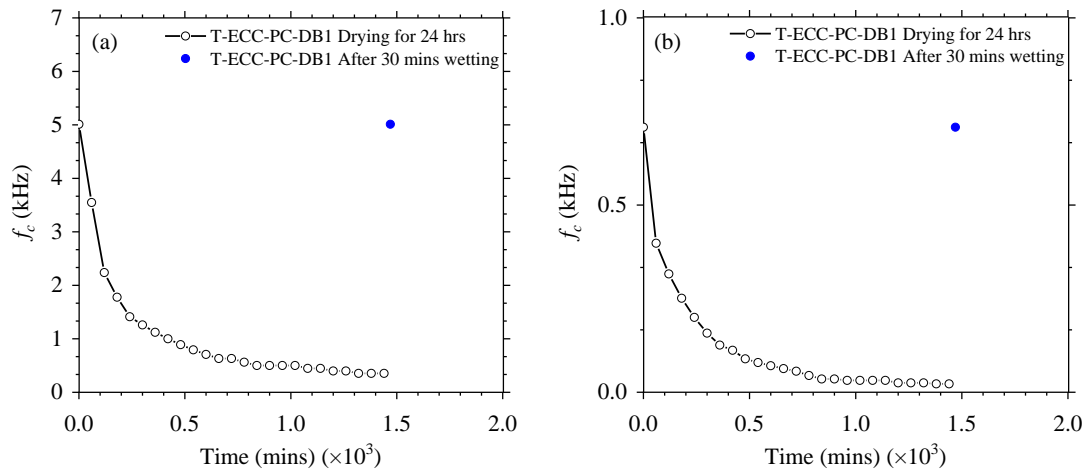
Figure 6.18: The change in cusp-point frequency, *fc*, for a) cycle (1-second part) and b) cycle (7-second part).

Table 6.1: The cusp-point frequency values for all samples in cycle (1-second part) and cycle (7-second part) before and after 1 day of drying (1440 min) and 1 day and 30 min (1470 min) of wetting and 4 days (5760 min) of wetting.

Sample Number	0 day	1 day (1440 min)	1 day+30 min (1470 min)	4 days (5760 min)
C1				
T-ECC-PC-DB1	5011.872	354.8134	5011.872	3548.134
T-ECC-PC-DB2	7079.458	707.9458	7943.282	3981.072
T-ECC-PC-DB3	7079.458	707.9458	7079.458	5011.872
E-ECC-NC-DB1	11220.18	5623.413	6309.573	7943.282
E-ECC-NC-DB2	7943.282	3162.278	6309.573	7079.458
C7				
T-ECC-PC-DB1	1000	22.38721	1000	630.9573
T-ECC-PC-DB2	1000	56.23413	630.9573	630.9573
T-ECC-PC-DB3	1000	35.48134	1000	1000
E-ECC-NC-DB1	3162.278	2238.721	1412.537	2238.721
E-ECC-NC-DB2	3162.278	2238.721	2238.721	2511.886

6.4 Equivalent circuit modelling

The same simplified equivalent circuit modelling displayed in Figures 5.22(a) and (b) stated in Section 5.6 is used to model the impedance response of the non-pre-cracked sample (E-ECC-NC-DB2) and pre-cracked sample (T-ECC-PC-DB1) presented in Figures 6.12(b) and (c), respectively. Figure 6.25(a) and 6.26(a) display the representative simulated and measured impedance response of E-ECC-NC-DB2 and E-ECC-PC-DB1, respectively, during the 24 hrs drying with the solid line represents the simulated response and the marked line represents the measured response. For clarity, the response at every 4 hr increment has been presented. Good agreement can be seen between the measured and simulated responses. With reference to temporal changes in R_{cp}, $C_{o,sm}$ and p_{sm} presented in Figure 6.25(b), it can be clearly seen that the R_{cp} increases as the drying process progresses, reflecting the evaporation of the water from the capillary pores. As the drying progresses, it could be expected that the capillary pore becomes more disconnected. Decreasing the overall polarization during the drying process causes a decrease in $C_{o,sm}$. In addition, the exponent p_{sm} slightly decreases as drying increases, indicating an increase in the depression angle.

It was assumed that the temporal changes in R_{cp}, $C_{o,sm}$ and p_{sm} of the non-pre-cracked sample were the same as the pre-cracked sample, as the main parameter affecting the drying process of the pre-cracked sample was the parallel circuit, R_c–CPE_c. It was found that the resistance R_c has a very large value due to the presence of the micro-cracks within the ECC matrix. It was also found that the R_c is increasing dramatically, from ~94 kΩ at 4 hr, to ~177 kΩ at 8 hr, ~298 kΩ at 12 hr, ~450 kΩ at 16 hr, ~628 kΩ at 20 hr and ~891 kΩ at 24 hr. This significant increase is related to the evaporation of the water from the crack. Figure 6.26(b) displays the temporal variations in $C_{o,c}$ and p_c to understand the influence of drying on the capacitive behaviour. It was found that the $C_{o,c}$ decreases as the evaporation of water from the micro-cracks increase. Consider for example, the $C_{o,c}$ decreases from 2.5×10^{-10} Fs$^{-0.10}$ at 4hrs of drying to 1.9×10^{-10} Fs$^{-0.10}$ at 24 hr. This reduction can be related to the replacement of water by air within the cracks and the decrease in the effective permittivity of micro-cracks with increasing the drying. It was also found that the p_c decreased as the drying increased.
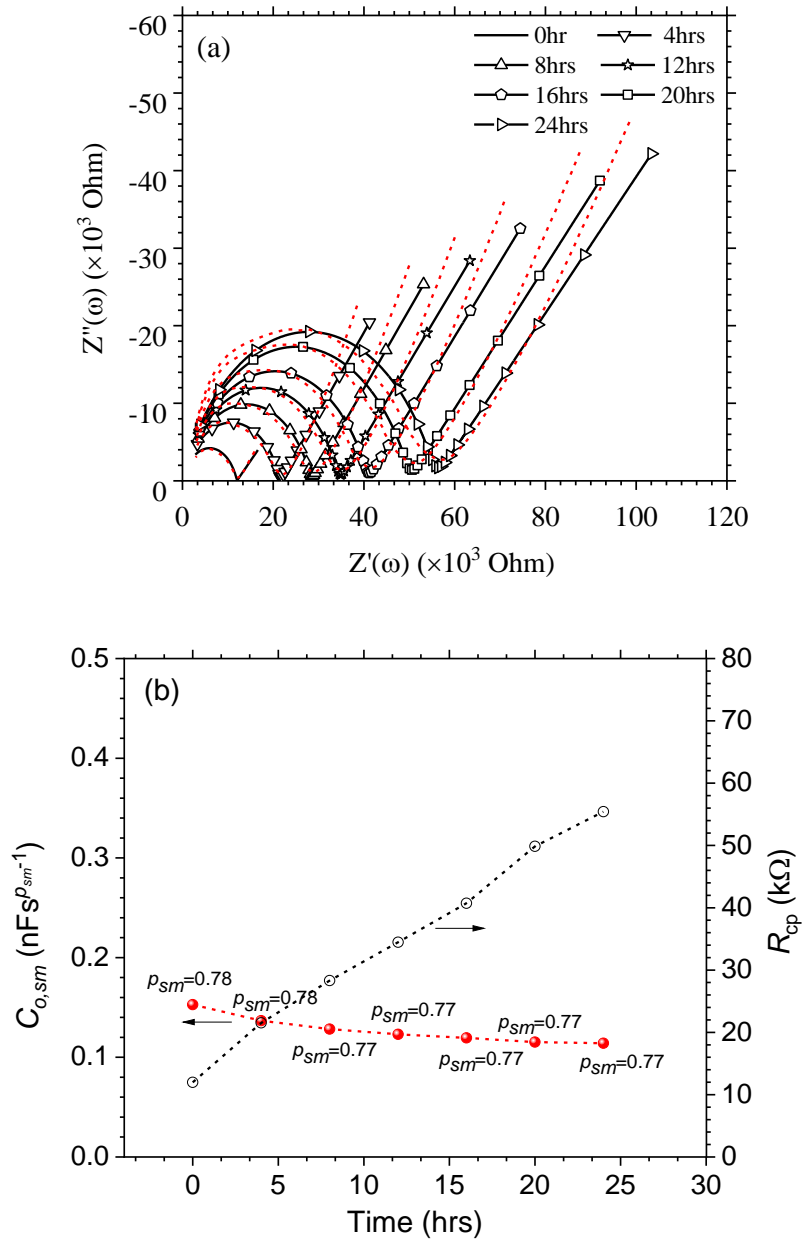
Figure 6.19: (a) Measured and simulated representative responses for the E-ECC-NC-DB2 sample during the drying process; and (b) variations in circuit parameters for the E-ECC-NC-DB2 sample.
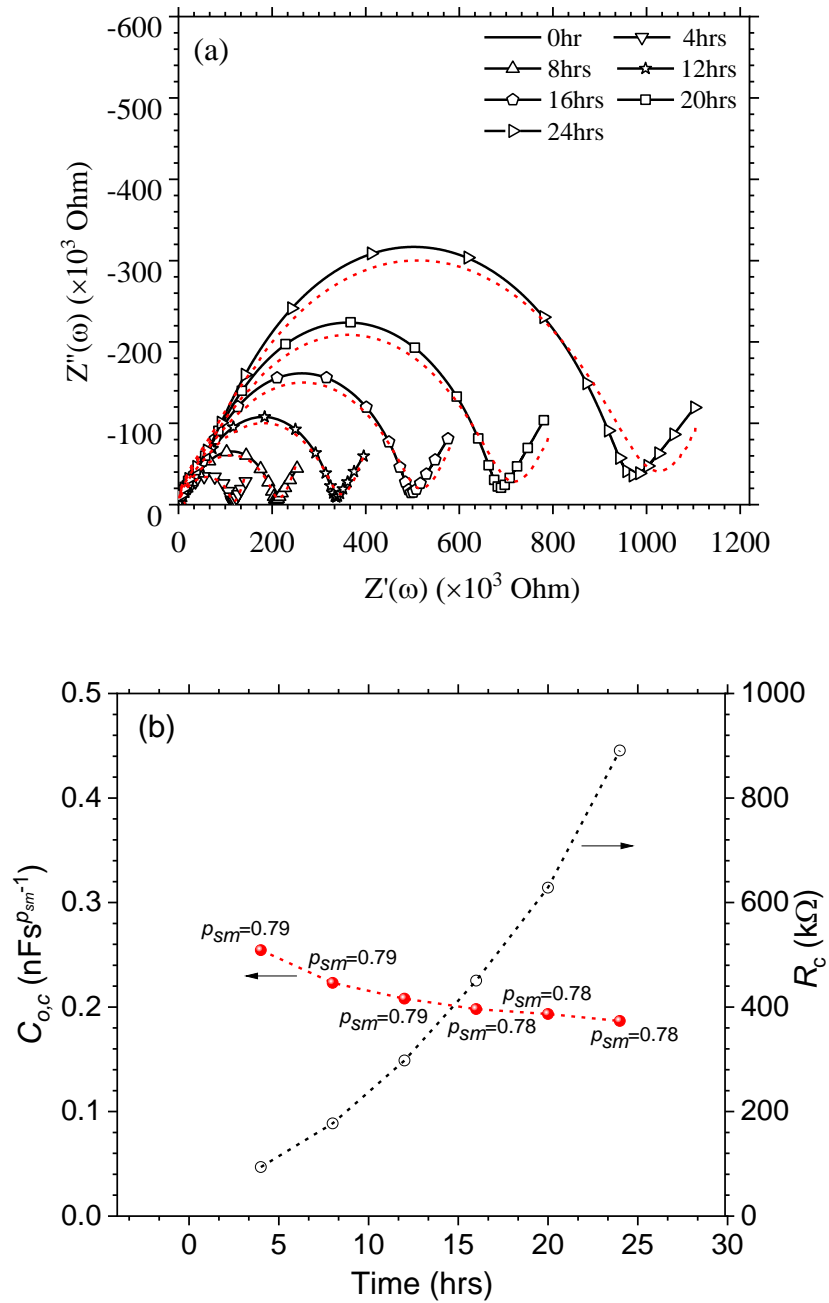
Figure 6.20: (a) Measured and simulated representative responses for the E-ECC-PC-DB1 sample during the drying process; and (b) variations in circuit parameters for the E-ECC-PC-DB1 sample.

6.5 Conclusions

This chapter provides several parameters which can be used to differentiate between the controlled and pre-cracked samples during the wetting and drying cycles. The following findings can be drawn:

- There is a reduction in the relative percentage change in mass during the drying process and a rise during the wetting process. In the early cycles, this increase and decrease were not noticeable between the non-cracked ECC and the cracked ECC. However, the relative percentage change of the cracked ECC increased to almost double due to the new hydration products that appeared along the crack.

- The drying process causes an increase of the resistance and reactance values. This increase will be significantly higher in the pre-cracked samples compared to the non-pre-cracked samples with approximately eight times higher in early cycle and fifteen times higher in the last cycle. While the larger crack width resulted in higher evaporation, thus higher resistance and reactance values.

- It was also shown that the relative permittivity of the pre-cracked sample at low-frequencies was very sensitive to drying compared with the non-pre-cracked sample. Consider, for example, the relative permittivity of the pre-cracked sample at 1 Hz at the last cycle decreases from $\sim 7 \times 10^7$ before drying to $\sim 7 \times 10^5$ after one day of drying compared with the non-pre-cracked sample decreases from $\sim 8 \times 10^7$ before drying to $\sim 2 \times 10^7$ after one day of drying.

- The drying process resulted in a decrease in the conductivity. This decrease will be greater in the pre-cracked samples compared to the non-pre-cracked samples. Consider, for example, the conductivity of the non-pre-cracked sample at 1Hz at the late cycle decreases from ~ 0.02 S/m before drying to ~ 0.002 S/m, while the pre-cracked sample decreases from ~ 0.02 S/m to ~ 0.0002 S/m. Additionally, the relative permittivity and conductivity plots of the pre-cracked samples after the drying process display an enhancement at high frequencies compared to the non-pre-cracked samples. Moreover, this enhancement shifted to the left along the Z' axis toward the origin with time.

- The wetting process reduces the impedance response, which is faster in cracked ECC compared to the non-cracked ECC when the sample is partially saturated, while the cracked ECC and non-cracked ECC match at approximately the same point when the samples are saturated.

- The wetting process causes an increase in the relative permittivity and conductivity. Additionally, the enhancement of the relative permittivity and conductivity of the cracked-ECC disappeared once the sample was submerged in water.

- An electrical model involving resistive and constant phase circuit elements was developed which could simulate the effect of drying on the un-cracked and cracked ECC matrix. It was found that the resistance '$R_{cp}{}'$' through the continuous capillary pore increases with increasing the drying process because the capillary pore becomes more disconnected. It was also found that capacitance '$C_{o,sm}$' reflecting the isolated pores decreases with increasing the drying process due to the reduction of the overall polarization within the matrix, and the exponent 'p_{sm}' decreases with increasing the drying process.

- The parallel circuit, R_c–CPE_c reflecting the crack/matrix interface, is the main parameter impacting the drying process of a pre-cracked sample. It was found that the interface resistance 'R_c' increases significantly with increasing the evaporation, from ~94 kΩ after 4hrs of drying to ~891 kΩ after one day of drying. It was also found that the interface capacitance '$C_{o,c}$' decreases with increasing the evaporation of the water from the micro-cracks due to the replacement of water by air within the cracks. In addition, the exponent 'p_c' decreases with increasing the drying process.

7 Conclusions and Recommendations for Future Work

7.1 General Remarks

In recent years, there has been a growing interest in the development of concrete with self-monitoring capabilities for use in condition and/or structural health monitoring. One of the recent developments has been through monitoring the electrical properties of a special type of concrete known as Engineered Cementitious Composite (ECC). The idea has been to use the ECC itself as a damage sensor due to its inherent damage-tolerant property when subjected to stresses beyond the elastic range. However, using this material as a sensor would necessarily mean that it would be subjected to constantly changing stress and ambient environmental conditions, which would in turn affect its electrical response.

The work presented in this thesis provides information on the electrical response of ECC under tensile straining and under several other related factors, including hydration, temperature, and moisture changes. The primary aim is to obtain the electrical response over a wide frequency range 1 Hz–10 MHz, although in some of the investigations, this was slightly reduced to 20 Hz–1 MHz due to the limitations of the test equipment. From the results presented, it has been shown that multi-frequency measurements provide useful information that can be further exploited to extract the influence of the above-listed contributing factors in isolation. The electrical response in the high frequency range is shown to be particularly useful for damage sensing. The following sections present the conclusions drawn from Chapters 4–6.

7.1.1 Conclusions from Hydration and Temperature Studies

From the work investigating the influence of cement hydration and temperature on the electrical response of ECC presented in Chapter 4, the following conclusions can be drawn:

- The ECC displays the classic impedance response of a cement-based material, comprising a low-frequency spur, a weak intermediate "plateau" region, and a single high-frequency bulk arc. Only one arc is evident as only one type of fibre is used in the mix (PVA fibres) and these fibres are non-conductive. The low-frequency spur represents the response resulting from polarization processes at

the electrode/specimen interface and constitutes part of a larger arc that would only form at frequencies significantly lower than the lower frequency limit used in the present study, viz ≪1Hz. The weak intermediate 'plateau' region is attributed to the presence of unburnt carbon in the fly-ash.

- Ongoing hydration and pozzolanic reactions are shown to result in an overall increase in impedance and a better definition of the high-frequency arc, which reflect the development of the pore structure over time. Between 7 and 180 days of curing, the average bulk resistivity of the ECC approximately triples, from ~10 Ω.m at 7 days to ~27 Ω.m at 28 days, further increasing to ~64 Ω.m at 90 days (or a sixfold increase) and ~117 Ω.m at 180 days (or an approximately twelvefold increase). Over the same period of time, the bulk resistivity of a mortar with a similar w/c ratio and containing no fly-ash shows only a twofold increase, from ~31 Ω.m at 7 days to ~71 Ω.m at 180 days.

- Dispersion of the polarisation processes is shown to result in a reduction in relative permittivity with increasing frequency and a corresponding increase in conductivity. The dispersive behaviour of ECC is caused by three main polarization mechanisms: an electrode polarization operating at frequencies of <1 kHz; a double-layer polarization operating over the frequency range of ~1 kHz–~100 kHz; and Maxwell-Wagner interfacial polarization operating over the frequency range of ~1 kHz–10 MHz).

- The relative permittivity at the upper frequency limit (i.e., > 1MHz) was not significantly influenced by ongoing hydration and pozzolanic reaction. When presented in the frequency domain and plotted on a log-log scale, the measured relative permittivity values over the entire 180-days curing period are shown to all merge to a constant value (see Figure 7.1(a)). Only a small reduction in value was observed.

- A general equation with an ageing exponent was used to model the temporal reduction in conductivity of all the mixes studied. It was found that the ageing factor for ECC is 0.73, which is approximately three times higher than that of a mortar mix with no fly-ash (= 0.25).

- The formation factor of the ECC was found to increase significantly over the 180 days of curing due to on-going pore structure refinement. This is in contrast to the formation factor of the mortar, which contained no fly-ash, which showed only a limited increase. While the formation factor of the ECC is smaller than that of the mortar during the early aging process (i.e., the ordinary mortar has

better performance than the ECC), it was found that the formation factor of the ECC consistently outperformed that of the mortar at longer timescales (i.e., beyond 42 days). At 180 days, the formation factor of the ECC reached ~900, which is almost double that of the mortar mix, reflecting the more tortuous and disconnected capillary pore network in the ECC mix. Based on the formation factor classification proposed by Suryanto (2020) and Broomfield (1997), the formation factor value obtained for the ECC at 180 days of curing falls under the class of " high " resistance to corrosion, while the value obtained for the mortar falls under the class of "low/moderate " resistance to corrosion.

- An electrical model comprising resistive and pseudo capacitance (known as the constant phase element (CPE)) components was developed to simulate the effect of hydration on the electrical response of the ECC mix studied. The CPE was particularly used to consider the dispersive electrical behaviour observed (i.e., the change in capacitance with frequency). It was found that the value of the resistive component representing the ionic conduction, 'R_{cp}', increases by a factor of almost twelve times between 14 and 180 days, from ~1 kΩ to ~12 kΩ. This is due to the continual refinement of the pore-structure resulting from on-going hydration and pozzolanic reaction. Over the same period of time, the value of the 'CPE-T_{sm}' parameter in the CPE, which represents the response of the solid matrix, increases by almost three times, from ~3×10^{-10} to ~10×10^{-10}, while the exponent 'CPE-P_{sm}' decreases from 0.84 to 0.71. The latter finding indicates that there is a further depression to the centre of the semicircle arc below the real ($Z'(\omega)$) axis.

- It was found that the un-burnt carbon/matrix interface plays an essential role in the ECC response. It was found that resistance at the interface of the carbon particles and the cement matrix 'R_{ci}' increased almost seven-fold from 14 days to 180 days because of the reduction in the interface size between the capillary pores and the un-burnt carbon. In addition, there is a reduction of the capacitive component of the interface 'CPE-T_{ci}' with increasing curing age, as the reduction of the interface with time causes lower capacitance of the un-burnt carbon. The exponent 'CPE-P_{ci}', which is very small in value, decreases from 0.18 to 0.07 with increasing curing age.

The following conclusions can be drawn from the work examining the effects of temperature:

- The resistive and reactive components of impedance are impacted by temperature at all test frequencies studied (i.e., 20 Hz–1 MHz). Increasing the temperature results in a gradual displacement of the impedance response to the left and a decrease in the semi-circle arc, reflecting a reduction in the impedance. Increasing the temperature also shortens the length of the semicircle arc, due to the frequency shift towards the lower frequencies with decreasing temperature. As a result, different portions of the actual impedance spectrum are evident when observed within the same frequency range.

- An Arrhenius plot was established for the conduction process in ECC. It was shown that when presented in an Arrhenius format, the bulk resistance of ECC over the temperature range 6.5–60°C displayed a linear response, highlighting the fact that electrical conduction in ECC involves a thermally activated process. The activation energy, E_a, for electrical conduction was evaluated as 21.7 kJ/mol (0.22 eV/ion).

- Equivalent circuit modelling was presented to simulate the temperature effects. It was found that the resistive component representing the ionic conduction 'R$_{cp}$' decreases as temperature increases. A fourfold reduction in value is evident over the temperature range 6.5–60°C. It was also found that increasing temperature results in an increase in the solid matrix capacitance '$C_{o,sm}$' and the exponent 'p_{sm}'.

7.1.2 Conclusions from the investigations on the Micro-cracking Effects

From the study on the influence of multiple micro-cracking on the electrical impedance of ECC presented in Chapter 5, the following conclusions can be drawn:

- The impedance response of cracked ECC within the frequency range 20 Hz–1 MHz displayed a classic impedance response, comprising a weakly developed low-frequency spur and a high-frequency arc, which is not dissimilar to the impedance response observed in the hydration study.

- When presented in the Nyquist format, it was shown that the formation and widening of multiple microcracks increased the sample impedance markedly and

resulted in a progressive displacement and enlargement in the radius of the intermediate arc. The increase in impedance was found to be affected by the pattern of the microcracks. It was found that the mean bulk resistance of the ECC with smaller crack widths (average ~56 microns) increased by seven times, from ~8 kΩ to ~56 kΩ. The ECC with larger microcrack widths (average ~81 micron) displayed a greater increase in bulk resistance, from ~22 kΩ to ~187 kΩ (an approximately ninefold increase).

- The successive formation and widening of multiple microcracks has the effect of reducing the continuity of the conduction pathway within the composite and increasing the circuitous path length, hence increasing the overall impedance. Conduction in cracked ECC occurs through several possible mechanisms across the microcrack, including direct contact between crack walls, broken particles bridging the microcrack, pore water in the microcrack, and PVA fibres coated with leached pore water. At this stage, it is not possible to delineate the contribution from each pathway.

- The relative permittivity of cracked ECC with small crack widths (average ~56 micron) displays a downward vertical displacement across the entire frequency range (see Figure 7.1(b)). The relative permittivity of cracked ECC with larger crack widths (average ~81 micron) displays a similar trend, but with an additional enhancement evident at frequencies >10kHz to ~low MHz at high tensile strains (see Figure 7.1(c)). It is postulated that this enhancement is attributed to the matrix/crack interfacial polarization. At 1MHz, however, polarization processes were not found to be significantly affected by the level of tensile strain. Given that the relative permittivity at 1 MHz was found to be sensitive to tensile straining and virtually insensitive to ongoing hydration, this parameter could be exploited when the matrix remains in a fully saturated condition, as a means of distinguishing changes in electrical properties due to damage within the composite and changes in electrical properties due to ongoing hydration. This may therefore provide a promising avenue for using this material for damage-monitoring without the interference from hydration.

- A nonlinear relationship was found between the tensile strain and the fractional change in resistivity (FCR). It was found that the average FCR value of cracked ECC at failure with a small crack width (average ~56 micron) is ~3, while that for a larger crack width (average ~81 micron) is four times higher (~13).

- An array of resistive and constant phase circuit elements connected in parallel was used to represent the presence of multiple microcracks within the ECC matrix. It was found that the crack/matrix interface component plays an essential role in the impedance response. An increase in the interface resistance, 'R_c', is evident as tensile strain increases, representing the physical separation resulting from micro-crack formation. The capacitive component 'CPE-$C_{o,c}$' was found to decrease as the strain increased, due to the increase in the total crack opening.

7.1.3 Conclusions from the Investigations focusing on Moisture Ingress and Drying

From Chapter 6, which discusses the influence of drying and wetting cycles on the electrical properties of un-cracked and cracked ECC, the following conclusions can be drawn:

- It was found that the drying process resulted in an increase in the impedance response. This increase is considerably higher in the cracked ECC compared to the un-cracked ECC. It was found that, compared with the un-cracked ECC, the bulk resistance of the cracked ECC was almost eightfold higher in the early cycle, and doubled to fifteenfold higher in the last cycle.
- The drying process resulted in a decrease in relative permittivity. In addition, the relative permittivity of cracked ECC at low frequencies is very sensitive to drying, with the relative permittivity of cracked ECC after one day of drying dropping from ~7×10^7 to ~7×10^5 (see Figure 7.1(e)) compared with that for the un-cracked ECC, which dropped from ~8×10^7 to ~2×10^7 (see Figure 7.1(d)). Moreover, the cracked ECC shows an enhancement of the relative permittivity at the range (>10 kHz to ~low MHz), which shifted toward the left with time.
- The wetting process leads to a decrease in the impedance response. When the sample is partially saturated, this decrease is faster for the pre-cracked samples compared to the non-pre-cracked samples. It was found that the average bulk resistance in the early cycle of the non-pre-cracked samples decreased from ~35 kΩ after one day of drying to ~18 kΩ after 30 min of wetting, while that of the pre-cracked sample decreased from ~300 kΩ to ~8 kΩ. In addition, when the samples are fully saturated (cured for 4 days after drying), the impedance

responses of the non-pre-cracked samples and pre-cracked samples match at approximately the same point ~8 kΩ.

- The wetting process causes an increase in the relative permittivity. This increase will be higher in the pre-cracked samples compared to the non-pre-cracked samples. Thus, the average relative permittivity at 1 Hz of the pre-cracked samples at early cycle increased fiftyfold from ~4×10^6 to ~2×10^8 after one day of drying and then being partially saturated (30 min wetting), while that of the controlled samples doubled from ~3×10^7 to ~6×10^7. Moreover, the relative permittivity of the non-pre-cracked samples and pre-cracked samples when the samples are fully saturated almost matches at the same points.

- The enhancement in the relative permittivity at high frequencies in the pre-cracked samples disappeared after the wetting process.

- An electrical model including resistive and constant phase circuit elements was developed to simulate the drying process of ECC while in the un-cracked and cracked states. It was found that the resistance of the ionic conduction, 'R_{cp}', increases as the drying process proceeds, due to the evaporation of the water from the capillary pores, which makes the pores more disconnected. It was also found that there is a reduction of the solid matrix capacitance '$C_{o,sm}$' with increasing drying time, due to the reduction of overall polarization within the matrix, and the exponent 'p_{sm}' also decreases as drying increases.

- The crack/matrix interface, which was modelled as a parallel circuit, R_c–CPE_c, plays an important role in the drying process of the cracked ECC. It was observed that the interface resistance 'R_c' increased ninefold during the period from 4 hrs of drying to one day of drying. It was also observed that interface capacitance '$C_{o,c}$' decreases as the evaporation of the water from the micro-cracks increases, because of the replacement of the water by air. It was also found that the exponent 'p_c' decreases with the increasing length of the drying process.
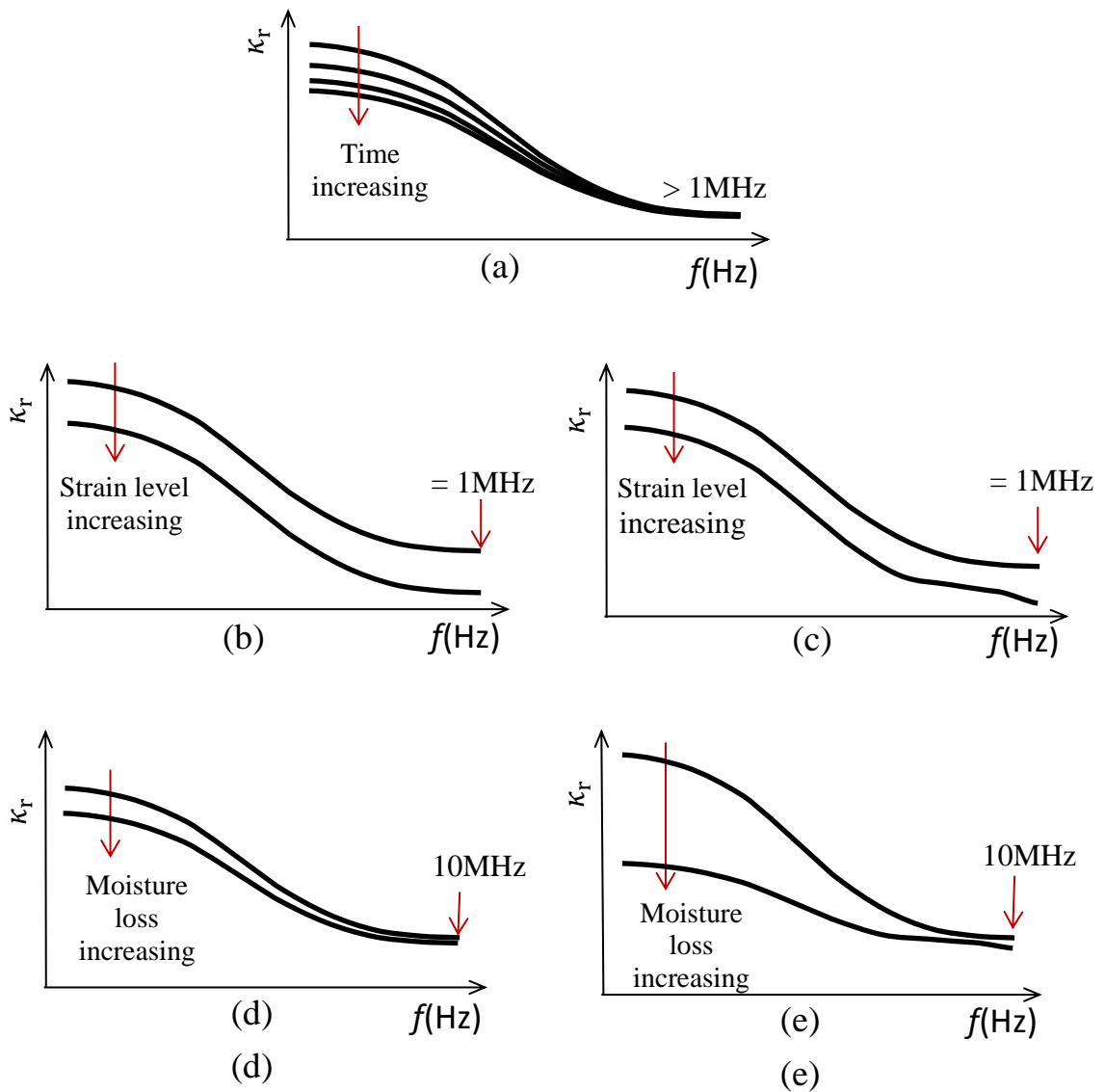
Figure 7.1: Schematic diagrams of the relative permittivity of (a) un-cracked ECC at different curing ages; (b) and (c) cracked ECC with small and large crack widths, respectively; (d) un-cracked ECC and (e) cracked ECC during the drying process.

7.2 Recommendations for future work

- To investigate the influence of hydration, wetting and drying, temperature, and cracking occurring simultaneously, to reflect real-world situations. This can be done through developing small-scale tests (i.e. a beam) to demonstrate the effectiveness of the ECC material for crack detection, which could be placed outdoors in an open yard (exposed to the natural environment) where all the factors affecting the electrical properties are combined together. After that,

electrical measurements can be taken at multi-frequencies to try to differentiate between the mechanical loading and non-mechanical loading.

To investigate the influence of compression on the electrical properties, as real structures can be affected by the compression and tension forces.

7.3 Challenges for development and deployment of self-sensing concrete

Although the intrinsic self-sensing concrete appeared almost two decades ago, many efforts are still required in order to overcome the challenges and allow its future development and deployment. According to Han et al. (2015), the main challenges are:

- To measure the sensing signals of the self-sensing concrete, these sensing signals include information about the state of the self-sensing concrete. However, if a proper sensing signal measurement and processing method is not used; environmental uncertainty and measurement noise may drown out the effective sensing signals. Furthermore, self-sensing concrete can be exposed to externally harsh environmental factors (i.e., chloride and high humidity), which could cause a change in the electrical properties of the self-sensing concrete, thus affecting the measurement accuracy. As a result, new electrode designs, measurement circuit designs, signal acquisition, and processing methods must be developed in order to fully, accurately, and deeply mine the effective information that reflects the state of the self-sensing concrete structures. The main goal is to create standard measurement methods and equipment for self-sensing concrete.

- Most of the previous studies focused on the sensing property of self-sensing concrete under uniaxial loading, which means that the self-sensing concrete can only measure one-axis strain or stress, while real structures are subjected to different loading and complex stress conditions. As a result, the overall sensing property of the self-sensing concrete for structural application should be determined. The sensing performance parameters (i.e., input/output range, linearity, repeatability, hysteresis, and signal to noise ratio) of the self-sensing concrete on the 1, 2, and 3 axis directions under complex stress conditions should be obtained in future work.

- Since the self-sensing concrete can be used in structural health monitoring of civil infrastructures such as bridges, buildings, offshore structures, and tunnels,

as well as traffic detection and border or military security, there must be in-depth studies on the application of self-sensing concrete in the aforementioned fields. It is recommended that future studies on the application of self-sensing concrete aim to establish a uniform method, specification, and guidance for the design and construction of self-sensing concrete structures.

REFERENCES

Ackermann, K.C. (2018) *Self-sensing concrete for structural health monitoring of smart infrastructures*, MSc. thesis, University of Rhode Island. Available at: https://digitalcommons.uri.edu/cgi/viewcontent.cgi?article=2268&context=theses (Accessed 10 January 2021)

Annamdas, V.G. and Soh, C.K. (2010) 'Application of Electromechanical impedance technique for Engineering Structures: Review and Future Issues', Journal of intelligent material systems and structures, 21(1), pp.41-59

ASCE (2013) *Report Card for America's Infrastructure* [online]. Available from: https://ascelibrary.org/doi/pdf/10.1061/9780784478837 (Accessed 1 January 2021)

Azhari, F. and Banthia, N. (2012) 'Cement-based sensors for piezoresistive sensing', *Cement and Concrete Composites*, 34(7), pp.866-873

Baeza, F.J., Galao, O., Zornoza, E. and Garcés, P. (2013) 'Multifunctional cement composites strain and damage sensors applied on reinforced concrete (RC) structural elements', *Materials*, 6(3), pp.841-855

Barneyback, R.S. and Diamond, S. (1981) 'Expression and analysis of pore fluids from hardened cement pastes and mortars', *Cement and Concrete Research*, 11, pp.279-285

Basheer, P.A.M., Nolan, É.A., McCarter, W.J. and Long, A.E. (2000) 'Effectiveness of In Situ Moisture Preconditioning Methods for Concrete', *Journal of Materials in Civil Engineering*, 12(2), pp.131-138

Bentz, D.P. (2007) 'A virtual rapid chloride permeability test', *Cement and Concrete Composites*, 29(10), pp.723-731

Bhalla, S. (2004) *A mechanical impedance approch for structural for identification, health monitoring and non-destructive evaluation using piezo-impedance transducers*, PhD. thesis, Nanyang Technological University.

Blaber, J., Adair, B. and Antoniou, A. (2015) 'Ncorr: Open-Source 2D Digital Image Correlation Matlab Software', *Experimental Mechanics*, 55(6), pp.1105–1122

Brouwers, H.J.H. and van Eijk, R.J. (2003) 'Alkali concentrations of pore solution in hydrating OPC', *Cement and Concrete Research*, 33, pp.191-196

Brownjohn, J.M.W. (2007) 'Structural Health Monitoring of Civil Infrastructure', *Philosophical Transactions: Mathematical, Physical and Engineering Sciences*, 365(1851), pp.589-622

Brownjohn, J.M.W., Xia, P.Q., Hao, H. and Xia, Y. (2001) 'Civil structure condition assessment by FE model updating:: methodology and case studies', *Finite Elements in Analysis and Design*, 37(10), pp.761-775

Bruck, H.A., McNeil, S.R., Sutton, M.A. and Peters, W.H. (1989) 'Digital Image Correlation Using Newton-Raphson Method of Partial Differential Correction', *Experimental Mechanics*, 29(3), pp.261-267

Cabinet Office (2011) *Government Construction Strategy* [online]. Available from: https://assets.publishing.service.gov.uk/government/uploads/system/uploads/attachment_data/file/61152/Government-Construction-Strategy_0.pdf (Accessed 1 January 2021)

Campanella, C.E., Cuccovillo, A., Campanella, C., Yurt, A. and Passaro, V.M.N. (2018) 'Fibre Bragg Grating Based Strain Sensors: Review of Technology and Applications', Sensors, 18(9)

Capoluongo, P., Ambrosino, C., Campopiano, S., Cutolo, A., Giordano, M., Bovio, I., Lecce, L. and Cusano, A. (2007) 'Modal analysis and damage detection by Fiber Bragg grating sensors', *Sensors and Actuators A: Physical*, *133*(2), pp.415-424

Castellote, M., Andrade, C. and Alonso, M.C. (2002) 'Standardization, to a reference of 25 C, of electrical resistivity for mortars and concretes in saturated or isolated conditions', *Materials Journal*, 99(2), pp.119-128

Cement, C.E.N. (2000) 'Part 1: Compositions, specifications and conformity criteria for common cements', *European standard EN*, pp.197-1

Chaki, S. and Bourse, G. (2009) 'Guided ultrasonic waves for non-destructive monitoring of the stress levels in prestressed steel strands', *Ultrasonics*, 49(2), pp.162-171

Chan, T.H.T., Yu, L., Tam, H.Y., Ni, Y.Q., Liu, S.Y., Chung, W.H. and Cheng, L.K. (2006) 'Fiber Bragg grating sensors for structural health monitoring of Tsing Ma bridge: Background and experimental observation', *Engineering Structures*, 28(5), pp.648-659

Chang, P.C., Flatau, A. and Liu, S.C. (2003) 'Review Paper: Health Monitoring of Civil Infrastructure', *Structural Health Monitoring*, 2(3), pp.257-267

Chen, B., Liu, J. and Wu, K. (2005) 'Electrical responses of carbon fiber reinforced cementitious composites to monotonic and cyclic loading', *Cement and concrete research*, 35(11), pp.2183-2191

Chen, P.W. and Chung, D.D.L (1993) 'Carbon fiber reinforced concrete as a smart material capable of non-destructive flaw detection', *Smart Materials and Structures*, 2(1), pp.22–30

Chen, W. and Brouwers, H.J.H. (2010) 'Alkali binding in hydrated Portland cement paste', *Cement and Concrete Research*, 40(5), pp.716-722

Chen, Y., Cui, Y. and Gong, W. (2017) 'Crack Propagation Calculations for Optical Fibers under Static Bending and Tensile Loads Using Continuum Damage Mechanics', *Sensors*, 17(11)

Chen, Y., Yu, J. and Leung, C.K. (2018) 'Use of high strength strain-hardening cementitious composites for flexural repair of concrete structures with significant steel corrosion', *Construction and Building Materials*, 167, pp.325-337

Chia, L. and Huang, Y. (2017) 'Dispersion effectiveness of carbon nanotubes in smart cementitious materials', *Advances in Cement Research*, 29(6), pp.246-257

Chintalapudi, K., Paek, J., Gnawali, O., Fu, T.S., Dantu, K., Caffrey, J., Govindan, R., Johnson, E. and Masri, S. (2006) 'Structural damage detection and localization using netshm', *In the Fifth International Conference on Information Processing in Sensor Networks*, pp.475-482

Choi, S., Park, S., Bolton, R., Stubbs, N. and Sikorsky, C. (2004) 'Periodic monitoring of physical property changes in a concrete box-girder bridge', *Journal of Sound and Vibration*, 278(1-2), pp.365-381

Chowdhury, F.H., Raihan, M.T. and Islam, G.M.S. (2015) 'Application of different structural health monitoring system on bridges: An overview', *IABSE-JSCE Joint Conference on Advances in Bridge Engineering-III*, 21-22 August. Dhaka: Bangladesh, pp.440-449

Chrisp, T.M., Starrs, G., McCarter, W.J., Rouchotas, E. and Blewett, J. (2001) 'Temperature-conductivity relationships for concrete: An activation energy approach', *Journal of materials science letters*, 20(12), pp.1085-1087

Christensen, B.J., Coverdale, T., Olson, R.A., Ford, S.J., Garboczi, E.J., Jennings, H. M. and Mason, T.O. (1994) 'Impedance spectroscopy of hydrating cement-based materials: measurement, interpretation, and application', *Journal of the American Ceramic Society*, 77(11), pp.2789-2804

Chung, D. (2002) 'Electrical Conduction Behavior of Cement-Matrix Composites', *Journal of Materials Engineering and Performance*, 11(2), pp.194-204.

Chung, D.D.L. (2000) 'Cement-matrix composites for smart structures *Smart*', *Smart Materials and Structures*, 9(4), pp.389-401

Cowled, C. (2017) *On the Influence of Structural Complexity on the Global Vibration Characteristics of Steel Truss Bridges*, PhD thesis, Queensland University of Technology. Available at: https://eprints.qut.edu.au/115793/1/Craig_Cowled_Thesis.pdf (Accessed 5 January 2021)

Culshaw, B., Pierce, S.G. and Staszekski, W.J. (1998) 'Condition monitoring in composite materials: An integrated systems approach', *Proceedings of the Institution of Mechanical Engineers, Part I: Journal of Systems and Control Engineering*, 212(3), pp.189-202

Deng, H. and Li, H. (2018) 'Assessment of self-sensing capability of carbon black engineered cementitious composites', *Construction and Building Materials*, 173, pp.1-9

Deraemaeker, A. and Worden, K. (2010) *New trends in vibration based structural health monitoring*, New York: SpringerWien

Downey, A., D'Alessandro, A., Laflamme, S. and Ubertini, F. (2017) 'Smart bricks for strain sensing and crack detection in masonry structures', *Smart Materials and Structures*, 27(1), pp.015009

Doyle, C., Quinn, S. and Dulieu-Barton, J.M. (2006) 'Evaluation of Rugged "Smart Patch" Fibre-Optic Strain Sensors', *Applied Mechanics and Materials*, 3-4, pp.343-348

Duan, W.H., Wang, Q. and Quek, S.T. (2010) 'Applications of Piezoelectric Materials in Structural Health Monitoring and Repair: Selected Research Examples', *Materials*, 3(12), pp.5169–5194

Dullien F.A.L. (1992) *Porous media: Fluid transport and pore structure*, 2nd Ed., London: Academic

Elwalwal, H.M., Mahzan, S.B.H. and Abdalla, A.N. (2017) 'Crack Inspection Using Guided Waves (GWs)/Structural Health Monitoring (SHM): Review', *Journal of Applied Sciences*, 17, pp.415-428

Farhey, D.N. (2005) 'Bridge Instrumentation and Monitoring for Structural Diagnostics', *Structural Health Monitoring*, 4(4), pp.301-318

Farrar, C.R. and Worden, K. (2007) 'An introduction to structural health monitoring', *Philosophical Transactions of the Royal Society A: Mathematical, Physical and Engineering Sciences*, 365(1851), pp.303-315

Farrar, C.R., and Lieven, N.A.J. (2007) 'Damage prognosis: the future of structural health monitoring', *Philosophical Transactions of the Royal Society A: Mathematical, Physical and Engineering Sciences*, 365, pp.623-632

Fayyad, T.M. and Lees, J.M. (2014) 'Application of Digital Image Correlation to reinforced concrete fracture', *Procedia Materials Science*, 3, pp.1585-1590

Fayyad, T.M. and Lees, J.M. (2017) 'Experimental investigation of crack propagation and crack branching in lightly reinforced concrete beams using digital image correlation', *Engineering Fracture Mechanics*, 182, pp.487-505

Fottenburg, W.G. (1969) 'Some Applications of Holographic Interferometry', *Experimental Mechanics*, 8, pp.281-285

Frangopol, D.M., Dong, Y. and Sabatino, S. (2017) 'Bridge life-cycle performance and cost: analysis, prediction, optimisation and decision-making', *Structure Infrastructure Engineering,* 13, pp.1239-1257

Frank, T.E., Lepech, M.D. and Billington, S.L. (2018) 'Experimental testing of reinforced ECC beams subjected to various cyclic deformation histories', *Journal of Structural Engineering ASCE*, 144(6), pp. 04018052

García-Macíasa, E., D'Alessandrob, A., Castro-Trigueroc, R., Pérez-Mirad, D. and Ubertini, F. (2017), 'Micromechanics modeling of the uniaxial strain-sensing property of carbon nanotube cement-matrix composites for SHM applications', *Composite Structures*, 163, pp.195-215

Hall, C. and Hoff, W.D. (2002) *Water transport in brick, stone and concrete*, London

Han, B., Guan, X. and Ou, J. (2007) 'Electrode design, measuring method and data acquisition system of carbon fiber cement paste piezoresistive sensors', *Sensors and Actuators A: Physical*, 135(2), pp.360-369

Han, B., Wang, Y., Dong, S., Zhang, L., Ding, S., Yu, X. and Ou, J. (2015) 'Smart concretes and structures: A review', *Journal of Intelligent Material Systems and Structures*, 26(11), pp.1303-1345

Han, B., Zhang, K., Burnham, T., Kwon, E. and Yu, X. (2013) 'Integration and road tests of a self-sensing CNT concrete pavement system for traffic detection', *Smart Materials and Structures,* 22(1)

Han, B.G., Yu, Y. and Han, B.Z. (2008) 'Development of a wireless stress/strain measurement system integrated with pressure-sensitive nickel powder-filled cement-based sensors', *Sensors and Actuators A: Physical*, 147(2), pp.536–543

Hasted, J.B. (1973) *aqueous dielectrics*, chapman and hall: London.

Hedegaard, B.D., French, C.E.W. and Shield, C.K. (2017) 'Time-dependent monitoring and modeling of I-35W St. Anthony Falls Bridge. I: Analysis of monitoring data', *Journal of Bridge Engineering*, 22(7)

Herbert, E.N. and Li, V.C. (2013) 'Self-healing of microcracks in engineered cementitious composites (ECC) under a natural environment', *Materials*, 6(7), pp.2831-2845

Highways Agency (2007) BD 63/07 Inspection of Highway Structures. In: Design Manual for Roads and Bridges, vol. 3, HMSO, London, UK

Highways England (2017) *Design Manual for Roads and Bridges-Volume 3: Highway Structures: Inspection and Maintenance. Section 1: Inspection. Part 4: Inspection of Highway Structures*.

Hou, T.C. (2008) *Wireless and electromechanical approaches for strain sensing and crack detection in fiber reinforced cementitious materials*, PhD the University of Michigan.

Hou, T.C. and Lynch, J.P. (2005a) 'Conductivity-based Strain Monitoring and Damage Characterization of Fiber Reinforced Cementitious Structural Components', *In: Proceedings of SPIE 12th Annual International Symposium on Smart Structures and Materials, San Diego, CA, USA*, pp. 419-430

Hou, T.C. and Lynch, J.P. (2005b) 'Monitoring strain in engineered cementitious composites using wireless sensors', *In Proceedings of the International Conference on Fracture (ICF XI), Turin, Italy*, pp.20-25

Hu, W., Tang, D., Teng, J., Said, S. and Rohrmann, R. (2018) 'Structural Health Monitoring of a Prestressed Concrete Bridge Based on Statistical Pattern Recognition of Continuous Dynamic Measurements Over 14 Years', *Sensors*, 18

Huang, Y., Li, H. and Qian, S. (2018) 'Self-sensing properties of engineered cementitious composites', *Construction and Building Materials*, 174, pp.253-262

Huang, Y.H., Liu, L., Sham, F.C., Chan, Y.S. and Ng, S.P. (2010) 'Optical Strain Gauge vs. Traditional Strain Gauges for Concrete Elasticity Modulus Determination', *Optik*, 121(18), pp.1635–1641

Hung, P. and Voloshin, A.S. (2003) 'In-Plane Strain Measurement by Digital Image Correlation', *Journal of the Brazilian Society of Mechanical Sciences and Engineering*, 25(3)

Ishai, P.B., Talary, M.S., Caduff, A., Levy, E. and Feldman, Y. (2013) 'Electrode polarization in dielectric measurements: a review', *Measurement science and technology*, 24(10), pp.102001

Iwamoto, M. (2012) 'Maxwell–Wagner effect', in Bhushan, B. (ed.). *Encyclopedia of Nanotechnology*, Dordrecht: Springer, pp. 1276–1285

Jacobs, S., Matthys, S., De Roeck, G., Taerwe, L., De Waele, W. and Degrieck, J. (2007) 'Testing of a Prestressed Concrete Girder to Study the Enhanced Performance of Monitoring by Integrating Optical Fiber Sensors', *Journal of Structural Engineering*, 133(4), pp.541-549

Janke, L., Czaderski, C. and Motavalli, M. (2005) 'Applications of shape memory alloys in civil engineering structures—overview, limits and new ideas', Materials and Structures, 38(5), pp.578-592

Jayawardhana, M., Zhu, X., Liyanapathirana, R. and Gunawardana, U. (2017) 'Compressive sensing for efficient health monitoring and effective damage detection of structures', *Mechanical Systems and Signal Processing*, 84, pp.414-430.

Kharroub, S., Laflamme, S., Song, C., Qiao, D., Phares, B. and Li, J. (2015) 'Smart sensing skin for detection and localization of fatigue cracks', *Smart Materials and Structures,* 24(6), pp.1-9

Kim, B., Min, C., Kim, H., Cho, S., Oh, J., Ha, S. and Yi, J. (2019) 'Structural Health Monitoring with Sensor Data and Cosine Similarity for Multi-Damages', *Sensors*, 19(14)

Kim, J., McCarter, W.J. and Suryanto, B. (2018) 'Performance assessment of reinforced concrete after long-term exposure to a marine environment', *Construction and Building Materials*, 192, pp.569-583

Kim, J., McCarter, W.J., Suryanto, B., Nanukuttan, S., Basheer, P.M. and Chrisp, T.M. (2016) 'Chloride ingress into marine exposed concrete: A comparison of empirical-and physically-based models', *Cement and Concrete Composites*, 72, pp.133-145

Kojima, S., Sakata, N., Kanda, T. and Hiraishi, T. (2004) 'Application of direct sprayed ECC for retrofitting dam structure surface-application for Mitaka-Dam', *Concrete Journal*, 42(5), pp.135-139

LabVIEW (2017) [online]. Available from: http://www.ni.com/download/labview-development-system-2017/6698/en/ (accessed 21 January 2021).

Lee, S.W., Tan, K.H. and Yang, E.H. (2018) 'Seismic behaviour of interior reinforced-concrete beam–column sub-assemblages with engineered cementitious composites', *Magazine Concrete Research*, 70(24), pp.1280-1296

Li, H., Yia, T., Renb, L., Lic, D. and Huod, L. (2014) 'Reviews on Innovations and Applications in Structural Health Monitoring for Infrastructures', *Structural Monitoring and Maintenance*, 1(1), pp.1-45

Li, M., Lin, J., Lynch, J.P. and Li, V.C. (2012) 'Multifunctional carbon black Engineered Cementitious Composites for the protection of critical infrastructure', *In: Proc. Int. Conf. on HPFRCC*, 6, 99-106.

Li, M., Lin, V.W.J., Lynch, J.P. and Li, V.C. (2013) 'Carbon Black Engineered Cementitious Composites - Mechanical and Electrical Characterization', *ACI Special Publication*, 292, 1-16

Li, V.C. (2003) 'On Engineered Cementitious Composites (ECC)', *Journal of Advanced Concrete Technology*, 1(3), pp.215-230

Li, V.C. (2008) 'Engineered Cementitious Composites (ECC): Material, Structural and Durability Performance', in E. G. Nawy, ed. *Concrete Construction Engineering Handbook: 6000 Broken Sound Parkway*, USA: Florida, pp.1-46

Li, V.C. (2012) 'Tailoring ECC for special attributes: A review', *International Journal of Concrete Structures and Materials*, 6(3), pp.135-144

Li, X., Li, M. and Song, G. (2015) 'Energy-dissipating and self-repairing SMA-ECC composite material system', *Smart materials and structures*, 24(2)

Li, Z., Leung, C. and Xi, Y. (2009) *Structural Renovation in Concrete,* London: Taylor & Francis

Lin, V.W., Li, M., Lynch, J.P. and Li, V.C. (2011) 'Mechanical and electrical characterization of self-sensing carbon black ECC', *In Nondestructive Characterization for Composite Materials, Aerospace Engineering, Civil Infrastructure, and Homeland Security*, 7983, pp.798316

Liu, H., Zhang, Q., Gu, C., Su, H. and Li, V.C. (2016) 'Influence of micro-cracking on the permeability of engineered cementitious composites', *Cement and Concrete Composites*, 72, pp.104-113

Liu, Z.Q. (2006) *Study on damage self-monitoring and self-repair of SMA smart concrete beam*, PhD. thesis, China: Harbin Institute of Technology

Ma, H., Herbert, E., Ohno, M. and Li, V.C. (2019) 'Scale-linking model of self-healing and stiffness recovery in engineered cementitious composites (ECC)', *Cement and Concrete Composites*, 95, pp.1-9

Macdonald, J.R. (1996) 'Analysis of dispersed, conducting-system frequency-response data', *Journal of Non-Crystalline Solids*, 197(2-3), pp.83-110

Malesa, M., Szczepanek, D., Kujawińska, M., Świercz, A. and Kołakowski, P. (2010) 'Monitoring of civil engineering structures using Digital Image Correlation technique', in *ICEM 14 – 14th International Conference on Experimental Mechanics*. 10 June, 2010

Mason, T., Campo, M., Hixson, A. and Woo, L. (2002) 'Impedance spectroscopy of fiber-reinforced cement composites', *Cement and Concrete Composites*, 24(5), pp.457-465

McCarter, W. and Brousseau, R. (1990) 'The A.C. response of hardened cement paste', *Cement and Concrete Research*, 20(6), pp.891-900

McCarter, W., Garvin, S. and Bouzid, N. (1988) 'Impedance measurements on cement paste', *Journal of Materials Science Letters*, 7(10), pp.1056-1057

McCarter, W., Starrs, G. and Chrisp, T. (1999) 'Immittance spectra for Portland cement/fly ash-based binders during early hydration', *Cement and Concrete Research*, 29(3), 377-387.

McCarter, W., Starrs, G. and Chrisp, T. (2004) 'The complex impedance response of fly-ash cements revisited', *Cement and Concrete Research*, 34(10), pp.1837-1843

McCarter, W., Taha, H., Suryanto, B. and Starrs, G. (2015) 'Two-point concrete resistivity measurements: interfacial phenomena at the electrode–concrete contact zone', *Measurement Science and Technology*, 26, pp.1-13

McCarter, W.J. (1995) 'Effects of temperature on conduction and polarization in Portland cement mortar', *Journal of the American Ceramic Society*, 78(2), pp.411-415

McCarter, W.J. and Garvin, S. (1989) 'Dependence of electrical impedance of cement-based materials on their moisture condition', *Journal of Physics D: Applied Physics*, 22(11), pp.1773

McCarter, W.J., Chrisp, T., Starrs, G., Holmes, N., Basheer, L., Basheer, M. and Nanukuttan, S.V. (2010) 'Developments in monitoring techniques for durability assessment of cover-zone concrete'. *Computer-Aided Design*, *17*(6), pp.294-303

McCarter, W.J., Chrisp, T.M., Butler, A. and Basheer, P.A.M (2001) 'Near-surface sensors for condition monitoring', *Construction and Building Materials,* 15(2-3), pp.115-124

McCarter, W.J., Chrisp, T.M., Starrs, G., Adamson, A., Owens, E., Basheer, P.A.M., Nanukuttan, S.V., Srinivasan, S. and Holmes, N. (2012) 'Developments in performance monitoring of concrete exposed to extreme environments', *Journal of Infrastructure Systems*, 18(3), pp.167-175

McCarter, W.J., Emerson, M. and Ezirim, H. (1995) 'Properties of concrete in the cover zone: developments in monitoring techniques', *Magazine of Concrete Research*, 47(172), pp.243-251

McCarter, W.J., Starrs, G. and Chrisp, T.M. (2000) 'Electrical conductivity, diffusion, and permeability of Portland cement-based mortars', *Cement and Concrete Research*, 30(9), pp.1395-1400

McCarter, W.J., Starrs, G. and Chrisp, T.M. (2002) 'Electrical monitoring methods in cement science', *Structure and performance of cements*, pp.442-456

McCarter, W.J., Starrs, G., Kandasami, S., Jones, R. and Chrisp, M. (2009) 'Electrode configurations for resistivity measurements on concrete', *ACI Materials Journal*, 106(3), pp. 258–264

McCarter, W.J., Suryanto, B., Taha, H.M., Nanukuttan, S. and Basheer, P.A.M (2017) 'A testing methodology for performance-based specification', *Journal of Structural Integrity and Maintenance,* 2(2), pp.78-88

McCormick, N. and Lord, J. (2012) 'Digital image correlation for structural measurements', *Proceedings of the Institution of Civil Engineers - Civil Engineering*, 165(4), pp.185-190

Meoni, A., D'Alessandro, A., Downey, A., Laflamme, S. and Ubertini, F. (2018) 'Strain monitoring in masonry structures using smart bricks', *In: Sensors and Smart Structures Technologies for Civil, Mechanical, and Aerospace Systems*, 10598, pp.105981T

Moradllo, M.K., Qiao, C., Isgor, B., Reese, S. and Weiss, W.J. (2018) 'Relating formation factor of concrete to water absorption', *ACI Materials Journal*, 115(6), pp.887-898

Ncoor v1.2 (2018) *Open Source 2D-DIC Matlab Software* [online]. Available from: http://www.ncorr.com/ (accessed 02 February 2021).

NIST (2019) *Virtual cement and concrete testing laboratory (VCCTL) software, version 9.5. Gaithersburg, USA. National Institute of Standards and Technology (NIST)* [online]. Available from: https://www.nist.gov/services-resources/software/vcctl-software (Accessed 01 March 2021)

Ou, J. (2005) 'Some recent advances of intelligent health monitoring systems for civil infrastructures in HIT', *In Fundamental Problems of Optoelectronics and Microelectronics II*, 5851, pp.147-162

Ozbulut, O.E., Jiang, Z. and Harris, D.K. (2018) 'Exploring scalable fabrication of self-sensing cementitious composites with graphene nanoplatelets', *Smart Materials and Structures*, 27(11), p.115029

Pang, C., Yu, M., Gupta, A. and Bryden, K. (2013) 'Investigation of smart multifunctional optical sensor platform and its application in optical sensor networks', *Smart Structures and Systems*, 12(1), pp.23-39

Park, S., Ahmad, S., Yun, C. and Roh, Y. (2006) 'Multiple Crack Detection of Concrete Structures Using Impedance-based Structural Health Monitoring Techniques', *Experimental Mechanics*, 46, pp.609-618

Park. G., Sohn., H., Farrar, C.R. and Inman, D.J. (2003) 'Overview of Piezoelectric Impedance-Based Health Monitoring and Path Forward', The Shock and Vibration Digest, 35(6), pp.451–463

Peeters, B., Maeck, J. and Roeck, G.D. (2001) 'Vibration-based damage detection in civil engineering: excitation sources and temperature effects', *Smart Materials and Structures*, 10, pp.518-527

Post, D. (1983) 'Moiré Interferometry at VPI and SU', *Experimental Mechanics*, 23(2), pp.203-210

Presas, A., Luo, Y., Wang, Z., Valentin, D. and Egusquiza, M. (2018) 'A Review of PZT Patches Applications in Submerged Systems', Sensors, 18(7)

Prodromakis, T. and Papavassiliou, C. (2009) 'Engineering the Maxwell–Wagner polarization effect', *Applied Surface Science*, 255(15), pp.6989-6994

Rana, S., Subramani, P., Fangueiro, R. and Correia, A.G. (2016) 'A review on smart self-sensing composite materials for civil engineering applications', *AIMS Materials Science*, 3(2), pp.357-379

Ranade, R., Zhang, J., Lynch, J. and Li, V. (2014) 'Influence of micro-cracking on the composite resistivity of Engineered Cementitious Composites', *Cement and Concrete Research*, 58, pp.1-12

Reynolds, J.A. and Hough, J.M. (1957) 'Formulae for dielectric constant of mixtures', *Proceedings of the Physical Society. Section B*, 70(8), pp.769-775

Reza, F., Batson, G.B., Yamamuro, J.A. and Lee, J.S. (2003) 'Resistance changes during compression of carbon fiber cement composites', *Journal of materials in civil engineering*, 15(5), pp.476-483

Reza, F., Yamamuro, J.A. and Batson, G.B. (2004) 'Electrical resistance change in compact tension specimens of carbon fiber cement composites', *Cement & Concrete Composites*, 26(7), pp.873-881

Riches, O., Hill, C. and Baralos, P. (2019) 'Queensferry Crossing, UK: durability, maintenance, inspection and monitoring', In *Proceedings of the Institution of Civil Engineers-Bridge Engineering*, 172(2), pp.175-188

Riding, K.A., Thomas, M.D., Hooton, R.D., Obla, K.H. and Weiss, W.J. (2018) 'Performance-based specifications for concrete exposed to chlorides', *Concrete International*, 40, pp.41-47

Risch, B.G., Fox S., Delden R.A.V., Comteq D. and Ijzerweg T.B.V. (2010) 'Lifetime prediction of fiber optic cable materials for nuclear power applications: Evaluation of failure mechanism, end of life criteria, and test methodology', in *the 59th International Wire and Cable Symposium*. Providence, RI, USA, pp.183–191

Şahmaran, M. and Li, V.C. (2009) 'Influence of microcracking on water absorption and sorptivity of ECC', *Materials and structures*, 42(5), pp.593-603

Sasmal, S., Ravivarman, N. and Sindu, B.S. (2017) 'Synthesis, characterisation and performance of piezo-resistive cementitious nanocomposites', *Cement and Concrete Composites*, 75, pp.10-21

Schneider, C.A., Rasband, W.S., Eliceiri, K.W. (2012) 'NIH Image to ImageJ: 25 years of image analysis' *Nature Methods*, 9, pp.671–675

Schwan, H.P., Schwarz, G., Maczuk, J. and Pauly, H. (1962) 'On the low-frequency dielectric dispersion of colloidal particles in electrolyte solution1', *The Journal of Physical Chemistry*, 66(12), pp.2626-2635

Schwarz, G. (1962) 'A theory of the low-frequency dielectric dispersion of colloidal particles in electrolyte solution', *The Journal of Physical Chemistry*, 66(12), pp.2636-2642

Shi, Z.Q. and Chung, D.D.L (1999) 'Carbon fiber-reinforced concrete for traffic monitoring and weighing in motion', *Cement and Concrete Research*, 29(3), pp.435-439

Snyder, K.A., Feng, X., Keen, B.D. and Mason, T.O. (2003) 'Estimating the electrical conductivity of cement paste pore solutions from OH^-, K^+ and Na^+ concentrations', *Cement and Concrete Research*, 33(6), pp.793-798

Sohn, H. (2006) 'Effects of environmental and operational variability on structural health monitoring', *Philosophical Transactions of the Royal Society A: Mathematical, Physical and Engineering Sciences*, 365(1851), pp.539-560

Song, G., Wang, C. and Wang, B. (2017) 'Structural Health Monitoring (SHM) of Civil Structures', *Applied Sciences*, 7(8), pp.789

Spragg, R., Villani, C. and Weiss, J. (2016) 'Electrical properties of cementitious systems: formation factor determination and the influence of conditioning procedures', *Advances in Civil Engineering Materials*, 5(1), pp.124-148

Starrs, G. and McCarter, W.J. (1998) 'Immittance response of cementitious binders during early hydration', *Advances in cement research*, 10(4), pp.179-186

Sun, Z. and Sun, H. (2018) 'Jiangyin Bridge: An example of integrating structural health monitoring with bridge maintenance', *Structural Engineering International*, 28(3), pp.353-356

Suryanto, B., Buckman, J.O., McCarter, W.J. and Taha, H. (2018) 'In-situ dynamic WetSEM imaging and electrical impedance measurements on Portland cement during early hydration', *Materials Characterization*, 142, pp.86-100

Suryanto, B., Kim, J., McCarter, W.J., Starrs, G. and Aitken, M.W. (2020b) 'Assessing the Performance and Transport Properties of Concrete using Electrical Property Measurements', *Journal of Advanced Concrete Technology*, 18(7), pp.437-455

Suryanto, B., McCarter, W., Starrs, G. and Ludford-Jones, G. (2016) 'Electrochemical immittance spectroscopy applied to a hybrid PVA/steel fiber engineered cementitious composite', *Materials & Design*, 105, pp.179-189

Suryanto, B., McCarter, W.J., Starrs, G. and Chrisp, T.M. (2017c) 'Characterization of fly-ash using electrochemical impedance spectroscopy', *Procedia engineering*, 171, pp.705-714

Suryanto, B., McCarter, W.J., Starrs, G. and Jablonski, M. (2017a) 'Assessing the performance of engineered cementitious composites under cyclic wetting and drying', *In International Conference on Strain-Hardening Cement-Based Composites*, pp.573-581

Suryanto, B., McCarter, W.J., Starrs, G., Wilson, S.A. and Traynor, R.M. (2015) 'Smart cement composites for durable and intelligent infrastructure', *Procedia Engineering*, 125, pp.796-803

Suryanto, B., Saraireh, D. and Tambusay, A. (2020a) 'Temperature dependence and activation energy of electrical conduction in an engineered cementitious composite', *In IOP Conference Series: Materials Science and Engineering*, (930(1), pp.012053

Suryanto, B., Tambusay, A. and Suprobo, P. (2017b) 'Crack mapping on shear-critical reinforced concrete beams using an open source digital image correlation software', *Civil Engineering Dimension*, 19(2), pp.93–98

Sutton, M.A., Cheng, M.Q., Peters, W.H., Chao Y.J. and McNeill, S.R. (1986) 'Application of an Optimized Digital Correlation Method to Planar Deformation Analysis', *Image and Vision Computing*, 4(3), pp.143-151

Sutton, M.A., McNeill, S.R., Jang, J. and Babai, M. (1988) 'Effects of Sub-pixel Image Restoration on Digital Correlation Error', *Journal of Optical Engineering,* 27(10), 870-877.

Sutton, M.A., Turner, J.L., Bruck, H.A. and Chae, T.A. (1991) 'Full-field Representation of Discretely Sampled Surface Deformation for Displacement and Strain Analysis', *Experimental Mechanics*, 31(2), pp.168-177

Sutton, M.A., Wolters, W.J., Peters, W.H., Ranson, W.F. and McNeil, S.R. (1983) 'Determination of Displacements Using an Improved Digital Correlation Method', *Image and Vision Computating*, 1(3), pp.133-139

Taha, H.M., McCarter, W.J., Suryanto, B. and Starrs, G. (2017) 'Frequency-and time-domain dependency of electrical properties of cement-based materials during early hydration', *Advances in Civil Engineering Materials*, 6(2), pp.65-83

Tambusay, A., Suryanto, B. and Suprobo, P. (2018) 'Visualization of Shear Cracks in a Reinforced Concrete Beam Using the Digital Image Correlation', *International Journal on Advanced Science, Engineering and Information Technology*, 8(2)

Tambusay, A., Suryanto, B. and Suprobo, P. (2020) 'Digital image correlation for cement-based materials and structural concrete testing', *Civil Engineering Dimension*, 22(1), pp.6-12

Tennyson, R.C., Mufti, A.A., Rizkalla, S., Tadros, G. and Benmokrane, B. (2001) 'Structural Health Monitoring of Innovative Bridges in Canada with Fiber Optic Sensors', *Smart Materials and Structures*, 10(3), pp.560–573

Teomete, E., and Kocyigit, O.I. (2013) 'Tensile strain sensitivity of steel fiber reinforced cement matrix composites tested by split tensile test', *Construction and Building Materials*, 47, pp.962-968

Torrents, J.M., Mason, T.O., Peled, A., Shah, S.P. and Garboczi, E.J. (2001) 'Analysis of the impedance spectra of short conductive fiber-reinforced composites', *Journal of Materials Science*, 36(16), pp.4003–4012

Tsui Chang, M. (2017) *The Evaluation of Cementitious Pore Solution Composition and Electrical Resistivity Using X-Ray Fluorescence (XRF)*, MSc. thesis, University of Oregon State . Available at: https://digitalcommons.uri.edu/cgi/viewcontent.cgi?article=2268&context=theses (Accessed 15 February 2021)

UK HM Treasury (2014) *National Infrastructure Plan* [online]. Available from: https://assets.publishing.service.gov.uk/government/uploads/system/uploads/attachment_data/file/381884/2902895_NationalInfrastructurePlan2014_acc.pdf (Accessed 1 January 2021)

Vilaplana, J.L., Baeza, F.J., Galao, O., Zornoza, E. and Garcés, P. (2013) 'Self-sensing properties of alkali activated blast furnace slag (BFS) composites reinforced with carbon fibers', *Materials*, 6(10), pp.4776-4786

Vishay Micro-Measurements (2007) *Strain gage installations for concrete structures (Application Note TT-611)*. Available from: http://www.vishaypg.com/docs/11091/tt611.pdf (Accessed 10 January 2021)

Wang, B., Ou, J.P. and Zhang, X.Y. (2007) 'Experimental research on sensing properties of CFRP bar and concrete beams reinforced with CFRP bars', *Journal of Harbin Institute of Technology*, 39(2), pp. 220-224

Wang, W., Wu, S.G. and Dai, H.Z. (2006) 'Fatigue behavior and life prediction of carbon fiber reinforced concrete under cyclic flexural loading', *Materials Science and Engineering: A*, 434(1-2), pp.347–351

Wang, Y.Y., Chen, D.J. and Chiang, F.P. (1993) 'Material testing by computer aided speckle interferometry', *Experimental Techniques*, 17(5), pp.30-32

Wansom, S. and Kanokkanchana, K. (2017) 'Electrical impedance response for physical simulations of composites with conductive fiber-bridged insulating cracks', *Journal of Materials Science*, 52(17), pp.10023-10037

Wen, S. and Chung, D.D.L. (2000) 'Uniaxial tension in carbon fiber reinforced cement, sensed by electrical resistivity measurement in longitudinal and transverse directions', *Cement and Concrete Research*, 30(8), pp.1289-1294

Wen, S. and Chung, D.D.L. (2001) 'Uniaxial compression in carbon fiber reinforced cement, sensed by electrical resistivity measurement in longitudinal and transverse directions', *Cement and Concrete Research*, 31(2), pp.297-301

Wen, S. and Chung, D.D.L. (2003) 'A comparative study of steel-and carbon-fibre cement as piezoresistive strain sensors', *Advances in cement research*, 15(3), pp.119-128

Wen, S. and Chung, D.D.L. (2005) 'Strain sensing characteristics of carbon fiber reinforced cement', *ACI Materials Journal*, *102*(4), pp.244

Wen, S. and Chung, D.D.L. (2006) 'Self-sensing of flexural damage and strain in carbon fiber reinforced cement and effect of embedded steel reinforcing bars', *Carbon*, *44*(8), pp.1496-1502

Wen, S. and Chung, D.D.L. (2007a) 'Piezoresistivity-based strain sensing in carbon fiber-reinforced cement', *ACI materials journal*, 104(2), pp.171.

Wen, S. and Chung, D.D.L. (2007b) 'Electrical-resistance-based damage self-sensing in carbon fiber reinforced cement', *Carbon*, 45(4), pp.710-716

Whittington, H.W., McCarter, J. and Forde, M.C. (1981) 'The conduction of electricity through concrete', *Magazine of concrete research*, 33(114), pp.48–60

Wu, L., Farzadnia, N., Shi, C., Zhang, Z. and Wang, H. (2017) 'Autogenous shrinkage of high performance concrete: A review', *Construction and Building Materials*, 149, pp.62-75

Wu, Z.S. (2003) 'structural health monitoring and intelligent infrastructure in Japan', *Structural Health Monitoring and Intelligent Infrastructure Conference*, 13-15 November. Tokyo: Japan, pp.153-170

Yang, P., Chowdhury, S. and Neithalath, N. (2018) 'Strain sensing ability of metallic particulate reinforced cementitious composites: Experiments and microstructure-guided finite element modeling', *Cement and Concrete Composites*, 90, pp.225-234

Yıldırım, G., Öztürk, O., Al-Dahawi, A., Ulu, A.A. and Şahmaran, M. (2020) 'Self-sensing capability of Engineered Cementitious Composites: Effects of aging and loading conditions', *Construction and Building Materials*, 231, pp.117132

Yoo, D.Y., You, I., Zi, G. and Lee, S.J. (2019) 'Effects of carbon nanomaterial type and amount on self-sensing capacity of cement paste', *Measurement*, 134, pp.750-761

Appendix-A

Table A-1 presents σ_{ref} values for ECC mixes produced at different times with $t_{ref} = 28$ days. It is interesting to notice that for all ECC mixes, the exponent n is always similar and equal to 0.73. This implies that the effect of hydration for any ECC mix can always be determined using this relationship with the need of measuring the impedance response at 28 days.

Table A-1: Average conductivity of ECC mixes at 28-d curing ($\sigma 28$).

Mix No.	$\sigma 28$ ($\times 10^{-4}$ S/cm)	N	F_{28} (MPa)
MB (a)	3.67	0.73	33.1
MB (b)	3.69	0.73	45.1
MB (c)	3.88	0.73	40.4
MB (d)	2.35	0.73	49.4
MB (e)	4.89	0.73	42.8

Table A-2: Fitting parameters used in the simulation for PC (MF0) mix.

Circuit elements	Curing Age (days)						
	14	21	28	42	63	90	180
Rs (Ω)	482	460	447	430	410	389	350
R_{cp} (Ω)	2807	3160	3442	3888	4376	4862	5849
CPE-T_{sm} $(\times 10^{-10})$	1.5	1.5	1.5	1.5	1.6	1.7	1.9
CPE-P_{sm}	0.84	0.84	0.83	0.83	0.82	0.81	0.80
R_{cp-el} $(k\Omega)$	100	100	100	100	100	100	100
CPE-T_{cp-el} $(\times 10^{-4})$	4.1	4.0	3.9	3.9	3.8	3.7	3.7
CPE-P_{cp-el}	0.76	0.75	0.75	0.75	0.75	0.75	0.74

Table A-3: Fitting parameters used in the simulation for ECC (MB) mix.

Circuit elements	Curing Age (days)						
	14	21	28	42	63	90	180
R_s (Ω)	421	400	385	340	263	174	22
R_{cp} (Ω)	1052	1606	2147	2995	4385	6062	11651
CPE-T_{sm} ($\times 10^{-10}$)	3.2	6.1	7.0	8.0	8.8	9.0	9.8
CPE-P_{sm}	0.84	0.79	0.77	0.75	0.74	0.73	0.71
R_{c-f} (Ω)	0.1	0.1	0.1	0.1	0.1	0.1	0.1
R_{ci} (kΩ)	20	38	48	60	77	92	144
CPE-T_{ci} ($\times 10^{-6}$)	8.4	7.1	6.7	6.1	5.4	5.0	3.9
CPE-P_{ci}	0.18	0.14	0.12	0.11	0.10	0.09	0.07
R_{c-cp} (Ω)	1052	1606	2147	2995	4385	6062	11651
CPE-T_{c-cp} ($\times 10^{-10}$)	3.2	6.1	6.0	8.0	8.8	9.0	9.8
CPE-P_{c-cp}	0.84	0.79	0.78	0.75	0.74	0.73	0.71
R_{cp-el} (kΩ)	100	100	100	100	100	100	100
CPE-T_{cp-el} ($\times 10^{-4}$)	5.1	4.8	4.5	4.3	4.0	3.9	3.6
CPE-P_{cp-el}	0.76	0.75	0.75	0.75	0.75	0.75	0.75

Table A-4: Circuit parameters from fitting for specimens (P1 and P2) under varying temperatures

Parameters	P1	P2	Mean	SD	CoV (%)
6.5°C					
R_{cp} (kΩ)	50.1	50.6	50.4	0.25	0.01
CPE-$C_{o,sm}$ (nFs^{p-1})	2.1	2.1	2.1	0.00	0.00
CPE-p_{sm}	0.64	0.64	0.64	0.00	0.00
10°C					
R_{cp} (kΩ)	43.8	42.4	43.1	0.7	0.02
CPE-$C_{o,sm}$ (nFs^{p-1})	2.2	2.2	2.20	0.00	0.00
CPE-p_{sm}	0.64	0.64	0.64	0.00	0.00
15°C					
R_{cp} (kΩ)	38.6	38.1	38.4	0.25	0.01
CPE-$C_{o,sm}$ (nFs^{p-1})	2.3	2.3	2.30	0.00	0.00
CPE-p_{sm}	0.64	0.64	0.64	0.00	0.00
20°C					
R_{cp} (kΩ)	32.6	32.9	32.8	0.15	0.01
CPE-$C_{o,sm}$ (nFs^{p-1})	2.4	2.3	2.4	0.05	0.02
CPE-p_{sm}	0.64	0.65	0.65	0.01	0.01
30°C					
R_{cp} (kΩ)	24.0	23.6	23.8	0.20	0.01
CPE-$C_{o,sm}$ (nFs^{p-1})	2.4	2.3	2.4	0.05	0.02
CPE-p_{sm}	0.65	0.65	0.65	0.00	0.00
40°C					
R_{cp} (kΩ)	19.3	18.6	19.0	0.35	0.02
CPE-$C_{o,sm}$ (nFs^{p-1})	2.5	2.3	2.4	0.10	0.04
CPE-p_{sm}	0.65	0.65	0.65	0.00	0.00

Table A-4: Circuit parameters from fitting for specimens (P1 and P2) under varying temperatures (Continued).

<u>50°C</u>

R_{cp} (kΩ)	15.0	14.7	14.9	0.15	0.01
CPE-$C_{o,sm}$ (nFs^{p-1})	2.6	2.4	2.5	0.10	0.04
CPE-p_{sm}	0.65	0.66	0.66	0.01	0.01

<u>60°C</u>

R_{cp} (kΩ)	12.1	11.9	12.0	0.10	0.01
CPE-$C_{o,sm}$ (nFs^{p-1})	2.6	2.4	2.5	0.10	0.04
CPE-p_{sm}	0.66	0.66	0.66	0.00	0.00

Appendix-B

B1: Hydration effects of the 1ˢᵗ series and the 2ⁿᵈ series:
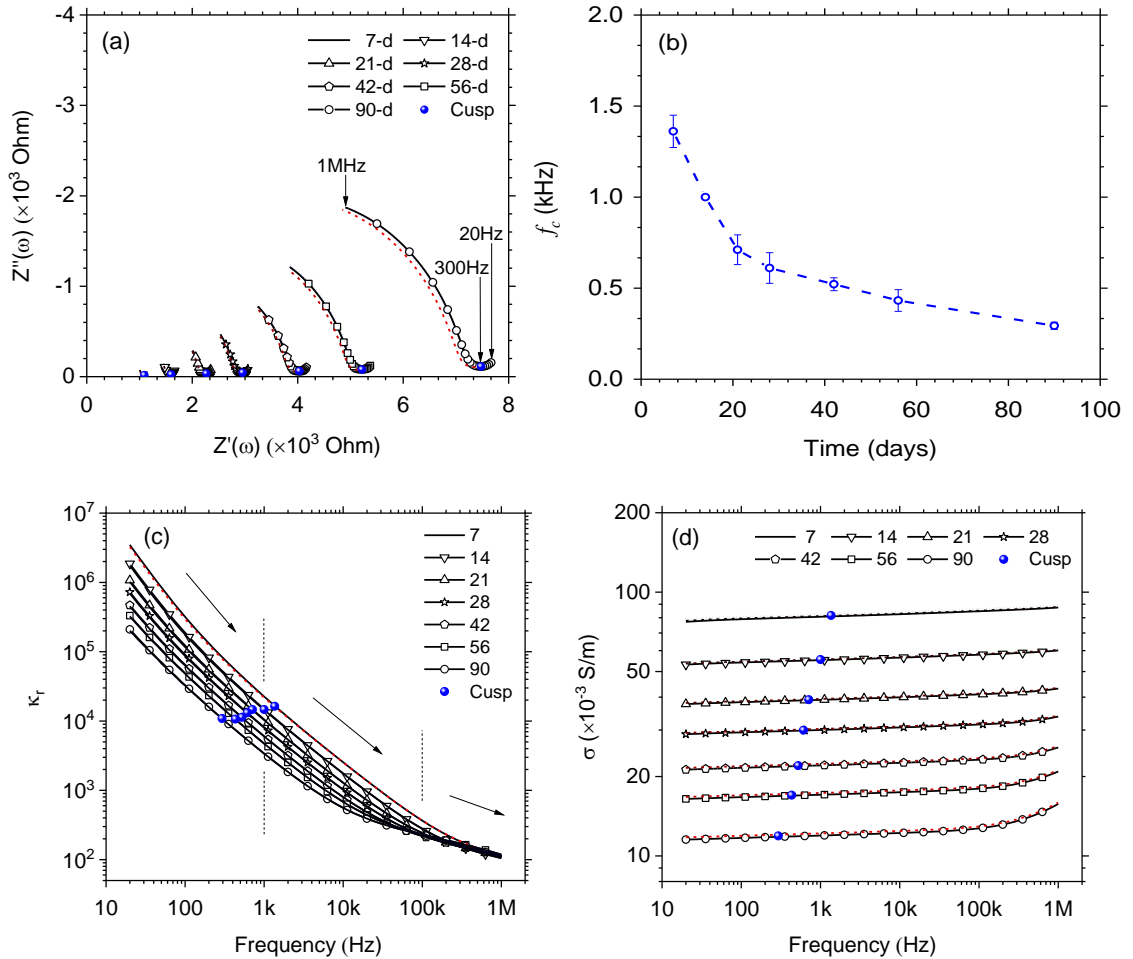
Figures B-1: Influence of curing on the electrical properties of prisms E-ECC-S-(P1–P3) over the initial 90 days of curing: (a) impedance response; (b) variation in cusp-point frequency, f_c; (c) relative permittivity versus frequency; and (d) conductivity versus frequency. The solid markers in (c) and (d) indicate the permittivity/conductivity corresponding to the cusp point of the impedance response presented in (a).
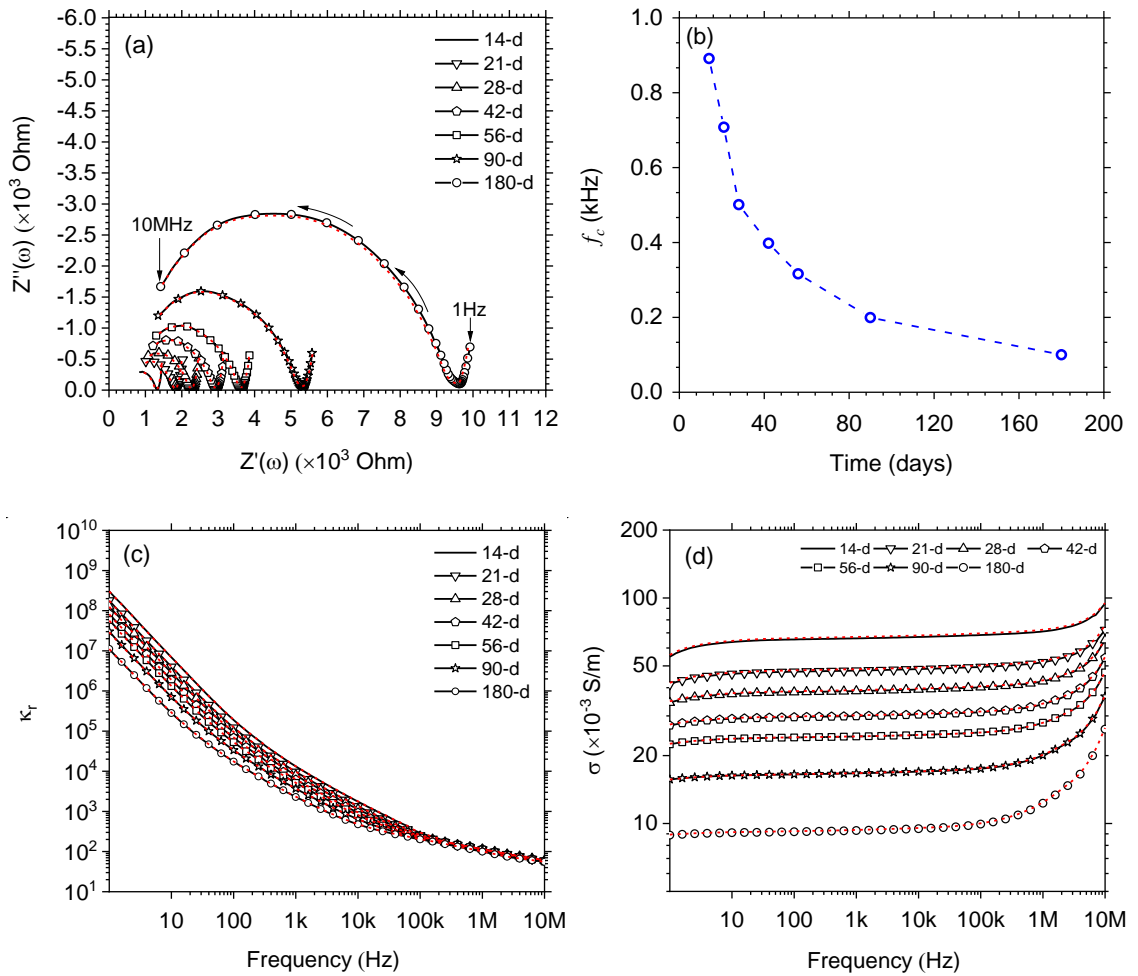
Figures B-2: Influence of curing on the electrical properties of prisms E-ECC-L-(P1–P2) over the initial 180 days of curing: (a) impedance response; (b) variation in cusp-point frequency, f_c; (c) relative permittivity versus frequency; and (d) conductivity versus frequency.

B3: Digital Image Correlation (DIC):

There has been a growing demand within the engineering industry to evaluate the displacement and strains within materials. Several studies have been conducted on optical techniques in order to evaluate the fracture parameters and material strengths, such as holography (Fottenburg, 1969), moiré interferometry (Post, 1983), and speckle inteferometry (Wang et al., 1993). These optical techniques have been used successfully in various applications to analyse macroscopic parameters. However, it requires strict implementation. Thus, it is a time-consuming and laborious procedure to stabilize the system (Hung and Voloshin, 2003).

For a more practical technique, researchers Sutton et al. (1983, 1986, 1988, 1991) and Bruck et al. (1989) have developed a non-contact optical measurement technique called digital image correlation (DIC) (Hung and Voloshin, 2003). DIC is a fast-growing technique that offers a low-cost manner of measuring material deformation (Fayyad and Lees, 2014; Tambusay et al., 2018). The DIC technique normally requires applying a speckle pattern on the specimen surface, ideally as a high contrast random speckle intensity pattern (in other words, randomly distributed black dots on a white background) (Tambusay et al., 2018).

The DIC technique works by conducting a comparison of images that were taken at various loading stages. This necessitates the capture of a reference image in an undamaged state as well as a current image when deformation occurs (Fayyad and Lees, 2014). The reference image is broken down into small subsets and the current image is then analysed through comparing the small subsets and tracking their new positions. This allows the DIC software to measure the relative displacement of an area through using image registration algorithms (McCormick and Lord, 2012; Blaber et al., 2015).

Although DIC is comparatively a new monitoring technique, it has many applications in the civil engineering industry. This technique permits structures monitoring without the expensive maintenance and bothersome installation as required through other alternative techniques, such as strain gauges (Huang et al., 2010), ultrasound sensors (Chaki and Bourse, 2009) and fibre optic sensors (Tennyson et al., 2001). Malesa et al. (2010) pointed out that catastrophes, such as the railway bridge near Dublin (over Malahide estuary), Ireland, 2009; and the highway truss bridge in Minneapolis (over Mississippi), USA, 2007, could have been anticipated and avoided if a reliable, comparatively cheap, and automatic monitoring system such as DIC had been applied to these structures.

The DIC technique was used to obtain full-field measurements in a variety of civil engineering applications. Tambusay et al. (2018) used the DIC technique to examine the shear behaviour of reinforced concrete beams and to find out how efficient the low-cost DIC system is in terms of visualizing the crack initiation and propagation. Figure B-3

presents the longitudinal strain plots which were obtained from the beam surface through the use of the DIC technique. The magnitude of strain increases with increasing the stage of load due to the increase in crack width. It was found that DIC demonstrated its ability to examine the shear failure in concrete and to track the crack formation and propagation even with a limited crack width (<0.2 mm). Fayyad and Lees (2017) stated the effectiveness of the DIC technique to monitor crack propagation is based on the use of a high resolution camera.
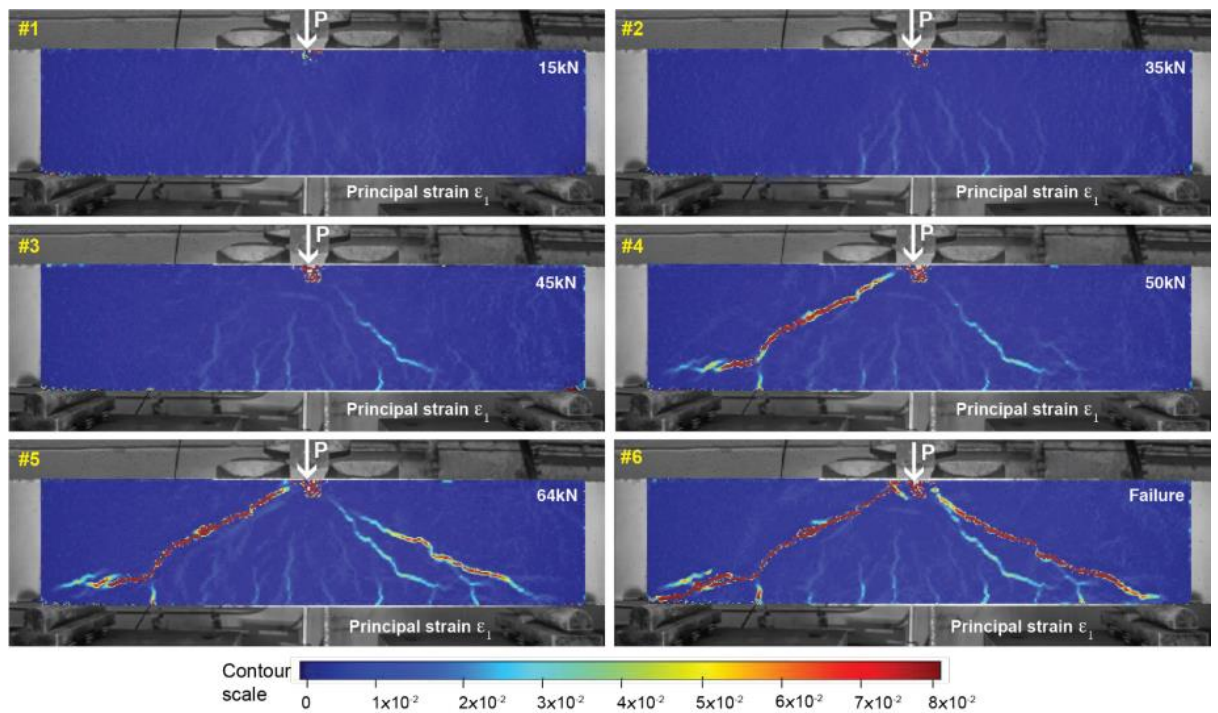
Figure B-3: Plots of longitudinal strain acquired from the beam surface using the DIC technique (Tambusay et al., 2018).

B4: Equivalent circuit Modelling:

Table B-1: Circuit parameters from fitting for specimens E-ECC-S-(P1–P3) over the initial 90 days of curing.

Parameters	E-ECC-S-P1	E-ECC-S-P2	E-ECC-S-P3	Mean	SD	CoV (%)
28-day						
R_{cp} (kΩ)	2.79	2.76	2.78	2.77	15.9	0.6
CPE-$C_{o,sm}$ (nFs^{p-1})	0.73	0.66	0.76	0.72	0.05	7.2
CPE-p_{sm}	0.74	0.75	0.74	0.74	0.004	0.6
56-day						
R_{cp} (kΩ)	4.96	4.88	4.97	4.94	48.2	1.0
CPE-$C_{o,sm}$ (nFs^{p-1})	1.11	1.10	1.07	1.09	0.02	1.9
CPE-p_{sm}	0.73	0.72	0.72	0.72	0.005	0.7
90-day						
R_{cp} (kΩ)	7.14	7.02	7.01	7.09	65.1	0.9
CPE-$C_{o,sm}$ (nFs^{p-1})	1.73	1.64	1.70	1.69	0.05	2.7
CPE-p_{sm}	0.69	0.69	0.69	0.69	0.002	0.3

Table B-2: Circuit parameters from fitting for specimens E-ECC-L-(P1-P2) over the initial 180 days of curing.

Parameters	E-ECC-L-P1	E-ECC-L-P2	Mean	SD	CoV (%)
28-day					
R_{cp} (kΩ)	2.27	2.63	2.45	0.18	0.104
CPE-$C_{o,sm}$ (nFs^{p-1})	1.51	1.55	1.53	0.02	0.018
CPE-p_{sm}	0.70	0.70	0.70	0.00	0.000
56-day					
R_{cp} (kΩ)	3.63	3.61	3.62	0.01	0.004
CPE-$C_{o,sm}$ (nFs^{p-1})	1.68	1.70	1.69	0.01	0.008
CPE-p_{sm}	0.69	0.69	0.69	0.00	0.000
90-day					
R_{cp} (kΩ)	5.30	5.28	5.29	0.01	0.003
CPE-$C_{o,sm}$ (nFs^{p-1})	1.77	1.79	1.78	0.01	0.008
CPE-p_{sm}	0.68	0.68	0.68	0.00	0.000
180-day					
R_{cp} (kΩ)	9.46	9.45	9.46	0.01	0.001
CPE-$C_{o,sm}$ (nFs^{p-1})	2.22	2.22	2.22	0.00	0.000
CPE-p_{sm}	0.67	0.67	0.67	0.00	0.000

Table B-3: Circuit parameters representing the micro-cracks for specimens E-ECC-S-DB3 and E-ECC-S-DB4 at various strain levels (+ = not determined).

Parameters	Tensile strain, ε_t				
	1%	**2%**	**3%**	**4%**	**4.9%**
E-ECC-S-DB3					
R_c (kΩ)	5.2	13.3	23.7	35.3	62.4
CPE- $C_{o,c}$ (pFs^{p-1})	47.3	20.9	13.9	13.4	11.7
CPE- p_c	0.94	0.94	0.93	0.92	0.91
E-ECC-S-DB4					
R_c (kΩ)	1.8	5.4	10.4	19.2	+
CPE- $C_{o,c}$ (pFs^{p-1})	134	48.2	32.2	31.4	+
CPE- p_c	0.90	0.90	0.89	0.86	+

Notes: For DB3, R_{cp}= 8kΩ; CPE-$C_{o,sm}$= 304pFs$^{-0.26}$ and p_{sm}= 0.74, whereas for DB4, R_{cp}= 8kΩ; CPE-$C_{o,sm}$= 793pFs$^{-0.33}$ and p_{sm}= 0.67.

Table B-4: Circuit parameters representing the micro-cracks for specimens E-ECC-L-DB2 and E-ECC-L-DB3 at various strain levels (+ = not determined).

Parameters	Tensile strain, ε_t			
	1%	**2%**	**3%**	**4%**
E-ECC-L-DB2				
R_c (kΩ)	18.5	39.9	63.9	86.7
CPE- $C_{o,c}$ (pFs^{p-1})	20.1	10.4	8.4	7.7
CPE- p_c	0.94	0.93	0.92	0.91
E-ECC-L-DB3				
R_c (kΩ)	5.1	32.9	72.4	147.3
CPE- $C_{o,c}$ (pFs^{p-1})	340.7	64.1	41.1	31.3
CPE- p_c	0.88	0.86	0.85	0.84

Notes: For DB2, R_{cp}= 21kΩ; CPE-$C_{o,sm}$= 6.7nFs$^{-0.47}$ and p_{sm}= 0.53, whereas for DB3, R_{cp}= 21kΩ; CPE-$C_{o,sm}$= 6.9nFs$^{-0.47}$ and p_{sm}= 0.53.

Appendix-C

Table C-1: Circuit parameters from fitting for the E-ECC-NC-DB2 sample during the drying process.

Circuit elements	Time (hrs)						
	0hr	4hrs	8hrs	12hrs	16hrs	20hrs	24hrs
R_{cp} (Ω)	11982	21532	28326	34474	40723	49858	55434
CPE-T_{sm} ($\times 10^{-10}$)	1.5	1.4	1.3	1.2	1.2	1.2	1.1
CPE-P_{sm}	0.78	0.78	0.77	0.77	0.77	0.77	0.77

Table C-2: Circuit parameters from fitting for the E-ECC-NC-DB2 sample during the drying process.

Circuit elements	Time (hrs)					
	4hrs	8hrs	12hrs	16hrs	20hrs	24hrs
R_c (Ω)	93692	177420	297630	450470	628380	891000
CPE-T_c ($\times 10^{-10}$)	2.5	2.2	2.1	2.0	1.9	1.9
CPE-P_c	0.79	0.79	0.79	0.78	0.78	0.78

Appendix-D

The electro-mechanical tensile properties of an engineered cementitious composite

Danah Saraireh
School of Energy, Geoscience, Infrastructure and Society, Institute for Infrastructure and Environment, Heriot-Watt University, Edinburgh, Scotland, UK

Benny Suryanto
School of Energy, Geoscience, Infrastructure and Society, Institute for Infrastructure and Environment, Heriot-Watt University, Edinburgh, Scotland, UK (Orcid:0000-0002-3979-9994) (corresponding author: b.suryanto@hw.ac.uk)

William John McCarter
School of Energy, Geoscience, Infrastructure and Society, Institute for Infrastructure and Environment, Heriot-Watt University, Edinburgh, Scotland, UK (Orcid:0000-0002-1949-2856)

Steven Walls
School of Energy, Geoscience, Infrastructure and Society, Institute for Infrastructure and Environment, Heriot-Watt University, Edinburgh, Scotland, UK

The influence of ongoing cement hydration and multiple microcrack formation on the electrical impedance of an engineered cementitious composite (ECC) is presented. Impedance measurements were obtained over the frequency range 20 Hz–1 MHz and displayed in the Nyquist format. In addition, the permittivity and conductivity were de-embedded from the measured impedance and presented in both time and frequency domains to elucidate the nature of conduction and polarisation processes. It was found that, over a curing period of 90 days, the ECC displayed a classic impedance response. Both conductivity and relative permittivity were found to be frequency dependent due to bulk relaxation processes operating within the composite. Tensile straining was shown to result in a detectable change in the impedance response, but retained a similar overall profile. When presented in the frequency domain, a downward displacement in both conductivity and relative permittivity profiles was evident with increasing tensile strain. It is shown that the relative permittivity at the high-frequency end could be exploited as a potentially useful indicator for strain/damage detection. The influence of microcracking on the piezo-resistive response of the composite is discussed based on crack patterns obtained from both visual observations and digital image correlation.

Notation

F_{28}	28-day compressive strength (50 mm cube)
F_{90}	90-day compressive strength (50 mm cube)
F	tensile stress (MPa)
f	frequency (Hz)
f_c	cusp-point frequency (Hz)
f_{cr}	first crack tensile stress (MPa)
f_{tu}	tensile strength (MPa)
g_{db}	geometrical constant for dogbone-shaped specimens ($= 245.28/m$)
g_p	geometrical constant for prism specimens ($= 88.48/m$)
$R_{db,28}$	28-day electrical resistance for dogbone-shaped specimen (Ω)
$R_{p,28}$	28-day electrical resistance for prism specimen (Ω)
$Z(\omega)$	electrical impedance (Ω)
$Z'(\omega)$	resistive (real) component of impedance (Ω)
$Z''(\omega)$	reactive (imaginary) component of impedance (Ω)
ε_t	tensile strain after start of test
ε_{tu}	tensile strain capacity
κ_o	permittivity of free space (8.854×10^{-12} F/m)
κ_{cr}	average relative permittivity of microcracks
$\kappa'_t(\omega)$	relative permittivity
$\kappa_{r,i}$	initial bulk relative permittivity of composite (at $\varepsilon_t = 0$)
$\kappa_{r,t}$	bulk relative permittivity of composite at strain ε_t after start of test
$\rho(\omega)$	bulk resistivity ($\Omega.m$)
ρ_{28}	28-day electrical resistivity ($\Omega.m$)
ρ_i	initial bulk resistivity (at $\varepsilon_t = 0$) ($\Omega.m$)
ρ_t	bulk resistivity at strain ε_t after start of test ($\Omega.m$)
$\sigma(\omega)$	bulk conductivity (S/m)
$\phi_{r,i}$	initial volume at start of test
ϕ_{cr}	volume fraction of microcracks at strain ε_t
$\phi_{r,t}$	total volume at strain ε_t after start of test
ω	angular frequency

Introduction

Concrete is the most widely used construction material, with a large proportion of infrastructure worldwide built using concrete in one form or another. While most key infrastructure is designed for an intended working life of at least 100 years, premature deterioration remains commonplace (Kim *et al.*, 2016; Li *et al.*, 2009). Although some deterioration may not have a direct implication on structural integrity, immediate repair may be required so as not to impair in-service performance (Frangopol *et al.*, 2017). The earlier any deterioration is detected, the earlier appropriate remedial measures can be taken, thereby avoiding the need for costly repairs at a later stage (McCarter *et al.*, 2017; Pines and Aktan, 2002). With the ever-increasing amount of infrastructure around the world and the continual deterioration of existing infrastructure, it is expected that structural inspection and maintenance will have an increasing role to play for the foreseeable future.

It is common practice to undertake periodic visual inspections to enable the effective management and maintenance of

1

Advances in Cement Research

The electro-mechanical tensile properties
of an engineered cementitious composite
Saraireh, Suryanto, McCarter and Walls

infrastructure (Omar and Nehdi, 2018; Pines and Aktan, 2002); however, this requires direct site visits by qualified engineers at predetermined times during the life of a structure (HE, 2017). While visual inspection is relatively straightforward to undertake and allows evidence to be gathered directly on site, it only provides a snapshot of information in time – it is the change in condition over time that needs to be assessed so as to provide a reliable assessment of structural health (Choi et al., 2004; Hedegaard et al., 2017; Kim et al., 2018). A further limitation of visual inspection is that some damage may not be readily visible, thereby remaining undetected until advanced stages, which may involve costly repairs. A number of automated structural health monitoring systems have been developed to mitigate the shortcomings of traditional on-site inspections, with some already implemented in real structures and bridges (Abé and Fujino, 2017; Agdas et al., 2015; Lynch et al., 2017; Soga, 2018; Spencer Jr et al., 2017). Such systems typically require the installation of an extensive network of surface-mounted or embedded sensors and monitoring of their responses over time. A similar approach was employed in the work presented here, although the concrete itself was used as the sensor. Developments in this field include moisture sensors (McCarter et al., 2012), weigh-in-motion and traffic sensors (Han et al., 2011; Shi and Chung, 1999) and strain/damage sensors (Azhari and Banthia, 2012; Yoo et al., 2019). While the sensing capabilities of cement-based strain/damage sensors have been well documented, they may only be able to be employed under limited damage levels as the relationship between damage and strain increases non-linearly after cracking.

Recently, damage-tolerant cement-based materials known as engineered cementitious composite (ECCs) have been identified as potential damage sensors (Hou, 2008; Hou and Lynch, 2005; Lin et al., 2011; Ranade et al., 2014). The damage-tolerant property of ECCs originates primarily from their ability to exhibit multiple fine cracks when subjected to tensile stresses beyond the elastic range, generally displaying tensile strain hardening behaviour with a tensile capacity of the order of a few percent and an average crack width under 100 μm at maximum strain (Chen et al., 2018; Frank et al., 2018; Lee et al., 2018; Li, 2008; Ma et al., 2019; Suryanto et al., 2015). This is different from ordinary concrete and fibre-reinforced concrete, which generally fail locally due to a single crack. With regard to damage sensing, work has predominantly focused on the piezo-resistive properties of ECCs. Hou (2008) employed the four-point measurement technique to study the piezo-resistivity of a standard ECC mix under both DC and AC currents, with the latter applied at 5 kHz. They demonstrated that the composite displayed a quasi-linear piezo-resistive response during strain hardening resulting from the formation of multiple microcracks. Hou and Lynch (2005) further studied the piezo-resistive response of ECC mixes containing steel and carbon fibre using four-point DC measurements. They showed that the ECCs displayed a

linear relationship between the change in resistivity and tensile strain, and found that these ECCs were less sensitive to mechanical strain due to the presence of crack-bridging conductive fibres. To minimise bridging effects, Lin et al. (2011) added carbon black to the standard ECC mix to increase the contrast of the composite resistivity before and after cracking. The four-point AC measurement technique was employed, with measurements undertaken at 100 Hz. It was found that the sensitivity of the composite to cracking improved. Employing the two-point method and a constant AC current of 1 kHz, Ranade et al. (2014) tested moderate- and high-volume fly ash (FA) ECC mixes with different microcrack characteristics. It was found that, although the high-volume FA mix exhibited a greater number of microcracks, it exhibited less sensitivity to cracking than the moderate-volume FA mix due to its smaller microcrack widths.

To date, much work has focused on the piezo-resistive properties of ECCs using DC and fixed-frequency AC resistivity measurements. Little attention has been directed towards investigating the electrical properties of ECC over a wide frequency spectrum. When subjected to AC, porous materials such as ECCs can be expected to display both conductive and capacitive behaviour – the former due primarily to ionic conduction processes and the latter due to polarisation processes operating within the material (Suryanto et al., 2016, 2018a). The measurement of both quantities could provide more detailed information with regard to the strain/damage sensing capabilities of ECCs. In addition to mechanical loading, it is anticipated that the electrical properties of the ECCs are also influenced by cement hydration, but this aspect has been overlooked in prior studies. These aspects are addressed in this work.

Experimental programme

Materials and mix proportions
The mix proportions for the ECC used in this experimental programme are provided in Table 1. The binder comprised a blend of CEM I 52.5N Portland cement according to BS EN 197-1:2011 (BSI, 2011) and fine FA (Superpozz SV80, supplied by ScotAsh Ltd) at a cement/FA ratio of 1:1.8. To improve the dimensional stability of the mix, fine silica sand with a mean particle size of 120 μm was added at a sand/cement ratio 0.6:1 by mass; this particle size and amount were considered to ensure that the matrix toughness was low enough to allow tensile strain hardening behaviour. A typical oxide analysis of these materials is presented in Table 2. The water/binder ratio was set at a relatively low value (0.28) to produce a mix with adequate viscosity for fibre dispersion. The only fibres incorporated into the mix were Kuralon K-II REC15 polyvinyl alcohol (PVA) fibres, which have been specifically developed for use in ECCs by Kuraray Japan. The fibres had an average length of 12 mm, diameter of 39 μm

Advances in Cement Research

The electro-mechanical tensile properties
of an engineered cementitious composite
Saraireh, Suryanto, McCarter and Walls

Table 1. ECC mix proportions

Cement: kg/m³	FA: kg/m³	Silica sand: kg/m³	HRWR: kg/m³	PVA fibres: kg/m³
454	818	273	4.54	26 (2% by vol.)

Table 2. Oxide analysis and physical properties of materials

	Cement	FA	Silica sand
Chemical analysis: wt%			
Silicon dioxide (SiO₂)	19.9	52.7	98.8
Aluminium oxide (Al₂O₃)	4.8	26.6	0.21
Ferric oxide (Fe₂O₃)	3.1	5.6	0.09
Potassium oxide (K₂O)	ND[a]	ND	0.03
Calcium oxide (CaO)	62.4	2.4	ND
Magnesium oxide (MgO)	2.2	1.2	ND
Sodium oxide (Na₂O) equivalent	0.54	1.7	ND
Sulfur trioxide (SO₃)	3.0	0.3	ND
Free calcium oxide	ND	0.03	ND
Total phosphates	ND	0.5	ND
Loss on ignition	ND	<2.0	0.14
Physical properties			
Specific gravity	3.15	2.20	2.65
Surface area: m²/kg	375	1300	ND
Fineness: % retained on 25 μm sieve	ND	<25	ND
Cumulative amount retained: %			
500 μm	ND	ND	0.1
355 μm	ND	ND	0.5
250 μm	ND	ND	1.5
180 μm	ND	ND	6.0
125 μm	ND	ND	46.0
90 μm	ND	ND	83.0
63 μm	ND	ND	96.5

[a]Not determined

Chemical analysis in Table 2 uses the following notation: SiO_2, Al_2O_3, Fe_2O_3, K_2O, CaO, MgO, Na_2O, SO_3.

and tensile strength of 1.60 GPa, and were supplied with a proprietary oil-based coating agent (1.2% by mass) to reduce excessive bonding with the hardened ECC matrix. To aid fibre dispersion and improve the workability of the mix, high-range water-reducing (HRWR) admixture (MasterGlenium ACE499) was added at a dosage of 1% by cement weight.

Test specimens, fabrication and curing

A Hobart planetary motion mixer with a capacity of 10 l was used to prepare the mix presented in Table 1 in a single batch. In total, 13 specimens were produced, comprising

- three $40 \times 40 \times 160$ mm (long) prismatic specimens (P1–P3) to monitor the influence of continued hydration
- four dogbone-shaped specimens (DB1–DB4) of dimensions in accordance with the recommendations of the Japan Society of Civil Engineers (JSCE, 2008) to determine the mechanical and electrical properties under uniaxial tensile loading
- six 50 mm cuboidal specimens (C1–C6) to determine compressive strengths.

The prisms had two $45 \times 65 \times 2$ mm (thick) perforated stainless steel electrodes placed 140 mm apart (see Figure 1(a)). The electrodes had 10 mm round holes at a 15 mm staggered pitch to allow ease of infiltration by the ECC during casting and thereby ensuring intimate bonding (Suryanto *et al.*, 2018b). The dimensions of the dogbone-shaped specimens are shown in Figure 1(b). This figure also shows the electrode configuration employed, comprising two wire electrodes wrapped securely at the opposing ends of the central neck of the specimens. The wire electrodes were covered with several coats of silver-loaded conductive paint to seal any gaps and ensure intimate contact with the specimen.

The prisms were cast into a single-use three-gang polystyrene mould, whereas the dogbone and cube specimens were cast in custom-made plexiglass and three-gang steel moulds, both of which had been treated with a proprietary release agent (Sika Everbuild 206). Immediately after casting, all the specimens were covered with thick cling film and allowed to cure for 24 h. The specimens were then demoulded and stored in a curing tank at $20 \pm 2°C$ until they were required for testing. After 2 weeks, the dogbone-shaped specimens were removed from the curing tank and allowed to dry for $\sim$3 h; the wire electrodes, discussed above, were then attached to the specimens and coated with conductive paint. When the paint was dry, the samples were returned to the tank until required for testing at 28 days.

Test procedures and equipment

The work undertaken involved the testing of three prisms to study the influence of ongoing cement hydration and the testing of four dogbone-shaped specimens to obtain the electro-mechanical properties of the composite under tensile straining.

Hydration study and compressive strength

A Keysight E4980AL precision LCR meter was employed to acquire the electrical impedance of prisms P1–P3 over the initial 90 days after casting. The impedance was recorded at 20 spot frequencies per decade over the frequency range 20 Hz–1 MHz. The LCR meter was operated in voltage drive mode, at a constant signal amplitude of 350 mV, and controlled by a desktop computer (PC), which was also used for data acquisition. Communication with the LCR meter was established by means of the built-in USB interface in the LCR, which was accessed by the PC through Keysight IO Library Suite software (version 2017.1). To manage the overall running of the experiment, a customised virtual instrument was developed in the LabView environment (LabView, 2017),

3

Advances in Cement Research

**The electro-mechanical tensile properties
of an engineered cementitious composite**
Saraireh, Suryanto, McCarter and Walls
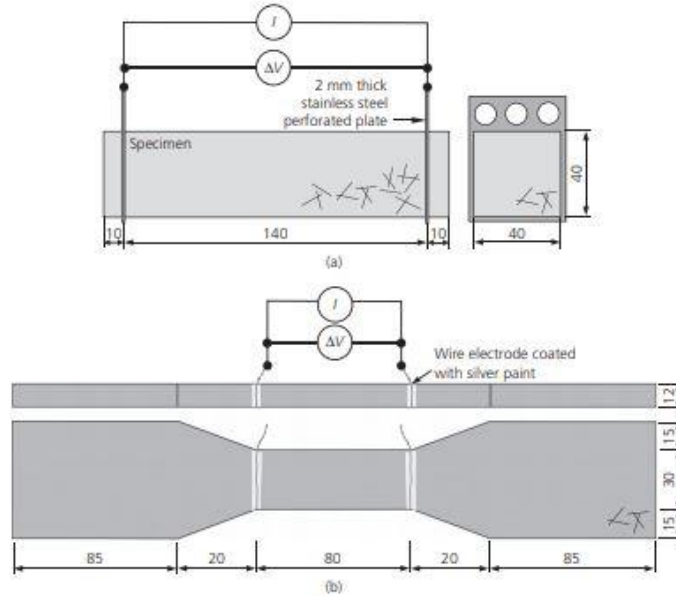
Figure 1. Schematic illustration of testing arrangement for two-point measurements using: (a) embedded perforated plate electrodes; (b) surface-applied (silver-coated) wire electrodes (dimensions in mm)

which permits full control of the LCR meter. This virtual instrument was also used to process the raw impedance data, present the results in both tabular and graphical forms, and store the processed data in a CSV format for further analysis. In the electrical measurements, four individually screened, short coaxial leads were used. At the time of testing, leads from the high-current and high-potential terminals on the LCR meter were connected to one electrode and the low-current and low-potential terminals to the other, following the two-point configuration (McCarter et al., 2015).

In addition to electrical measurements, the compressive strengths of the ECC were determined from C1–C6 using a 3000 kN Avery–Dennison testing machine under a loading rate of 50 kN/min. The strengths obtained on days 28 and 90 of the curing period (F_{28} and F_{90}, respectively) are listed in Table 3, together with the tensile strain capacity ε_{tu}, the first

crack strength f_{cr} and ultimate tensile strength f_{tu}, determined from the dogbone-shaped specimens (DB1–DB4).

Piezo-impedance study
On the 28th day of curing, tensile testing was performed on specimens DB1–DB4 using a 100 kN 4206 Instron machine (see Figure 2(a)). Prior to testing, each specimen was aligned in the machine and clamped at both ends using pneumatic grips. Loading was then performed under a cross-head speed of 0.5 mm/min. Tensile stresses were determined by dividing load cell readings from the test machine by the cross-sectional area of the narrower (central) section (approximately 30×12 mm^2), whereas the longitudinal strains within this region were determined from the average of two linear variable differential transducer (LVDT) readings. These LVDTs were attached prior to testing at the bottom end of the bone-neck region, one on each side, through two lightweight plastic

Table 3. Summary of mechanical properties. The coefficients of variation for the results are shown in brackets

ε_{tu}: %	f_{cr}: MPa	f_{tu}: MPa	F_{28}: MPa	F_{90}: MPa
3.91 (19.1%)	2.96 (10.7%)	4.38 (10.0%)	51.2 (1.94%)	63.7 (4.40%)

Advances in Cement Research

**The electro-mechanical tensile properties
of an engineered cementitious composite**
Saraireh, Suryanto, McCarter and Walls

(a)

Two-points electrical measurement

Gauge length for LVDT

Top electrode for
two-points
measurement

Region of
interest for DIC
strain mapping

Plastic mounting
block for LVDT

Bottom electrode

(b)
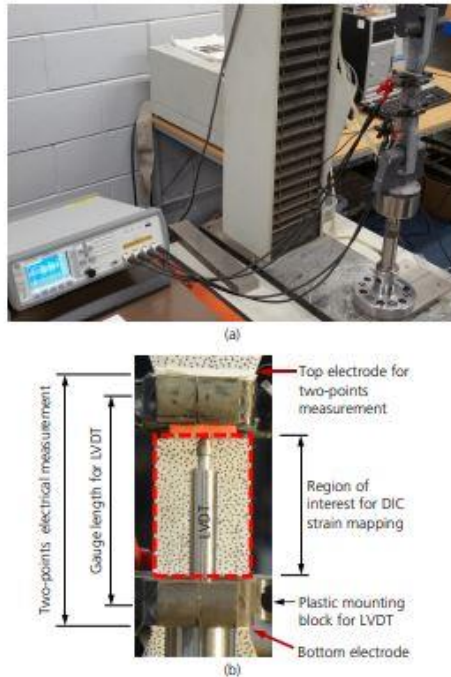
Figure 2. (a) Test setup; (b) Close-up of measurement during
uniaxial tensile testing

mounting blocks (see Figure 2(b)). The gauge length was
~60 mm. All data were recorded using a 16-bit USB data
acquisition system at a sampling rate of 1 s.

In addition to the stress and strain readings, simultaneous
electrical measurements were undertaken during the loading
process to study the influence of multiple microcracking, using
the same measurement system employed for testing the prisms.
Prior to testing, the pair of wire electrodes at the opposing
ends of the central neck of each sample (the distance
was ~80 mm) were connected to the LCR meter through
individually screened coaxial leads, with the connection at
the electrodes made using alligator clips (see Figure 2(a)).
Electrical measurements were then taken throughout the
installation process and during tensile loading at 13 spot
frequencies covering five decades (100 Hz, 200 Hz, 500 Hz,
1 kHz, 2 kHz, 5 kHz, 10 kHz, 20 kHz, 50 kHz, 100 kHz,
200 kHz, 500 kHz and 1 MHz). Low frequencies (<100 Hz)
were omitted from the sweep to minimise the duration
of the measurement. This sweep measurement was repeated

over a 3-s cycle, facilitating virtually continuous, real-time
monitoring during loading, thus minimising the influence of
time-dependent effects on the measured impedance.

To provide evidence of microcrack formation, digital images of
the front face of specimens DB1–DB4 were taken at 0.1 mm
displacement increments using an 18.4 MP Nikon 1 J4 mirror-
less digital camera, positioned approximately 300 mm from
the specimen. To remove inadvertent camera movement,
images were collected remotely using the Nikon wireless
mobility utility smartphone application (version 1.2.1). Prior
to testing, random black dots were manually drawn on the
front surface of specimens, which had been given a thin coat of
white acrylic paint (see Figure 2(b)). This was undertaken
to give a random pattern with a sharp contrast, thereby
facilitating automated strain mapping within the boundary
indicated in Figure 2(b). The images were then processed using
the digital image correlation (DIC) freeware Ncorr (version
1.2.1) (Blaber et al., 2015; Ncoor, 2018; Suryanto et al., 2017a;
Tambusay et al., 2020). In addition to this automated crack
mapping, more detailed crack mappings were undertaken
manually using ImageJ1 software (Schneider et al., 2012),
with the aim of obtaining the number of microcracks and the
width of each individual microcrack under various stages of
loading.

Data analysis and presentation

The impedance of a cement-based system ($Z(\omega)$ in Ω)
subjected to a small-signal sinusoidal electric field at an
angular frequency ω can be represented in a rectangular form
as (McCarter and Brousseau, 1990; McCarter et al., 2002;
Starrs and McCarter, 1998),

1. $Z(\omega) = Z'(\omega) - iZ''(\omega)\ \Omega$

where $Z'(\omega)$ is the resistive (real) component and $Z''(\omega)$ is the
reactive (imaginary) component. These two parameters are
commonly presented in the Nyquist format, with $Z''(\omega)$
plotted against $Z'(\omega)$ over a wide frequency range (see
Figure 3(a)). At any frequency, the impedance of the cementi-
tious system will result from two superposed phenomena –
conduction and polarisation, which are respectively quantified
by the bulk conductivity ($\sigma(\omega)$) and the relative permittivity
($\kappa'_r(\omega)$) of the system. Both parameters are generally presented
in the frequency domain (see, for example, Figures 3(b)
and 3(c)) to investigate the nature of conduction and relaxation
processes. These parameters can be de-embedded from the
resistive and reactive components through the relationships
(McCarter et al., 2004; Suryanto et al., 2016)

2. $\sigma(\omega) = \left(\dfrac{Z'(\omega)}{Z'(\omega)^2 + Z''(\omega)^2}\right) g_p\ \text{S/m}$

5

271

Advances in Cement Research

**The electro-mechanical tensile properties
of an engineered cementitious composite**
Saraireh, Suryanto, McCarter and Walls
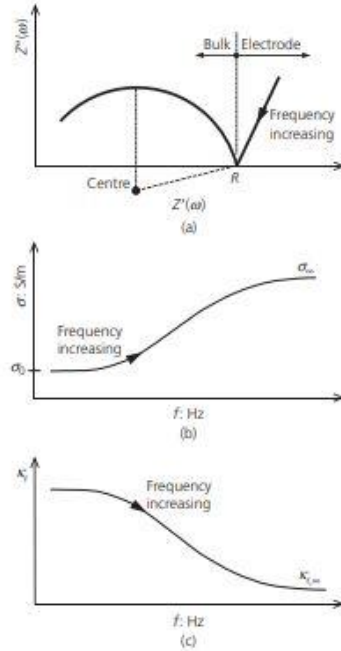
Figure 3. (a) Schematic illustration of complex impedance response of a cementitious system; (b) Idealised conductivity curve; (c) Idealised relative permittivity curve

$$3. \quad \kappa_r'(\omega) = \frac{1}{\kappa_o \omega} \left(\frac{Z''(\omega)}{Z'(\omega)^2 + Z''(\omega)^2} \right) g_\mathrm{P}$$

where κ_o is the permittivity of free space (8.854×10^{-12} F/m) and g_p is a geometrical constant that depends on the electrode geometry and the spatial positioning of the electrodes within the system.

The value of g_p was obtained from previous experiments using solutions of known conductivity, using the same polystyrene mould and perforated stainless steel electrodes as in the test prisms. A value of $g_\mathrm{p} = 88.48$/m was obtained. For specimens DB1–DB4, the calibration was done by converting the resistance measured from prism specimens P1–P3 at 28 days of curing ($R_{\mathrm{p},28}$) to resistivity (ρ_{28}) through the relationship

$$4. \quad \rho_{28} = R_{\mathrm{p},28} \frac{1}{g_\mathrm{P}} \ \Omega.\mathrm{m}$$

Accordingly, the geometrical constant for the dogbone-shaped specimens (g_{db}) could be calculated from

$$5. \quad g_{\mathrm{db}} = \frac{R_{\mathrm{db},28}}{\rho_{28}} \ /\mathrm{m}$$

where $R_{\mathrm{db},28}$ is the measured resistance for the dogbone-shaped specimen after 28 days curing. The value of g_{db} was determined to be 245.28/m.

Results and discussion

Hydration study

Complex impedance response (no tensile loading)
The impedance spectra for prisms P1–P3 over the initial 90-day period are presented in Nyquist format in Figure 4(a), with frequency increasing from right-to-left across the curve. For reasons of clarity, only every fifth data marker is highlighted on each curve. The solid curves represent the impedance spectrum of P1, while the dashed curves represent the spectra of P2 and P3. It is evident from this figure that there was excellent agreement between the notionally identical prisms, with each response comprising three distinct features.

(a) A small spur at the low-frequency (right-hand) side of the spectrum.
(b) A narrow U-shaped intermediate valley region.
(c) An arc at the high-frequency (left-hand) side which, with the intermediate plateau noted in (b) represents the bulk impedance response.

The low-frequency spur represents the response resulting from polarisation processes at the electrode/specimen interface (McCarter and Brousseau, 1990; McCarter et al., 1988) and constitutes part of a larger arc that would only form at frequencies significantly lower than the lower frequency limit used in the present study (i.e. <20 Hz). The U-shaped intermediate region can be attributed to the presence of unburnt carbon in the FA, the extent of which has been found to have direct proportion to the amount of free carbon content in the FA (McCarter et al., 2004; Suryanto et al., 2017b), which is quantified by its loss on ignition (see Table 2). By presenting the impedance data in Nyquist format, as in Figure 4(a), it is possible to separate the response of the electrodes from that of the bulk material, thereby allowing calculation of the bulk ionic resistance of the composite. This was obtained from the projected intercept of the low-frequency end of the bulk arc with the real axis. By doing so, the bulk resistance at 7 days was evaluated to be ~1.1 kΩ, increasing to ~2.9 kΩ at 28 days, ~5.1 kΩ at 56 days and ~7.3 kΩ at 90 days. The progressive increase in bulk resistance is indicative of continual refinement in the pore structure resulting from ongoing cement hydration and pozzolanic reactions, causing a reduction in ionic conduction with time.

Advances in Cement Research

**The electro-mechanical tensile properties
of an engineered cementitious composite**
Saraireh, Suryanto, McCarter and Walls
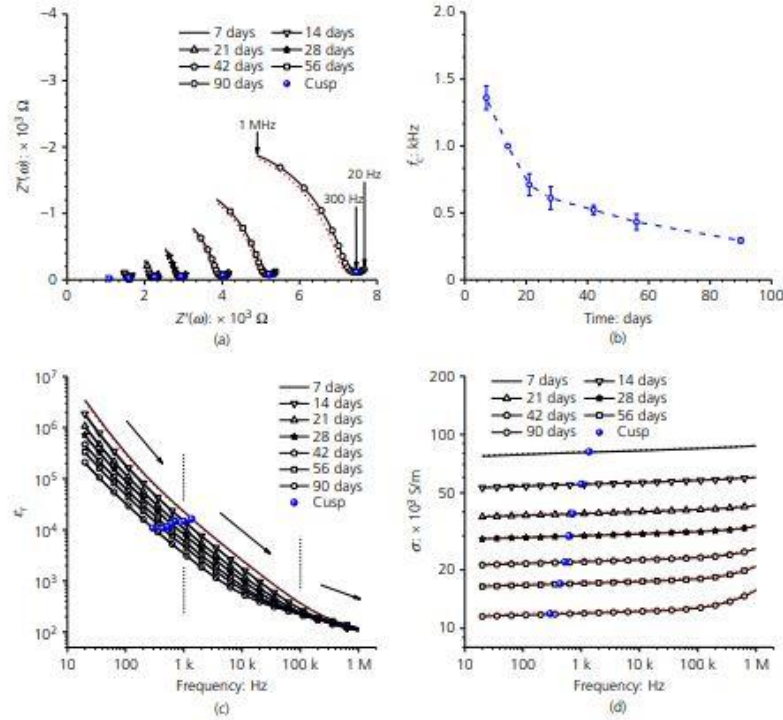
Figure 4. Influence of curing on the electrical properties of prisms P1–P3 over the initial 90 days of curing: (a) impedance response; (b) variation in cusp-point frequency f_c; (c) relative permittivity against frequency; (d) conductivity against frequency. The solid markers in (c) and (d) indicate the permittivity/conductivity corresponding to the cusp-point of the impedance response presented in (a)

With reference to Figure 4(a), it is evident that the progressive increase in bulk resistance was accompanied by displacement of the impedance spectrum to the right, implying an increase in the sample impedance over the entire frequency range. It is also interesting to observe that the definition of the bulk arc became more discernible over time when measured within the same frequency range (20 Hz–1 MHz). This manifests as a reduction in the cusp-point frequency (f_c) with increasing curing time across the entire impedance spectrum. For illustrative purposes, Figure 4(b) shows the change in f_c (i.e. the frequency corresponding to the minimum point within the U-shaped valley region) over the 90-day curing period, with the error bars representing ± one standard deviation (SD). A reduction in f_c was evident over the initial 21 days, followed by a more gradual decrease in frequency over the remainder of the test period, reflecting ongoing hydration and resulting microstructural changes within the composite.

To provide an improved understanding of these mechanisms, the frequency-dependent parameters (relative permittivity $\kappa_r'(\omega)$ and conductivity $\sigma(\omega)$) are now presented and discussed.

Relative permittivity and bulk conductivity (no tensile loading)

In a heterogeneous system such as an ECC, a number of polarisation processes can operate simultaneously within the system within an overlapping frequency range. Each process may relax according to its own time constant, which makes it difficult to determine accurately the contribution of each individual mechanism to the polarisability of the system.

The relative permittivity provides a relative measure of the polarisability of the system and, at any particular frequency of applied electrical field, quantifies the sum of all polarisation mechanisms operating at that frequency. Presenting the

7

Advances in Cement Research

**The electro-mechanical tensile properties
of an engineered cementitious composite**
Saraireh, Suryanto, McCarter and Walls

permittivity in the frequency domain can therefore give a clearer view of the dominant polarisation mechanisms (and the frequency range over which they operate). The relative permittivity $\kappa_r'(\omega)$, which was de-embedded from the impedance data of prisms P1–P3 using Equation 3, is presented in the frequency domain in Figure 4(c). It is apparent from this figure that a region of dispersion exists, as evidenced by the progressive reduction in permittivity up to the upper frequency limit. There is also a distinct change in the rate of dispersion across the entire frequency range presented. Consider, for example, the permittivity at 7 days, $\sim3.4 \times 10^6$ at 20 Hz; this decreased by almost two orders of magnitude to $\sim2.2 \times 10^4$ at 1 kHz, ~370 at 100 kHz and ~115 at 1 MHz. Within the frequency range, it is postulated that three dominant mechanisms of polarisation are operative.

(a) Polarisation processes at the electrode/sample interface, commonly referred to as electrode polarisation (Ishai et al., 2013; McCarter et al., 2009, 2015), which can result in anomalously high permittivity values. This is generally a low-frequency mechanism, typically relaxing in the low kHz range.

(b) Double-layer polarisation due to charges electrostatically held on the surfaces of the cement gel and other particles such as FA and fine sand (McCarter et al., 2002; Schwan et al., 1962; Schwarz, 1962). This is a low/medium-frequency mechanism and may operate up to the ~100 kHz region.

(c) Interfacial or space charge polarisation resulting from the accumulation of charges at the interface of two dissimilar materials with different relaxation times, also known as Maxwell–Wagner polarisation (Hasted, 1973; Iwamoto, 2012; McCarter et al., 2002; Prodromakis and Papavassiliou, 2009). In a cement-based system including ECCs, this can arise from translating charges that are blocked inside isolated pores and accumulate at pore water/hydrate interfaces. Interfacial polarisation is an intermediate-frequency mechanism, operating typically over high-kilohertz into the megahertz.
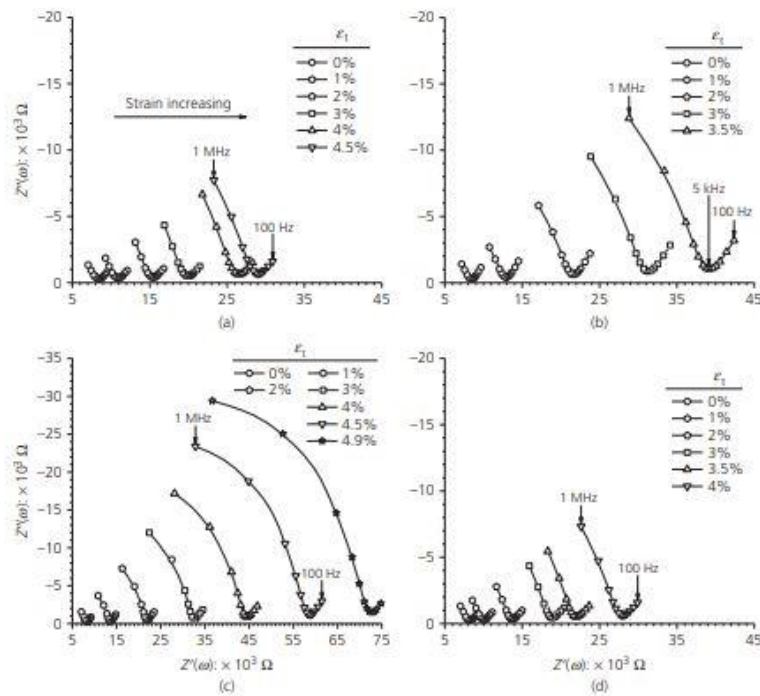
Figure 5. Variation in impedance response with tensile strain: (a) DB1; (b) DB2; (c) DB3; (d) DB4

Advances in Cement Research

The electro-mechanical tensile properties of an engineered cementitious composite
Saraireh, Suryanto, McCarter and Walls

With reference to Figure 4(c), it is proposed that the mechanism responsible for the decrease in permittivity at frequencies <1 kHz is the relaxation of polarisation processes at the electrode/sample interface, possibly overlapping with relaxation of double-layer process within the composite itself. Within the frequency range 1 kHz–1 MHz, it is proposed that the continuing decrease in permittivity is as a direct result of two superimposed mechanisms: the relaxation of double-layer processes, operating primarily within this frequency range, and the relaxation of interfacial (Maxwell–Wagner) processes, which have a more dominant influence at frequencies >100 kHz.

It is also interesting to note from the results presented in Figure 4(c) that there was a reduction in the magnitude of the dispersion/relaxation with increasing curing time, from ~five

orders of magnitude at 7 days to ~three orders of magnitude at 90 days. This is attributed, in part, to the reduction in relaxation time discussed above and to the change in the dispersive polarisation processes with time.

To further investigate the dispersive behaviour of the material, Figure 4(d) shows the bulk conductivity in the frequency domain, with the conductivity de-embedded from the impedance measured from prisms P1–P3 using Equation 2. Conductivity gives a measure of both ionic conduction through the movement of ions within the continuous capillary pore network, which is low-frequency feature, and a dispersive conduction contribution resulting from the relaxation of polarisation processes, which is dependent on the frequency of the applied field. It can be inferred from the conductivity plots shown in Figure 4(d) that dispersion resulted in a very gradual
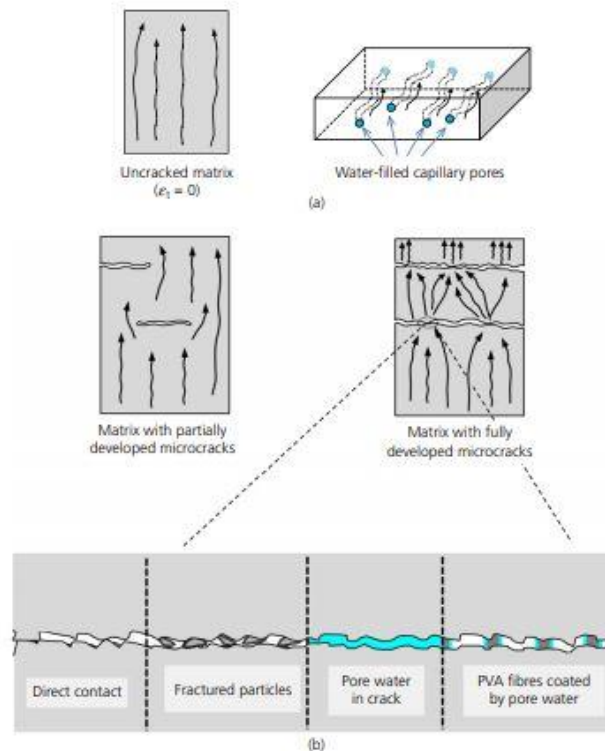
Figure 6. Schematic illustration of possible conduction pathways in (a) uncracked and (b) cracked ECC matrix showing possible bridging pathways

9

Advances in Cement Research

**The electro-mechanical tensile properties
of an engineered cementitious composite**
Saraireh, Suryanto, McCarter and Walls

increase in conductivity across the entire frequency range, indicating the existence of the relaxation of polarisation processes over the entire range. This would indicate that the polarisation mechanisms operate at an overlapping frequency range, resulting in a spread of the relaxation time. Owing to the gradual increase, it would be difficult to separate the underlying mechanisms from this presentation formalism, with the exception of the conductivity at 56 and 90 days of curing in which a more noticeable increase in conductivity was evident at frequencies greater than ~100 kHz. This is attributed primarily to the relaxation of interfacial processes, as discussed above.

Piezo-impedance study

Complex impedance response under tensile loading
The complex impedance plots of specimens DB1 to DB4 during tensile loading conducted on the 28th day of curing are presented in Figures 5(a)–5(d). Owing to the number of data points in each curve (i.e. measurements at 13 spot frequencies), the data markers were connected with B-splines and, for reasons of clarity, only the responses at 1% strain increments are presented. At any stage of loading, the cracked ECC displayed a classic response, comprising an arc forming the left-hand side of the plot and a spur forming the right-hand side, which is not dissimilar to the response observed in the hydration study (see Figure 4(a)). It is apparent from Figures 5(a)–5(d) that tensile straining resulted in the entire response being gradually displaced to the right, indicating an overall increase in impedance with increasing strain. With reference to Figures 6, this gradual increase is as a direct result of the successive formation and widening of multiple microcracks (Saraireh *et al.*, 2017; Wansom and Kanokkanchana, 2017), which have the effect of altering the conduction pathway within the composite, from a relatively straight pathway (Figure 6(a)) to a more tortuous one (Figure 6(b)). Accordingly, an increase in tensile strain has the effect of reducing the continuity and increasing the
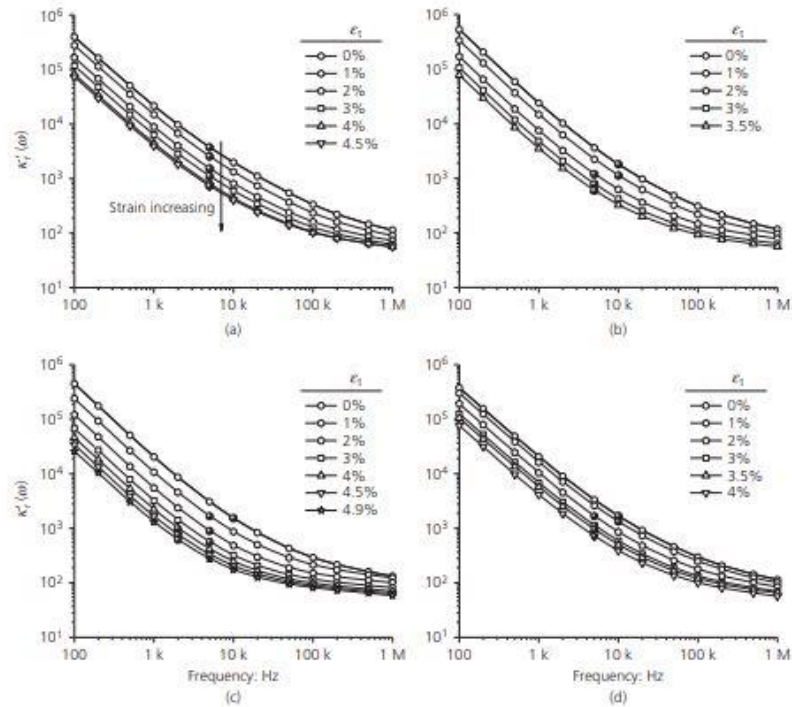
Figure 7. Relative permittivity against frequency at selected strain levels: (a) DB1; (b) DB2; (c) DB3; (d) DB4. The cusp-point frequency is shown as a solid marker

Advances in Cement Research

**The electro-mechanical tensile properties
of an engineered cementitious composite**
Saraireh, Suryanto, McCarter and Walls

circuitous path length, hence increasing the overall impedance of the ECC. Conduction will occur through several possible mechanisms across the microcrack as depicted in Figure 6(b); at this stage, however, it is difficult to delineate the contribution from each pathway.

Another interesting feature that is apparent from Figures 5(a)–5(d) relates to the definition of the high-frequency arc associated with the bulk response of the material including microcracks. The arc became more pronounced with an increase in strain, indicating a shift in time constant to the frequency range under investigation, as in the hydration study.

Relative permittivity and bulk conductivity under tensile loading

Figure 7 shows the relative permittivity of specimens DB1–DB4, computed using Equation 3, plotted in the frequency domain with varying tensile strains and marked at every 1% increment of strain. In general terms, the trend in the relative permittivity plots is, in many respects, similar to the respective specimens in the hydration study (see Figure 4(c)), characterised by a reduction in relative permittivity with increasing frequency across the entire frequency range. As before, this is due to the relaxation of superimposed polarisation mechanisms operating within the composite and the shift in time constant with increasing strain, which has the effect of shifting the relative permittivity curve to the left along the Z' axis toward the origin.

It is interesting to note that while the relative permittivity plots presented in Figure 4(c) all merge at frequencies greater than ~200 kHz, this was not the case for the plots presented in Figure 7, which display a progressive downward displacement with increasing strain across the entire frequency range, including high frequencies (i.e. >200 kHz). This can be associated
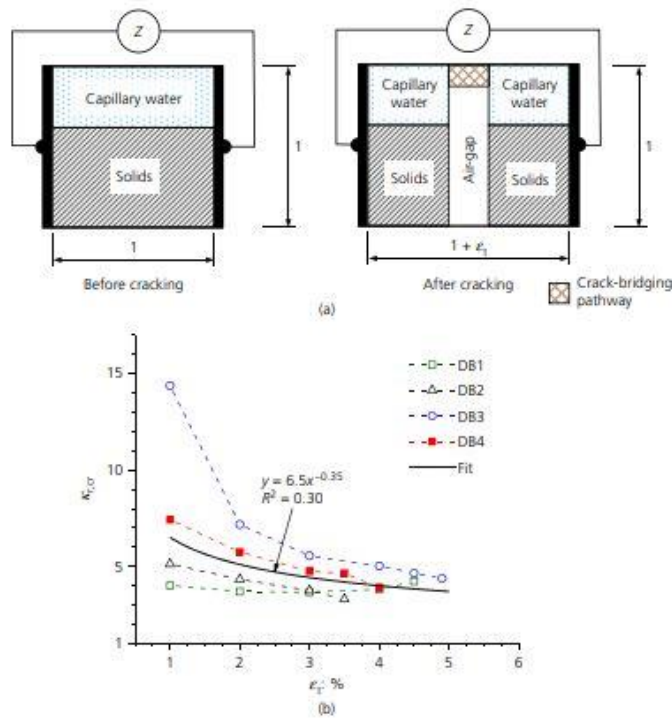
Figure 8. (a) Idealised representation of ECC before and after cracking; (b) Variation in relative permittivity of microcracks assuming a series mixing law (Equation 6)

11

Advances in Cement Research

The electro-mechanical tensile properties of an engineered cementitious composite
Saraireh, Suryanto, McCarter and Walls

with the progressive formation microcracks within the ECC matrix; as the relative permittivity of the air gap between two opposite cracked surfaces is ~ 1, multiple crack formation would have the effect of decreasing the overall polarisability of the system. To understand this aspect, consider the idealised system presented in Figure 8(a), composed of the saturated ECC matrix and a crack comprising an air gap and a crack-bridging pathway. The bridging pathway would represent all the possible pathways presented in Figure 6(b), so could be regarded as a smeared contribution. Given that the micro-cracks are, in essence, connected in series with the bulk ECC matrix, the permittivity of the microcracks could be estimated by the mathematical mixing law (Reynolds and Hough, 1957)

6. $\quad \dfrac{\phi_{r,t}}{\kappa_{r,t}} = \dfrac{\phi_{cr}}{\kappa_{cr}} + \dfrac{\phi_{r,i}}{\kappa_{r,i}}$

where $\kappa_{r,t}$ is the bulk relative permittivity of the composite at strain ε_t after the start of the test, κ_{cr} is the average relative permittivity of the microcracks and $\kappa_{r,i}$ is the bulk relative permittivity of the composite at the start of the test (i.e. $\varepsilon_t = 0$). Both $\kappa_{r,t}$ and $\kappa_{r,i}$ were evaluated at the upper frequency limit which, in the present study, was 1 MHz. With reference to the system shown in Figure 8(a), the total volume at strain ε_t after the start of the test is given by $\phi_{r,t} = \phi_{r,i} + \phi_{cr}$, where $\phi_{r,i}$ is the initial volume at the start of the test and ϕ_{cr} is the volume fraction of microcracks at strain ε_t.

Figure 8(b) shows the average relative permittivity of the microcracks computed using Equation 6 at discrete tensile strain levels. The results show that the value of the apparent permittivity of the microcracks was consistently higher than that of air (≈ 1), indicating the presence of other materials within the space between two microcrack surfaces. The plots also display the variations in calculated permittivity values,

Figure 9. Conductivity–frequency response under tensile load: (a) DB1; (b) DB2; (c) DB3; (d) DB4. The cusp-point frequency is shown as a solid marker

Advances in Cement Research
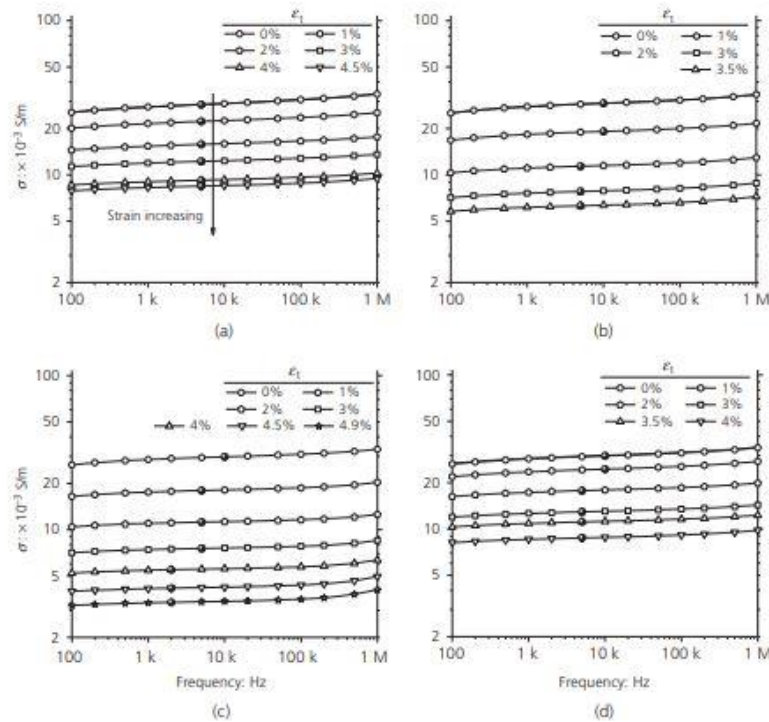
The electro-mechanical tensile properties
of an engineered cementitious composite
Saraireh, Suryanto, McCarter and Walls

with a general decreasing trend with increasing tensile strain up to ~4%, where the permittivity plateaus at ~4. The best-fit power equation was added to provide an alternative means of predicting the tensile strain in a fully saturated system from permittivity measurements. The variation in permittivity would indicate the spatial distribution in the number of physical pathways across the crack (see Figure 6(b)), while the reduction in permittivity with increasing strain is indicative of their temporal change during the loading process.

To highlight further the influence of crack formation on the bulk electrical properties of cracked the ECC, the bulk conductivity of specimens DB1–DB4 at varying strains is presented in the frequency domain in Figures 9(a)–9(d). As before, owing to the relaxation of the polarisation mechanisms operating within the ECC matrix, the conductivity gradually increased with frequency across the entire frequency range. Tensile straining was shown to result in a downward, parallel

displacement of the bulk conductivity curves, resembling the trend shown in Figure 4(d). This is as a direct result of the formation of microcracks with increasing load rather than pore refinement due to hydration, as the duration of the tensile test was short (less than 10 min). As the tensile strain increased, microcracks progressively formed within the ECC matrix, causing a reduction in conductivity with increasing strain.

To highlight the sensing capability of the composite, the conductivity of specimen DB2 is, for illustrative purposes, plotted against the tensile strain in Figure 10(a) together with the corresponding stress–strain relation. The conductivity is presented at selected spot frequencies (i.e. 100 Hz, 500 Hz, 5 kHz, 100 kHz, 500 kHz and 1 MHz) and the response near to the cusp-point frequency ($f_c = 5$ kHz) is highlighted with data markers. In this curve, only every tenth data marker is highlighted, for reasons of clarity. This figure clearly shows the dependence of bulk conductivity on both the tensile strain and
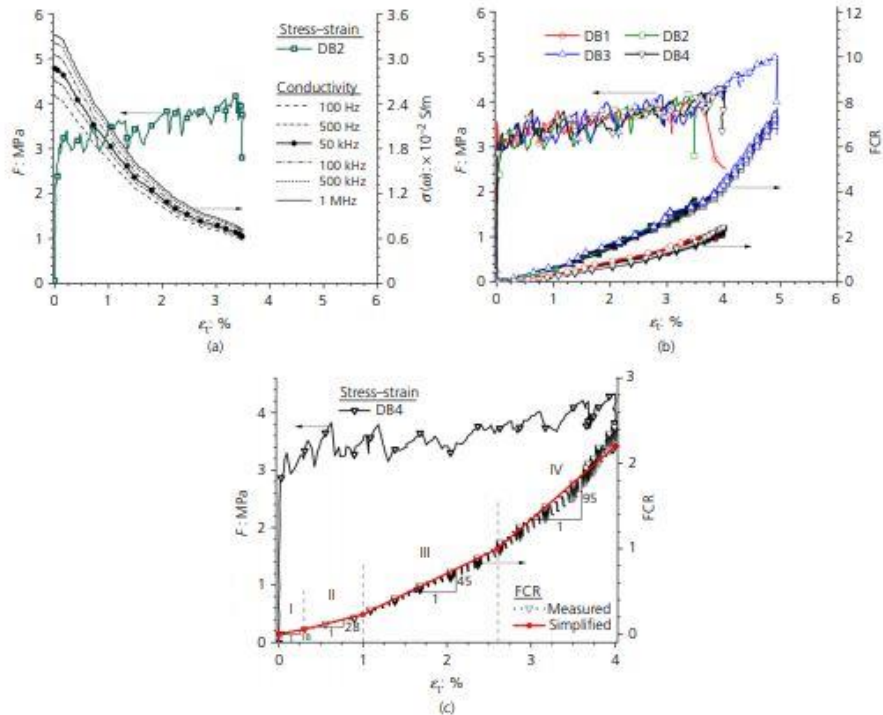

Figure 10. (a) Variation in bulk conductivity of specimen DB2 under varying tensile strains; (b) FCR for specimens DB1–DB4 under varying tensile strains; (c) Representation of FCR of specimen DB4 into contiguous linear segments. All curves are plotted alongside the stress–strain responses

13

Advances in Cement Research

**The electro-mechanical tensile properties
of an engineered cementitious composite**
Saraireh, Suryanto, McCarter and Walls

the test frequency. As the strain increases to ~0.15%, a reduction in conductivity is evident as microcracks began to develop within the ECC matrix; the dominant conduction path at this stage would be by way of the uncracked portion. This is then followed by a rapid reduction in conductivity with increasing strain, resulting in an approximately fivefold decrease in value. To investigate the sensitivity of the composite to mechanical strain, the bulk conductivity $\sigma(\omega)$ was converted to its reciprocal (bulk resistivity $\rho(\omega)$) and then used to calculate the fractional change in resistivity (FCR), which is defined as (Chia and Huang, 2017; Han et al., 2011; Ozbulut et al., 2018; Ranade et al., 2014; Wen and Chung, 2003; Yang et al., 2018; Yoo et al., 2019)

7. $\quad FCR = \dfrac{\rho_1 - \rho_i}{\rho_i}$

where ρ_1 is the bulk resistivity at strain ε_1 after the start of the test and ρ_i is the initial bulk resistivity (i.e. at zero strain).

Figure 10(b) shows the FCR values for the four dogbone-shaped specimens over the entire frequency range plotted against the fractional change in dimension (or strain), together with the stress–strain response measured from individual dogbone-shaped specimens. As before, for reasons of clarity, only the tenth data markers are highlighted in all the curves and the FCR is presented to highlight its sensitivity to frequency. It is interesting to note from the figure that, by presenting the resistivity data in a dimensionless format (i.e. FCR against the fractional change in dimension), this virtually removes the dependence of the FCR on frequency and the resistivity curves all collapse into a unique curve. It is evident that all the specimens exhibited a quasi-linear increase in FCR with strain, with a notable increase in slope with

Figure 11. (a) Progressive development of longitudinal strains on the front face of specimen DB3; (b) Observed and fitted crack width distribution at 4% strain from visual observations; (c) Fitted crack width distributions at varying strain levels

14

Advances in Cement Research

The electro-mechanical tensile properties
of an engineered cementitious composite
Saraireh, Suryanto, McCarter and Walls

increasing strain. The slope of specimen DB3 increased more appreciably at strain levels greater than ~3%, which coincides with the increase in the post-cracking stiffness shown in the figure, reflecting the slip hardening behaviour resulting from abrasion damage on the fibre surfaces as fibres are pulled out from the ECC matrix (Redon *et al.*, 2001). This figure also indicates that the FCRs of specimens DB2 and DB3 were very similar and consistently greater than the FCRs of the other two specimens, which also showed similar responses. The FCR at 4% strain was in the range 2.4–4.2; this is comparable to the values reported by Ranade *et al.* (2014) for a high-volume FA ECC mix and lower than those for the moderate-volume FA ECC mix.

By plotting the FCR against strain as in Figure 10(b), distinct regions can be delineated, as shown in Figure 10(c): region I (up to ~0.3% strain), region II (0.3–1% strain), region III

(1–3% strain) and region IV (>3% strain, with the slope values also provided in the figure. Considering the variations in FCR during the strain hardening discussed above, it is interesting to note that this is not evident in the stress–strain responses of specimens DB1–DB4 presented in Figure 10(b), with all specimens displaying a comparable overall stiffness during strain hardening. As the electrical response of the specimens was affected by the presence of microcracks, the apparent difference may thus originate from the distribution of the microcracks during loading. Attention thus turned to the number and width of individual microcracks during loading.

Crack mapping during tensile loading

To corroborate the electrical measurements regarding microcracking, Figures 11(a) and 12(a) show representative longitudinal strain maps for specimens DB3 and DB4, respectively, obtained using the DIC technique at every 0.5% strain
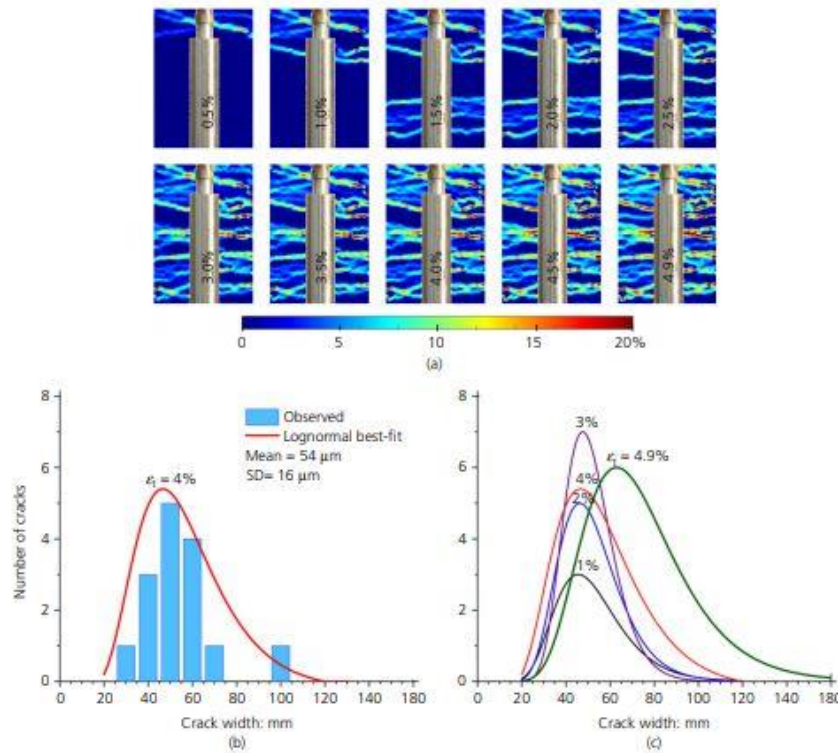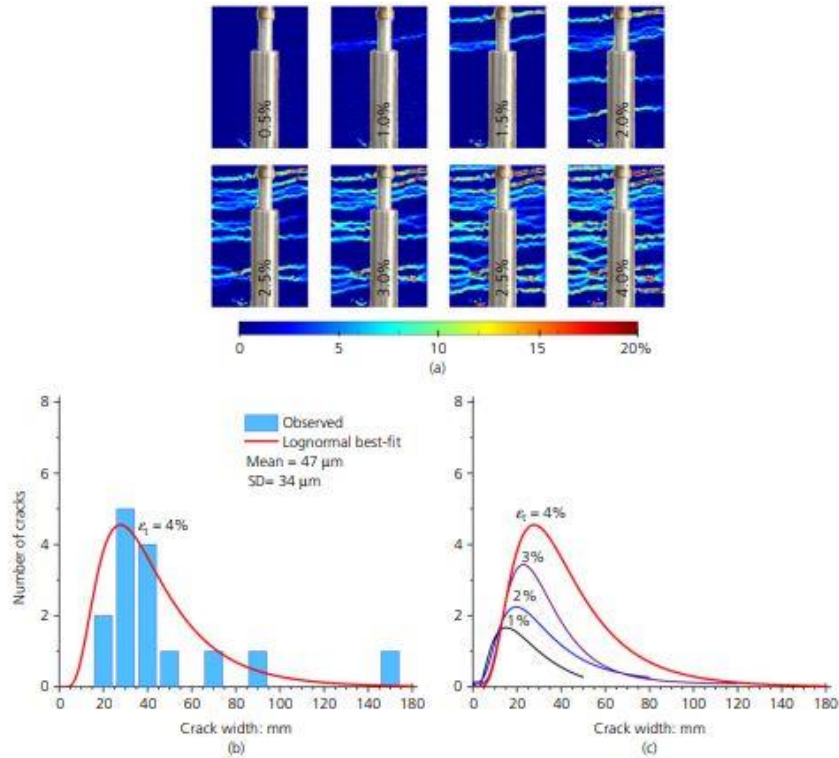

Figure 12. (a) Progressive development of longitudinal strains on the front face of specimen DB4; (b) Observed and fitted crack width distribution at 4% strain from visual observations; (c) Fitted crack width distributions at varying strain levels

15

Advances in Cement Research

**The electro-mechanical tensile properties
of an engineered cementitious composite**
Saraireh, Suryanto, McCarter and Walls

increment. The crack width distributions measured at 4% strain and the corresponding best-fit lognormal distribution curves for specimens DB3 and DB4 are plotted in Figures 11(b) and 12(b), respectively, with the best-fit lognormal distribution curves at 1% strain increment presented in Figures 11(c) and 12(c) to aid data interpretation. It is apparent from the crack width distribution of specimen DB3 (Figure 11(c)) that there was a significant increase in the number of cracks at 3% strain, whereas the average crack width over this strain range was relatively constant. The combined effect of this caused the displacement of the crack width distribution upwards. Thereafter, there was a notable increase in the average crack width from ~47 μm at 3% strain to 65 μm at 4.9% strain, thereby causing the distribution curve shown in Figure 11(c) to displace to the right. This trend agrees well with the strain maps shown in Figure 11(a), which display an increasing number of near-parallel bands of localised strain with a relatively constant colour range over the initial 3% strain, followed by a similar pattern of strain maps but with a notable increase in value. It could be inferred from the evolution of the crack pattern obtained that the increase in the FCR for specimen DB3 over the initial 3% strain is attributed primarily to microcrack formation whereas the increase in both values thereafter is due to the widening of existing microcracks.

With reference to the evolution of crack pattern of specimen DB4 (Figures 12(a) and 12(c)), it is evident that microcrack formation occurred constantly throughout the loading, from two fully-developed microcracks at 1% strain to 15 cracks at 4% strain, which was also accompanied by a notable increase in the average crack width. This would indicate that the predominant mechanism responsible for the increase in the FCR presented in Figure 10(b) was due to progressive crack formation, with a significant contribution of crack width increase at strain levels >3%. It is interesting to note from both specimens that, although they had more or less the same number of cracks (~15) with an average crack width of ~50 μm at 4% strain, the two specimens attained different FCR values, with those of specimen DB3 approximately twice those of specimen DB4. This would suggest the need for using the actual crack width distribution to allow for an accurate calculation of FCR; work is continuing on this aspect.

Conclusions

A multiple testing methodology of electrical impedance measurements, mechanical testing and detailed image analysis was employed to investigate the piezo-impedance properties of an ECC under direct tension, with the impedance measurements also used to provide complementary information on the influence of ongoing hydration. The following conclusions can be drawn from the results presented.

(a) A distinct impedance response was observed at all stages during the hydration process. Increasing hydration was

found to result in an overall increase in impedance and a better definition of the high-frequency arc, which reflects the development of pore structure over time. A progressive increase in bulk resistance was evident during the entire curing period, reflecting ongoing hydration and pozzolanic reactions.

(b) Dispersion in polarisation was shown to result in a reduction in relative permittivity with increasing frequency and a corresponding increase in conductivity. Ongoing hydration and pozzolanic reactions were found to have a negligible influence on the relative permittivity at the upper frequency limit (i.e. 1 MHz).

(c) Multiple microcrack formation increased the sample impedance markedly and resulted in a progressive displacement and enlargement in the radius of the bulk arc when presented in the Nyquist format.

(d) The relative permittivity at the high-frequency end (1 MHz) was found to be sensitive to tensile straining, while virtually insensitive to ongoing hydration. This parameter could therefore be exploited as a means of distinguishing changes in electrical properties due to ongoing hydration and changes in electrical properties due to damage within the composite, when the matrix remains in a fully saturated condition.

(e) The composite sensitivity to strain was affected by the distribution of microcracks. Larger FCR values were obtained from specimens with greater crack widths.

Acknowledgements

REFERENCES

Abé M and Fujino Y (2017) Monitoring of long-span bridges in Japan. *Proceedings of the Institution of Civil Engineers – Civil Engineering* **170(3)**: 135–144, https://doi.org/10.1680/jcien.16.00002.

Agdas D, Rice JA, Martinez JR and Lasa IR (2015) Comparison of visual inspection and structural-health monitoring as bridge condition assessment methods. *Journal of Performance of Constructed Facilities ASCE* **30(3)**: 04015049.

Azhari F and Banthia N (2012) Cement-based sensors for piezoresistive sensing. *Cement & Concrete Composites* **34(7)**: 866–873.

Blaber J, Adair B and Antoniou A (2015) Ncorr: open-source 2D digital image correlation mat-lab software. *Experimental Mechanics* **55(6)**: 1105–1122.

BSI (2011) BS EN 197-1:2011. Cement. Composition, specifications and conformity criteria for common cements. BSI, London, UK.

Chen Y, Yu J and Leung CK (2018) Use of high strength strain-hardening cementitious composites for flexural repair of concrete structures with significant steel corrosion. *Construction and Building Materials* **167**: 325–337.

Advances in Cement Research

The electro-mechanical tensile properties
of an engineered cementitious composite
Saraireh, Suryanto, McCarter and Walls

Chia L and Huang Y (2017) Dispersion effectiveness of carbon
nanotubes in smart cementitious materials. *Advances in Cement
Research* **29(6)**: 246–257, https://doi.org/10.1680/jadcr.17.00013.

Choi S, Park S, Bolton R, Stubbs N and Sikorsky C (2004) Periodic
monitoring of physical property changes in a concrete box-girder
bridge. *Journal of Sound and Vibration* **278(1–2)**: 365–381.

Frangopol DM, Dong Y and Sabatino S (2017) Bridge life-cycle
performance and cost: Analysis, prediction, optimisation and
decision-making. *Structure and Infrastructure Engineering*
13(10): 1239–1257.

Frank TE, Lepech MD and Billington SL (2018) Experimental testing
of reinforced ECC beams subjected to various cyclic
deformation histories. *Journal of Structural Engineering ASCE*
144(6): 04018052.

Han B, Zhang K, Yu X, Kwon E and Ou J (2011) Nickel particle-based
self-sensing pavement for vehicle detection. *Measurement*
44(9): 1645–1650.

Hasted JB (1973) *Aqueous Dielectrics*. Chapman & Hall, London, UK.

HE (Highways England) (2017) *DMRB Volume 3, Section 1, Part 4, BD
63/17 Highway Structures: Inspection and Maintenance. Inspection.
Inspection of Highway Structures*. HE, London, UK.

Hedegaard BD, French CEW and Shield CK (2017) Time-dependent
monitoring and modeling of I-35W St. Anthony falls bridge.
I: Analysis of monitoring data. *Journal of Bridge Engineering
ASCE* **22(7)**: 04017025.

Hou TC (2008) *Wireless and Electromechanical Approaches for Strain
Sensing and Crack Detection in Fiber Reinforced Cementitious
Materials*. PhD thesis, University of Michigan, Ann Arbor,
MI, USA.

Hou TC and Lynch JP (2005) Conductivity-based strain monitoring and
damage characterization of fiber reinforced cementitious structural
components. In *Proceedings of SPIE 5765, Smart Structures and
Materials 2005: Sensors and Smart Structures Technologies for
Civil, Mechanical, and Aerospace Systems* (Tomizuka M (ed.)).
SPIE, Bellingham, WA, USA, pp. 419–430.

Ishai PB, Talary MS, Caduff A, Levy E and Feldman Y (2013) Electrode
polarization in dielectric measurements: a review. *Measurement
Science and Technology* **24(10)**: 102001.

Iwamoto M (2012) Maxwell–Wagner effect. In *Encyclopedia of
Nanotechnology* (Bhushan B (ed.)). Springer, Dordrecht,
the Netherlands, pp. 1276–1285.

JSCE (Japan Society of Civil Engineers) (2008) *Recommendations for
Design and Construction of High Performance Fiber Reinforced
Cement Composites with Multiple Fine Cracks (HPFRCC)*. JSCE,
Tokyo, Japan.

Kim J, McCarter WJ, Suryanto B et al. (2016) Chloride ingress into
marine exposed concrete: a comparison of empirical-and
physically-based models. *Cement & Concrete Composites*
72: 133–145.

Kim J, McCarter WJ and Suryanto B (2018) Performance assessment of
reinforced concrete after long-term exposure to a marine
environment. *Construction and Building Materials* **192**: 569–583.

LabView (2017) See http://www.ni.com/download/labview-development-
system-2017/6698/en/ (accessed 01/01/2018).

Lee SW, Tan KH and Yang EH (2018) Seismic behaviour of interior
reinforced-concrete beam–column sub-assemblages with
engineered cementitious composites. *Magazine of Concrete
Research* **70(24)**: 1280–1296, https://doi.org/10.1680/jmacr.17.
00359.

Li VC (2008) Engineered cementitious composite (ECC): Material,
structural, and durability performance. In *Concrete Construction
Engineering Handbook* (Nawy EG (ed.)). CRC Press, Boca Raton,
USA, FL, pp. 24.1–24.46.

Li Z, Leung C and Xi Y (2009) *Structural Renovation in Concrete*. Taylor
& Francis, London, UK.

Lin VWJ, Li M, Lynch JP and Li VC (2011) Mechanical and electrical
characterization of self-sensing carbon black ECC. In *Proceedings
of SPIE 7983, Nondestructive Characterization for Composite
Materials, Aerospace Engineering, Civil Infrastructure, and
Homeland Security 2011* (Wu HF (ed.)). SPIE, Bellingham, WA,
USA, paper 798316.

Lynch JP, Farrar CR and Michaels JE (2017) Structural health monitoring:
technological advances to practical implementations (scanning the
issue). *Proceedings of the IEEE* **104(8)**: 1508–1512.

Ma H, Herbert E, Ohno M and Li VC (2019) Scale-linking model of
self-healing and stiffness recovery in engineered cementitious
composites (ECC). *Cement & Concrete Composites* **95**: 1–9.

McCarter WJ and Brousseau R (1990) The AC response of hardened
cement paste. *Cement and Concrete Research* **20(6)**: 891–900.

McCarter WJ, Garvin S and Bouzid N (1988) Impedance measurements
on cement paste. *Journal of Materials Science Letters* **7(10)**:
1056–1057.

McCarter WJ, Starrs G and Chrisp TM (2002) Electrical monitoring
methods in cement science. In *Structure and Performance of
Cements* (Bensted J and Barnes P (eds)) Taylor & Francis,
London, UK, pp. 442–456.

McCarter WJ, Starrs G and Chrisp TM (2004) The complex impedance
response of fly-ash cements revisited. *Cement and Concrete
Research* **34(10)**: 1837–1843.

McCarter WJ, Starrs G, Kandasami S, Jones R and Chrisp M (2009)
Electrode configurations for resistivity measurements on concrete.
ACI Materials Journal **106(3)**: 258–264.

McCarter WJ, Chrisp TM, Starrs G et al. (2012) Developments in
performance monitoring of concrete exposed to extreme
environments. *Journal of Infrastructure Systems ASCE* **18(3)**:
167–175.

McCarter WJ, Taha HM, Suryanto B and Starrs G (2015) Two-point
concrete resistivity measurements: interfacial phenomena at the
electrode–concrete contact zone. *Measurement Science and
Technology* **26(8)**: 085007.

McCarter WJ, Suryanto B, Taha HM, Nanukuttan S and Basheer PAM
(2017) A testing methodology for performance-based specification.
Journal of Structural Integrity and Maintenance **2(2)**: 78–88.

Ncoor (2018) See http://www.ncorr.com/ (accessed 01/01/2018).

Omar T and Nehdi ML (2018) Condition assessment of reinforced
concrete bridges: current practice and research challenges.
Infrastructure **3(3)**: 36.

Ozbulut OE, Jiang Z and Harris DK (2018) Exploring scalable fabrication
of self-sensing cementitious composites with graphene
nanoplatelets. *Smart Materials and Structures* **27(11)**: 115029.

Pines D and Aktan AE (2002) Status of structural health monitoring of
long-span bridges in the United States. *Progress in Structural
Engineering and Materials* **4(4)**: 372–380.

Prodromakis T and Papavassiliou C (2009) Engineering the
Maxwell–Wagner polarization effect. *Applied Surface Science*
255(15): 6989–6994.

Ranade R, Zhang J, Lynch J and Li VC (2014) Influence of micro-cracking
on the composite resistivity of engineered cementitious composites.
Cement and Concrete Research **58**: 1–12.

Redon C, Li VC, Wu C et al. (2001) Measuring and modifying interface
properties of PVA fibers in ECC matrix. *Journal of Materials in
Civil Engineering ASCE* **13(6)**: 399–406.

Reynolds JA and Hough JM (1957) Formulae for dielectric constant of
mixtures. *Proceedings of the Physical Society Section B* **70(8)**:
769–775.

Saraireh D, Walls S, Suryanto B, Starrs G and McCarter WJ (2017) The
influence of multiple micro-cracking on the electrical impedance
of an engineered cementitious composite. In *Strain-Hardening
Cement-Based Composites* (Mechtcherine V, Slowik V and Kabele
P (eds)). Springer, Dordrecht, the Netherlands, pp. 292–299.

17

Advances in Cement Research

**The electro-mechanical tensile properties
of an engineered cementitious composite**
Saraireh, Suryanto, McCarter and Walls

Schneider CA, Rasband WS and Eliceiri KW (2012) NIH Image to
 ImageJ: 25 years of image analysis. *Nature Methods* **9(7)**: 671–675.
Schwan HP, Schwarz G, Maczuk J and Pauly H (1962) On the
 low-frequency dielectric dispersion of colloidal particles in
 electrolyte solution. *Journal of Physical Chemistry* **66(12)**:
 2626–2635.
Schwarz G (1962) A theory of the low-frequency dielectric dispersion of
 colloidal particles in electrolyte solution. *Journal of Physical
 Chemistry* **66(12)**: 2636–2642.
Shi ZQ and Chung DDL (1999) Carbon fiber-reinforced concrete for
 traffic monitoring and weighing in motion. *Cement and Concrete
 Research* **29(3)**: 435–439.
Soga K (2018) Whole life sensing of infrastructure. In *Developments in
 Earthquake Geotechnics* (Iai S (ed.)). Springer, Cham, Switzerland,
 vol. 43, pp. 111–130.
Spencer BF Jr., Park JW, Mechitov KA, Jo H and Agha G (2017) Next
 generation wireless smart sensors toward sustainable civil
 infrastructure. *Procedia Engineering* **171**: 5–13.
Starrs G and McCarter WJ (1998) The immittance response of
 cementitious binders during early hydration. *Advances in Cement
 Research* **10(4)**: 179–186, https://doi.org/10.1680/adcr.1998.10.4.179.
Suryanto B, Wilson SA, McCarter WJ and Chrisp TM (2015) Self-healing
 performance of engineered cementitious composites under natural
 environmental exposure. *Advances in Cement Research* **28(4)**:
 211–220, https://doi.org/10.1680/jadcr.15.00022.
Suryanto B, McCarter WJ, Starrs G and Ludford-Jones GV (2016)
 Electrochemical immittance spectroscopy applied to a hybrid
 PVA/steel fiber engineered cementitious composite. *Materials &
 Design* **105**: 179–189.
Suryanto B, Tambusay A and Suprobo P (2017a) Crack mapping on
 shear-critical reinforced concrete beams using an open source

digital image correlation software. *Civil Engineering Dimension*
 19(2): 93–98, https://doi.org/10.9744/ced.19.2.93-98.
Suryanto B, McCarter WJ, Starrs G and Chrisp TM (2017b)
 Characterization of fly-ash using electrochemical impedance
 spectroscopy. *Procedia Engineering* **171**: 705–714.
Suryanto B, Buckman JO, McCarter WJ and Taha H (2018a) In situ
 dynamic WetSEM imaging and electrical impedance
 measurements on Portland cement during early hydration.
 Materials Characterization **142**: 86–100.
Suryanto B, Takaoka H, McCater WJ, Saraireh D and Taha H (2018b)
 Impedance measurements on an engineered cementitious
 composite: A critical evaluation of testing protocols. *Measurement*
 129: 445–456.
Tambusay A, Suryanto B and Suprobo P (2020) Digital image correlation
 for cement-based materials and structural concrete testing. *Civil
 Engineering Dimension* **22(1)**: 6–12.
Wansom S and Kanokkanchana K (2017) Electrical impedance
 response for physical simulations of composites with conductive
 fiber-bridged insulating cracks. *Journal Materials Science* **52(17)**:
 10023–10037.
Wen S and Chung DDL (2003) A comparative study of steel-and
 carbon-fibre cement as piezoresistive strain sensors. *Advances in
 Cement Research* **15(3)**: 119–128, https://doi.org/10.1680/adcr.2003.
 15.3.119.
Yang P, Chowdhury S and Neithalath N (2018) Strain sensing ability of
 metallic particulate reinforced cementitious composites:
 experiments and microstructure-guided finite element modelling.
 Cement & Concrete Composites **90**: 225–234.
Yoo DY, You I, Zi G and Lee SJ (2019) Effects of carbon nanomaterial
 type and amount on self-sensing capacity of cement paste.
 Measurement **134**: 750–761.

How can you contribute?

To discuss this paper, please submit up to 500 words to the
editor at journals@ice.org.uk. Your contribution will be
forwarded to the author(s) for a reply and, if considered
appropriate by the editorial board, it will be published as a
discussion in a future issue of the journal.